The Impact of Climate Model Resolution On Tropical–Extra-Tropical Interactions In The Pacific

A thesis submitted to the School of Mathematics of the University of East Anglia in partial fulfilment of the requirements for the degree of Doctor of Philosophy

By Andrew Dawson

June 2011

Abstract

A “low” horizontal resolution coupled climate model, typical of the Intergovernmental Panel on Climate Change fourth assessment report simulations, is shown to have serious systematic errors in the extra-tropical response to El Niño. A “high” resolution configuration of the same model has a much improved response that is similar to observations. The errors in the low resolution model are due to an incorrect representation of the atmospheric teleconnection mechanism that controls extra-tropical sea surface temperatures during El Niño.

It is demonstrated that a realistic simulation of the extra-tropical response to El Niño requires a realistic representation of the atmospheric basic state over the North Pacific. Sea surface temperature biases are a key influence on the atmospheric basic state, and therefore reducing these biases should be a priority in coupled model development. Increased horizontal resolution in the oceanic model component reduces the mean state sea surface temperature biases, and produces a more realistic representation of the extra-tropical response to El Niño. Increased horizontal resolution in the atmospheric component alone does not provide a significant improvement. This suggests that higher resolution in the oceanic model component is more valuable than increased atmospheric resolution for realistically representing this type of climate variability.

The extra-tropical response to El Niño in a climate with atmospheric CO_2 concentrations four times greater than the control climate, is weaker and has an altered spatial signature. Changes to the way Rossby waves are generated over the North Pacific are shown to be more important than changes to the atmospheric basic state in this climate change scenario. The change in the extra-tropical response to El Niño as a response to CO_2 forcing is much smaller than the change due to a reduction in horizontal resolution. This rules out the use of lower resolution coupled models for climate change studies of this process.

Acknowledgements

I am appreciative of the support I have received from both my supervisors, particularly for their patience and willingness to help me learn. Many thanks to David Stevens and Adrian Matthews. Thanks also to the Natural Environment Research Council for providing the funding that supported this research.

I am grateful to the software development teams at the Program for Climate Model Diagnostics and Intercomparison at Lawrence Livermore National Laboratory and the Computational and Information Systems Laboratory at the National Center for Atmospheric Research for developing, maintaining, and supporting the Climate Data Analysis Tools (CDAT) and the NCAR Command Language (NCL) respectively. These tools were used extensively for the data analysis and visualisation in this thesis. A personal mention should go to Charles Doutriaux from PCMDI for his diligent work in supporting CDAT.

Contents

List of tables

List of figures

Chapter 1

Introduction

The climate of a given region is often simply understood as the average weather, and it is something that affects our day to day lives in many ways. Warming of our climate is now unequivocal (*Trenberth et al.*, 2007), and the impact of such warming could include physical, economic, social, and ecological effects. Future climate change is a potentially large problem for humanity, with rising sea levels, decreases in snow and sea ice coverage, and increase in global drought being a few of the many likely physical impacts. It is therefore extremely important that we work to understand the science of our climate, and how it may change in the future.

1.1 The climate system

A more rigorous definition of climate is the statistical description in terms of the mean and variability of relevant quantities over a period of time ranging from months to thousands or millions of years (*Solomon et al.*, 2007). In a wider context climate can be understood as the state of the climate system. The climate system is the term used to describe the system consisting of the atmosphere, hydrosphere, cryosphere, biosphere, land surface, and the interactions between them.

The climate system is extremely complex, with each component having internal variability, and responding to external forcings from the other components. Therefore, in order to understand the behaviour of the climate and for example the effect of a particular perturbation such as increased atmospheric carbon dioxide concentrations due to human activity, it is necessary to consider the climate as a whole system rather than individual

components.

The climate system contains variability on many spatial and temporal scales. It is crucial that we have a good understanding of how the climate system works and how the physical mechanisms determining the variability in the climate system operate, in order for us to be able to understand the bigger questions such as finding out what the potential effects of climate change on our climate may be.

1.2 Climate variability and El Niño

The ocean–atmosphere coupled system exhibits many modes of variability. These range from intra-seasonal modes such as the Madden-Julian Oscillation (MJO; *Madden and Julian*, 1971), to inter-annual modes such as El Niño (e.g., *Philander*, 1990; *Trenberth*, 1997; *Clarke*, 2008), and even inter-decadal modes such as the Pacific Decadal Oscillation (e.g., *Tanimoto et al.*, 1993; *Mantua et al.*, 1997; *Allan*, 2000). Perhaps the most dominant mode of climate variability on a global scale is El Niño, or the El Niño-Southern Oscillation (ENSO). El Niño is characterised by warmer than normal sea surface temperatures (SSTs) in the eastern Pacific and cooler than normal SSTs in the western Pacific. There is an opposing anomalous state where the SSTs in the eastern Pacific are colder than normal. This state is known as La Niña. The tropical Pacific ocean can be described as being in a state of oscillation about these two extremes. However, the time period of the oscillation is not regular, and the amplitude of the El Niño or La Niña conditions is subject to much variation. El Niño is an important process both locally and remotely. Locally in the eastern Pacific, a warming of the SSTs leads to a reduction in biological productivity which has a large impact on the ecosystem in the region.

In order to understand El Niño in more detail, it is helpful to understand some of the basics of tropical atmospheric circulation. In the Pacific Ocean, SSTs are warmer in the west and cooler in the east. This east-west temperature contrast affects the atmospheric circulation. Relatively cold, dry air over the eastern Pacific, where SSTs are colder, sinks to the surface. This air then travels along the equator over increasingly warm SSTs. In the western Pacific this air is warmed and gathers moisture. The warming of the air causes it to rise and release energy as the moisture it carries condenses. The air then moves eastward back across the Pacific to where it began. This simple description of Pacific

circulation was proposed by *Bjerknes* (1969) and is referred to as the Walker circulation.

Let us now consider the effect of perturbations to the Walker circulation. If the Walker circulation increases in strength, then the surface easterly winds increase in strength. This increases upwelling of colder water in the eastern Pacific which in turn will strengthen the east-west SST contrast and therefore further strengthen the Walker circulation. Conversely if the Walker circulation decreases in strength then surface easterly winds at the equator will be weakened, resulting in a decrease of upwelled colder water in the eastern Pacific. This produces a reduction in the east-west SST contrast and hence a decrease in the strength of the Walker circulation. These are both examples of positive feedback systems, where a perturbation in one direction causes the system to tend more to the direction of that perturbation. The idea of these positive feedback systems in the Walker circulation forms the basis for our understanding of El Niño.

The structure of the Pacific, as with other ocean basins, can be approximated as a warm surface layer that is heated by solar radiation, overlying a layer of rapid temperature change (the thermocline) which is on top of a colder deep layer. The action of the easterly trade winds forces the warm surface water over to the west Pacific. The result of this is an increase in the depth of the surface layer and hence increased depth of the thermocline in the west Pacific, and a shallow surface layer that is mixed into the thermocline in the east Pacific. This results in what is known as the Pacific warm pool in the western Pacific and the Pacific cold tongue in the eastern Pacific. When an El Niño event occurs the trade winds weaken and the surface layer of the ocean must adjust to the reduced strength winds. The adjustment produces a shallower than normal thermocline in the western Pacific and a deeper than normal thermocline in the eastern Pacific, and is caused by the propagation of equatorial Kelvin and Rossby waves (*Clarke*, 2008). The net result of this oceanic adjustment is an eastward shift in the location of the warm pool.

As discussed previously, the ocean and atmosphere act as a coupled system in the Walker circulation. The strongest atmospheric coupling to the ocean occurs over the Pacific warm pool, in the form of deep convection. When the warm pool moves eastward during El Niño the location of this strong coupling also moves eastward. As well as changes to the Walker circulation, there are significant non-local impacts of the eastward shift in the Pacific warm pool, these effects are commonly referred to as teleconnections.

1.2.1 Teleconnections in the climate system

During El Niño there is anomalous convection over the western tropical Pacific. This anomalous convection persists through a vertical profile of the tropical atmosphere, implying that vertical motion exists throughout a profile of the tropical troposphere. At the tropopause this anomalous vertical motion becomes divergent motion. Due to conservation of angular momentum, this divergent motion leads to rotation in the upper troposphere. This anomalous vorticity in the upper troposphere generates large perturbations to the atmospheric circulation known as Rossby waves. Rossby waves are planetary scale waves, meaning their scale is comparable to the size of the Earth, and that they are capable of travelling all the way around the globe. A change in the dominant region of atmosphere–ocean coupling in the tropical Pacific could potentially lead to changes in atmospheric circulation on a global scale.

In the tropics, where the anomalous convection that drives Rossby waves is produced, the atmosphere has a baroclinic structure. Convergence at the surface induces cyclonic circulation, and divergence at the tropopause induces anti-cyclonic circulation, meaning that the sense of circulation at the surface and in the upper troposphere are opposite. Unlike the tropical atmosphere, the mid-latitude atmosphere has an equivalent barotropic vertical structure. This type of vertical structure allows upper tropospheric potential vorticity anomalies associated with Rossby wave propagation to induce a surface circulation (*Hoskins et al.*, 1985). Simply put, the effect of an equivalent barotropic vertical structure is that the sense of the circulation in the upper troposphere is the same as that at the surface. The implication of this in terms of El Niño teleconnections is that upper tropospheric Rossby wave anomalies are able to induce anomalous circulation at the surface in the extra-tropics. Surface circulation anomalies can then produce changes in SSTs through alterations to the surface heat balance.

This particular teleconnection from the tropical ocean, through the atmosphere, to the extra-tropical ocean is referred to as the atmospheric bridge (e.g., *Alexander et al.*, 2002). It describes a process whereby tropical SST anomalies are able to indirectly influence extra-tropical SST anomalies, through interactions with the atmosphere. This is an example of an inherently coupled process, and is the process that the majority of this thesis is dedicated to understanding.

Generally speaking, climate variability on all scales is a coupled phenomenon involving complex interactions between the atmosphere and ocean. This implies that numerical models of individual climate system components are not sufficient to properly study climate variability. The need to study coupled climate processes such as this is the driving force behind the development of coupled climate system models. The atmospheric bridge mechanism involves not only the interaction between the atmosphere and the ocean but also interactions between small and large spatial scales, that is between convective anomalies in the tropics and the global general circulation. It is therefore likely that this type of mechanism might be better represented in coupled models with higher horizontal resolution.

1.3 Coupled climate models

A coupled climate model is a numerical representation of the climate system, that allows the components within the system to interact. This type of model allows two-way feedback between each of the individual model components. For example atmospheric circulation is allowed to influence the ocean surface temperature, and in turn the changes in SST can influence the atmospheric circulation. Processes involving the land surface, sea ice, and biosphere have important roles to play in the climate system. However, the focus of this thesis is on the dynamics of the atmosphere and ocean, and their interactions. Therefore, processes directly involving sea ice, land surface, and biosphere components of the climate system are not discussed further.

The oceanic and atmospheric components of a climate model solve sets of equations relevant to the dynamics and thermodynamics of the body of fluid. Typically the equations are solved on a discretized representation of the globe (or represented as a finite sum of spectral modes in spectral models). Global grid point models apply a discretization where the whole surface of the Earth is divided into grid cells and the governing equations are integrated at each grid point or grid cell interior. The exact locations on the grid where solutions are found depends on the specific grid configuration.

The smallest feature that can be represented by a model depends on the distance between neighbouring grid points (or upon the largest retained wavenumber in the case of spectral models). This idea of what a model can and cannot represent is referred to as

resolution. When we describe the resolution of a model we are describing the size of the smallest features the model is able to represent. When we refer to increased or higher horizontal resolution, we mean that there are more grid points in a given area (or more wavelengths are retained in spectral models), and therefore the size of the smallest process that can be directly represented in the model is smaller. The shortest wave that can be resolved by finite differencing has a wavelength of $2\delta x$ where δx is the spacing between grid points, and therefore spans three grid points. For example, to represent a low pressure system there must be at least one grid point within the low pressure system and one either side. This is a one dimensional picture, and of course in two dimensions this would require grid points outside of the feature to the north, south, east, and west. In practical terms it is preferable to ensure that features of interest are much larger than this minimum scale in order to represent them in sufficient detail, and of course the resolution required for this depends upon the scale of the features that are of interest.

Consider the UK Met. Office Hadley Centre model HadCM3, which has a horizontal resolution of $3.75^\circ \times 2.5^\circ$ in longitude $\times$ latitude in the atmosphere. The discretization of the HadCM3 atmosphere in a sub-domain covering the North Atlantic and Europe is shown in figure 1.1a. This resolution corresponds to grid points being spaced every 3.75° in longitude and 2.5° in latitude. The implication of this is that atmospheric feature, such as a low pressure system, with a spatial scale smaller than $3.75^\circ \times 2.5^\circ$ cannot be represented directly in the model.

Climate models are very computationally expensive, requiring a large computing resource and a lot of time to run. An increase to the horizontal resolution of a model substantially increases the amount of computing time/power that is needed to integrate the model. For example, increasing the number of grid points in both the north-south and east-west directions by a factor of 3 increases the size of the grid by a factor of 9. This increase is illustrated in figure 1.1b. This increase in total grid size scales approximately linearly to the increase in computing time required to integrate the model. It is difficult to rationalise the large increase in the computing resources required for such a resolution increase in a coupled climate model without having a good understanding of the effect of increased resolution. It is not enough to determine if higher resolution produces better performance, it is also necessary to determine the reason for any performance differences.

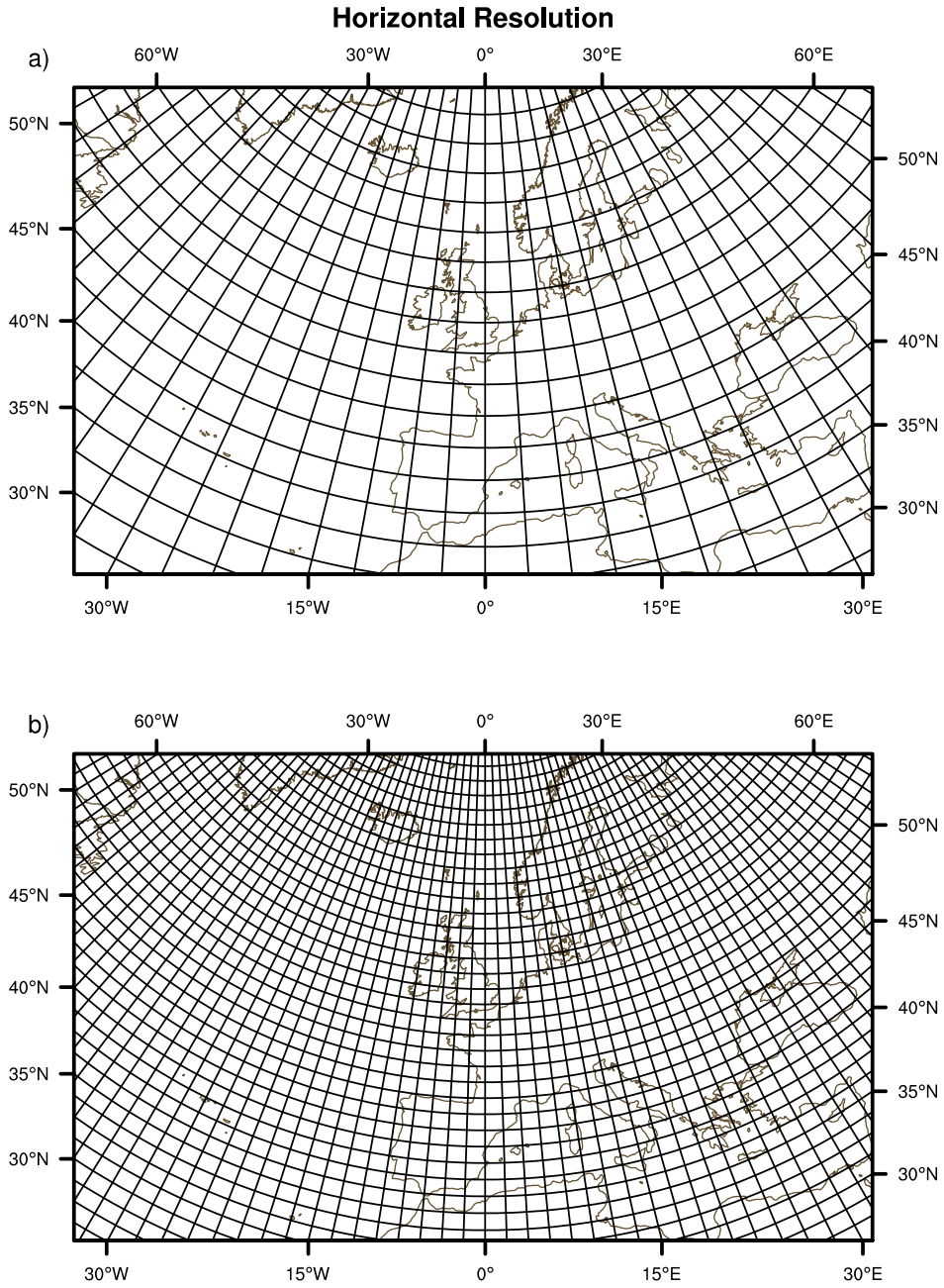

Figure 1.1: Example discretizations on the sphere. The grids are shown only for a sub-domain of the North Atlantic and Europe in order that their structure appear clearer. The grids are representative of the discretization in the atmospheric components of a) HadCM3 (*Pope et al.*, 2000; *Gordon et al.*, 2000), and b) HadGEM1 (*Johns et al.*, 2006).

If the performance gain is small or not well understood then it may be wise to invest extra computational resources elsewhere, for example, in additional vertical resolution or further physics elements.

Since the start of coupled climate modelling, horizontal resolution has competed for computing time with model physics and other elements, such as number and length of simulations. However, there has been steady increase in typical horizontal resolution over time. At the time of the first Intergovernmental Panel on Climate Change (IPCC) assessment report (*Houghton et al.*, 1990) the typical horizontal resolution of coupled models was 3–10° in the atmosphere and 2–10° in the ocean. This increased to 3–5° in the atmosphere and 1–5° in the ocean by the time of the IPCC's second assessment report (*Houghton et al.*, 1995). The coupled models used for the IPCC's third assessment report (TAR; *Houghton et al.*, 2001) had typical resolution of 2.5–5° in the atmosphere and 1–4° in the ocean. Most of the models up to and including those used in the TAR had to make use of flux correction techniques in order to suppress drift in the coupled system. This technique provides a way of perturbing the modelled surface heat, water and momentum fluxes so as to maintain a stable climate. By the time of the IPCC fourth assessment report (AR4; *Solomon et al.*, 2007) typical model resolution and physics had improved again, this time to a point where most models no longer needed to make flux corrections in order to maintain a stable climate. The typical resolutions of these models are 2° in the atmospheric component and 1°in the oceanic component.

The AR4 class models represent the current state of the art in coupled climate models. However, many coupled models of AR4 resolution suffer from systematic errors in simulating mean climate and its variability. The double inter-tropical convergence zone (ITCZ) problem (*Mechoso et al.*, 1995), where a persistent ITCZ south of the equator in the eastern and central equatorial Pacific is produced in addition to the observed ITCZ north of the equator, is common in AR4 models. This systematic error in simulating the mean climate in the tropical Pacific affects the location of the Walker circulation and the simulation of El Niño. Many AR4 models have an equatorial Pacific cold tongue that is too equatorially confined and extends too far into the western tropical Pacific. This implies an unrealistic simulation of coupled heat transfer mechanisms, such as tropical instability waves (TIWs, *Philander et al.*, 1986), in the tropics.

Increased horizontal resolution in coupled climate models has historically improved the accuracy of climate simulations (e.g., *Gordon et al.*, 2000; *Pope and Stratton*, 2002; *Johns et al.*, 2006). There is a growing body of evidence to show that resolving processes on scales as small as the oceanic mesoscale in coupled climate models can improve their ability to realistically represent large-scale mean climate and its variability. For example, *Roberts et al.* (2004) found that increasing the ocean resolution of the UK Met. Office coupled general circulation model (GCM) in its HadCM3 configuration to $1/3^\circ$ resulted in many improvements in the simulation of oceanic circulation.

The AR4 class models are the baseline for comparisons in this work. It seems likely that further increases from AR4 resolution will produce improved representations of coupled phenomena, particularly those with some dependence on multiple spatial scales such as the atmospheric bridge mechanism. It is the goal of this thesis to understand in detail the effect of horizontal resolution on these types of processes.

1.4 Thesis outline

The motivation for this thesis and necessary background information are given in this chapter. Details of the models and specific model integrations, observational datasets, and core data analysis methods that are used throughout the study are given in chapter 2. Chapter 3 assesses the performance of coupled models of both high and low horizontal resolution with respect to El Niño and the atmospheric bridge mechanism. The models and observations are used to further understand the physics of the extra-tropical response to El Niño, and thus determine the impact of horizontal resolution on the mechanism. The core findings of chapter 3 have been published in *Dawson et al.* (2011). Using the analysis framework built in chapter 3, chapter 4 investigates the effect of horizontal resolution on the modelled extra-tropical response to El Niño in more detail, through analysis of model integrations where the resolution of the oceanic and atmospheric components of the model are varied independently. The work in chapter 5 traces the source of errors in the representation of the extra-tropical response to El Niño in the low resolution coupled model by understanding how atmospheric errors may be caused by the oceanic component of the modelled coupled system. In chapter 6 an attempt to understand the potential effect of a warming climate on the dynamics of the extra-tropical response to El Niño using

a high resolution climate change simulation is made. The results are discussed within the framework of the previously developed knowledge of the impact of resolution on this process. Chapter 7 deviates somewhat from the previous work, and attempts to understand variability in the North Pacific Ocean on time scales longer than El Niño.

Chapter 2

Models, datasets, and analysis methods

This chapter introduces the coupled climate models that are used throughout this thesis, including details of the model configurations. There is also a discussion of the observational data sets used for comparison with model results. The core analysis techniques used to understand the behaviour of the models are then outlined.

2.1 High resolution climate modelling

The overall aim of this study is to determine the effect and potential benefits of increased horizontal resolution in coupled climate models. For this study we use two coupled climate models, a next-generation model with high horizontal resolution in both the atmospheric and the oceanic component, and a lower resolution model typical of the coupled climate forecast models used for the Intergovernmental Panel on Climate Change (IPCC) fourth assessment report (AR4; *Randall et al.*, 2007). The novel aspect to this study is that apart from horizontal resolution, there are as few differences between the two models as possible. This provides an excellent opportunity to study the effect of increased horizontal resolution in isolation from other changes.

2.1.1 HiGEM and HadGEM

The models used in this work are those developed as part of the UK High Resolution Global Environmental Modelling project (UK-HiGEM; *Shaffrey et al.*, 2009) and the UK

Japan Climate Collaboration (UJCC; *Roberts et al.*, 2009). The aim of these projects was to develop a high resolution coupled climate model based on the UK Met Office (UKMO) coupled climate model HadGEM1 (*Johns et al.*, 2006; *Martin et al.*, 2006; *Ringer et al.*, 2006), a model that has been used for contributions to the IPCC AR4. The product of these projects is the high resolution coupled model HiGEM. HiGEM sets a precedent for horizontal resolution in a coupled climate model, with resolution of $1.25^\circ \times 0.83^\circ$ longitude $\times$ latitude in the atmosphere and $1/3^\circ \times 1/3^\circ$ in the ocean (including sea ice). The lower resolution configuration, simply called HadGEM, has the same resolution as HadGEM1, that being $1.875^\circ \times 1.25^\circ$ in longitude and latitude in the atmosphere, and $1^\circ \times 1^\circ$, increasing to $1/3^\circ$ meridionally near the equator, in the ocean. The rationale for the increase in resolution in HiGEM is to be able to better represent small scale features, such as weather systems in the atmosphere and eddies and steep gradients in the ocean, and have the ability to resolve the interactions between these small scales features and the large scale climate. It is believed that the accurate representation of such small scale features is crucial to producing realistic climate models. For example tropical instability waves, whose size mean they cannot be properly resolved in a model with equivalent resolution to HadGEM, are significant in near surface momentum and heat balances both in the ocean and the atmosphere across the entire tropical Pacific (*Willett et al.*, 2006).

The atmospheric components of both HiGEM and HadGEM use a non-hydrostatic dynamical core (*Davies et al.*, 2005) formulated on an Arakawa C grid (*Haltiner and Williams*, 1980). A semi-Lagrangian integration scheme is used to advect the prognostic variables. The semi-Lagrangian formulation allows relatively long time steps while retaining numerical stability and high accuracy. It also preserves the values of conservative properties fairly accurately and is therefore particularly useful for an accurate represention of the advection of water vapour and other trace constituents (*Holton*, 2004). The oceanic component of the models is based on the Bryan-Cox code (*Bryan*, 1969; *Cox*, 1984) and is formulated on a spherical latitude-longitude grid. Convergence of the meridians results in a singularity at the poles, which is treated as a land point. Convergence of the meridians also requires that tracers and baroclinic velocities be Fourier filtered north of 80°N (*Shaffrey et al.*, 2009). The solution for the external mode (depth integrated velocities) is found using a linear implicit free surface scheme (*Dukowicz and Smith*, 1994).

Moving to higher resolution involved substantial changes to the physical parameterisations in HadGEM1. Full descriptions of these changes can be found in *Shaffrey et al.* (2009) and *Roberts et al.* (2009). There are significant improvements to the coupling between the atmosphere and ocean in HiGEM, in particular the effects of ocean currents on surface fluxes of moisture, momentum, and heat are included. The parameterisation for frozen soil run-off is altered to improve the seasonal cycle of land surface moisture and temperature, and the threshold for activation of the moisture diffusion scheme, which prevents numerical instabilities in the atmospheric component, is increased in HiGEM since the higher resolution means the grid point storms this parameterisation is designed to suppress are less common. Most of the changes to parameters in the ocean reflect that higher horizontal resolution enables the use of less explicit numerical dissipation to maintain numerical stability. The adiabatic mixing scheme of *Gent and McWilliams* (1990) used in HadGEM1 is turned off or used with very low parameter values in HiGEM. HiGEM uses the scale selective biharmonic formulation of momentum dissipation rather than the Laplacian formulation of HadGEM.

There are multiple versions of the HiGEM models. Two versions are used in this study, version 1.1 and version 1.2. Version 1.1 is an earlier version of the model developed by the UK-HiGEM project, and was operated as part of the UJCC project and run on the Earth Simulator[1] supercomputer. A version of HadGEM1 that had been improved upon by the UKMO since the submission of results to the IPCC AR4 was used as a template for HiGEM1.1. The later 1.2 version was used by the UK-HiGEM project and run in the UK at HPCx[2]. There are some notable differences between these two versions. Eddies in the HiGEM1.1 ocean are weakly parameterised in the tropics and the mid-latitudes, with a stronger effect at high latitudes. This eddy parameterisation scheme is turned off in the HiGEM1.2 oceanic component. There are also differences in the background vertical diffusivity, and the mixing efficiency and depth scale parameterisations in the ocean mixed layer model. These differences could potentially mean different behaviours in HiGEM1.1 and HiGEM1.2.

Each of HiGEM1.1 and HiGEM1.2 has an equivalent lower resolution configuration, those being HadGEM1.1 and HadGEM1.2 respectively. These configurations attempt to

[1] see http://www.earthsimulator.org.uk
[2] see http://www.hpcx.ac.uk

be as close to the high resolution models as possible in terms of physics. The key differences between the high and low resolution configurations are in the resolution dependent parameters. The moisture diffusion parameter for the atmosphere must be decreased to account for the increased frequency of grid point storms with the HadGEM numerics compared to HiGEM. In the oceanic component the vertical level distribution in the lower resolution configurations is the same as that used in HadGEM1. This allows these configurations to use the same bathymetry as HadGEM1. The vertical level distribution in the high resolution configuration of the oceanic component is modified to produce a higher order numerical representation. The lower resolution configurations use the adiabatic mixing scheme of *Gent and McWilliams* (1990) referred to as the GM scheme, the same scheme used in HadGEM1. The high resolution configurations both use the adiabatic biharmonic scheme (biharmonic GM) of *Roberts and Marshall* (1998), with HiGEM1.1 also operating the GM scheme with very weak parameter values. The biharmonic adiabatic mixing scheme is more suited to higher resolution eddy resolving models because it acts strongly to suppress vorticity gradients at the grid scale but has a weaker effect at larger resolved scales. It is also necessary to parameterise some basin exchanges in the lower resolution configurations. Whilst the Red Sea and Persian Gulf entrances are resolved by HiGEM, they are too small to be resolved in HadGEM, and therefore exchanges with these basins must be parameterised.

2.2 Observational data

Comparing model simulations to observed data is a key part of this work, allowing us to determine how realistically a model has performed. The observational fields used in this study are all from gridded data products. Gridded data products are values of a particular physical quantity on a grid that is a discretized representation of the globe. A value of the quantity is provided for every grid cell in the domain (excluding grid cells over land for oceanic fields) and at every point in the data time series. Gridded fields are usually produced from more sparse observational data sets (e.g., atmospheric soundings, in situ measurements) using an interpolation technique. However, since the advent of satellite remote sensing, interpolation has been relied on much less when producing global gridded data products. The use of gridded data products ensures the observational data is spatially

and temporally complete and can be readily compared to the equivalent model output.

2.2.1 Sea surface temperature data

All the observed sea surface temperature data used in this study are from the UK Meteorological Office (UKMO) Hadley Centre's sea ice and sea surface temperature data set HadISST1.1 (*Rayner et al.*, 2003). This data set consists of a combination of monthly globally-complete fields of SST and sea ice concentration on a 1° latitude-longitude grid from 1870 to date. The relatively high resolution and spatial and temporal coverage of this SST data set makes it ideal for comparing with climate model output. The data is produced from observations, in-filled using a two stage reduced-space optimal interpolation (RSOI) technique (*Rayner et al.*, 2003; *Kaplan et al.*, 1997). This method involves reconstructing large patterns of spatial variability from empirical orthogonal functions (EOFs, discussed in section 2.3.1). This has implications on the validity of using EOF analysis to analyse the variability of the SST field for the full length of the time series, where there is a risk of recovering patterns of variability used to in-fill the sparse SST observations. However, this is not an issue when applying EOF analysis to recent portions of the data set where many in situ observations contribute to the field and the RSOI technique is not relied upon so heavily. This issue is discussed in detail in chapter 7.

2.2.2 Atmospheric fields

All of the atmospheric fields used in this study are from the NCEP/NCAR Reanalysis Project[3] (*Kalnay et al.*, 1996). This data set is produced using an analysis/forecast model system to perform data assimilation using past data from 1948 onwards. The result of this process is a globally and temporally complete data set, with fields available on 17 pressure levels and 28 sigma (model) levels.

The analysis/forecast model assimilates only certain variables. As a consequence, the influence of observations varies across the output variables. *Kalnay et al.* (1996) classify the output fields of the reanalysis into three categories: those that are strongly influenced by observations, those that are somewhat influenced by observations but will be strongly influenced by the model, and those that are not influenced by observations at all and are

[3]Reanalysis data provided by the NOAA/OAR/ESRL PSD, Boulder, Colorado, USA, from their web site at http:www.cdc.noaa.gov/

purely model derived. Fields that are strongly influenced by observations include upper level winds and geopotential. These are fields that tend to vary on spatial scales large enough so that they can be represented with a good deal of accuracy by assimilation of relatively sparse observations. Other fields such as precipitation are not assimilated into the model and thus are entirely based on model parameterisations. It is therefore worth bearing in mind the level of observational influence when interpreting reanalysis derived data. Throughout this thesis reanalysis will be referred to as observations, although here we have noted that strictly this is not the case.

The NCEP/NCAR reanalysis was chosen over the European Centre for Medium-Range Weather Forecasting (ECMWF) 40 year reanalysis project ERA-40 (*Uppala et al.*, 2006) primarily because of the longer length of the NCEP/NCAR reanalysis. The horizontal resolution of the ERA-40 reanalysis fields (about 1° latitude-longitude) is greater than that of the NCEP/NCAR reanalysis (2.5° latitude-longitude), but the benefit of this improved resolution does not outweigh the benefit of the longer NCEP/NCAR reanalysis time series. Due to its extended length, data from the new NCEP Twentieth Century Reanalysis Project[4] (20CR; *Compo et al.* 2011) is used in chapter 7. This data set uses the same analysis/forecast model as the NCEP/NCAR Reanalysis but has a temporal coverage from 1871–2008.

2.3 Data analysis techniques

There are several data analysis techniques that are used heavily throughout this work. The details of the core methods, empirical orthogonal function analysis, and regression analysis, are explained in detail here.

2.3.1 Empirical orthogonal function analysis

Empirical Orthogonal Function (EOF) analysis, also known as Principal Component Analysis (PCA), is a method that extracts mathematical relationships of variability between many variables. In climate studies these variables are often values of some field (e.g., sea surface temperature) at many locations in space, and for multiple times. A complete

[4]20th Century Reanalysis V2 data provided by the NOAA/OAR/ESRL PSD, Boulder, Colorado, USA, from their Web site at http://www.esrl.noaa.gov/psd/

discussion of EOF analysis can be found in *Preisendorfer* (1988).

The analysis involves finding spatial patterns of coherent variability that exist in the input data set. These spatial patterns are often referred to as modes of variability. The spatial patterns are the eigenvectors of the covariance matrix of the input data. The corresponding eigenvalues describe the amount of variance in the input data set that is explained or accounted for by a particular mode. The temporal evolution of each mode is found by projecting the input data onto that mode, producing a times series.

A detailed mathematical description of EOF analysis, a discussion of the application of EOF analysis on large data sets, and relevant procedures for the application and interpretation of EOF analysis are given in appendix B.

2.3.2 Regression analysis

Regression analysis is a statistical tool that may be used to evaluate the relationship between one or more independent variables, X_1,X_2,...,X_n, and a single dependent variable, Y. This work uses simple linear regression extensively to understand the linear relationship between one independent variable (a time-series of sea surface temperature) and a dependent variable at each grid point in the observed or modelled field. This technique allows the investigation of how the temporal variability of atmospheric and oceanic fields are related to the variability of sea surface temperature at a particular point in space (or an area average).

2.3.2.1 Simple Linear Regression

If an exact linear relationship exists between the independent and dependent variables then this can be expressed in the form of the equation for a straight line,

$$Y = \alpha + \beta X. \tag{2.1}$$

In reality it is unlikely that the relationships between a given independent and dependent variable will be exactly linear. Instead the values of α and β are chosen so as to produce a straight line that best fits the data points in X–Y space. This approach produces a model of the form

$$\hat{Y} = \hat{\alpha} + \hat{\beta} X, \tag{2.2}$$

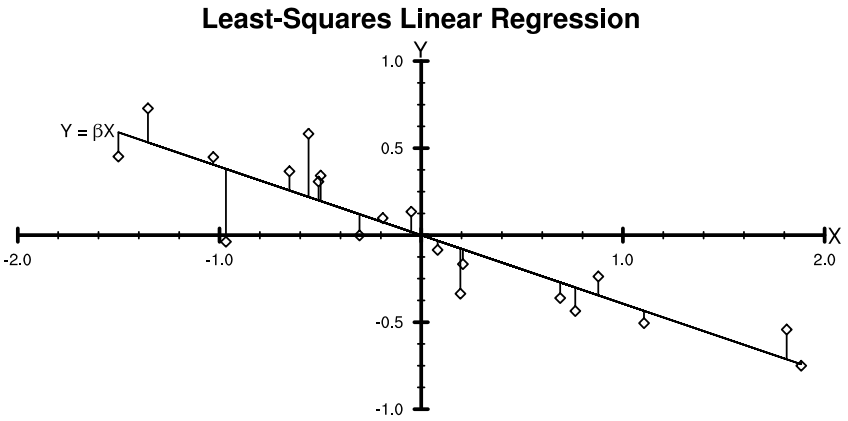

Figure 2.1: An example of simple linear regression. The diamonds mark observed data points and the solid line is the line of best fit as given by equation 2.8. The vertical lines show the residuals, the sum of the squares of which are minimised.

where $\hat{Y}$ is the estimated value of the dependent variable at a given value of the independent variable X, and $\hat{\alpha}$ and $\hat{\beta}$ are the regression coefficients. Here best fit refers to the least-squares residual approach. This approach requires that the sum of the squared residuals (vertical lines in figure 2.1) be minimized. Mathematically this requires the solution of the minimisation problem

$$Q(\alpha,\beta) = \sum_{i=1}^{n} (y_i - \alpha - \beta x_i)^2, \tag{2.3}$$

where n is the number of observations. The values of α and β that minimize Q are

$$\hat{\beta} = \frac{\sum_{i=1}^{n} (x_i - \bar{x})(y_i - \bar{y})}{\sum_{i=1}^{n} (x_i - \bar{x})^2}, \tag{2.4}$$

$$\hat{\alpha} = \bar{y} - \hat{\beta}\bar{x}, \tag{2.5}$$

where an overbar indicates the sample mean (e.g., *von Storch and Zwiers*, 1999; *Wilks*, 2006). The regressions in this work are performed exclusively with anomaly time series, meaning that both the independent and dependent variables have a mean of zero. This allows us to use a simplified form for $\hat{\alpha}$ and $\hat{\beta}$:

$$\hat{\beta} = \frac{\sum_{i=1}^{n} x_i y_i}{\sum_{i=1}^{n} {x_i}^2}, \tag{2.6}$$

$$\hat{\alpha} = 0, \tag{2.7}$$

and hence replace equation 2.2 with

$$\hat{Y} = \hat{\beta} X. \tag{2.8}$$

The best fit line produced using equation 2.8 is shown as the solid line in figure 2.1.

2.3.2.2 Regression Maps

The simple linear regression technique is used to understand the relationship between the time series of a field at every grid point and a given time series. This involves computing the regression coefficient, $\hat{\beta}$, for the dependent time series and the time series at each grid point in the dependent variable. The resulting grid of regression coefficients can be visualised as a regression map (e.g., *Kiladis and Weickmann*, 1992). This map allows the identification of climate signals associated with a given time series.

For example, using gridded vorticity anomalies as the dependent variable and an SST index representative of the SST variability due to El Niño as the independent variable allows one to visualise atmospheric circulation signals associated with El Niño, and hence to establish links between El Niño and atmospheric properties in remote locations. However, it is important to understand that the regression technique does not allow us to directly establish any type of cause and effect mechanism, it just shows mutual relationships between time series.

Chapter 3

The North Pacific extra-tropical response to El Niño in coupled climate models

This chapter aims to understand the role of horizontal resolution in the simulation of the extra-tropical response to El Niño in coupled climate models. The performance of coupled models at high and lower horizontal resolutions are compared to observations.

3.1 El Niño and the atmospheric bridge

El Niño is one of the major modes of global climate variability. For coupled models to be used for both long and short term climate prediction, they must be able to accurately represent El Niño. An accurate representation of El Niño not only requires realistic tropical SST anomalies, but also an accurate representation of the extra-tropical SST response, as extra-tropical SSTs are also important in the climate system, with SST gradients influencing the location of mid-latitude storm tracks (*Norris*, 2000; *Inatsu et al.*, 2002; *Brayshaw et al.*, 2008). *Deser and Blackmon* (1995) used empirical orthogonal function (EOF) analysis of observed winter SST anomalies to understand North Pacific El Niño teleconnections. Their EOF 1 pattern is a canonical representation of the spatial distribution of El Niño SST anomalies in both the tropical Pacific and the extra-tropical North Pacific.

Tropical SST anomalies during El Niño lead to convection anomalies in the tropics.

These convection anomalies lead to anomalous divergence and associated anomalous vorticity in the upper troposphere. These vorticity anomalies drive atmospheric Rossby waves that affect global atmospheric circulation. These large-scale atmospheric teleconnections alter the surface energy balance in the extra-tropics, largely due to surface wind speed anomalies affecting sensible and latent heat fluxes (*Deser and Blackmon*, 1995; *Alexander*, 1992a), but changes in near surface temperature, humidity, and cloud distribution also have a role to play (*Alexander et al.*, 2002). The atmosphere acts as a bridge spanning from the tropical Pacific to the extra-tropical North Pacific, hence this teleconnection mechanism is often referred to as the atmospheric bridge.

Most models used for the Intergovernmental Panel on Climate Change (IPCC) fourth assessment report (AR4) have an inaccurate representation of the meridional extent of El Niño SST anomalies in the eastern tropical Pacific, and produce SST anomalies that extend too far to the west (*Randall et al.*, 2007). Another common problem in AR4 models is the inability to accurately simulate the temporal variation of SSTs during El Niño, with variability generally occurring on time scales faster than observed (*AchutaRao and Sperber*, 2002). *Navarra et al.* (2008) found that increased atmosphere resolution alone was unable to eliminate the systematic westward shift of El Niño SST anomalies in coupled models. However, it has been shown that high resolution in the atmosphere component of a coupled model can improve the representation of El Niño, in particular the temporal SST variability in the tropics (*Guilyardi et al.*, 2004; *Navarra et al.*, 2008). *Shaffrey et al.* (2009) found that the simulation of tropical El Niño SST anomalies is improved in integrations of HiGEM1.2. The ability of HiGEM1.2 to simulate TIWs improves the representation of mean climate, which in turn improves the simulation of El Niño.

In this chapter we will conduct a detailed examination of the differences in the global simulation of El Niño between the low resolution model HadGEM1.2 and the high resolution model HiGEM1.2. We will build on the preliminary findings of *Shaffrey et al.* (2009), which focused on the core tropical variability of El Niño, while we focus particularly on the physical mechanisms involved in the extra-tropical response to El Niño. The HiGEM1.2 and HadGEM1.2 models are very similar in parameterisation and configuration; their only difference is the horizontal resolution and accompanying changes to certain model parameters such as sub-gridscale mixing that need to be made to ensure

stability. The overall aim is to determine the improvement that can be made by moving to higher horizontal resolution. This not only means determining if the performance of the high resolution model is better or worse than the low resolution model, but also understanding the reasons for any performance differences. Coupled modelling is computationally expensive and increases in horizontal resolution compete for computational resources with other model improvements, such as increasing the vertical resolution or addition of further "physics" elements. Hence, it is important that resolution should not be increased without understanding where and why it is needed.

3.2 Sampling and data analysis

The aim of the work in this chapter is to examine the way in which extra-tropical SSTs in the North Pacific vary in relation to El Niño. This problem requires careful consideration of the data sampling technique, and how the chosen analysis methods will be applied to the data.

For this study all data fields are first averaged into individual November-March (NDJFM) seasonal means. This reflects the tendency for effects of El Niño both locally in the tropical Pacific, and in the North Pacific from teleconnections, to be more pronounced during boreal winter (*Philander*, 1990). The more standard December-February (DJF) definition of boreal winter is not particularly well suited to this experiment. It takes the atmosphere around two weeks to respond to anomalous SSTs in the tropical Pacific, and then the North Pacific SSTs integrate the forcing from the atmospheric bridge over several months (*Alexander et al.*, 2002). Hence, the extension of the sampling period is crucial so as to include both tropical SST variability and the extra-tropical North Pacific SST response.

A sampling period of 50 NDJFM seasons is used throughout this study. The size of this sampling period is constrained by both the amount of reliable observed SST data available and the length of the HiGEM1.2 and HadGEM1.2 integrations. Observed SST in the tropical Pacific can be considered reliable from the late 1950s onwards. For this study observed winter seasons from 1957/58–2006/07 are used. The number of years of model integrations available from both HiGEM1.2 and HadGEM1.2 at the time of the study is 70 years. Both models experience a significant adjustment period during the first

20 years of integration. This period is removed and the following 50 years are used for analysis.

Initially empirical orthogonal function (EOF) analysis is used to understand the spatial and temporal variability of Pacific SST anomalies associated with El Niño. EOF analysis involves the mathematical decomposition of a temporal-spatial data set into distinct modes of variation. A detailed description of this method is given in chapter 2. A spatial domain for the EOF analysis is defined as 120°E–100°W, 20°S–60°N. This reflects the necessity of including the tropical Pacific in order to capture tropical SST variability directly due to El Niño, and the North Pacific SST response. This is the same region used by *Deser and Blackmon* (1995) in their observational analysis of North Pacific SST variability in relation to El Niño.

The response of the atmosphere to the tropical SST forcing associated with El Niño is examined using the linear regression technique described in chapter 2. Maps of atmospheric anomalies are produced by regressing the field onto a suitable SST index. The SST index used for all regression maps is defined as the time series of the area average of SST anomaly in the region 178°W–106°W, 6°S–6°N. This is the same region used by *Deser and Blackmon* (1995). This area is located so as to capture the core tropical SST variability during El Niño. this time series will be referred to as the Equatorial Pacific (EP) index. Regression maps represent the anomaly in response to a 1°C change in the EP SST index.

3.3 North Pacific SST variability associated with El Niño

Prior to interpretation of EOF analysis it is essential to determine which EOFs are potentially physically meaningful, and which EOFs are likely to be purely mathematical modes of variability or noise. The method of *North et al.* (1982)is used to determine which EOFs are degenerate and which could have a physical interpretation. This method is described in detail in appendix B. When an EOF is degenerate, its pattern and those from neighbouring EOFs are mixed. Attempting to interpret degenerate EOFs is unwise as the patterns, which may represent independent processes in the underlying dynamics, cannot be separated.

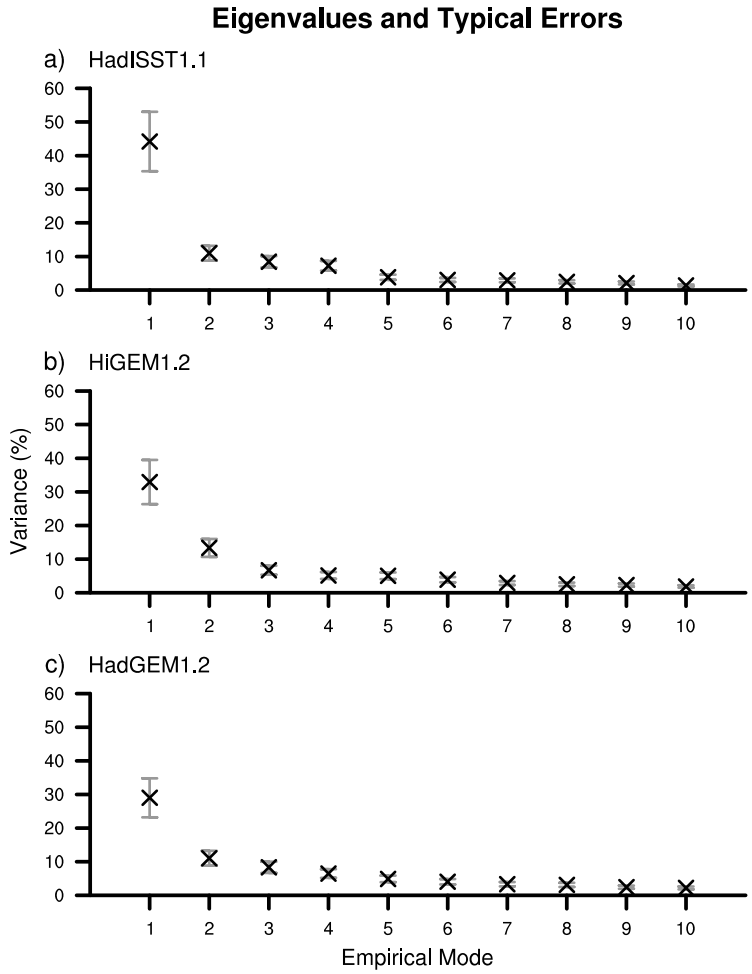

Figure 3.1: EOF eigenvalues and typical errors, expressed as percentage of variance explained, calculated using the method of *North et al.* (1982). a) HadISST1.1, b) HiGEM1.2, and c) HadGEM1.2.

The magnitude of the first 10 eigenvalues, expressed as percentage of variance explained, along with typical errors calculated using the method of *North et al.* (1982) for HadISST1.1, HiGEM1.2, and HadGEM1.2 are shown in figure 3.1. This clearly shows that EOF 1 of NDJFM Pacific SST anomaly is not degenerate in any of the data sets, as the typical error for the first eigenvalue λ_1 is much smaller than the difference $\lambda_1 - \lambda_2$ in all cases. EOF 2 is also not degenerate for HiGEM1.2, however the size of the typical error for λ_2 in HadISST1.1 and HadGEM1.2 is comparable to the size of $\lambda_2 - \lambda_3$. This means that EOF 2 for HadISST1.1 and HadGEM1.2 should be treated with great caution as the typical error in EOF 2 will be comparable to the size of EOF 3, and hence the variance of modes 2 and 3 cannot be separated reliably. The remaining EOFs are also degenerate, the

implication is that none of the variance after mode 1 can be reliably separated.

Deser and Blackmon (1995) show EOF 2 of observed NDJFM Pacific SST anomaly for northern winters 1951/1952–1991/1992 using data from the Comprehensive Ocean-Atmosphere Data set (COADS) (*Woodruff et al.*, 1987, 1993). In their analysis EOF 2 is not shown to be degenerate and is described as a North Pacific mode. Upon analysis of HadISST 1.1 for this time period, EOF 2 appears to be well separated, in contrast to the period 1957/58–2006/07, shown in figure 3.1. This suggests that EOF 2 in HadISST 1.1 is sensitive to the particular time period chosen for the analysis, at least when working with relatively short high quality observation record.

With EOF 2 of observed SST anomaly being degenerate in our case, analysis based on EOF 1 will be acceptable, however analysis based on EOF 2 would be unwise since a comparison with observational data would not be valid, and anything based on EOF 3 or further would be physically meaningless.

Figure 3.2 shows normalised EOF 1 of NDJFM Pacific SST anomaly for each of HadISST1.1, HiGEM1.2, and HadGEM1.2. The normalised maps are constructed by correlation of the principal component time series associated with EOF 1 (PC 1) and the data time series (columns of the design matrix, equation B.1). This is a measure of the spatial localisation of the co-varying part between NDJFM Pacific SST anomaly and its primary mode of temporal variability, in other words it shows the areas in which the observed or modelled SST varies in the same way as the centre of action of EOF1. Correlations that are not significant at the 5% level are marked with hatching. Significance is determined by a Student's t-test using the Fisher Z transformation (*Wilks*, 2006)

$$Z = \frac{1}{2} \ln \left(\frac{1+r}{1-r} \right), \tag{3.1}$$

where r is the Pearson correlation coefficient. Note that since $-1 \leq r \leq 1$ the Z transformation can be expressed in terms of inverse hyperbolic tangent

$$Z = \tanh^{-1} r. \tag{3.2}$$

Under the null hypothesis that $r = 0$ the distribution of Z approximates a Gaussian distribution with $\mu = 0$ and $\sigma = (n-3)^{-\frac{1}{2}}$ where n is the sample size. Testing at the 5%

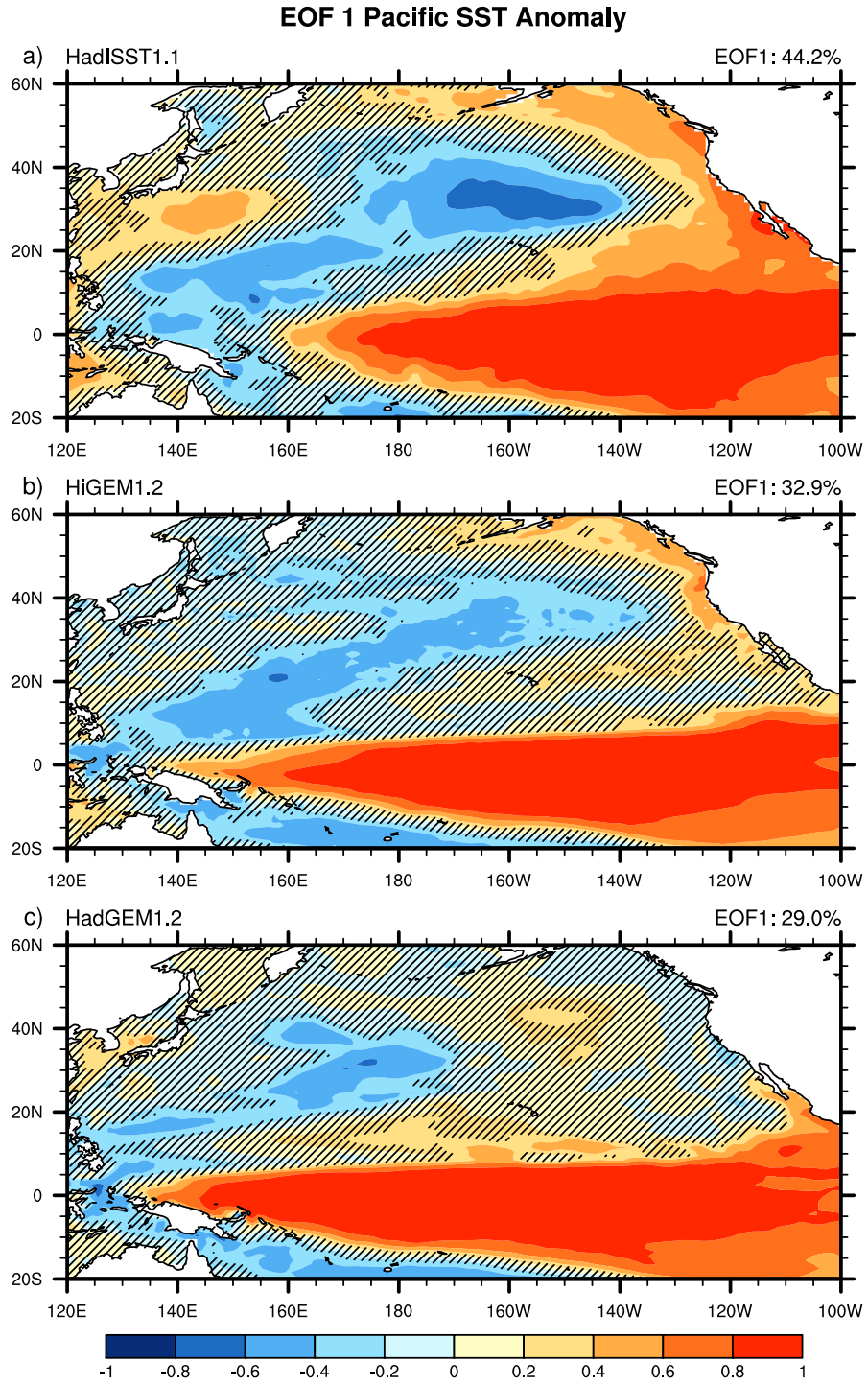

Figure 3.2: EOF 1 of northern winter (NDJFM) Pacific SST anomaly normalised by correlation. Correlations not significant at the 5% level are hatched. The contour interval is 0.2. a) HadISST1.1, b) HiGEM1.2, and c) HadGEM1.2.

significance level produces the significant Z value

$$Z_{sig} = 1.96\sigma, \tag{3.3}$$

where any Z value satisfying $|Z| > Z_{sig}$ is deemed to be locally significant at the 5% level. The corresponding significant correlation value can be determined using equation 3.2. For these EOF calculations $n = 50$ giving $\sigma = (50-3)^{-\frac{1}{2}}$ which yields a critical Z transform value of 0.286. This corresponds to correlations with absolute value 0.278 or higher. Therefore any location with a correlation with an absolute value of 0.278 or higher is deemed to be significant at the 5% level.

EOF 1 of observed NDJFM Pacific SST anomaly (figure 3.2a) shows statistically significant warming of the eastern equatorial Pacific cold tongue, and corresponding cooling in the western Pacific warm pool. This describes the eastward movement of the Pacific warm pool during El Niño. The suggestion that EOF 1 shows El Niño variability can be confirmed by examining the periodicity of PC 1 and showing that it corresponds to El Niño. Figure 3.3 is a plot of the NINO3 index[1] and PC 1 for the time period 1957/1958–2006/2007. The NINO3 index (*Trenberth*, 1997) is a time series of SST averaged over the region 5°N–5°S and 150°–90°W and is representative of the core SST variability in the eastern equatorial Pacific cold tongue during El Niño. The correlation coefficient between PC 1 and the NINO3 index is 0.94. Clearly PC 1 is capturing El Niño very well. This is suitable confirmation that EOF 1 is a physical, rather than a purely mathematical mode of variability.

EOF 1 in both HiGEM1.2 and HadGEM1.2 (figures 3.2b and 3.2c) have significant tropical correlations similar to those of the observations, however the equatorial warming extends considerably further westward across the Pacific Ocean than is observed. This pattern of extended warming is commonly noted in many other coupled climate forecast models (*Randall et al.*, 2007). The core differences between the high and low resolution models are in the extra-tropical component of El Niño. This component of El Niño is characterised in the observed data set by warming of SSTs along the coast of North America and south of Japan, and cooling in the central North Pacific.

[1] NINO3 index available from the Climate Prediction Center http://www.cpc.ncep.noaa.gov/data/indices/

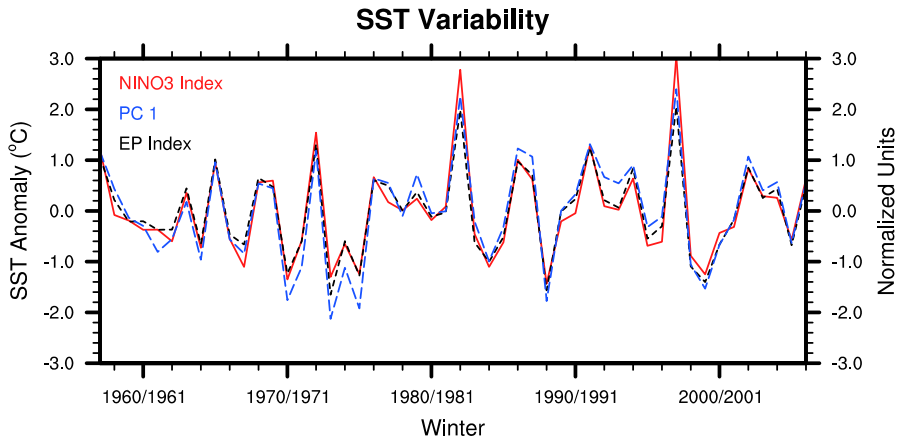

Figure 3.3: Nino3 index (°C, red line), PC 1 for observed NDJFM Pacific SST anomaly (normalized units, blue line), and the EP index (°C, black line) for northern winters of 1957/1958–2006/2007.

Generally speaking, extra-tropical correlations are weaker in HiGEM1.2 than in observations; despite this, there are still similarities between HiGEM1.2 and the observations. There is significant warming along the coast of North America, and cooling in the central North Pacific. The Western North Pacific region is simulated poorly by HiGEM1.2 with negligible correlations there compared with those of up to 0.6 as seen in the observations.

HadGEM1.2, like HiGEM1.2, shows considerably weaker correlations in the extra-tropics, however it also exhibits an almost entirely different extra-tropical pattern. There are very few areas of significant correlation in the North Pacific compared with observations. There is a significant warm anomaly in the central Pacific at (150°W, 43°N) in an area that should show a cool anomaly, and there is no significant anomaly along the North American coast. There is a small amount of significant warming around the South-East Asian coast however, like HiGEM1.2, HadGEM1.2 simulates this region rather poorly in general.

EOF analysis has shown that both high and low resolution coupled models produce El Niño-like conditions in the tropical Pacific as their primary mode of SST variability. The main difference between the high resolution and low resolution models is their ability to reproduce the correct North Pacific SST response to the tropical El Niño conditions. This suggests that it is the atmospheric processes that control the North Pacific

SST response to El Niño that are failing in HadGEM1.2, rather than the model's ability to simulate El Niño conditions.

3.4 Atmospheric response to El Niño

The reason for the differences in the extra-tropical SST response to El Niño in the observations and the two models is now examined, using the framework of the atmospheric bridge discussed in section 3.1.

3.4.1 Tropical atmospheric forcing during El Niño

During El Niño the Pacific warm pool moves eastward, driving anomalous convection in the central tropical Pacific. The latent heat release in this anomalous convection then forces an upper tropospheric response. The energy used to evaporate water is transported with the water vapour. When the vapour condenses back to liquid (or solid) form this energy is released. Here, surface precipitation rate is used as a measure of this vertically integrated latent heat release. This relationship is valid provided that horizontal advection of cloud particles between their formation and arrival at the surface is negligible, which is a reasonable assumption for the large spatial scales considered here.

Bearing in mind the caveats of the reanalysis precipitation field discussed in chapter 2, it is worth first comparing reanalysis precipitation to a satellite derived product. Regression maps of precipitation rate anomaly for November–March for NCEP/NCAR reanalysis and the NOAA Climate Prediction Center (CPC) Merged Analysis of Precipitation (CMAP[2]) are shown in figure 3.4. Both products show statistically significant positive precipitation rate anomalies in the central tropical Pacific and negative anomalies in the western Pacific in the vicinity of the Pacific warm pool. The satellite based precipitation product has considerably larger magnitude anomalies than the reanalysis product, the largest anomaly in the central tropical Pacific being almost twice the magnitude of that in the reanalysis. It appears that in this case the reanalysis precipitation under-represents the anomalous precipitation associated with El Niño. Although there are clearly differences between the magnitudes of the reanalysis precipitation and satellite derived precipitation

[2]CMAP Precipitation data provided by the NOAA/OAR/ESRL PSD, Boulder, Colorado, USA, from their Web site at http://www.esrl.noaa.gov/psd/

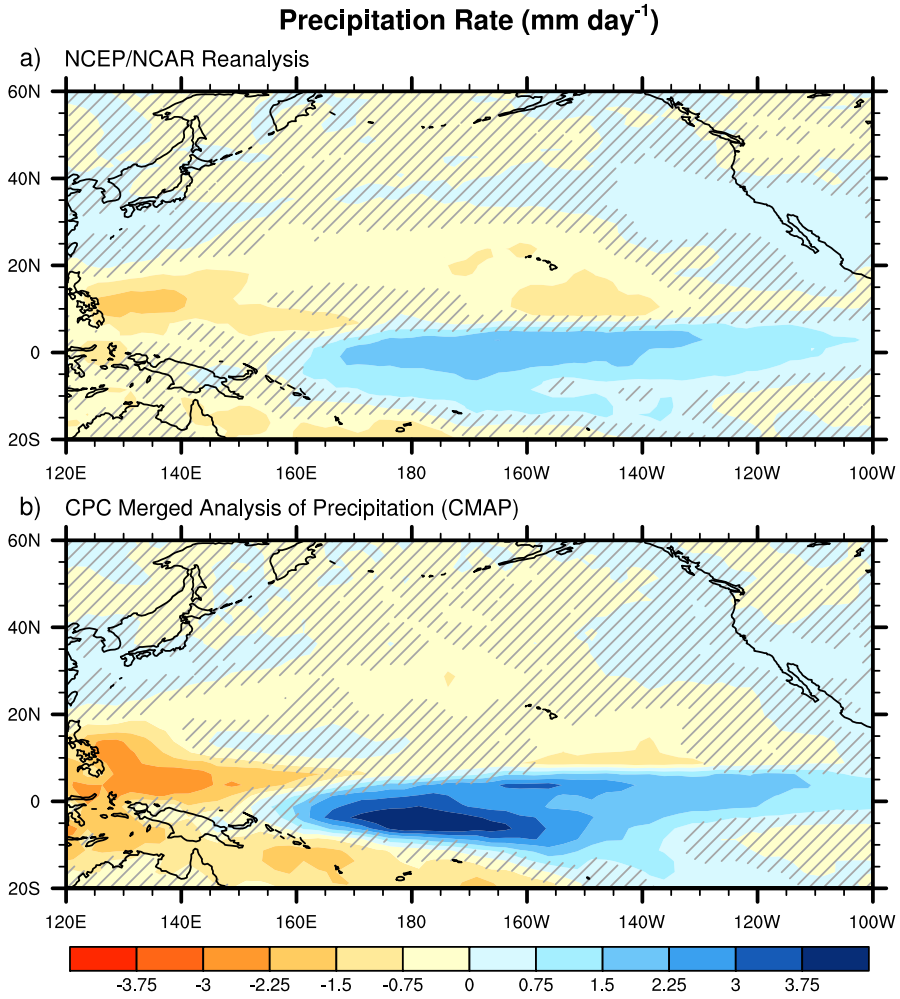

Figure 3.4: Northern winter (NDJFM) precipitation rate (mm day^{-1}) anomaly patterns associated with a 1 °C departure of the EP index. The contour interval is 0.75 mm day^{-1}. a) NCEP/NCAR Reanalysis, b) CPC Merged Analysis of Precipitation (CMAP).

measurements, we note that the spatial patterns are consistent between the two.

Regression maps of precipitation rate anomaly for November–March for observations, HiGEM1.2, and HadGEM1.2 are shown in figure 3.5. The largest observed precipitation rate anomalies are in the central tropical Pacific, consistent with an El Niño. The precipitation rate anomaly patterns produced in both model are distinctly different to observations, with the largest anomalies situated in the western tropical Pacific. This is likely due to the greater westward extent of the tropical SST anomalies in both HiGEM1.2 and HadGEM1.2. There are slight differences between the precipitation rate anomaly patterns in HiGEM1.2 and HadGEM1.2. HiGEM1.2 has less of a split inter-tropical convergence zone (ITCZ). This is because the cold tongue error is not as pronounced in HiGEM1.2 as

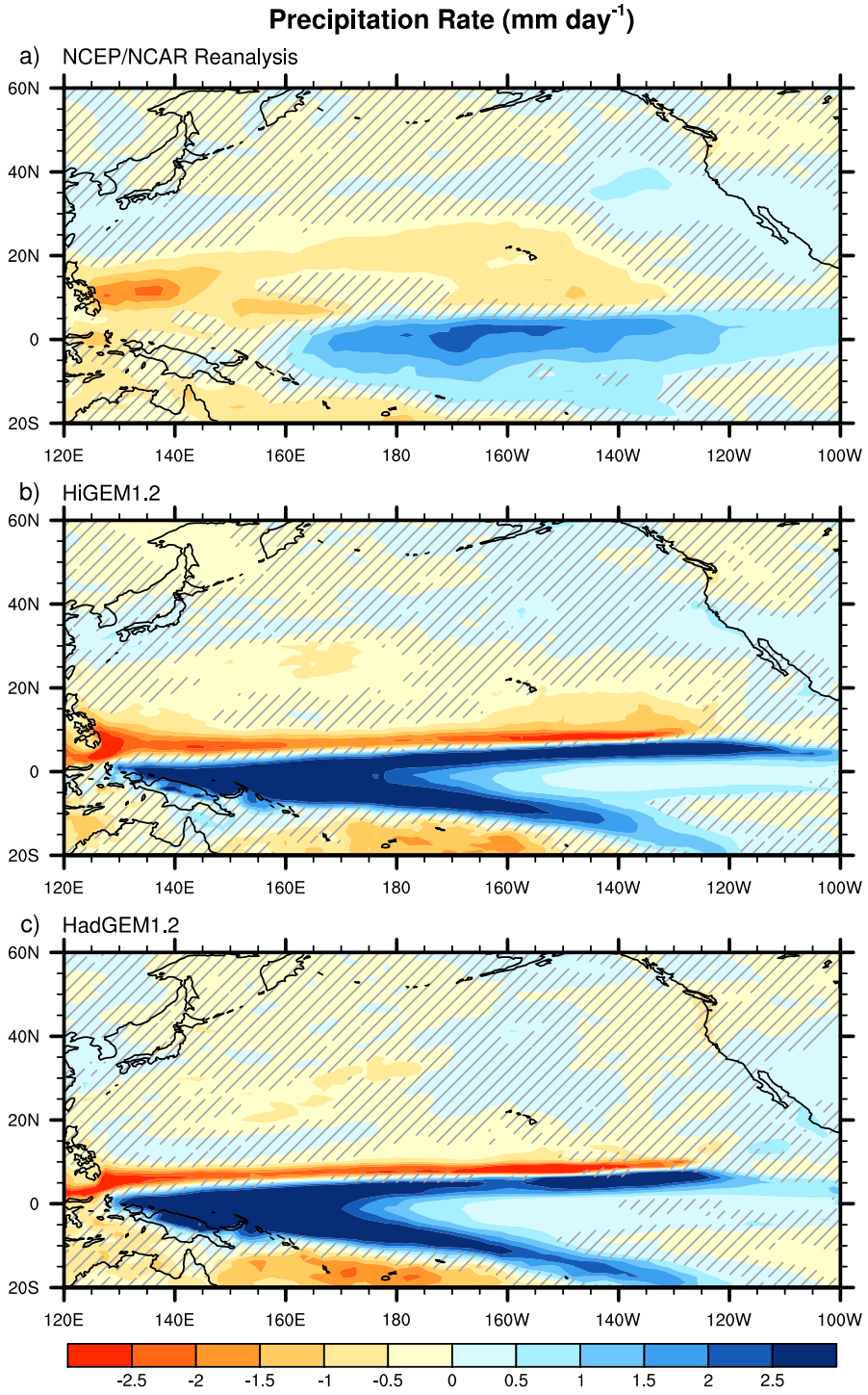

Figure 3.5: Northern winter (NDJFM) precipitation rate (mm day^{-1}) anomaly patterns associated with a 1 °C departure of the EP index. The contour interval is 0.5 mm day^{-1}. a) NCEP/NCAR Reanalysis, b) HiGEM1.2, and c) HadGEM1.2.

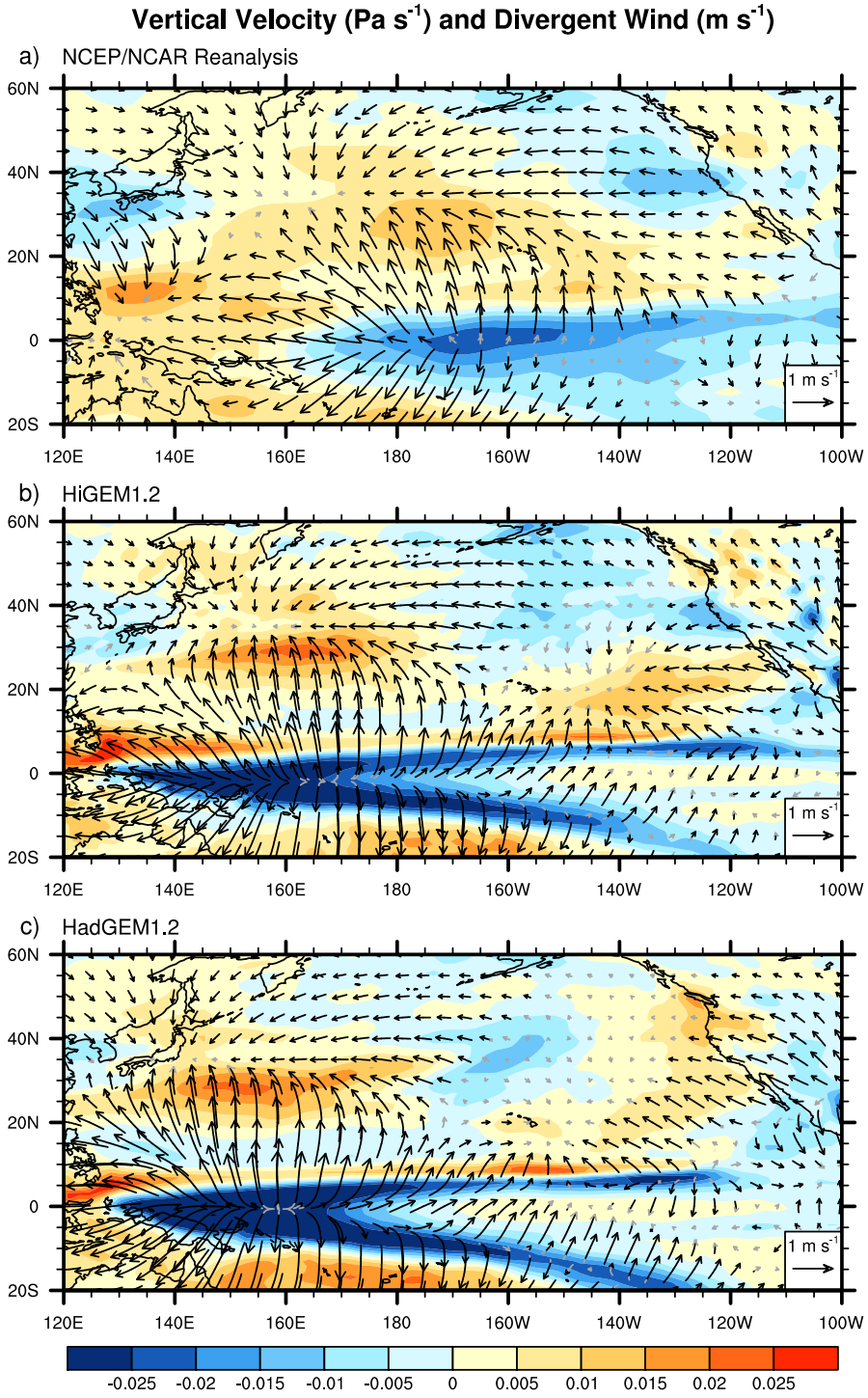

Figure 3.6: Northern winter (NDJFM) 500 hPa vertical velocity (ω; colours, Pa s^{-1}) and 200 hPa divergent component of wind (arrows, m s^{-1}) anomaly patterns associated with a 1 °C departure of the EP index. The contour interval is 5×10^{-3} Pa s^{-1}. a) NCEP/NCAR Reanalysis, b) HiGEM1.2, and c) HadGEM1.2.

it is in HadGEM1.2 (*Shaffrey et al.*, 2009).

Figure 3.6 shows regression maps of vertical velocity (actually ω, the Lagrangian tendency of pressure measured in Pa s^{-1}) anomaly at 500 hPa and the anomalous divergent component of the wind at 200 hPa. The main centre of anomalous 200 hPa divergence and 500 hPa vertical velocity in the observations and both models is over the large precipitation anomaly in the tropics. Hence, in areas where large amounts of latent heat are being released, there is large scale ascent throughout the troposphere, consistent with the tropical atmospheric dynamics discussed previously.

There is a difference in the longitude of tropical heating between HiGEM1.2 and HadGEM1.2, of the order of 5–10°. This change in longitude is small when compared to the total longitudinal extent of the tropical heating, which is about 40°. The shift in the longitude of tropical heating between HiGEM1.2 and HadGEM1.2 is also small when compared to the difference in the longitude of heating between observations and the models, which is of the order of 25°. As we will show, the extra-tropical response to El Niño in HiGEM1.2 is very similar to the observed response even though tropical heating is shifted approximately 25°W from observations to HiGEM1.2. This suggests that the relatively small intra-model difference in heating longitude is not likely to be a major factor in the performance differences between HiGEM1.2 and HadGEM1.2.

Figures 3.5 and 3.6 provide a clear illustration of the initial stages of the atmospheric bridge. Latent heat is released in the tropics, air ascends, and there is divergence in the upper troposphere. It is clear that HiGEM1.2 and HadGEM1.2 have different patterns of anomalous precipitation, vertical motion and divergence to the observed atmosphere. However the initial part of the atmospheric bridge (tropical heating and upper tropospheric forcing) appears to be similar in the high and low resolution models.

This suggests that the differences in extra-tropical response to El Niño between HiGEM1.2 and HadGEM1.2 cannot be explained simply in terms of inadequate surface forcing for that atmospheric bridge. Although there may be some subtle, yet significant differences in surface forcing, it is also likely that the HadGEM1.2 atmosphere is behaving quite differently to that of HiGEM1.2 in order to produce its extra-tropical response.

3.4.2 Upper atmospheric circulation response to El Niño

Regression maps of 200 hPa stream function anomaly for NDJFM for reanalysis data, high resolution, and low resolution coupled models are shown in figure 3.7. These show the upper level circulation anomalies associated with El Niño. The observations (figure 3.7a) show a deepened Aleutian low (negative, cyclonic stream function anomaly) over the North Pacific, this is part of a wave train that originates in the Pacific and extends across Canada (anticyclonic) and into the North Atlantic (cyclonic). This anomalous wave train is excited by vorticity anomalies in the upper troposphere induced by anomalous divergence over regions of strong anomalous convection (*Sardeshmukh and Hoskins*, 1988). The wave train has a zonal wavenumber of approximately 4–5.

The extra-tropical circulation structure in HiGEM1.2 is similar to that in the observations over the Pacific-North American (PNA) region. The wave train is somewhat different when it reaches the Atlantic; the anticyclonic anomaly over Canada extends into the mid-Atlantic, and the cyclonic anomaly is shifted eastward to Scandinavia. In a separate study, it was found that removing years when large El Niño events occur from the analysis of North Atlantic variability in HiGEM1.2, the spatial pattern of the North Atlantic Oscillation (NAO) is closer to observations (S. Keeley, personal communication). This extension into the mid-Atlantic may go some way to explain this result.

The stream function anomalies associated with El Niño in HadGEM1.2 have a very different pattern to, and are generally weaker than those in HiGEM1.2 and observations. The negative stream function anomaly over the North Pacific is slightly westward, at the date line, compared to that in HiGEM1.2 and observations. The downstream wave train then shows a much more separated structure that is quite unlike the pattern seen in both the observations and HiGEM1.2.

Hence, the upper level circulation anomalies significantly deviate from observed behaviour in HadGEM1.2. This suggests that atmospheric Rossby waves that are excited in the upper troposphere are generated and/or propagate differently in HadGEM1.2 than in HiGEM1.2 and observations. This will be investigated further in sections 3.5 and 3.6. Before determining the cause of the difference between the high and low resolution models it is worthwhile to show that these upper level circulation anomalies do indeed affect the surface in the extra-tropics, and to understand how these surface anomalies can explain

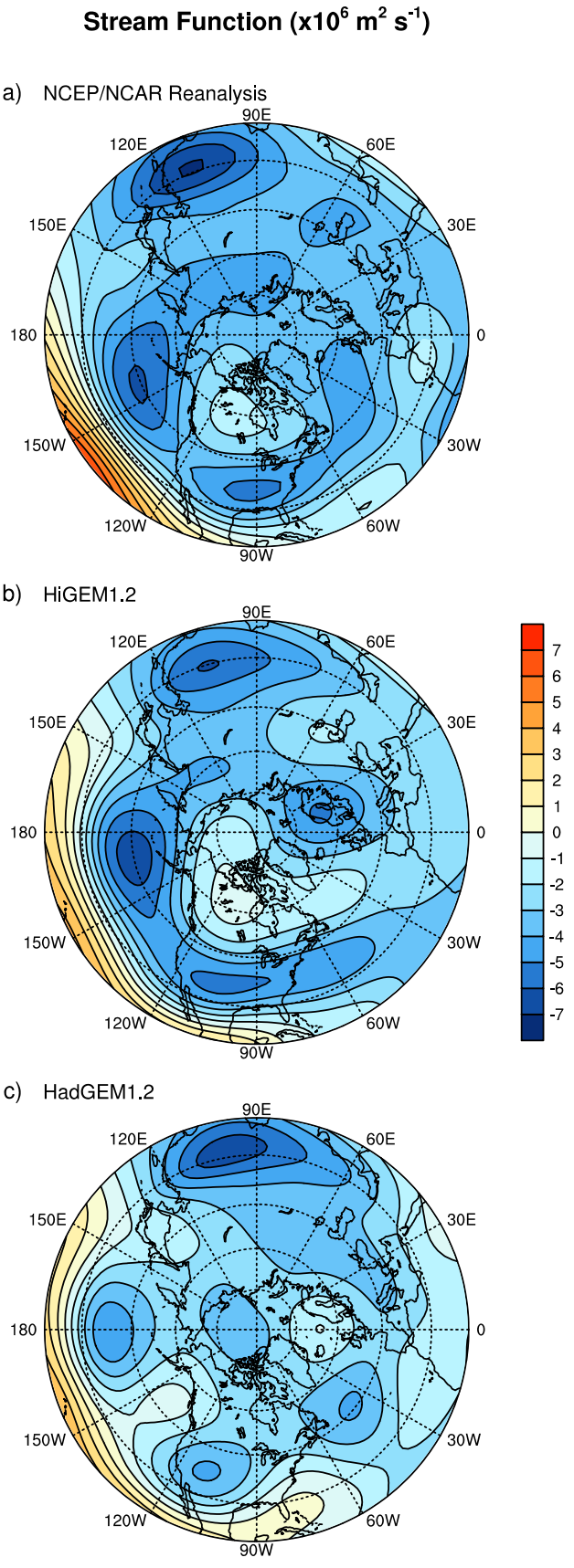

Figure 3.7: Northern winter (NDJFM) 200 hPa stream function ($m^2\ s^{-1}$) anomaly patterns associated with a 1 °C departure of the EP index. The contour interval is $10^6\ m^2\ s^{-1}$. a) NCEP/NCAR Reanalysis, b) HiGEM1.2, and c) HadGEM1.2.

the different extra-tropical SST anomalies seen in HadGEM1.2.

3.4.3 Surface atmospheric circulation

Figure 3.8 shows regression maps of extra-tropical North Pacific surface wind anomalies overlaid on SST anomalies for observations, HiGEM1.2, and HadGEM1.2. The sense of the circulation corresponds well to the 200 hPa stream function anomalies above (figure 3.7), consistent with the upper tropospheric potential vorticity anomalies inducing a surface circulation through an approximately equivalent barotropic vertical structure (e.g. *Hoskins et al.*, 1985). The surface wind anomalies in HadGEM1.2 are considerably weaker than those in HiGEM1.2, having about half the magnitude. This suggests that any SST response due to this anomalous surface wind may also be weaker.

3.4.4 Surface energy balance

Previous studies (e.g., *Luksch and von Storch*, 1992; *Alexander*, 1990, 1992b; *Deser and Blackmon*, 1995; *Alexander et al.*, 2002) have shown that the extra-tropical SST response to El Niño is controlled by alterations to surface heat fluxes caused by anomalous surface circulation. In order to understand how surface heat fluxes control the extra-tropical SST response to El Niño, the total net upward heat flux Q_T is separated into its components:

$$Q_T = Q_{SW} + Q_{LW} + Q_S + Q_L, \tag{3.4}$$

where Q_{SW} is the flux of shortwave (solar) radiation, Q_{LW} is the flux of longwave (terrestrial) radiation, Q_S is the sensible (turbulent) heat flux, and Q_L is the surface latent (evaporative) heat flux. All fluxes are defined as positive upwards from the ocean to the atmosphere.

Figure 3.9 shows the components of the total heat flux anomaly associated with El Niño for observations, HiGEM1.2, and HadGEM1.2. A positive (negative) anomaly corresponds to a cooling (warming) of the ocean (note the reversed colour scale). Longwave (Q_{LW}) and shortwave (Q_{SW}) flux anomalies make a negligible contribution to the total heat flux anomaly in observations and both models. In observations and HiGEM1.2, the heat flux anomalies are consistent with SST anomalies in the extra-tropics. Heat flux anomalies in HadGEM1.2 are generally consistent with SST anomalies. However, HadGEM1.2

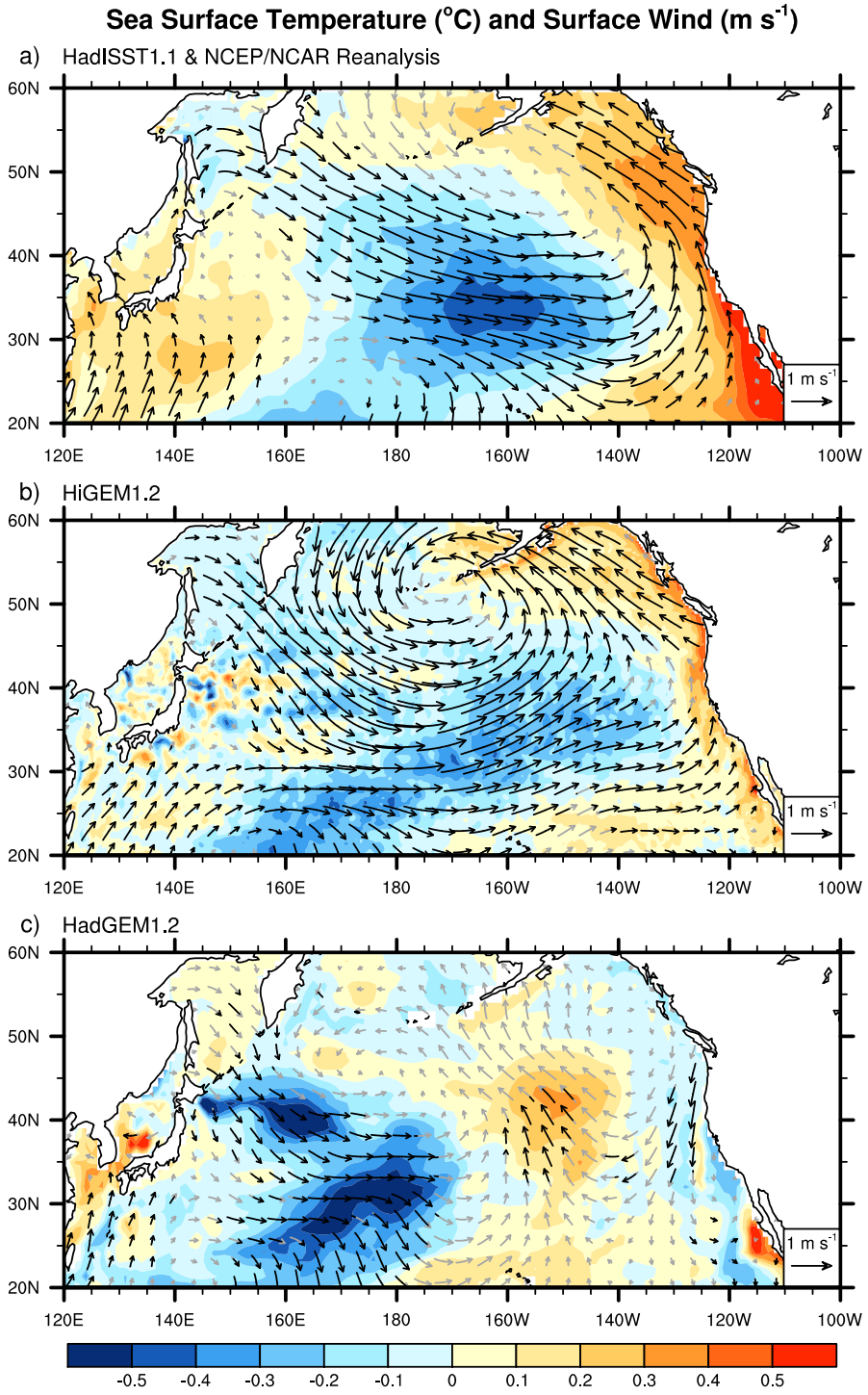

Figure 3.8: Northern winter (NDJFM) SST (colours, °C) and surface wind (arrows, m s^{-1}) anomaly patterns associated with a 1 °C departure of the EP index. The contour interval is 0.5 °C. a) NCEP/NCAR Reanalysis / HadISST1.1, b) HiGEM1.2, and c) HadGEM1.2.

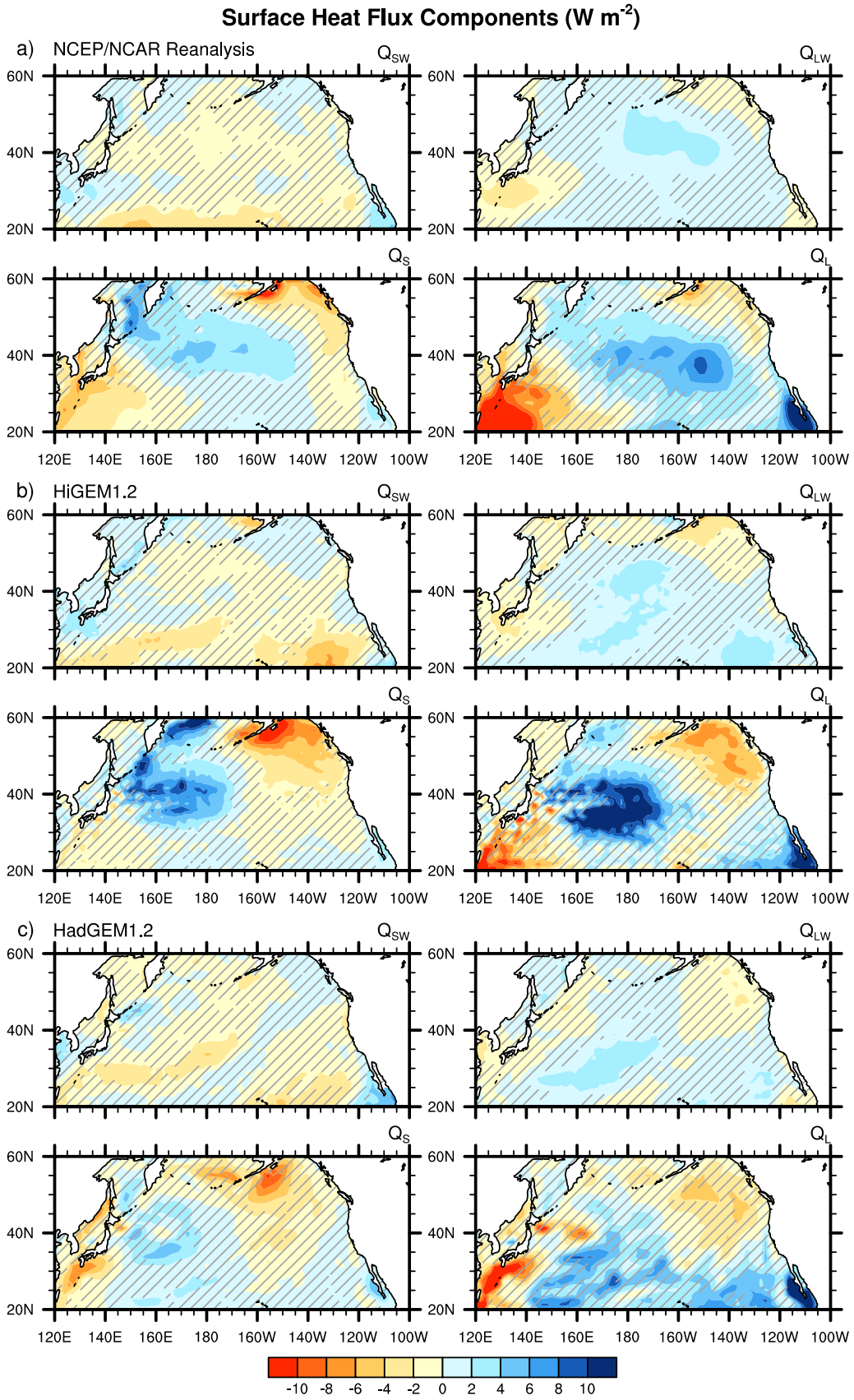

Figure 3.9: Northern winter (NDJFM) surface heat flux component anomaly patterns associated with a 1°C departure of the EP index. Components are as specified in equation 3.4 and are all defined as positive upwards. The contour interval is 2 W m^{-2}. a) NCEP/NCAR Reanalysis, b) HiGEM1.2, and c) HadGEM1.2.

has a weak heat flux anomaly response along the North American coast. The sign of this anomaly implies a warm SST anomaly yet HadGEM1.2 lacks a significant warm SST anomaly in this region (figures 3.2 and 3.8).

HiGEM1.2 has larger magnitude heat flux anomalies over the central North Pacific than observations. However, the SST response in the central North Pacific has a greater magnitude in observations than in HiGEM1.2 (figure 3.8). Differences in ocean dynamics could be a cause of this discrepancy. If the HiGEM1.2 oceanic mixed layer is deeper than that in observations, then anomalous energy input at the surface would heat a larger volume of water, thus reducing the temperature change observed at the surface. It is also possible that internal ocean heat transports have a role to play. If, for example, the HiGEM1.2 ocean transports heat back into regions where it is lost due to surface fluxes in a way that the real ocean does not, the result would be a different SST response to surface flux anomalies. However, the influence of these internal oceanic processes appears to be secondary to the atmosphere–ocean interactions in determining the overall extra-tropical SST response to El Niño.

Understanding exactly how surface circulation anomalies affect surface heat fluxes requires these fluxes to be studied in more detail. The sensible heat flux Q_S measures the amount of heat transferred between the atmosphere and ocean due to conduction and convection through turbulent eddies. The bulk aerodynamic formula for sensible heat flux is

$$Q_S = \rho_a c_p c_H V(z_r)\left[T_{sea} - T_{air}(z_r)\right], \tag{3.5}$$

where ρ_a is the density of air, c_p is the specific heat capacity for dry air at a constant pressure, c_H is the aerodynamic transfer coefficient for temperature, V is the wind speed at the reference height z_r, T_{sea} is the sea surface temperature, and T_{air} is the air temperature at the reference height z_r. The North Pacific winter sea surface temperature is higher than the air temperature, $T_{sea} - T_{air} > 0$, and the sensible heat flux is positive (upwards), with the ocean losing energy to the atmosphere. The variable components of Q_S are the wind speed and the difference between air and sea temperature, usually with changes in wind speed mainly determining sensible heat flux anomalies. The bulk aerodynamic formula

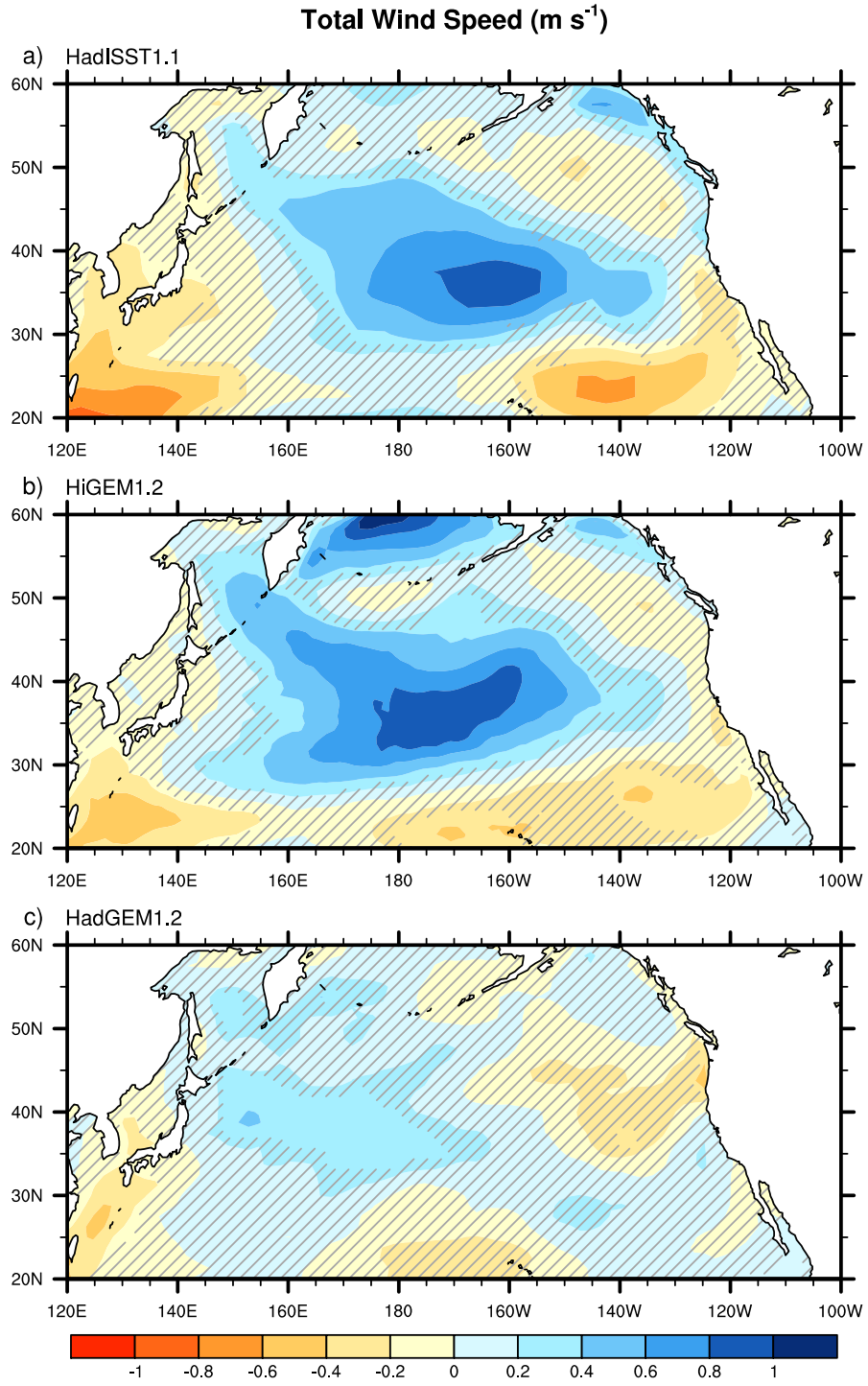

Figure 3.10: Northern winter (NDJFM) total wind speed anomaly associated with a 1°C departure of the EP index. The contour interval is 0.2 m s^{-1}. a) NCEP/NCAR Reanalysis, b) HiGEM1.2, and c) HadGEM1.2.

for surface latent heat flux is

$$Q_L = \rho_a L c_E V(z_r)\left[q_s - q_a(z_r)\right], \tag{3.6}$$

where ρ_a is the density of air, L is the enthalpy of vaporisation, c_E is the aerodynamic transfer coefficient for humidity, V is the wind speed at the reference height z_r, q_{sea} is the specific humidity saturated at the sea surface temperature, and q_{air} is the specific humidity at the reference height z_r. Similarly to the sensible heat flux, the bulk aerodynamic formula for latent heat flux also depends on, and is usually determined by total wind speed. The specific humidity difference between the reference height, z_r, and the sea surface is the other variable term.

Figure 3.10 shows the 10 m total wind speed anomaly associated with El Niño; positive (negative) anomalies correspond to increased (decreased) wind speed (note the reversed colour scale). In general, wind speed anomalies are consistent with the hypothesis that wind speed modulation of sensible and latent heat fluxes controls the extra-tropical North Pacific SST response to El Niño, with increased wind speed over cool SST anomalies and decreased wind speed over warm SST anomalies in the observations and both models.

However, this relationship does not hold in the region along the North American coast north of 40°N. In observations and HiGEM1.2, the total wind speed anomaly in this region is positive. This implies positive (upward) heat flux anomalies and cool SST anomalies, yet there are downward heat flux anomalies and the underlying SST anomalies are warm. HadGEM1.2 shows negative total wind speed anomalies along the North American coast implying negative (downward) heat flux anomalies and warm SST anomalies. However, even though there are downward heat flux anomalies, there are no significant warm SST anomalies.

Figure 3.11 shows regression maps of the difference $T_{sea} - T_{air}$ (note the reversed colour scale). There is a negative anomaly in the sea−air temperature difference in the North American coastal region in observations and HiGEM1.2. This leads to the negative (downward) heat flux anomalies and warm SST anomalies. The reason for the reduction in the sea−air temperature difference can be traced to the direction of the anomalous surface winds. The anomalous surface winds along the North American coast are predominantly

from the south in observations and HiGEM1.2. This implies they will advect warmer air from over warmer SSTs northward. Hence, the direction of the anomalous wind can be as important as the magnitude in controlling the surface energy balance.

Figure 3.12 shows regression maps of the difference $q_{sea} - q_{air}$ (note the reversed colour scale). A similar argument as for the sensible heat flux explains the negative (downward) latent heat flux anomalies along the North American coast. The warm air advected northward by the southerly wind anomalies in the observations and HiGEM1.2 has a higher humidity. Hence the sea−air specific humidity difference will be reduced, decreasing evaporation and leading to the negative (downward) latent heat flux anomalies.

To fully understand the mechanisms of the extra-tropical response in HadGEM1.2 we must understand why the downward (heat into the ocean) heat flux anomaly along the North American coast does not produce significant warm SST anomalies. There must be another heat transport process acting in HadGEM1.2 that counteracts the heat flux anomaly. Coastal upwelling is a process where equatorward winds along an oceanic eastern (western) boundary in the northern (southern) Hemisphere cause offshore surface currents, known as Ekman transport (*Gill*, 1982). The offshore movement of surface waters causes water from below the surface to be upwelled to replace them. Subsurface waters are generally cooler than the surface water they replace, hence upwelling generally corresponds to cooler SSTs. Note that the anomalous poleward winds (figure 3.8) in observations and HiGEM1.2 will suppress upwelling along the North American coast. This is not the case in HadGEM1.2, where the generally weak equatorward wind anomalies will not act to suppress upwelling.

The following analysis concentrates on the closed region bounded by the North American coast and the section from 149°W, 60°N to 124°W, 40°N. The study region is indicated by the hatching in figure 3.13. This particular region is chosen as it is an area where the anomalous SSTs associated with El Niño are simulated well by HiGEM1.2 but HadGEM1.2 has no significant SST anomaly (figures 3.2b,c and 3.8b,c).

Regression maps of oceanic vertical velocity at 50 m depth for HiGEM1.2 and HadGEM1.2 are shown in figure 3.14. A positive (negative) anomaly corresponds to a cooling (warming) of the surface waters (note the reversed colour scale). HiGEM1.2 has a warming anomaly that is constrained tightly to the coast. Offshore there is a mixture of warming

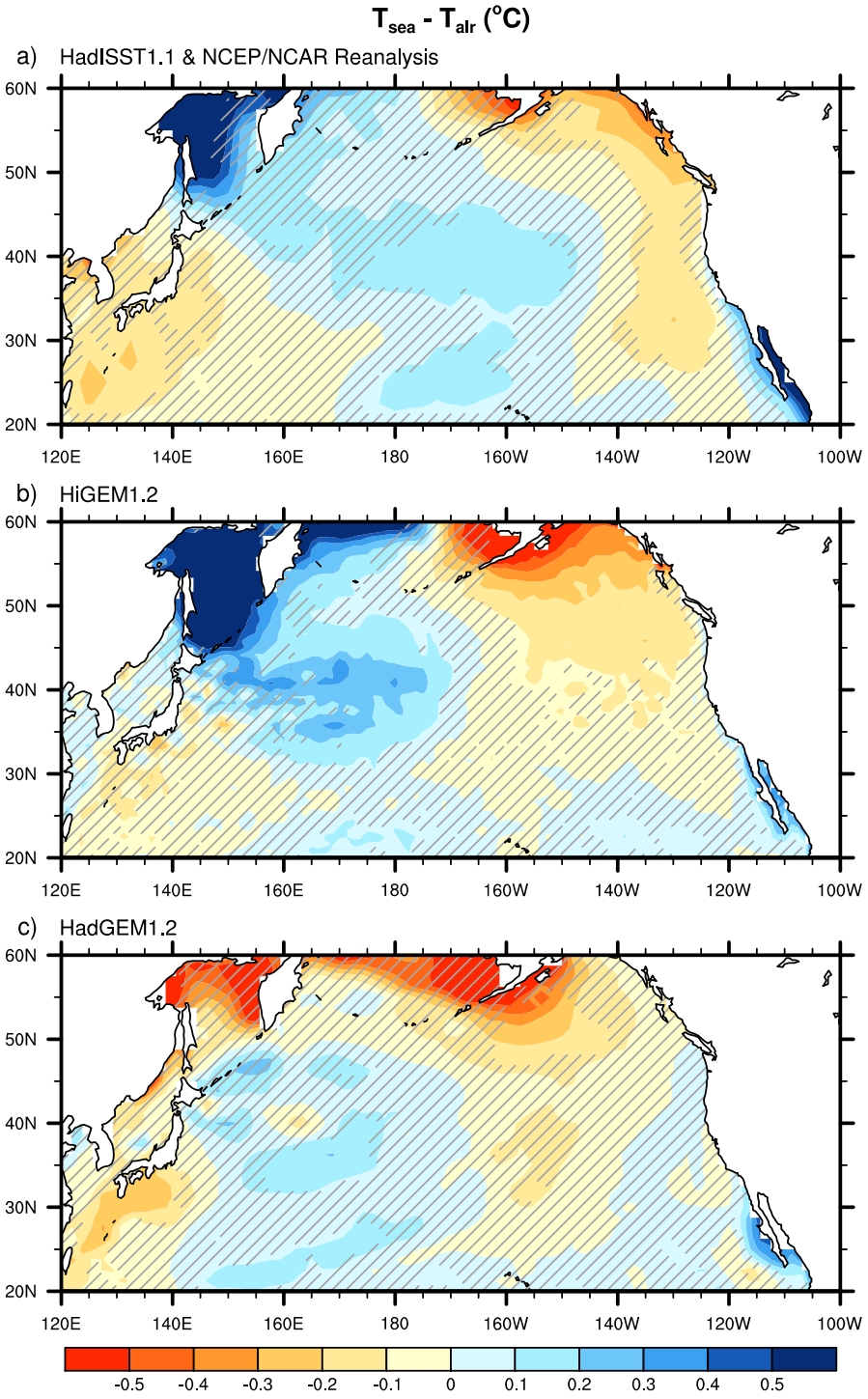

Figure 3.11: Anomalous difference between northern winter (NDJFM) SST and 2 m air temperature (°C). Anomalies correspond to a 1 °C departure of the EP index. The contour interval is 0.1 °C. a) HadISST1.1 and NCEP/NCAR Reanalysis, b) HiGEM1.2, and c) HadGEM1.2.

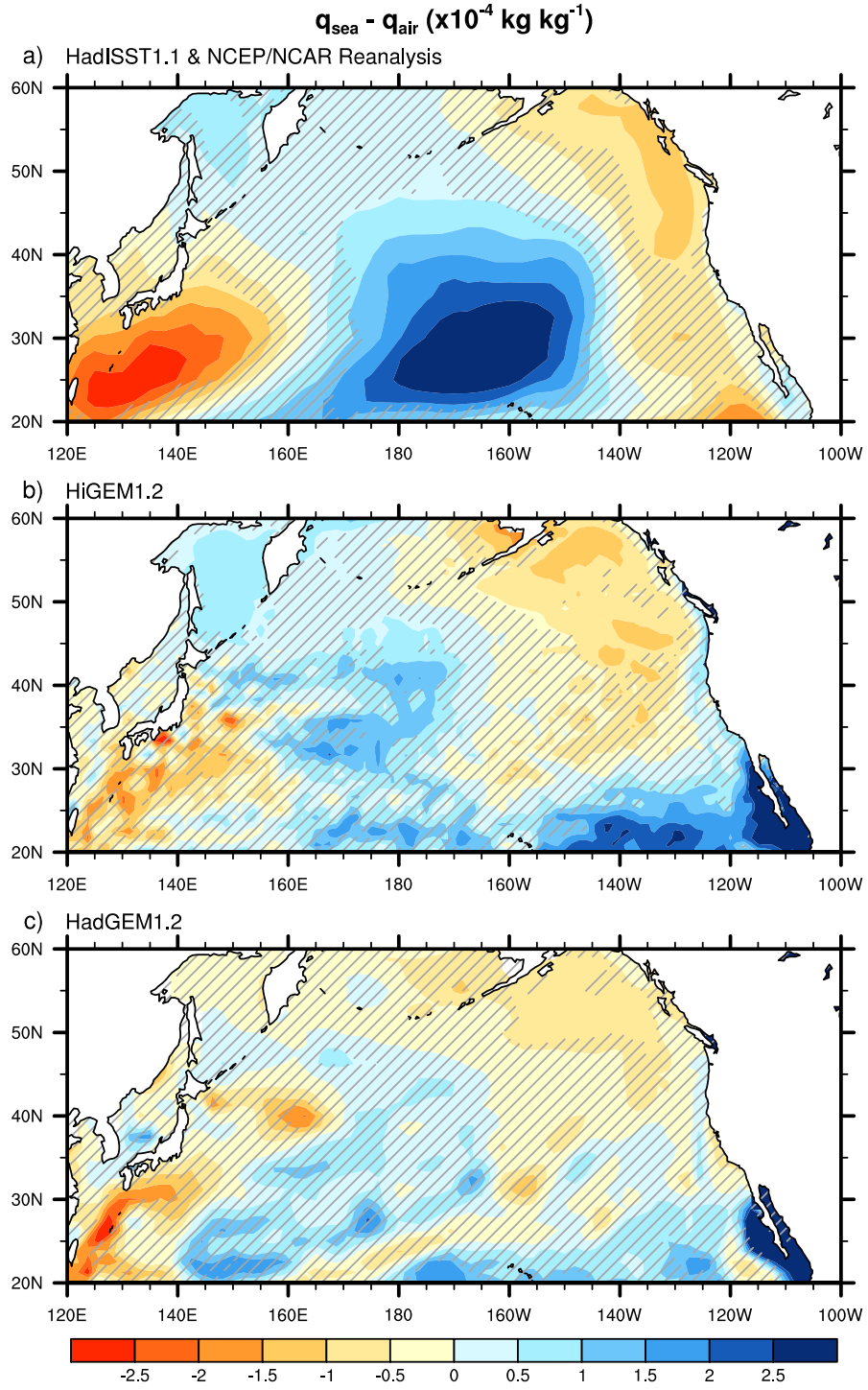

Figure 3.12: Anomalous difference between northern winter (NDJFM) specific humidity saturated at the sea surface temperature and 2 m specific humidity ($\times 10^{-4}$ kg kg^{-1}). Anomalies correspond to a 1 °C departure of the EP index. The contour interval is 0.5×10^{-4} kg kg^{-1}. a) HadISST1.1 and NCEP/NCAR Reanalysis, b) HiGEM1.2, and c) HadGEM1.2.

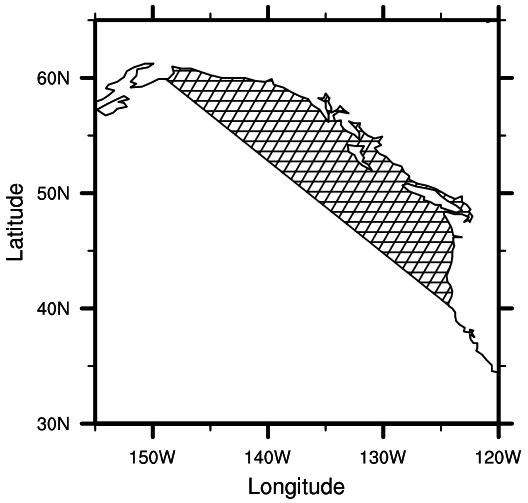

Figure 3.13: Study region for coastal upwelling analysis. The hatched region is used for regression maps and calculation of area-integrated vertical velocity.

and cooling anomalies. In general this supports the idea that the anomalous surface winds in HiGEM1.2 act to suppress coastal upwelling in this region. HadGEM1.2 has a much weaker anomalous vertical velocity response than HiGEM1.2. This can be expected given the surface wind anomalies in HadGEM1.2 are also weaker than those in HiGEM1.2 (figures 3.8a,b). Since anomalous vertical velocity varies in both sign and magnitude on small spatial scales, it is difficult to be confident in the interpretation of these regression maps. A complementary analysis of upwelling is required.

A time series of this coastal upwelling is calculated from the vertical velocity at 50 m depth, averaged over the closed region bounded by the coast and the section from 149°W, 60°N to 124°W, 40°N. This time series was then regressed onto the EP SST index to produce a single value that can be interpreted as the anomalous volume flux ($m^3\ s^{-1}$) into the coastal region associated with El Niño. A negative (positive) value indicates suppressed (enhanced) upwelling, and implied temperature increase (decrease) in the surface waters.

In HiGEM1.2 the anomalous volume flux associated with El Niño is negative ($-3.2 \times 10^5\ m^3\ s^{-1}$) indicating that upwelling is suppressed. This is as expected given the surface wind and SST anomalies. This finding is complimentary to the result of the surface heat flux analysis, suggesting that along with advection of warm air, suppressed upwelling is a contributing factor to the presence of the warm SST anomaly along the North American coast in HiGEM1.2. However, in HadGEM1.2 the anomalous volume flux is positive

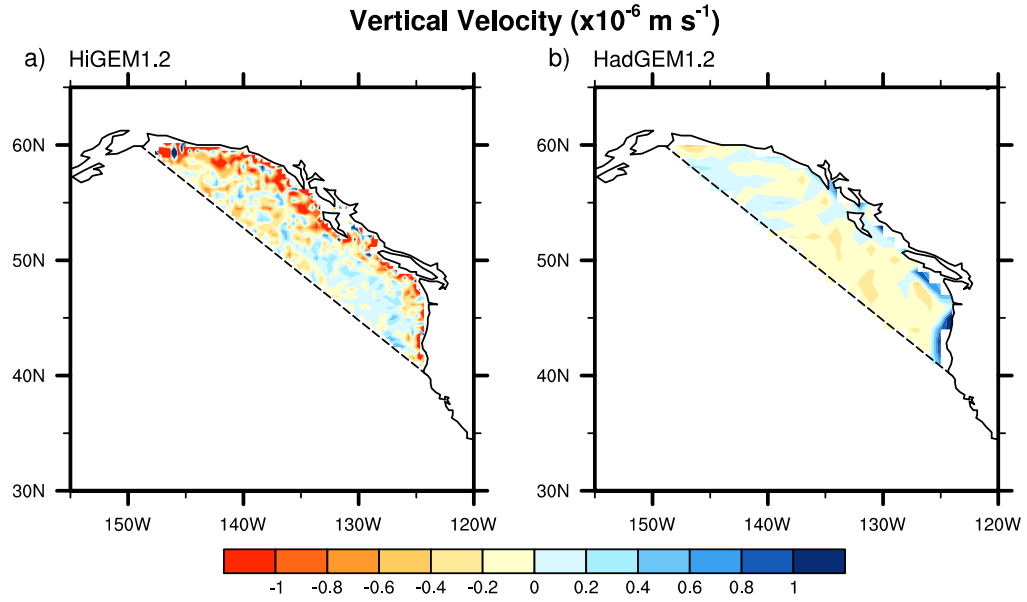

Figure 3.14: Northern winter (NDJFM) oceanic vertical velocity (10^{-6} m s^{-1}) anomaly associated with a 1 °C departure of the EP index. The contour interval is 0.2×10^{-6} m s^{-1}. a) HiGEM1.2, and b) HadGEM1.2.

(0.5×10^5 m^3 s^{-1}). The implication of this is that more cool water is upwelled into the upper layer of the ocean. Hence, there is an opposing flux of heat out of the surface waters which counteracts the anomalous heat input by the surface heat fluxes. This could explain the lack of a statistically significant warm anomaly along the North American coast in HadGEM1.2 (figure 3.2c).

3.5 Stationary Rossby wave propagation

The upper tropospheric anomalies associated with El Niño in HadGEM1.2 are quantitatively and qualitatively different to those in HiGEM1.2 and the observed atmosphere (section 3.4.2). These differences in circulation anomalies are then responsible for significant differences in the extra-tropical SST component of El Niño between the observations and models. In this section, the mechanisms responsible for the differences in the circulation anomalies are investigated.

The behaviour of these anomalies is governed by Rossby wave dynamics; planetary-scale waves that propagate westward relative to the time-mean background flow. The

propagation paths of Rossby waves are therefore dependent on the basic state of the atmosphere. Given that HadGEM1.2 has very different upper troposphere stream function anomalies than the observations (figure 3.7), it is likely that the basic state of the HadGEM1.2 atmosphere is also significantly different in order to influence Rossby wave propagation to such an extent.

Figure 3.15 shows time-mean zonal wind for observations, HiGEM1.2 and HadGEM1.2 in the Pacific sector. The basic state in HiGEM1.2 is similar to that in observations, but with a more elongated taper to the region of mean easterlies in the tropics. However, the basic state in HadGEM1.2 shows significant differences from the observed mean state. In HadGEM1.2, there is a clear separation between the Asian-Pacific and North American jets, with the Asian-Pacific jet continuing into North America, while the North American jet entrance is over Hawaii. The region of mean easterlies in the tropics is also much more tapered and elongated in HadGEM1.2 than in observations. Although there are clear differences between the mean zonal wind fields from the observations, HiGEM1.2, and HadGEM1.2, the dynamical implications of these differences are not immediately clear.

3.5.1 Theoretical Rossby wave propagation on a varying background flow

In order to investigate the atmospheric background state, it is useful to examine tropospheric stationary wave patterns, following the work of *Hoskins and Ambrizzi* (1993). These patterns describe the environment through which a locally excited wave train must propagate in the atmosphere (*Hoskins and Ambrizzi*, 1993). To study stationary wave patterns, the stationary Rossby wavenumber will be examined, which is derived by applying stationary wave conditions to the barotropic Rossby wave dispersion relation. The dispersion relation for barotropic Rossby waves is derived formally by finding wave type solutions of the linearised form of the non-divergent barotropic vorticity equation (*Holton*, 2004).

$$\frac{D}{Dt}(\xi + f) = 0, \tag{3.7}$$

where f is the Coriolis parameter and

$$\xi = \frac{\partial v}{\partial x} - \frac{\partial u}{\partial y}, \tag{3.8}$$

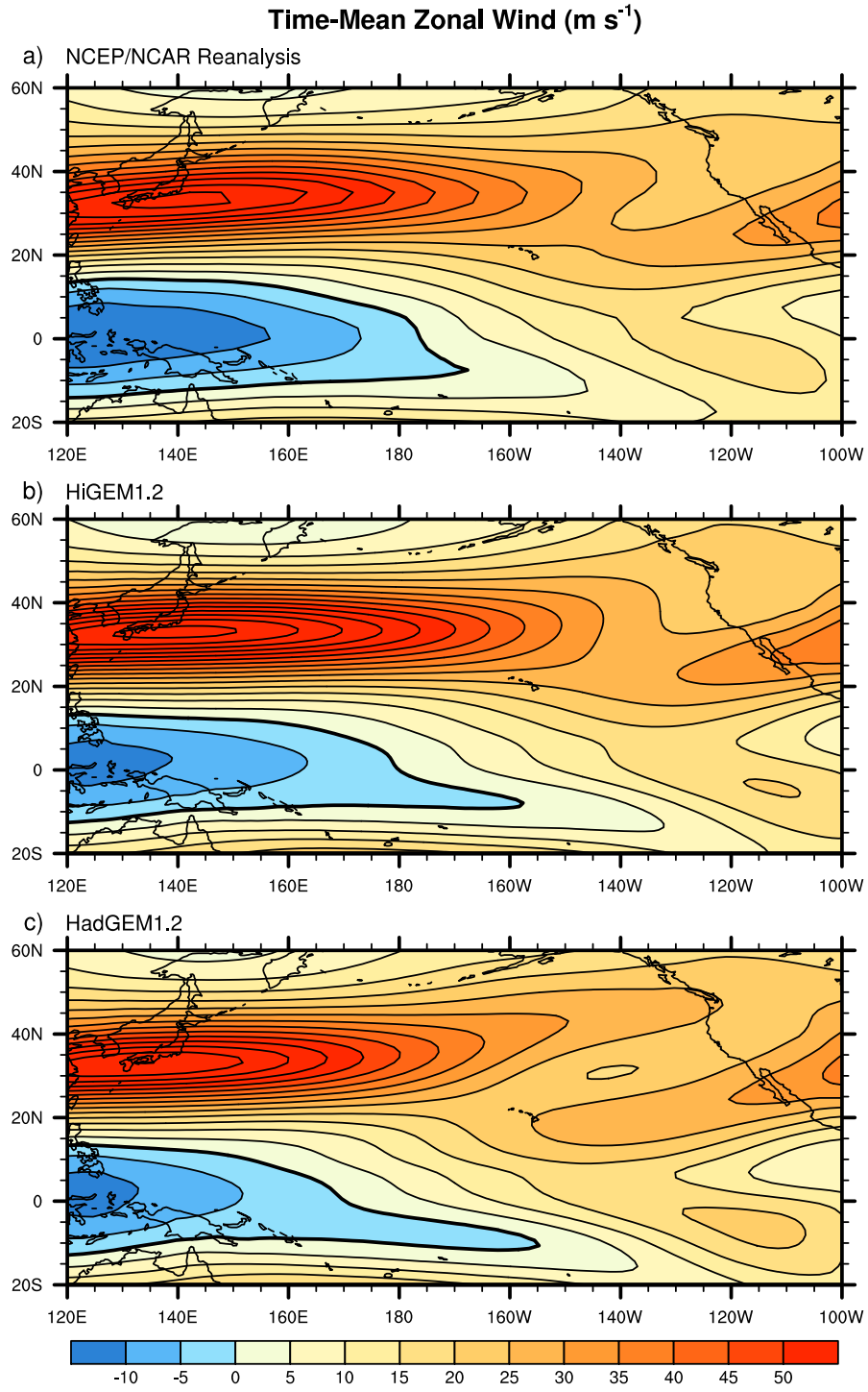

Figure 3.15: 50 year time-mean northern winter (NDJFM) zonal wind (m s^{-1}) at 200 hPa. The contour interval is 5 m s^{-1}, the zero contour is thickened. a) NCEP/NCAR Reanalysis, b) HiGEM1.2, and c) HadGEM1.2.

is the relative vorticity, where u and v are the eastward and northward components of the flow respectively. Assuming a β-plane approximation, $f = f_0 + \beta y$ (e.g., *Pedlosky*, 1990), and linearising about a constant basic state zonal velocity such that

$$u = \bar{u} + u', \quad v = v', \tag{3.9}$$

and

$$\xi' = \frac{\partial v'}{\partial x} - \frac{\partial u'}{\partial y}, \quad \bar{\xi} = -\frac{\partial \bar{u}}{\partial y}, \tag{3.10}$$

and defining a perturbation stream function ψ'

$$u' = -\frac{\partial \psi'}{\partial y}, \quad v' = \frac{\partial \psi'}{\partial x}, \tag{3.11}$$

yields the linearised barotropic vorticity equation

$$\left(\frac{\partial}{\partial t} + \bar{u}\frac{\partial}{\partial x}\right)\nabla^2\psi' + \beta_* \frac{\partial \psi'}{\partial x} = 0, \tag{3.12}$$

where

$$\beta_* = \beta - \frac{\partial^2 \bar{u}}{\partial y^2}, \tag{3.13}$$

is the meridional (south-north) gradient of absolute vorticity. Seeking solutions of the form

$$\psi' = e^{i(kx+ly-\omega t)}, \tag{3.14}$$

and substituting into equation 3.12, the barotropic Rossby wave dispersion relation is shown to be

$$\omega = \bar{u}k - \frac{\beta_* k}{K^2}, \tag{3.15}$$

where $K = \left(k^2 + l^2\right)^{\frac{1}{2}}$ is the total horizontal wavenumber.

In order to examine stationary wave patterns the phase speed, $c = \frac{\omega}{k}$, is required to be zero. This will yield a relation for the wavenumber a wave must have to remain stationary against the background flow. This condition requires $\omega = 0$ in equation 3.15. Applying this condition and rearranging gives the stationary Rossby wavenumber

$$K = K_s = \left(\frac{\beta_*}{\bar{u}}\right)^{\frac{1}{2}}. \tag{3.16}$$

Stationary Rossby waves can exist provided the background flow is westerly ($\bar{u} > 0$) and there is no reversal of the meridional vorticity gradient ($\beta_* > 0$).

It can be shown that the group velocity of stationary waves is parallel to the total wavenumber vector $\mathbf{K} = (k,l)$. The group velocity vector is

$$\mathbf{c}_g = (c_{gx},c_{gy}) = \left(\frac{\partial \omega}{\partial k},\frac{\partial \omega}{\partial l}\right). \tag{3.17}$$

From the dispersion relation (equation 3.15) we can find the components of group velocity:

$$c_{gx} = \bar{u} - \frac{\beta_*}{k^2+l^2} + \frac{2\beta_* k^2}{(k^2+l^2)^2} = \frac{\omega}{k} + \frac{2\beta_* k^2}{K^4}, \tag{3.18}$$

$$c_{gy} = \frac{2\beta_* kl}{(k^2+l^2)^2} = \frac{2\beta_* kl}{K^4}. \tag{3.19}$$

For stationary waves, $\omega = 0$, $K = K_s$ and

$$\mathbf{c}_g = \frac{2\beta_* k}{K^4}(k,l). \tag{3.20}$$

Hence the the group velocity of stationary waves is parallel to the total wavenumber.

The WKB approximation states that if the basic flow $\bar{u}(y)$ is independent of x then k will be constant, but l will vary so as to satisfy the local dispersion relation. If the basic flow $\bar{u}(y)$ varies more slowly in y than the scale of the waves, then the same equations are valid for almost-plane waves. Hence, for stationary Rossby waves:

$$k = \text{constant}, \tag{3.21}$$

$$k^2 + l^2 = K_s^2. \tag{3.22}$$

Let α be the angle between $\mathbf{c}_g$ and the x-axis, then

$$\tan\alpha = \frac{l}{k}, \tag{3.23}$$

$$\cos\alpha = \frac{k}{(k^2+l^2)^{\frac{1}{2}}} = \frac{k}{K_s}. \tag{3.24}$$

Moving with the group velocity $\mathbf{c}_g$ along a ray path, the rates of changes of k and l are

$$\frac{Dk}{Dt} = 0, \tag{3.25}$$

$$\frac{Dl}{Dt} = \frac{dl}{dK_s}\frac{DK_s}{Dt} = \frac{K_s}{l}\frac{DK_s}{Dt}. \tag{3.26}$$

Expanding the material derivative of K_s gives

$$\frac{Dl}{Dt} = \frac{K_s}{l}\left(\frac{\partial K_s}{\partial t} + c_{gx}\frac{\partial K_s}{\partial x} + c_{gy}\frac{\partial K_s}{\partial y}\right), \tag{3.27}$$

but given that $K_s = K_s(y)$ this simplifies to

$$\frac{Dl}{Dt} = \frac{K_s}{l}c_{gy}\frac{\partial K_s}{\partial y}. \tag{3.28}$$

The group velocity vector (equation 3.17) can be expressed in terms of its unit direction vector and the group speed c_g

$$\mathbf{c}_g = c_g\frac{1}{(k^2+l^2)^{\frac{1}{2}}}(k,l) = \frac{c_g}{K_s}(k,l). \tag{3.29}$$

The y-component of which is

$$c_{gy} = \frac{c_g}{K_s}l. \tag{3.30}$$

This allows us to write the material derivative of l as

$$\frac{Dl}{Dt} = c_g\frac{\partial K_s}{\partial y}. \tag{3.31}$$

The bending of the ray is expressed as

$$\frac{D}{Dt}(\tan\alpha) = \frac{1}{k}\frac{Dl}{Dt}, \tag{3.32}$$

and thus substituting in equation 3.31 gives

$$\frac{D}{Dt}(\tan\alpha) = \frac{1}{k}c_g\frac{\partial K_s}{\partial y}. \tag{3.33}$$

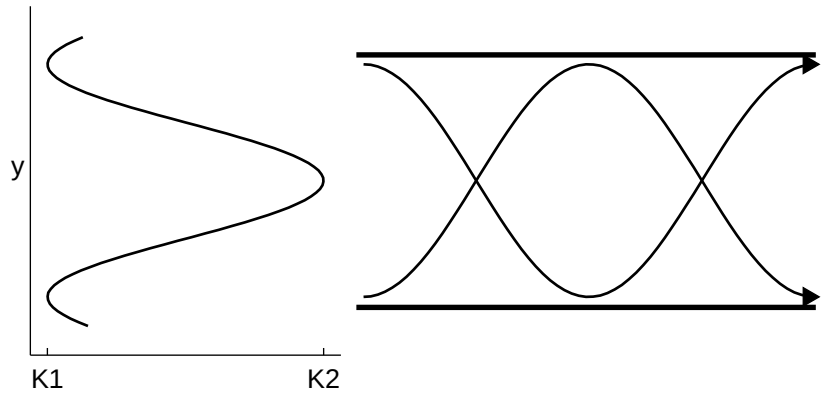

Figure 3.16: The waveguide effect of a local maximum in K_s. Waves of wavenumber k, with $K_1 < k < K_2$, will be trapped in the waveguide. Adapted from *Hoskins and Ambrizzi* (1993).

Given that

$$\frac{D}{Dt}(\tan\alpha) = \frac{d}{d\alpha}(\tan\alpha)\frac{D\alpha}{Dt} = \sec^2\alpha\frac{D\alpha}{Dt}, \tag{3.34}$$

we can express the material derivative of α in terms of the meridional gradient of K_s

$$\frac{D\alpha}{Dt} = \frac{k}{K_s^2}c_g\frac{\partial K_s}{\partial y}. \tag{3.35}$$

Equation 3.35 shows that $\frac{D\alpha}{Dt}$ has the same sign as $\frac{\partial K_s}{\partial y}$, hence if K_s increases with latitude then α will increase and Rossby rays will turn (be refracted) toward larger y. Likewise if K_s decreases with latitude then α will decrease and Rossby rays will turn (be refracted) toward smaller y. More generally, this means that Rossby rays are always refracted toward latitudes with larger K_s. This condition implies that a local maximum in K_s would trap waves, and act as a waveguide. This is illustrated in figure 3.16, where waves with wavenumber between K_1–K_2 would be trapped in the waveguide.

Hoskins and Ambrizzi (1993) discuss the validity of the WKB approximation for analysis of Rossby wave propagation. They concluded that even though the theory is not strictly valid due to the scale of the Rossby waves and the scale of the basic flow being similar, the theory can be qualitatively useful. *Karoly* (1983) extended this ray theory to flows with both a mean zonal flow, $\bar{u}$, and a mean meridional flow, $\bar{v}$. Whilst being more complete, the equations are considerably more complicated than those for the case of background zonal flow only. *Hoskins and Ambrizzi* (1993) reasoned that since in large scale flow $\bar{u}$ dominates $\bar{v}$, and latitudinal gradients dominate over longitudinal gradients of

the basic flow, it is likely that most of the useful results that could come from ray theory could be obtained by the consideration of the terms $\bar{u}$, β_*, and K_s alone.

As shown in *Hoskins and Karoly* (1981), the effect of spherical geometry can be included in the WKB treatment, and the poleward absolute vorticity gradient may be written as in *Hoskins and Ambrizzi* (1993):

$$\beta_M = \left(2\Omega - \left(\frac{1}{\cos\phi} \frac{\partial}{\partial\phi} \right)^2 \left(\cos^2\phi\, \bar{v} \right) \right) \frac{\cos^2\phi}{a}, \tag{3.36}$$

where β_M is $\cos\phi$ times the meridional gradient of absolute vorticity on the sphere, ϕ is the latitude and

$$\bar{v} = \frac{\bar{u}}{a\cos\phi}, \tag{3.37}$$

is the relative rotation rate of the atmosphere. This allows the stationary wavenumber to be written in terms of an equivalent zonal wavenumber on the Mercator projection:

$$K_s = \left(\frac{2\Omega}{\bar{v}} - \frac{1}{\bar{v}} \left(\frac{1}{\cos\phi} \frac{\partial}{\partial\phi} \right)^2 \left(\cos^2\phi\, \bar{v} \right) \right)^{\frac{1}{2}} \cos\phi. \tag{3.38}$$

To illustrate this theory, the 50 year 1957–2006 NDJFM time-mean 200 hPa flow is examined. Figure 3.17a shows the time-mean northern winter zonal wind at 200 hPa for observations. Figure 3.17b shows the meridional gradient of absolute vorticity as defined in equation 3.13. The regions with strong jets in figure 3.17a have strong maxima of β_M with minima to the North and South of the jet. As noted by *Hoskins and Ambrizzi* (1993) this term differs significantly from β alone, and shows that the inclusion of the background relative vorticity in the derivation of the Rossby dispersion relation is critical. The zonal stationary wavenumber is shown in figure 3.17c. There is a local maximum in K_s in the vicinity of the African/Asian jet, extending out into the North Pacific. There are other local maxima of K_s stretching from the equatorial Pacific in the region of mean westerlies out over North America and the North Atlantic, from Central America across into the African jet, and in the vicinity of the Southern hemisphere jet.

Figure 3.17 has shown that the application of this theory can yield some useful results in terms of determining possible properties of Rossby wave propagation. The relevance of stationary wavenumber to this study is discussed in detail in the next section.

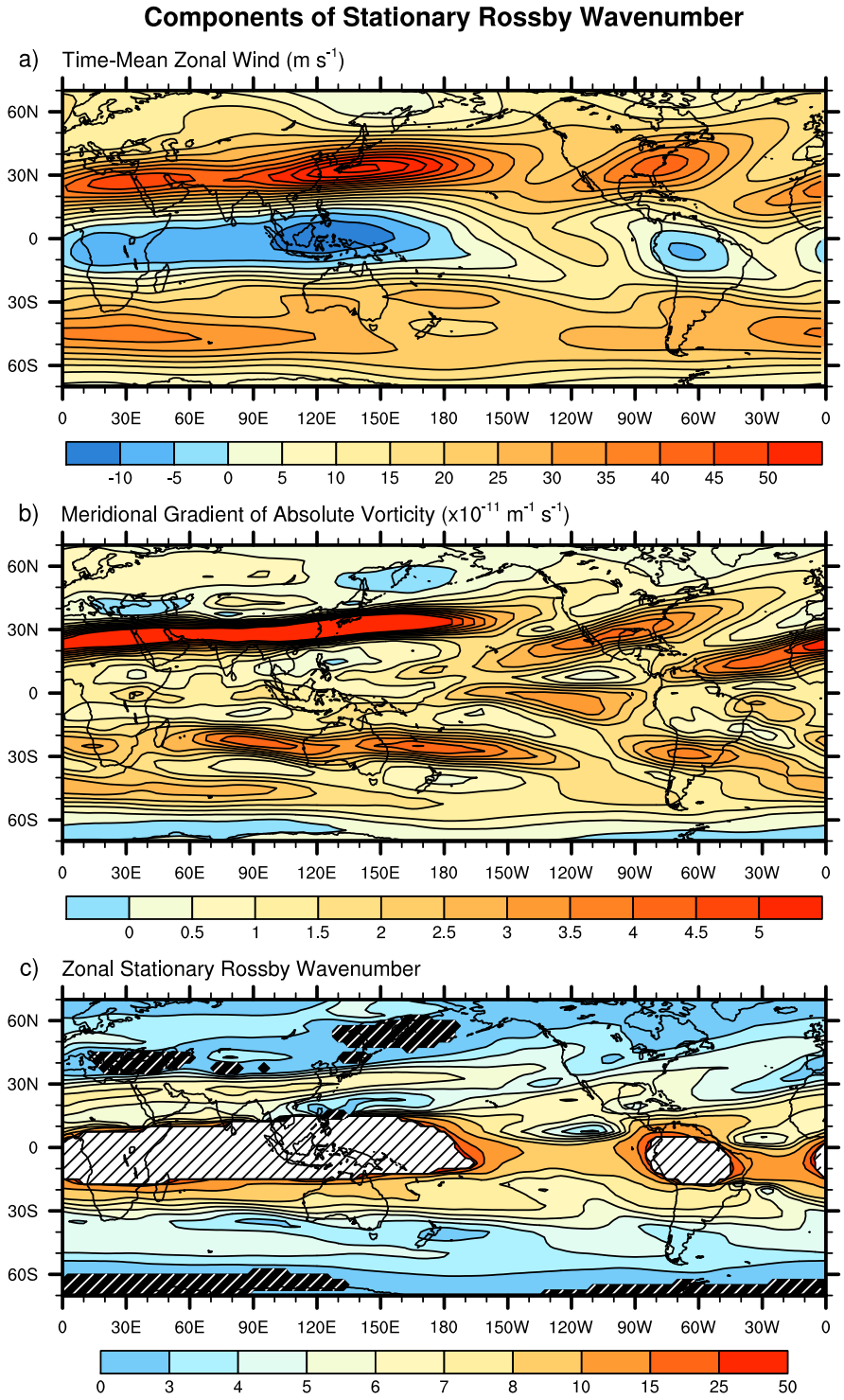

Figure 3.17: Northern winter (NDJFM) background flow at 200 hPa for the period 1957–2006 from NCEP/NCAR Reanalysis. a) Zonal wind component (contour interval: 5 m s^{-1}), b) Mercator coordinate meridional gradient of absolute vorticity, β_M (contour interval: 0.5×10^{-11} m^{-1} s^{-1}), and c) zonal stationary wavenumber K_s for $\beta_M > 0$, $\bar{u} > 0$. Light (dark) hatching indicates areas where $\bar{u}$ (β_M) is negative.

3.5.2 Stationary wavenumber over the North Pacific

Figure 3.18 shows zonal stationary Rossby wavenumber over the North Pacific (*zonal* wavenumber is the number of zonal wavelengths that will fit around a latitude circle). In the observed atmosphere there is a local maximum in K_s in the vicinity of the Asian-Pacific jet, extending out over the North Pacific. There is another local maximum in observed K_s stretching from the tropical Pacific out over North America. These waveguides, of typical zonal wavenumber 5, are quite open in structure, almost merging into one-another in the central North Pacific.

HiGEM1.2 (figure 3.18b) shows more extensive regions of reversed meridional absolute vorticity gradient (dark hatching) where Rossby waves will not propagate, especially over the equatorial Pacific. However, HiGEM1.2 does replicate the rather open waveguide structure of the observations well in the central North Pacific. The waveguides in HiGEM1.2 have typical zonal wavenumber 4–5 and appear to merge somewhat over the central North Pacific.

HadGEM1.2 (figure 3.18c) shows a rather different waveguide structure in the central North Pacific. The two main waveguides are much more well defined in HadGEM1.2, with each being a separate structure. The two waveguides are divided by an area of reversed meridional absolute vorticity gradient (dark hatching) at 140°W 30°N, which will strongly repel Rossby waves and across which they will not propagate.

As an example, consider Rossby waves of zonal wavenumber 4–5 propagating in the observed atmosphere. This wavenumber is chosen because it corresponds approximately to the wavenumber of the Northern Hemisphere wave train produced as a response to El Niño forcing (figure 3.7). These waves are likely to be partially refracted into the tropical Pacific waveguide when they reach the end of the Asian-Pacific jet waveguide due to the close proximity of the two waveguides. This would also be true of Rossby waves in the HiGEM1.2 atmosphere. However, in the HadGEM1.2 atmosphere this is less likely due to the relative separation of the two waveguides and the area of reversed meridional absolute vorticity gradient blocking the refraction of Rossby waves into the tropical waveguide.

This subtle, yet dynamically significant feature of the HadGEM1.2 atmospheric mean state could potentially send Rossby waves along very different propagation paths, and

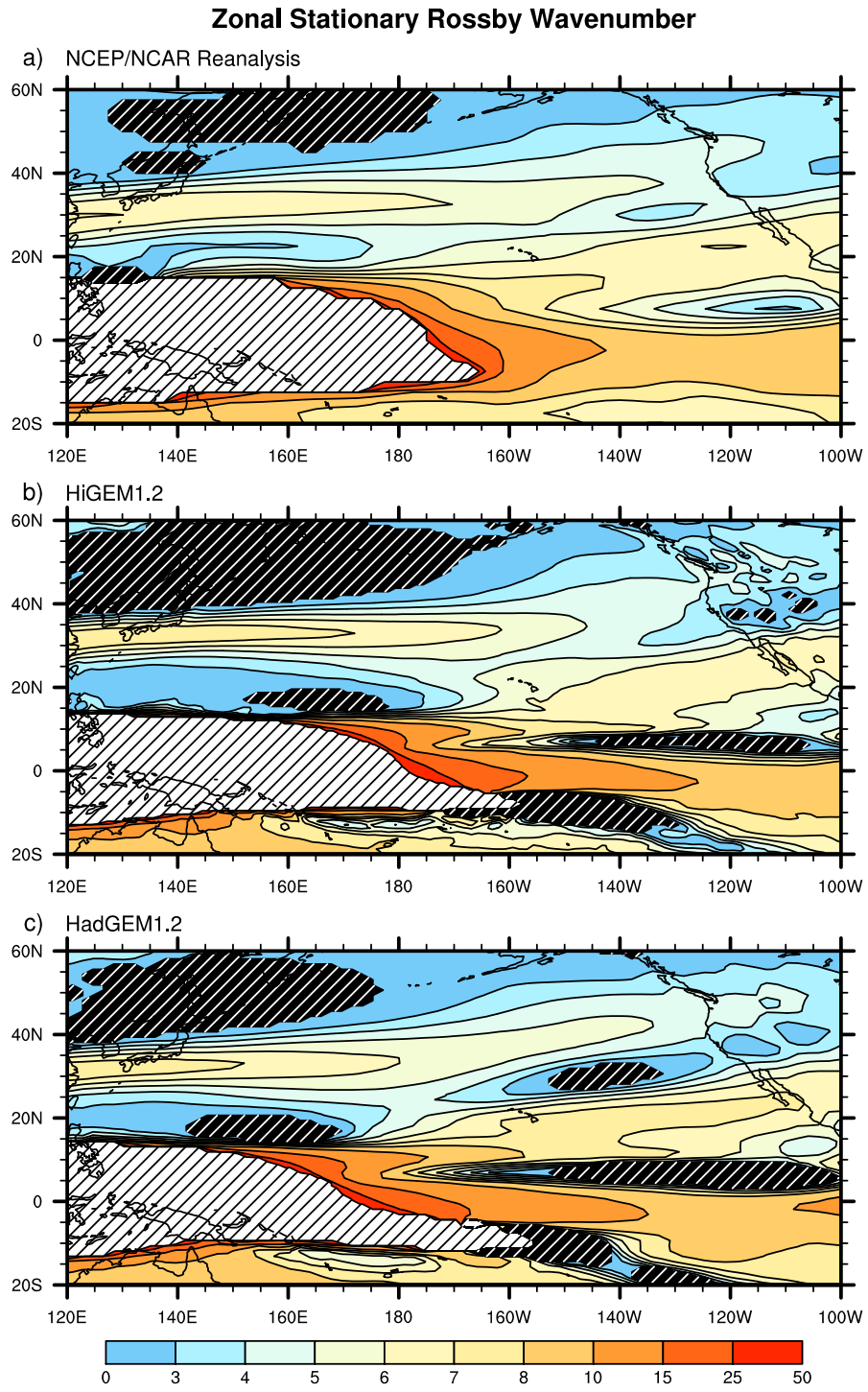

Figure 3.18: Zonal stationary wavenumber (K_s) computed from northern winter (NDJFM) 50 year time-mean zonal wind at 200 hPa. Light (dark) hatching indicates areas where $\bar{u}$ (β_M) is negative. a) NCEP/NCAR Reanalysis, b) HiGEM1.2, and c) HadGEM1.2.

hence induce very different circulation anomalies than exist in the observed atmosphere.

3.6 Rossby wave generation: theory and application

Analysis of the atmospheric background state showed that Rossby waves in HadGEM1.2 are likely to propagate differently to those in the observed atmosphere, leading to a different extra-tropical response to El Niño. Here, we take a step backward and examine the spatial patterns of Rossby wave generation in the observations and models. If there are significant differences in both the generation and propagation of Rossby waves between the observations and models, these two factors combined could then explain the differences in the extra-tropical responses to El Niño. Tropical convection and atmospheric heating due to anomalous SSTs has a major role in the generation of atmospheric planetary scale waves (*Hoskins and Karoly*, 1981). The vertical convective motion leads to convergence at the surface and divergence in the upper troposphere, which induces an anomalous upper level vorticity source, referred to as the Rossby wave source (RWS); (*Sardeshmukh and Hoskins*, 1988). It is the RWS that forces the Rossby wave train that forms a large component of the El Niño teleconnection signal in the extra-tropical atmosphere. The RWS can give a more insightful view of the forcing mechanisms producing Rossby waves than is possible to gain from examining surface forcing alone as in figures 3.5 and 3.6.

Consider the non-linear barotropic vorticity equation

$$\left(\frac{\partial}{\partial t}+\mathbf{v}\cdot\nabla\right)\zeta=-\zeta D+F, \tag{3.39}$$

where $\mathbf{v}$ is the horizontal velocity vector, ζ is absolute vorticity, D is horizontal divergence, and F is the friction term. The classical theory of Rossby wave dynamics is an idealised case that considers a non-divergent flow. Although a simplification of real world atmosphere dynamics, this approach is valid given that the non-divergent component of wind is typically an order of magnitude greater than the irrotational component. In order to understand Rossby wave dynamics in a realistic atmosphere, the horizontal wind vector can be decomposed into non-divergent (rotational) and irrotational (divergent) components such that

$$\mathbf{v}=\mathbf{v}_\psi+\mathbf{v}_\chi. \tag{3.40}$$

Using this decomposed horizontal wind field in equation 3.39 yields an equation that can be understood in terms of classical Rossby wave theory, but also retains an irrotational flow component in a forcing term:

$$\left(\frac{\partial}{\partial t}+\mathbf{v}_\psi\cdot\nabla\right)\zeta = S+F, \tag{3.41}$$

where $\mathbf{v}_\psi$ is the non-divergent component of the horizontal wind vector associated with ζ, and S is the Rossby wave source term. For equations 3.39 and 3.41 to be consistent requires the RWS to be specified as

$$S = -\nabla\cdot\left(\mathbf{v}_\chi\zeta\right) = -\zeta\nabla\cdot\mathbf{v}_\chi - \mathbf{v}_\chi\cdot\nabla\zeta. \tag{3.42}$$

The first term in the RWS is stretching of absolute vorticity by the divergence of the wind. The second term is advection of absolute vorticity by the divergent component of the wind. This expression for the RWS may be linearised about an ambient flow. This will allow the investigation of which terms contribute most heavily to the RWS. Hence, the full RWS will be specified as

$$S = \bar{S} + S', \tag{3.43}$$

where

$$\bar{S} = -\left(\underbrace{\bar{\zeta}\nabla\cdot\bar{\mathbf{v}}_\chi}_{\text{term 1}} + \underbrace{\bar{\mathbf{v}}_\chi\cdot\nabla\bar{\zeta}}_{\text{term 2}}\right), \tag{3.44}$$

and

$$S' = -\left(\underbrace{\bar{\zeta}\nabla\cdot\mathbf{v}'_\chi}_{\text{term 1}} + \underbrace{\zeta'\nabla\cdot\bar{\mathbf{v}}_\chi}_{\text{term 2}} + \underbrace{\zeta'\nabla\cdot\mathbf{v}'_\chi}_{\text{term 3}} + \underbrace{\bar{\mathbf{v}}_\chi\cdot\nabla\zeta'}_{\text{term 4}} + \underbrace{\mathbf{v}'_\chi\cdot\nabla\bar{\zeta}}_{\text{term 5}} + \underbrace{\mathbf{v}'_\chi\cdot\nabla\zeta'}_{\text{term 6}}\right), \tag{3.45}$$

where $\bar{S}$ is the time-mean RWS and S' is the perturbation RWS.

The time-mean and perturbation RWS components for the 1957–2006 observed northern winter 200 hPa flow are shown in figure 3.19. The time-mean RWS, $\bar{S}$, is strongly negative over the extra-tropical North Pacific and North Atlantic. It is strongly positive over North Africa, Asia, and the tropical North Atlantic. Note that a positive RWS corresponds to a cyclonic (anticyclonic) vorticity forcing in the Northern (Southern) Hemisphere. A

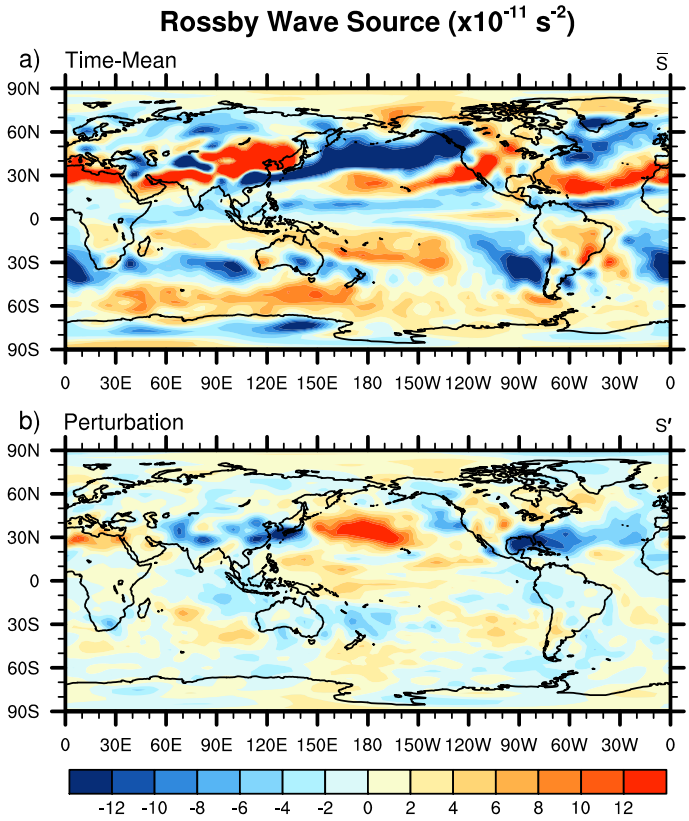

Figure 3.19: a) 50 year time-mean northern winter (NDJFM) 200 hPa Rossby wave source $\bar{S}$ (equation 3.44, 10^{-11} s^{-2}). b) Northern winter 200 hPa Rossby wave source anomaly S' (equation 3.45, 10^{-11} s^{-2}) patterns associated with a 1 °C departure of the EP index. The contour interval is 2×10^{-11} s^{-2}.

negative RWS corresponds to an anticyclonic (cyclonic) vorticity forcing in the Northern (Southern) Hemisphere. The perturbation RWS S', for El Niño events, has a positive anomaly over the western North Pacific and a negative anomaly over southern Japan and the eastern Asian continent. There is also a strong negative anomaly over the Gulf of Mexico and western tropical Atlantic Ocean.

Further to figure 3.19a, the individual terms making up the time-mean RWS (equation 3.44) are shown in figure 3.20. Stretching of mean absolute vorticity by the divergence of the mean wind (term 1) is dominant over advection of mean absolute vorticity by the divergent component of the mean wind (term 2) in almost all regions in the time-mean RWS. The vortex stretching term has most influence in Northern Hemisphere mid-latitudes. Advection of vorticity provides a generally weak global contribution in comparison to vortex stretching. There is an area of strong negative advection of vorticity

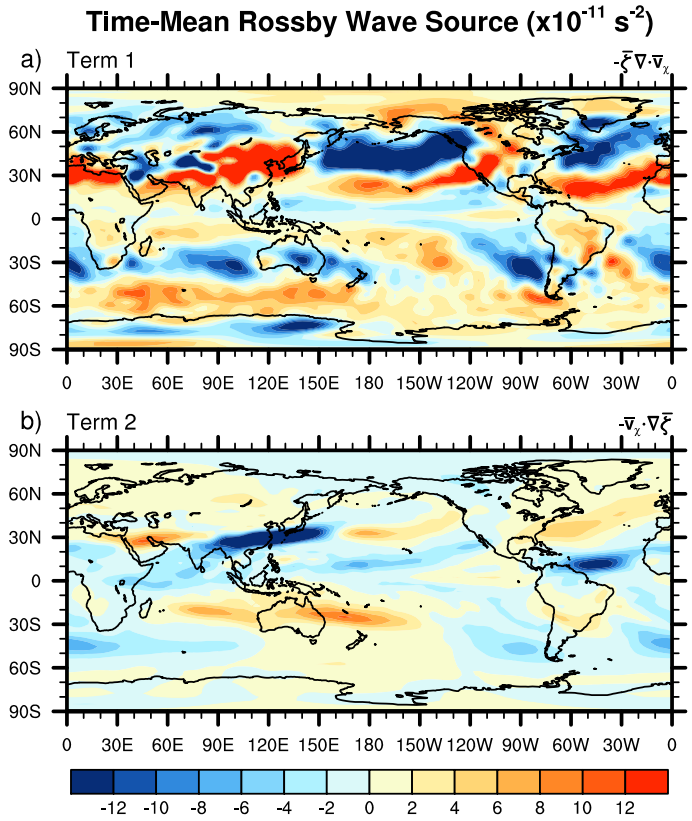

Figure 3.20: Individual terms making up the 50 year time-mean northern winter (NDJFM) Rossby wave source (10^{-11} s^{-2}) at 200 hPa, as specified in equation 3.44. The contour interval is 2×10^{-11} s^{-2}. a) Term 1 (vortex stretching): $-\bar{\zeta}\nabla\cdot\bar{\mathbf{v}}_\chi$, and b) Term 2 (advection of vorticity): $-\bar{\mathbf{v}}_\chi\cdot\nabla\bar{\zeta}$.

over southern Japan, due to the mean northwards divergent outflow from the warm pool advecting anticyclonic vorticity from the equatorward flank of the Asian jet.

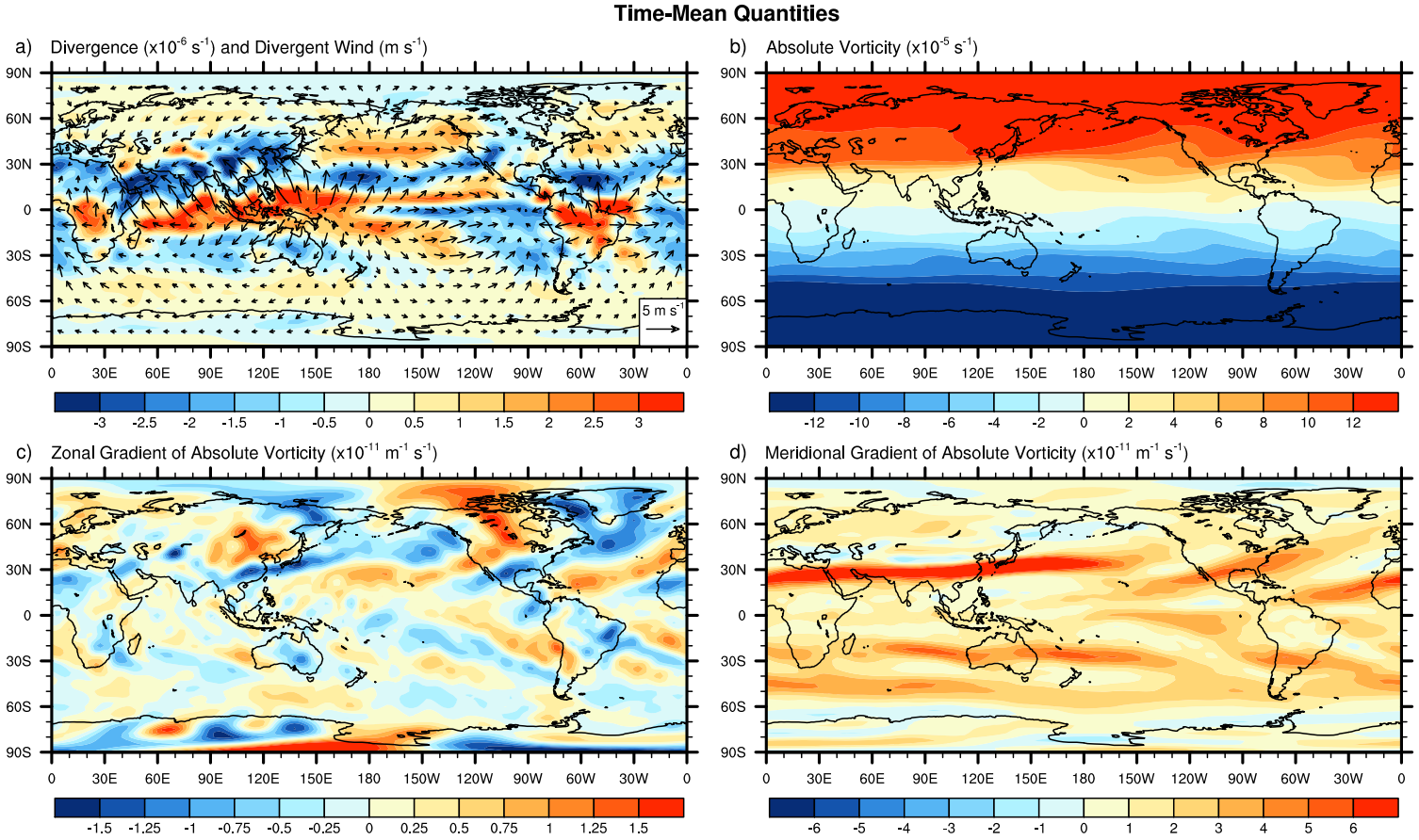

Figure 3.21: Individual terms making up the components of 50 year time-mean northern winter (NDJFM) Rossby wave source at 200 hPa (equation 3.44). a) Divergence and divergent component of wind (contour interval: 0.5×10^{-6} s^{-1}), b) Absolute vorticity (contour interval: 2×10^{-5} s^{-1}), c) Zonal gradient of absolute vorticity (contour interval: 0.25×10^{-11} m^{-1} s^{-1}), and d) Meridional gradient of absolute vorticity (contour interval: 10^{-11} m^{-1} s^{-1}).

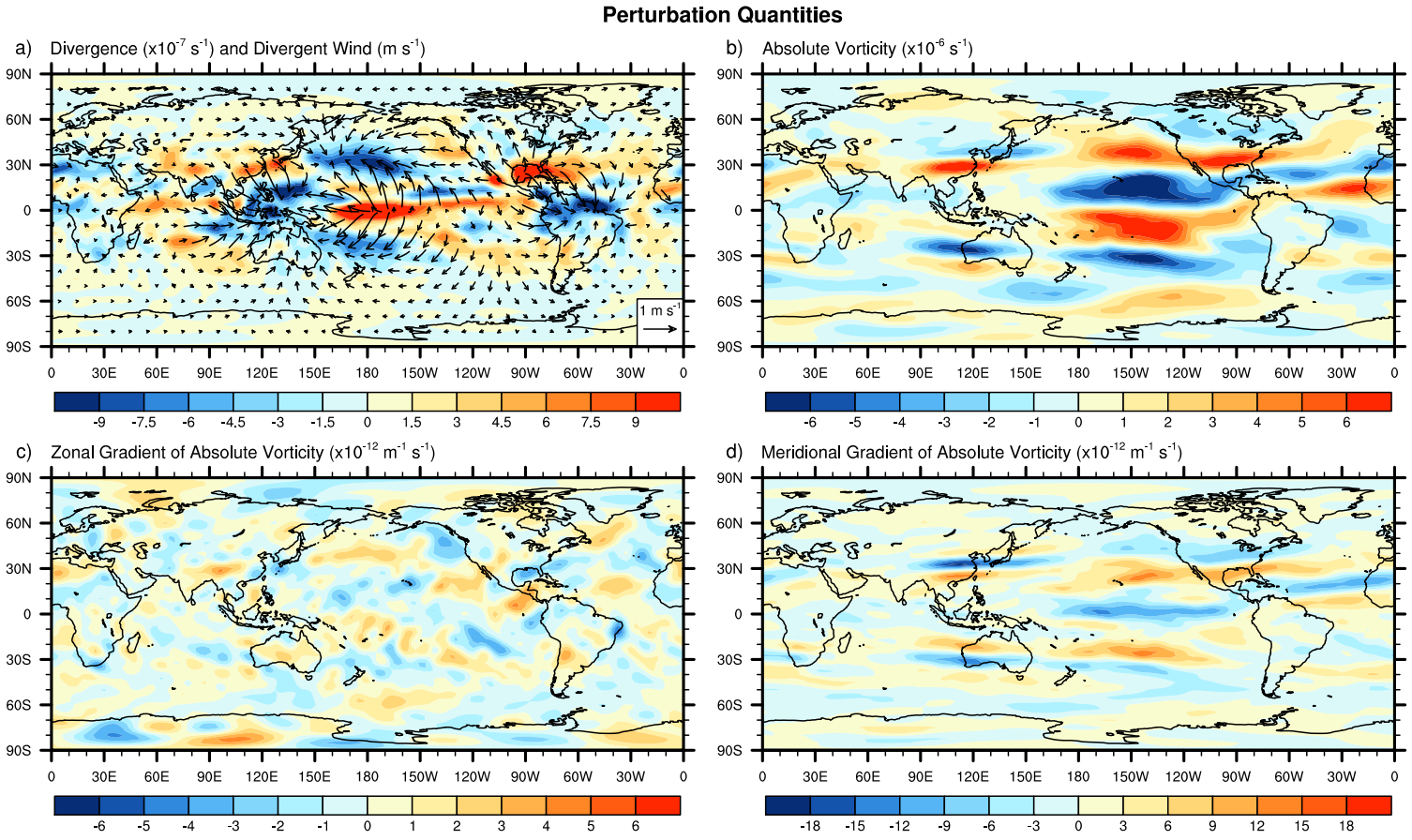

Figure 3.22: Individual terms making up the components of northern winter 200 hPa Rossby wave source anomaly (equation 3.45) regression maps. a) Divergence and divergent component of wind (contour interval: 0.5×10^{-7} s^{-1}), b) Absolute vorticity (contour interval: 10^{-6} s^{-1}), c) Zonal gradient of absolute vorticity (contour interval: 10^{-12} m^{-1} s^{-1}), and d) Meridional gradient of absolute vorticity (contour interval: 3×10^{-12} m^{-1} s^{-1}).

Figures 3.21 and 3.22 show the individual physical quantities that make up each term in the time-mean and perturbation RWS. The strong vortex stretching in the time-mean RWS in the Northern Hemisphere mid-latitudes (figure 3.20a) is due to strong divergence (figure 3.21a) in the Northern Hemisphere mid-latitudes combined with large values of absolute vorticity. Time-mean absolute vorticity (figure 3.21b) is small in the tropics and large in the mid-latitudes and polar regions. This effectively damps the contribution of tropical divergence to the time-mean RWS and enhances the contribution of mid-latitude divergence.

A similar decomposition for the perturbation RWS can be made. Stretching of mean absolute vorticity by the anomalous divergence (Term 1; figure 3.23a) provides the largest contribution to global perturbation RWS, closely resembling the total perturbation RWS (figure 3.19b). Anomalous divergence (figure 3.22a) is strong in the tropics and Northern Hemisphere mid-latitudes, and to a lesser extent in the Southern Hemisphere mid-latitudes. Mid-latitude divergence anomalies are enhanced and tropical anomalies are damped by multiplication by absolute vorticity (figure 3.21b).

The stretching of anomalous vorticity over the eastern tropical Pacific (figure 3.22b) by the strong mean divergence there (figure 3.21a) leads to a forcing through term 2 (figure 3.23b), though this term is generally weak. A similar situation is produced over south-east Asia, however it is much more localised.

Advection of anomalous vorticity by the divergent component of mean wind and advection of mean absolute vorticity by the divergent component of anomalous wind (terms 4 and 5 in equation 3.45; figures 3.24a and 3.24b) make strong but localised contributions to the total perturbation RWS. Term 4 is strongest over south-east Asia where the divergent component of mean wind (figure 3.21a) has a strong north-south component and meridional gradient of vorticity anomaly (figure 3.22d) is large. Term 5 is strongest over east Asia, to the east of Australasia, over the southern USA, and the northern part of South America. These are all regions where the meridional gradient of mean absolute vorticity is large and where there is strong anomalous divergence/convergence, and hence a strong divergent component of anomalous wind.

Stretching of anomalous vorticity by the anomalous divergence and advection of anomalous vorticity by the divergent component of anomalous wind (terms 3 and 6 in

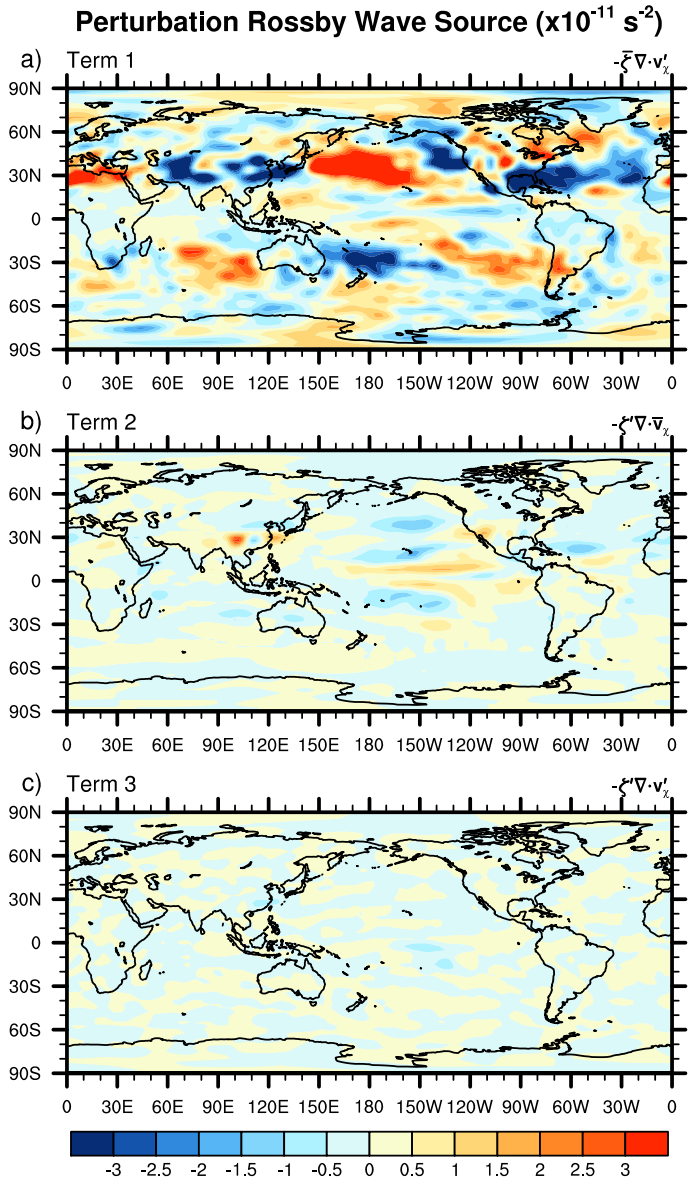

Figure 3.23: Northern winter (NDJFM) 200 hPa Rossby wave source anomaly terms as specified in equation 3.45, associated with a 1 °C departure of the EP index. The contour interval is 0.5×10^{-11} s^{-2}. a) Term 1: $-\bar{\zeta}\nabla\cdot\mathbf{v}'_\chi$, b) Term 2: $-\zeta'\nabla\cdot\bar{\mathbf{v}}_\chi$, and c) Term 3: $-\zeta'\nabla\cdot\mathbf{v}'_\chi$.

equation 3.45; figures 3.23c and 3.24c) provide the smallest contribution to the perturbation RWS. These are the quadratic perturbation terms. Their small magnitude in comparison with the other terms making up the perturbation RWS, shows the validity of neglecting these terms when linearising equation 3.39.

The RWS decompositions for HiGEM1.2 and HadGEM1.2 (not shown) are qualitatively similar to that for the observations.

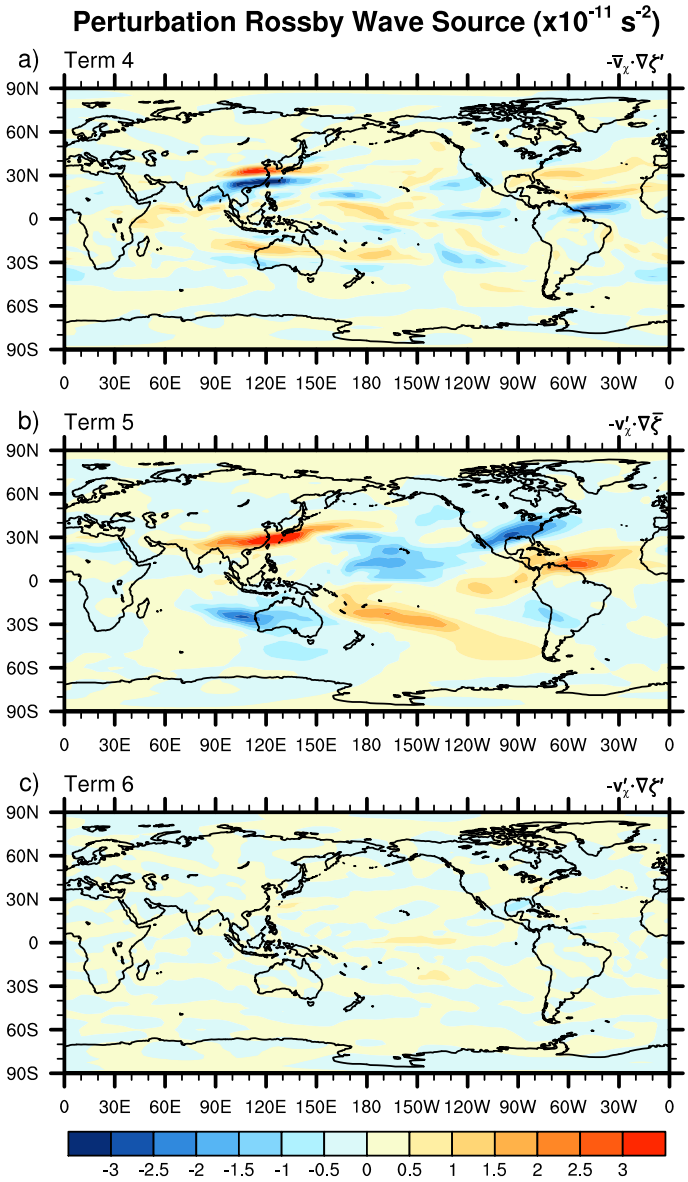

Figure 3.24: Northern winter (NDJFM) 200 hPa Rossby wave source anomaly terms as specified in equation 3.45, associated with a 1 °C departure of the EP index. The contour interval is 0.5×10^{-11} s^{-2}. a) Term 4: $-\bar{\mathbf{v}}_\chi \cdot \nabla\zeta'$, b) Term 5: $-\mathbf{v}'_\chi \cdot \nabla\bar{\zeta}$, and c) Term 6: $-\mathbf{v}'_\chi \cdot \nabla\zeta'$.

3.6.1 Rossby wave source over the North Pacific

Regression maps of the RWS anomaly associated with El Niño for observations, HiGEM1.2, and HadGEM1.2 are shown in figure 3.25. In order to understand RWS in the context of anomalous Rossby wave response to El Niño, the contour of stationary zonal wavenumber $K_s = 4$ is overlaid on RWS in figure 3.25. The wave train seen in figure 3.7 has a zonal wavenumber of approximately 4–5. Since these are not pure harmonic plane

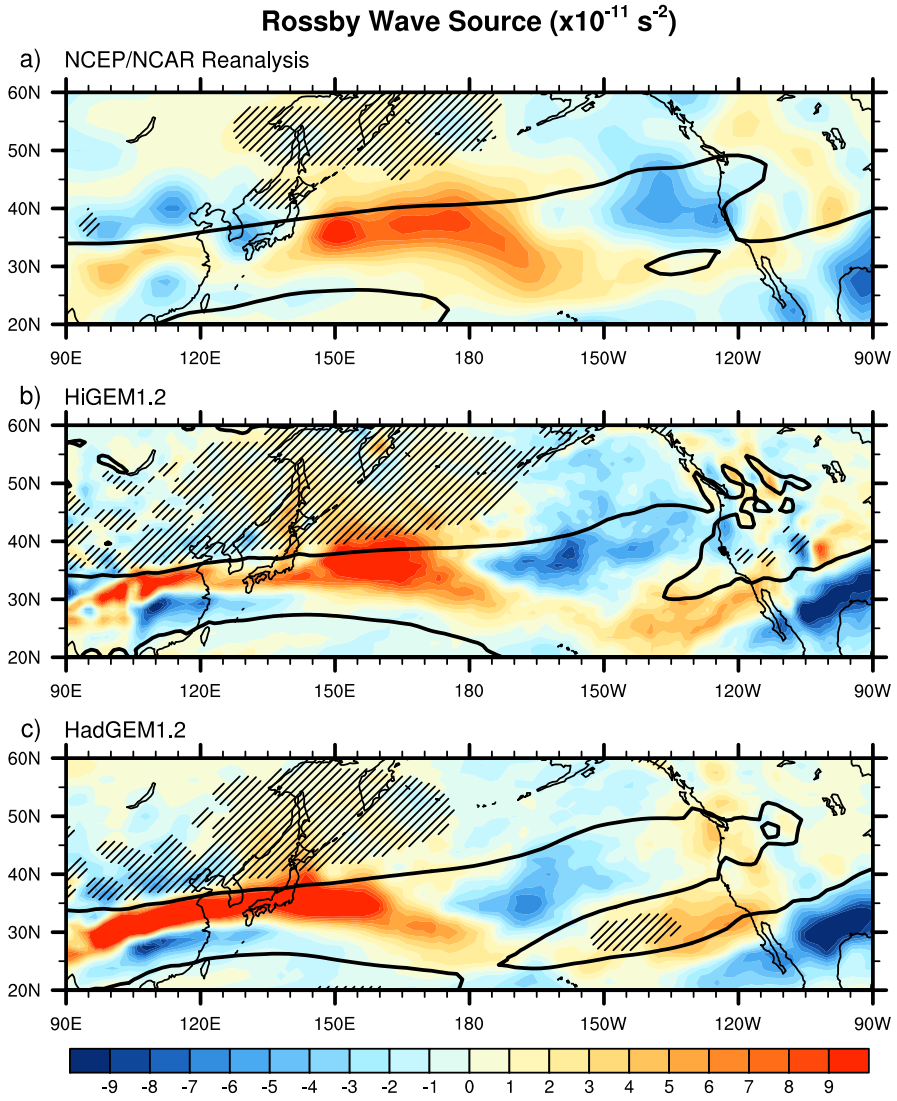

Figure 3.25: Rossby wave source anomaly patterns (colors, 10^{-11} s^{-1}) associated with a 1 °C departure of the EP index. The contour interval is 10^{-11} s^{-2}. Stationary wavenumber $K_s = 4$ is shown by a thick contour. Hatching indicates regions with reversed absolute vorticity gradient as in figure 3.18. a) NCEP/NCAR Reanalysis, b) HiGEM1.2, and c) HadGEM1.2.

waves it is reasonable to choose the waveguide of zonal wavenumber 4 as an approximation to the propagation paths of these waves. Regions of reversed absolute vorticity gradient are hatched as in figure 3.18.

In the observations there is a positive RWS anomaly associated with El Niño in the North-West Pacific. This generates the cyclonic (positive vorticity) anomaly over the extra-tropical North Pacific seen in figure 3.7a (cyclonic, negative stream function anomaly). This RWS anomaly is strong, and also is spread over a large area. This implies significant generation of Rossby waves both inside and outside of the $K_s \geq 4$ waveguide.

Waves of zonal wavenumber 4 or higher generated inside the waveguide will tend to follow it, and likely exit in the vicinity of the central Pacific waveguide, possibly entering it and following it across North America. Waves generated outside the Asian-Pacific jet waveguide may follow other trajectories.

A similar situation is seen in HiGEM1.2. Although the RWS anomaly is a different shape and has a greater westerly extent, being present in the Asian jet over land, the wave generation in HiGEM1.2 is active both inside and outside the $K_s \geq 4$ waveguide, suggesting similar wave propagation mechanisms are operating to those in the observations. However, in HadGEM1.2 the RWS is elongated and constrained more tightly into the jet. As a consequence of this, most wave generation is inside the $K_s \geq 4$ waveguide. This implies that most of the waves generated there will be trapped inside the Asian-Pacific jet waveguide. Unlike the observations or HiGEM1.2, the waveguide in HadGEM1.2 does not exit in the vicinity of the central Pacific waveguide, instead it remains distinct and is oriented more to the north-east. However, it is clear that the RWS in HiGEM1.2 and HadGEM1.2 are more similar to one another than they are to the RWS in observations. In both HiGEM1.2 and HadGEM1.2 there is a negative RWS anomaly at 165°W, further west than in observations. There is a strong negative anomaly at 100°W in both HiGEM1.2 and HadGEM1.2 that is considerably stronger than in observations. Even though there are differences between the RWS anomaly patterns in HiGEM1.2 and HadGEM1.2, these differences in the generation of Rossby waves are less significant than the influence of the atmosphere background state on the preferred propagation paths of Rossby waves, in determining the extra-tropical response to El Niño.

3.7 Discussion

The global simulation of El Niño in the low resolution coupled model HadGEM1.2, which has resolution typical of the models used in the AR4 climate change assessment, is compared with the simulation in HiGEM1.2, a higher resolution version of the same model, and observations. The spatial distribution of tropical SST anomaly during El Niño is simulated well by both HiGEM1.2 and HadGEM1.2. It is in the extra-tropical SST response where the high and low resolution models differ greatly. HiGEM1.2 is capable of reproducing the large scale cold anomaly in the central North Pacific associated with El Niño

as seen in observations. It also produces a warm anomaly along the Pacific coast of North America. HadGEM1.2 on the other hand, simulates the North Pacific SST response very poorly, only managing a small portion of the cold anomaly that should exist in the central North Pacific, and no significant warm anomaly along the Pacific coast of North America.

An analysis of tropical convective forcing showed similar patterns of convection in HiGEM1.2 and HadGEM1.2. Although there are small differences between the high and low resolution models, this suggests that there is more to the incorrect North Pacific SST response than simply inadequate surface forcing for the atmospheric bridge. The anomaly response in the upper troposphere of HadGEM1.2 is very different to observations, whereas HiGEM1.2 showed similar circulation anomalies to those seen in the reanalysis data set. This suggests that upper tropospheric wave anomalies are being excited and propagated in an unrealistic manner in HadGEM1.2.

The extra-tropical SST response to El Niño in HiGEM1.2 and HadGEM1.2 can be explained by the anomalous surface circulation that is induced by the upper-tropospheric circulation anomalies. The majority of the extra-tropical SST response is explained by altered surface sensible and latent heat fluxes caused by changes in total wind speed, consistent with previous studies (e.g., *Luksch and von Storch*, 1992; *Deser and Blackmon*, 1995). The direction of the surface circulation anomalies also has an important role. The advection of warmer, more humid air over the North American coastal region is a key factor in HiGEM1.2 producing an accurate response there. The direction of the anomalous circulation in this region is also important for upwelling. In HiGEM1.2 these winds act to suppress upwelling, but in HadGEM1.2 they are favourable to upwelling. Hence, HiGEM1.2 has a more realistic extra-tropical SST response as it simulates the large scale upper tropospheric response to El Niño well, and hence the surface circulation anomalies in the extra-tropics. HadGEM1.2 has a different upper level response and does not produce the surface circulation anomalies required in order to produce a realistic extra-tropical SST response.

The mechanisms giving rise to the extra-tropical circulation anomalies were explored through analysis of the dynamics of the atmospheric basic state, the medium through which Rossby waves propagate. Seemingly subtle differences in the time-mean zonal

wind fields between HadGEM1.2 and the observed atmosphere were shown to have significant dynamical consequences. HadGEM1.2 tends to propagate waves out of the Asian-Pacific jet in a more constrained manner, sending them north of a position that would allow them to freely enter the waveguide associated with the North American Jet. A critical area of reversed absolute vorticity gradient, through which Rossby waves will not propagate, reinforced the separation of the two waveguides. HiGEM1.2 had a very similar Pacific regional waveguide structure to the observed atmosphere.

The Rossby wave source diagnostic was used to analyse Rossby wave generation. Rossby wave source was found to be similar between HiGEM1.2 and HadGEM1.2 over the North Pacific region. The RWS anomaly in HadGEM1.2 is more elongated and constrained more tightly into the Asian-Pacific jet waveguide than in HiGEM1.2 however, it seems that differences in RWS anomaly are less important than the differences in preferred Rossby wave propagation paths. Given the large differences in waveguide structure, and the smaller differences in Rossby wave generation, it would be unreasonable to expect HadGEM1.2 to simulate the extra-tropical SST response to El Niño correctly.

Whilst we have shown that differences in Rossby wave propagation can explain the differences in extra-tropical response to El Niño in high and low resolution coupled models, it is possible that there are processes that we have not discussed that make some contribution. *Hurrell et al.* (2006) showed that increasing horizontal resolution, along with some minor changes to model physics, in an atmosphere model improved the position and strength of mid-latitude storm tracks. An improved representation of storm tracks could lead to more accurate feedback of baroclinic eddies on to the mean state, thus altering Rossby wave propagation paths. The idealised study of *Franzke et al.* (2000) suggests that baroclinic eddies in the storm track can directly interact with Rossby waves, modulating their amplitude. This would provide an extra influence on Rossby wave propagation in addition to the basic state. Since the physics of the extra-tropical response to El Niño are explained well by differences in the basic state, this type of direct interaction is likely to be a process of secondary importance.

The atmospheric response to tropical SST anomalies is a complicated and interconnected system. Here we have studied a major subcomponent of this system. We considered the effect of tropical SST anomalies on the tropical and extra-tropical atmosphere,

and how these atmospheric anomalies produce extra-tropical SST anomalies. Further processes then occur that we have not discussed in this work. The extra-tropical SST anomalies themselves will induce extra-tropical atmospheric circulation anomalies. These anomalies are typically modest in comparison with internal atmospheric variability (*Kushnir et al.*, 2002). *Peng and Robinson* (2001) showed that the atmospheric response to an extra-tropical SST anomaly is strongly dependent on transient eddies, and that the response projects strongly onto patterns of atmospheric internal variability. As discussed in *Kushnir et al.* (2002), we can use a simple linear scaling of the atmospheric response presented by *Peng and Robinson* to an SST anomaly comparable to that produced in the extra-tropical response to El Niño, to show that the magnitude of the atmospheric response to an extra-tropical SST anomaly is around an order of magnitude smaller than that induced by El Niño SST anomalies. This suggests that the atmospheric response to El Niño SST anomalies dominates over secondary atmospheric feedback from extra-tropical SST anomalies.

The resolution of HadGEM1.2 is typical of the coupled climate models used in the IPCC fourth assessment report (*Randall et al.*, 2007). Climate models need to be able to simulate El Niño and the extra-tropical SST response when used for climate change experiments. This is because the behaviour of other parts of the climate system (e.g. monsoons, tropical cyclones, mid-latitude storm tracks) are closely linked to El Niño and its extra-tropical SST response. Here we have shown that an improved simulation of the mean state in a relatively high resolution model has led to an improvement in this aspect of the variability.

Although it has been established that increased horizontal resolution in a coupled climate model improves the representation of the extra-tropical response to El Niño, there is still much to understand. It is not yet clear whether it is increased atmospheric or oceanic horizontal resolution that is most important, or indeed whether increases to both are necessary to accurately represent the extra-tropical response to El Niño. It also remains unclear what mechanisms, or lack thereof, might cause the erroneous atmospheric basic state in the lower resolution coupled model.

Chapter 4

The effect of independent variations to atmospheric and oceanic horizontal resolution on the North Pacific extra-tropical response to El Niño

This chapter continues the work in chapter 3 by examining the performance, with respect to the extra-tropical response to El Niño, of the atmosphere and ocean components of HiGEM and HadGEM separately. An attempt is made to understand whether it is in the atmospheric or oceanic component of the coupled system where horizontal resolution is more valuable.

4.1 Introduction

In chapter 3 it was shown that HadGEM1.2, a typical climate resolution coupled model, is not capable of accurately reproducing the observed extra-tropical response to El Niño. It was also shown that a high resolution configuration of the same model, HiGEM1.2, has a much improved response that is similar to observations. The errors in the low resolution model were traced to an unrealistic atmospheric background state, which changes

the propagation characteristics of Rossby waves. Erroneous Rossby wave anomalies alter atmospheric circulation in the troposphere, causing erroneous surface circulation anomalies. These anomalies then alter the extra-tropical North Pacific SSTs through surface fluxes.

Although it is clear that the high resolution coupled model HiGEM1.2 reproduces the extra-tropical response to El Niño more accurately than HadGEM1.2, it remains unclear whether it is improvement to the atmosphere or ocean resolution that is most critical for this improved response. In this chapter, the bulk of the analysis from chapter 3 will be repeated with a different set of HiGEM and HadGEM integrations. The aim is to determine where resolution is most important in the coupled models in order to reproduce the observed extra-tropical response to El Niño.

4.2 Model integrations

In this chapter integrations from the 1.1 series of HiGEM and HadGEM are used. The main differences between the 1.1 and 1.2 versions are in the parameterisation of oceanic eddies and the oceanic mixed layer, the latter being particularly relevant to atmosphere–ocean coupling. Different types of experiments were performed with the 1.1 and 1.2 series models. The 1.1 series of models have, in addition to coupled control configurations, been integrated in atmosphere-only and cross-resolution configurations.

HiGEM1.1 and HadGEM1.1 are coupled control integrations, the 1.1 series counterparts to the models used in chapter 3. The lengths of these control integrations are similar to the lengths of their 1.2 counterparts. Excluding ocean model adjustment time, approximately 70 years of complete winter seasons are available for each of HiGEM1.1 and HadGEM1.1. To be consistent with the work in chapter 3, 50 years of winter seasons are used for this study. The winter seasons used are those for years 21–70 of each integration, rather than the last 50 years. Again this is for consistency with previous work.

The atmosphere-only integrations utilize only the atmosphere components of the coupled models: the high resolution HiGAM1.1 and the low resolution HadGAM1.1. The integrations are forced using SST and sea ice boundary conditions from the second Atmospheric Model Intercomparison Project (AMIP II; *Taylor et al.*, 2000). Due to the limitation of forcing the atmosphere models with reliable SST observations, the integration

Atmospheric resolution	Oceanic resolution	
	$1-\frac{1}{3}^\circ$ ≈110 km	$\frac{1}{3}^\circ$ ≈33 km
N96: 1.5° ≈135 km	HadGEM1.1	LoHi
N144: 1.0° ≈90 km	HiLo	HiGEM1.1

Table 4.1: Summary of 1.1 series coupled integrations. Columns are ocean model resolution and rows are atmosphere model resolution.

length is much shorter than that of the coupled integrations used in chapter 3. Complete winter seasons are available for 1978/79–2001/02 for HiGAM1.1 and 1978/79–1997/98 for HadGAM1.1. The spin-up period of the atmosphere models is much shorter than that of the ocean models. Although these shorter integrations are not ideal for comparing to 50 year coupled integrations, they should still be able to show us the capabilities of the atmospheric model components with respect to the extra-tropical response to El Niño.

The cross-resolution configurations of the 1.1 series models are as described in *Roberts et al.* (2009). These configurations allow the investigation of the effect of varying the atmosphere and ocean resolution independently of one another. In keeping with the terminology used by *Roberts et al.*, these configurations are referred to as HiLo and LoHi. The HiLo configuration uses the HiGEM resolution atmosphere (HiGAM1.1) coupled with the HadGEM resolution ocean (HadGOM1.1). The LoHi configuration uses the HadGEM resolution atmosphere (HadGAM1.1) coupled with the HiGEM resolution ocean (HiGOM1.1). A summary of these integrations is given in table 4.1. These integrations are shorter than the coupled control integrations of both the 1.1 and 1.2 series models. Taking into account the adjustment period for the ocean component, there are 30 years of complete winter seasons available. Although this is a smaller sample size than used in chapter 3 and may not necessarily yield a fair comparison to those integrations, some useful insight may still be gained.

4.3 Coupled models: HiGEM1.1 and HadGEM1.1

Although both HiGEM1.1 and HiGEM1.2 share HadGEM1(*Johns et al.*, 2006) as a common ancestor, they are somewhat different models. Before comparing the atmosphere-only and cross-resolution integrations with HiGEM1.2 and HadGEM1.2, it is sensible to first establish the comparison between the 1.1 and 1.2 version coupled models. If the 1.1 version models perform in the same way as their 1.2 counterparts then it could be considered appropriate to make direct comparisons between 1.1 and 1.2 series integrations. It is however, more likely that there will be differences between the 1.1 and 1.2 coupled integrations. If this is the case then an understanding of the atmospheric bridge in the 1.1 versions will need to be gained. This will allow us to establish some understanding of how the individual components of the 1.2 series models may behave.

4.3.1 Simulation of El Niño SST anomalies

The accuracy of the simulation of the extra-tropical response to El Niño in a model can be assessed by examining the leading mode of SST anomaly in the Pacific and comparing to observations. EOF 1 of boreal winter Pacific SST anomaly for HiGEM1.1 and HadGEM1.1 is shown in figure 4.1. The EOFs are calculated and displayed using the same methods as for those shown in chapter 3. The tropical component of the SST anomaly pattern in HiGEM1.1 is virtually identical to that in HiGEM1.2 (figure 3.2b). The signs of the extra-tropical anomalies in HiGEM1.1 match well with those in observations, however very few of the correlations are statistically significant. Therefore, it cannot be said with any real certainty that these warming and cooling patterns are genuine. This suggests that there is a weaker coupling from the tropics to the extra-tropics in HiGEM1.1 than in HiGEM1.2 or indeed the observations. HiGEM1.1 does perform well in the region around south-east Asia and Japan, a region which is simulated poorly in the other integrations discussed so far.

HadGEM1.1 shows warming centred on the equator like HadGEM1.2. There is also a secondary area of significant warming to the north of this extending to 20°N and spanning most of the Pacific basin. This is very unlike the observed SST anomaly pattern (figure 3.2a). The extra-tropics appear to be simulated more realistically than in HadGEM1.2, with significant warming along the North American coast and cooling in the

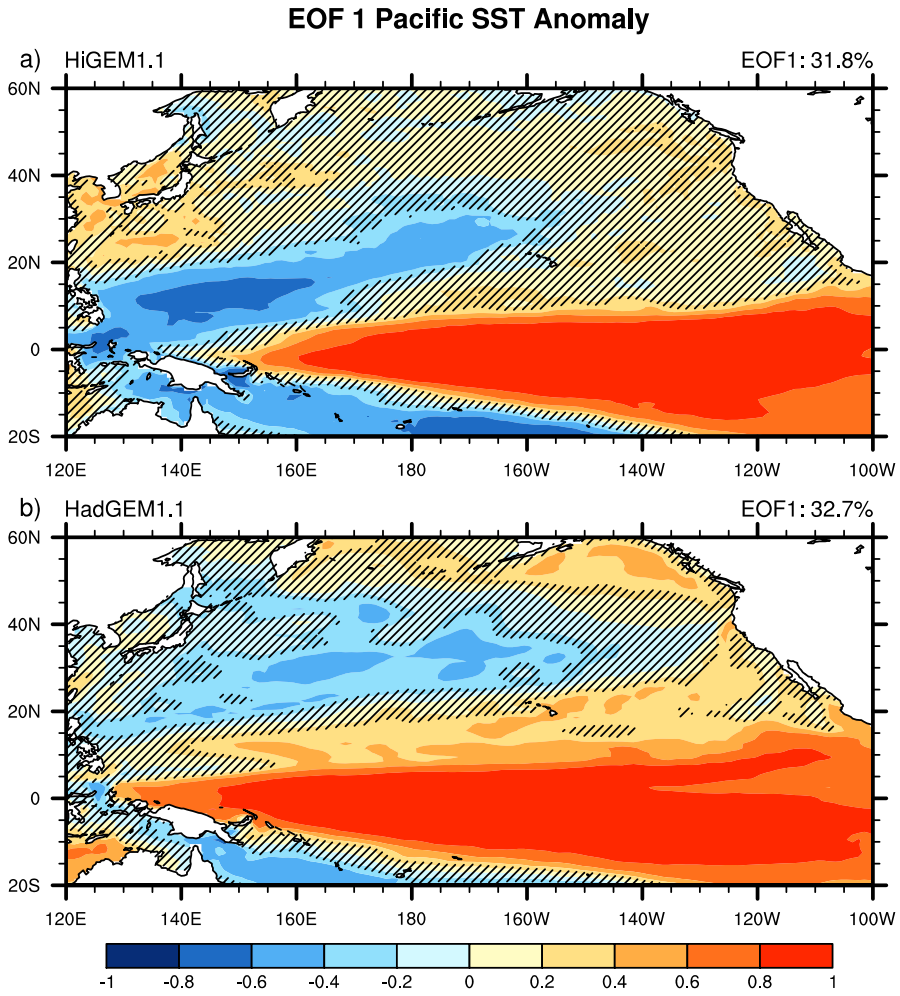

Figure 4.1: EOF 1 of northern winter (NDJFM) Pacific SST anomaly normalised by correlation. Correlations not significant at the 5% level are hatched. The contour interval is 0.2. a) HiGEM1.1, and b) HadGEM1.1.

central Pacific. The western North Pacific is simulated poorly, with no significant correlations in the region around south-east Asia and Japan. This is much like HadGEM1.2.

It is clear that there are differences in behaviour between the 1.1 and 1.2 model versions. By completing the analysis seen in chapter 3 for HiGEM1.1 and HadGEM1.1, we can gain a better understanding of how the atmospheric bridge teleconnection is working in the 1.1 versions, and how it relates to the atmospheric bridge teleconnection in the 1.2 versions.

4.3.2 Upper tropospheric circulation

Figure 4.2 shows regression maps of 200 hPa stream function anomaly for HiGEM1.1 and HadGEM1.1. Over the Pacific, the stream function response is weaker in HiGEM1.1 than HiGEM1.2 (the stream function contours are more widely spaced). This could explain the weaker extra-tropical SST response, since weaker associated surface circulation anomalies will have less influence on the surface heat fluxes that control the extra-tropical SST response. The cyclonic stream function anomaly over the North Pacific is further west than in HiGEM1.2 or observations. The cyclonic anomaly over North America is also shifted westward in comparison to HiGEM1.2.

The cyclonic stream function anomaly over the North Pacific in HadGEM1.1 is also shifted westward, and is weaker, in comparison with that in HadGEM1.2. This anomaly is centred approximately 30° further west than in the observed field. The stream function contours over North America are widely spaced, which is very unlike HadGEM1.2 (also HiGEM and observations). The noted weakening of this circulation centre is certainly incorrect, however it seems to have reduced the errors in North Pacific SST anomaly (figure 4.1b) relative to HadGEM1.2.

4.3.3 Atmospheric background state

Figure 4.3 shows the zonal stationary Rossby wavenumber for boreal winter 200 hPa zonal wind in the Pacific domain for HiGEM1.1 and HadGEM1.1. The stationary wavenumber is calculated using the method described in section 3.5, and plotted using the same conventions as in figure 3.18. HiGEM1.1 shows a waveguide structure much like that of HiGEM1.2. The two main waveguides in the Pacific region merge together more closely in HiGEM1.1 than in HiGEM1.2, with the contour $K_s = 5$ being shared between the two waveguides.

In HadGEM1.1, the two main waveguides in the Pacific region are separate, well defined structures. The waveguide coming out of the Asian jet is longer and is oriented more to the north than its observational equivalent (figure 3.18a) and is longer than the same waveguide in HiGEM1.1. The region of reversed absolute vorticity gradient between the two waveguides is larger than in HadGEM1.2. These findings suggest that, like HadGEM1.2, preferred Rossby wave propagation paths due to an incorrect atmospheric

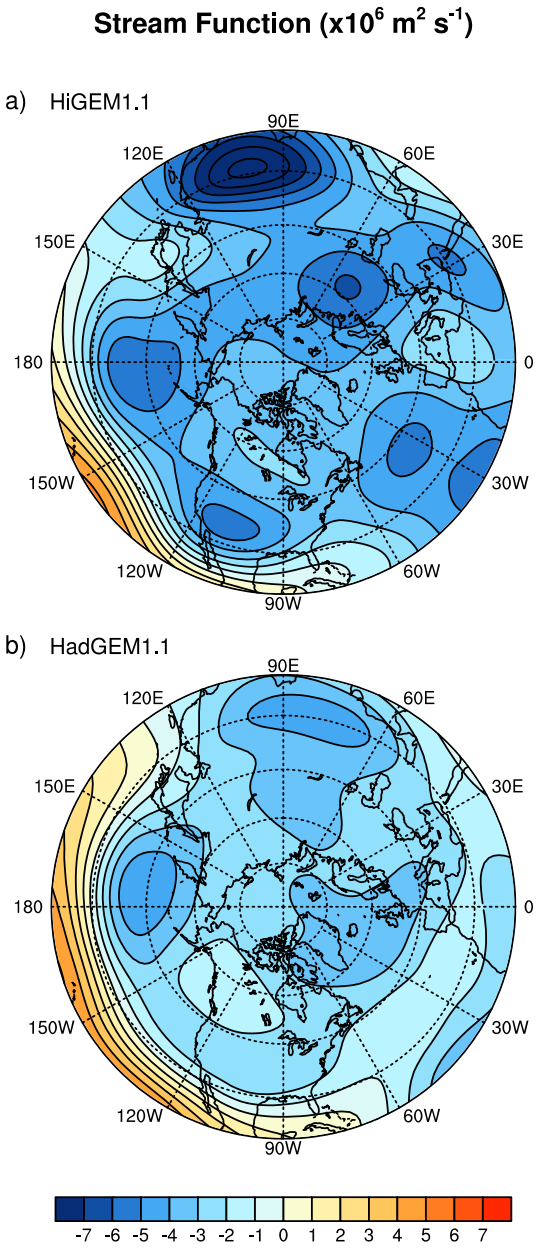

Figure 4.2: Northern winter (NDJFM) 200 hPa stream function (10^6 m^2 s^{-1}) anomaly patterns associated with a 1 °C departure of the EP index. The contour interval is 10^6 m^2 s^{-1}. a) HiGEM1.1, and b) HadGEM1.1.

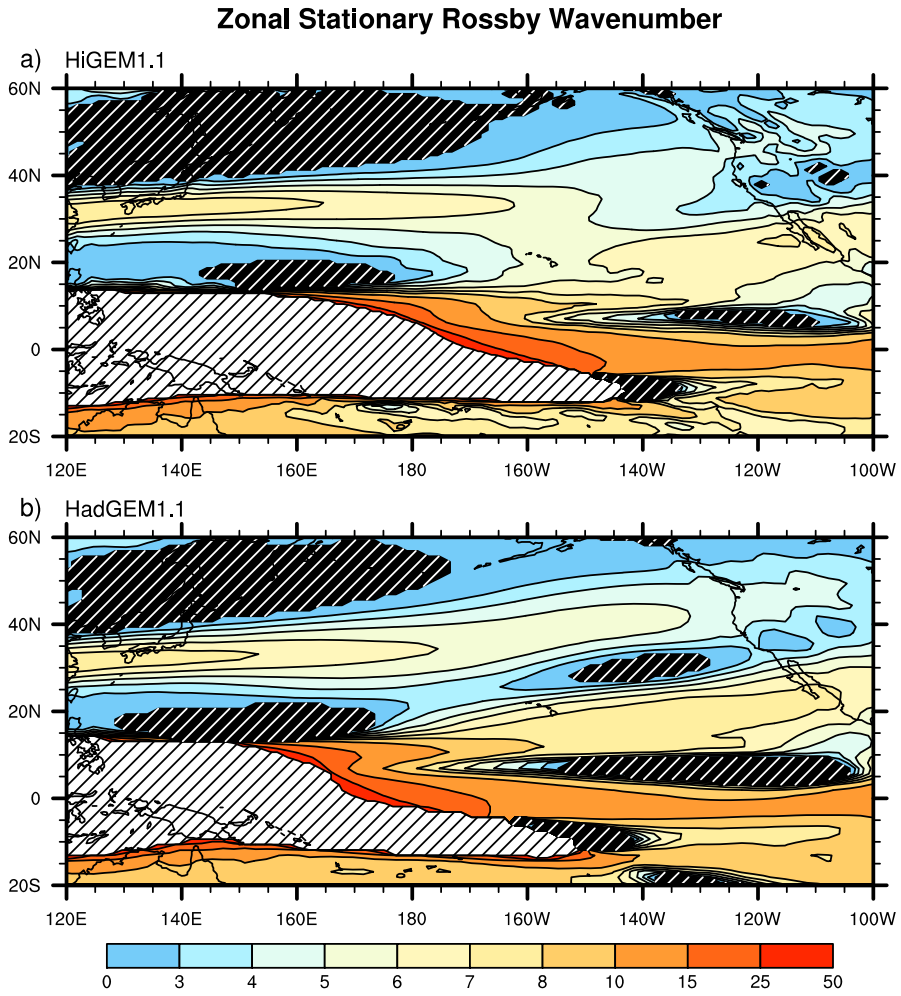

Figure 4.3: Zonal stationary wavenumber for northern winter (NDJFM) time-mean zonal wind at 200 hPa. Light (dark) hatching indicates areas where $\bar{u}$ (β_M) is negative. a) HiGEM1.1, and b) HadGEM1.1.

background state are partly responsible for HadGEM1.1's incorrect upper tropospheric response seen in figure 4.2b.

4.3.4 Rossby Wave Source

Regression maps of 200 hPa Rossby wave source (RWS) anomaly for HiGEM1.1 and HadGEM1.1 are shown in figure 4.4. The contour of stationary wavenumber 4 is overlaid and areas of reversed absolute vorticity gradient are hatched as in figure 3.25. In general the pattern of RWS anomalies associated with El Niño in HiGEM1.1 is very similar to that in HiGEM1.2, with the majority of RWS anomaly occurring within the $K_S = 4$ waveguide. The positive anomaly over the western North Pacific is positioned slightly to the west of

its position in HiGEM1.2. There is a negative anomaly at 165°W, a positive anomaly to the south and east of this, and a negative anomaly at 100°W. The latter negative anomaly is much stronger than in observations, as is also the case in HiGEM1.2.

The RWS anomaly associated with El Niño in HadGEM1.1 is somewhat different from that in HadGEM1.2. The positive RWS anomaly over East Asia and the North-West Pacific is more broken than in HadGEM1.2. The RWS anomaly in HadGEM1.1 at 170°E is weaker than that in HadGEM1.2. HadGEM1.1 also shows strong RWS anomalies immediately to the west of the region of reversed absolute vorticity gradient at 170°W, where HadGEM1.2 has relatively weak RWS anomaly. HadGEM1.1 also has a negative RWS anomaly at 100°W that is much stronger than in observations, although not as strong as in HiGEM1.1. Patterns of RWS anomaly are similar between HiGEM1.1 and HiGEM1.2, but are quite different between HadGEM1.1 and HadGEM1.2. This could be due to differences in the tropical component of El Niño or in the mean ocean state. RWS anomaly patterns in HadGEM1.2 have some features in common with observed patterns however, they are largely different in the Pacific region. RWS anomaly patterns in HadGEM1.1 appear to deviate further from the baseline of observations.

4.3.5 Summary

The leading mode of SST anomaly variation in HiGEM1.1 compares well to that in HiGEM1.2 in the tropics. However coupling to the extra-tropics is generally much weaker than in HiGEM1.2. The exception to this is the western North Pacific, HiGEM1.1 is the only model to capture the warming observed there. HadGEM1.1 appears to be doing a better job of simulating the extra-tropical response to El Niño than HadGEM1.2. However, there are still significant discrepancies between HadGEM1.1 and the observations.

There are several differences in the upper tropospheric stage of the atmospheric bridge between HiGEM1.1 and HiGEM1.2. Of particular relevance is the weakened anomalous cyclonic circulation over the North Pacific. This seems to be affecting the strength of the SST response in the North Pacific. It should be noted that the sense of circulation appears to be correct, and therefore that the warm SST anomalies in the north-east Pacific that are not statistically significant in figure 4.1a are likely to be physically meaningful.

The atmospheric response in HadGEM1.1 is unrealistic compared to observations.

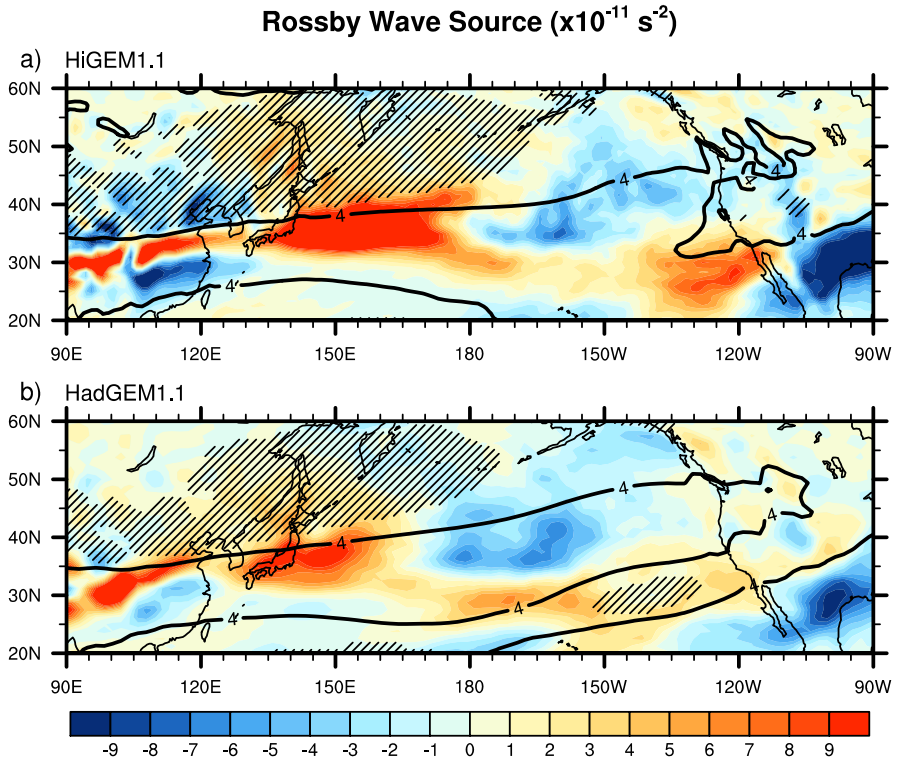

Figure 4.4: Rossby wave source anomaly patterns (colors, 10^{-11} s^{-2}) associated with a 1 °C departure of the EP index. The contour interval is 10^{-11} s^{-2}. Stationary wavenumber $K_s = 4$ is shown by a thick contour. Hatching indicates regions with reversed absolute vorticity gradient as in figure 4.3. a) HiGEM1.1, and b) HadGEM1.1.

The anomalous circulation over North America is very weak compared to observations, and is weaker than the response in HadGEM1.2. It seems likely that the error in extra-tropical SST response caused by the severely weakened anomalous centre of circulation over North America, is less than the error caused by having this anomalous circulation with a slightly different location. Based purely on figure 4.1b it is tempting to conclude that the HadGEM1.1 SST response is superior to that in HadGEM1.2. However, this response is due to forcing from an unrealistic atmospheric anomaly pattern, and it is therefore an unrealistic SST response.

HiGEM1.1 has a North Pacific waveguide structure that is much like that of HiGEM1.2 and the observations. This implies that the atmospheric background state is similar in HiGEM1.1 and HiGEM1.2. Atmospheric background state is critical for the propagation of Rossby wave anomalies, which explains why the upper tropospheric anomaly

patterns in HiGEM1.1 are so similar to those in HiGEM1.2. HadGEM1.1 also has a Pacific waveguide structure much like that of its 1.2 counterpart HadGEM1.2. Two distinct waveguides are present in the Pacific domain, separated by an area of reversed absolute vorticity gradient through which Rossby waves will not propagate. The result of this is a poor representation of upper tropospheric anomalies in response to El Niño. These incorrect anomalies then influence surface circulation, and hence surface heat fluxes, in an incorrect manner that produces the extra-tropical SST response seen in figure 4.1b.

RWS anomalies in HiGEM1.1 are similar to those in HiGEM1.2. The positive RWS anomaly over the North-West Pacific in HiGEM1.1 is situated slightly west of its location in HiGEM1.2. This could go some way to explaining the westward shift relative to HiGEM1.2 of the cyclonic stream function anomalies over the North Pacific and North America in HiGEM1.1 (figure 4.2a). RWS anomalies in HadGEM1.1 are actually quite different to those in HadGEM1.2. The presence of strong anomalies in locations in HadGEM1.1 where there are only small anomalies in HadGEM1.2 contributes to the incorrect upper tropospheric anomalies seen in figure 4.2b.

In general, the extra-tropical response to El Niño in HiGEM1.1 is very similar to that in HiGEM1.2. The magnitude of the response is weaker however, the physics producing the extra-tropical SST response are consistent with the extra-tropical anomalies in figure 4.1a, even though they are not statistically significant. Anomalies in the HiGEM1.1 upper troposphere show the same patterns as in HiGEM1.2, although in general they are shifted to the west slightly. This should be borne in mind when comparing atmosphere-only and cross-resolution integrations to the results of chapter 3.

The comparison between HadGEM1.1 and HadGEM1.2 is less simple. There are many differences in the behaviour of the atmospheric bridge mechanism. Given this, it is probably not safe to make direct comparisons between 1.1 integrations and HadGEM1.2. Instead the results of atmosphere-only and cross-resolution integrations should be directly compared to the HadGEM1.1 integration results shown in this section. It is then possible to understand the effect of resolution in each part of the coupled 1.1 version models, and make the tentative assumption that this holds for 1.2 versions also.

4.4 Atmospheric components: HiGAM1.1 and HadGAM1.1

The aim of repeating the analysis in chapter 3 for atmosphere-only integrations is to determine whether or not it is purely the resolution of the atmosphere that prevents the extra-tropical response to El Niño from occurring correctly in HadGEM1.1. If the resolution of the atmosphere is simply too low to resolve the atmospheric bridge mechanism in the coupled model then this should also be the case when the atmosphere model is uncoupled and forced with observed SST. However, if the ability of the low resolution coupled model to reproduce the atmospheric bridge is not purely an issue of atmospheric resolution, then the low and high resolution atmosphere-only models may behave more like each other. Since these are not coupled simulations, it is not possible to diagnose the entire feedback system which generates the observed extra-tropical SST anomalies in the North Pacific. However, the upper tropospheric component of the atmospheric bridge mechanism can be scrutinised, allowing some inferences as to the possible behaviour of the whole feedback system to be made.

4.4.1 Upper tropospheric circulation

Regression maps of 200 hPa stream function anomaly for HiGAM1.1, and HadGAM1.1 are shown in figure 4.5. The index for the regression is the same area average of the AMIP II boundary condition SST used throughout chapter 3. A general observation is that the anomalies in HiGAM1.1 and HadGAM1.1 have magnitudes (gradients of stream function) of the order of one and a half times those in observations. This could be due to the sample size (approximately 20 winters) being much smaller than the 50 winter sample size used throughout chapter 3. However, a shorter 20 year sample of observations (shown later in chapter 5; figure 5.8) does not show a notable increase in the strength of the upper tropospheric response, suggesting sampling cannot explain the stronger than observed response in the atmosphere only integrations presented here. It is possible then, that the atmospheric component systematically tends to favour a stronger response to the anomalous forcing of El Niño than the real atmosphere.

The anomaly patterns seen in HiGAM1.1 (figure 4.5a) generally match those in the observed atmosphere (figure 3.7a) very closely. There is circulation centred over north-eastern Europe in HiGEM1.1 that is not so well defined in the observations. However,

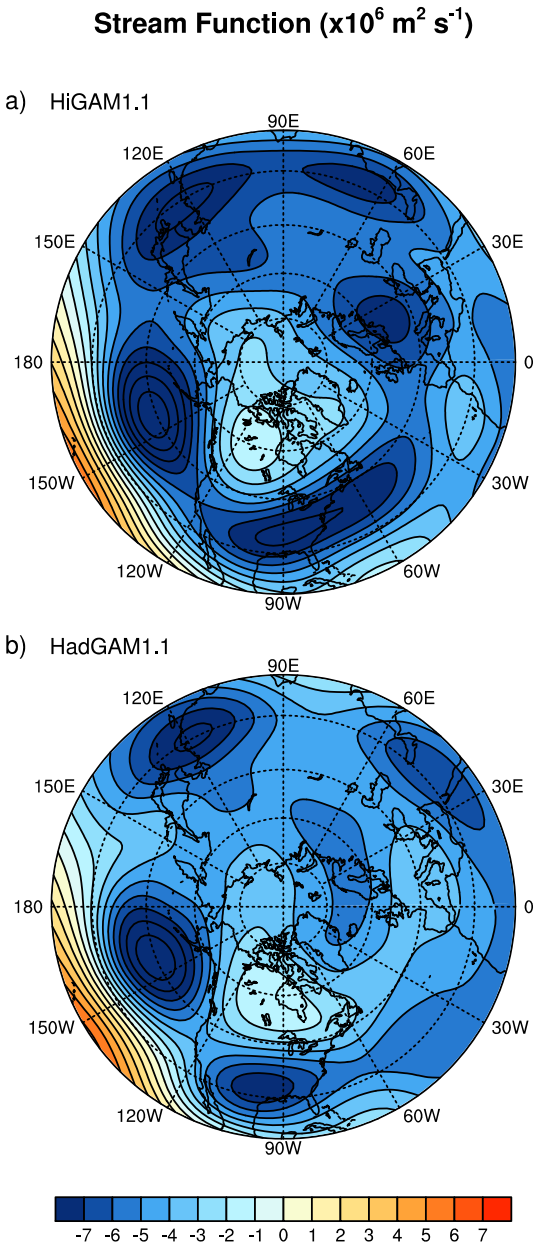

Figure 4.5: Northern winter (NDJFM) 200 hPa stream function (10^6 m^2 s^{-1}) anomaly patterns associated with a 1 °C departure of the EP index. The contour interval is 10^6 m^2 s^{-1}. a) HiGAM1.1, and b) HadGAM1.1.

the stream function anomalies fit in generally with the latitudinal position of the observed wave train, and match very closely to anomalies seen in HiGEM1.2 (figure 3.7b). The anomaly patterns in HadGAM1.1 are also similar to observations. The deepened Aleutian low and the part of the wave train over North America have the same position and orientation as the observed anomalies. The portion of the wave train in the Atlantic sector is somewhat different than observations, having a more southerly extent. However this is very similar to the response in HiGEM1.2 (figure 3.7b). The atmospheric responses in the high resolution HiGAM1.1 and the low resolution HadGAM1.1 are similar. This is different from the coupled models where the response is improved in the high resolution configurations compared to the lower resolution configurations. HadGAM1.1 shows a clear improvement over HadGEM1.1 and HadGEM1.2.

This result shows that the low resolution atmosphere-only model is not suffering from the same issues as HadGEM1.1/1.2. Given the findings in chapter 3, it might be reasonable to expect that the RWS and Rossby wave propagation paths in HadGAM1.1 will be more similar to observations than those in HadGEM1.1/1.2.

4.4.2 Atmospheric background state

Zonal stationary Rossby wavenumber is calculated from the NDJFM mean 200 hPa zonal wind for each of the atmosphere-only integrations. Maps of K_s for these integrations are shown in Figure 4.6. As with stream function, both the high and low resolution models compare well to each other, and also to the observed K_s map (figure 3.18a). Of particular relevance is the mid-Pacific wave guide structure noted in section 3.5. HadGAM1.1 does not exhibit the split wave guide seen in HadGEM1.1/1.2, rather it has a structure much like that seen in the observed K_s. The region of reversed absolute vorticity gradient seen in the central East Pacific in HadGEM1.1/1.2 is also absent in HadGAM1.1. As speculated in section 4.4.1, the preferred Rossby wave propagation paths in HadGAM1.1 are similar to those in observations, and crucially they are extremely similar to those in HiGAM1.1. This suggests that the atmosphere components of the models have similar performance in terms of the atmospheric bridge, when uncoupled and forced with known SST fields. Possible reasons for this will be discussed after diagnosing the Rossby wave source.

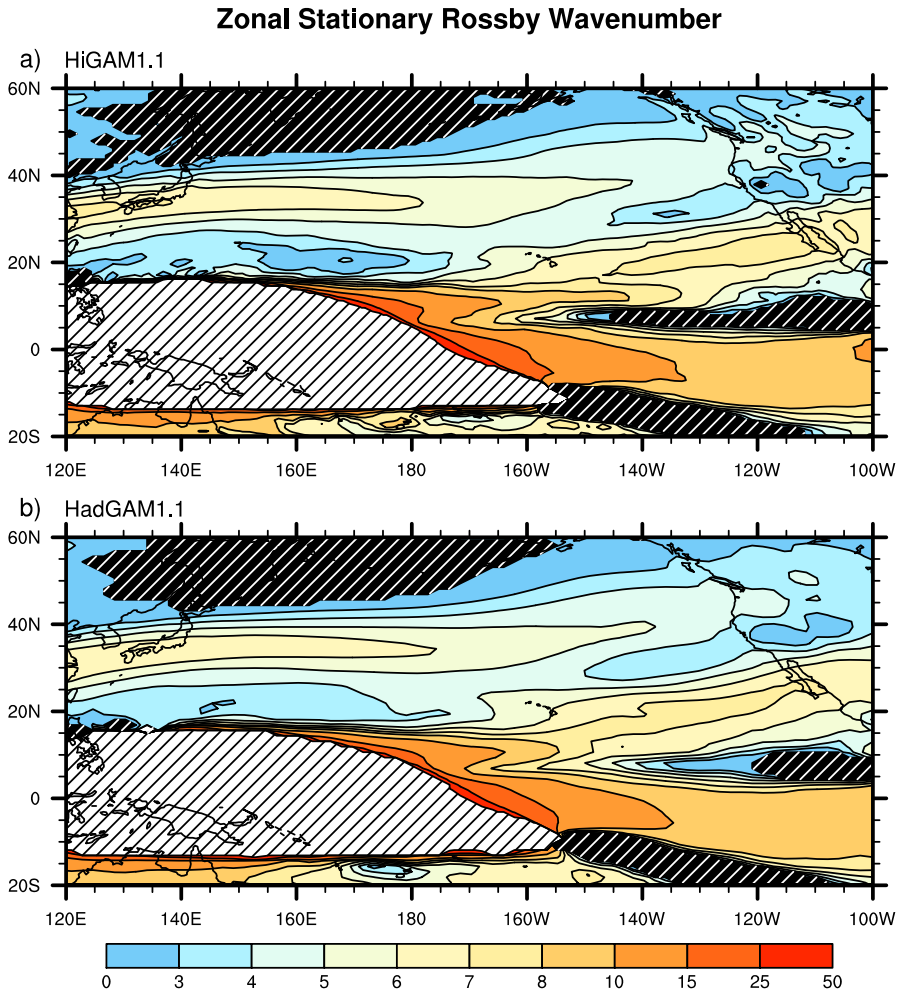

Figure 4.6: Zonal stationary wavenumber for northern winter (NDJFM) time-mean zonal wind at 200 hPa. Light (dark) hatching indicates areas where $\bar{u}$ (β_M) is negative. a) HiGAM1.1, and b) HadGAM1.1.

4.4.3 Rossby wave source

The RWS is a forcing term. It depends partly on convective forcing at the surface in the tropics, which leads to divergence at the tropopause. Since both high and low resolution atmosphere models are forced with the same observed SST boundary conditions, we might expect that the RWS will be at least very similar between the two.

Regression maps of RWS anomaly at 200 hPa for HiGAM1.1 and HadGAM1.1 are shown in figure 4.7. As for figure 3.25, the contour of stationary Rossby wavenumber 4 is overlaid and regions of reversed absolute vorticity gradient are hatched. It is clear that the RWS anomaly patterns in HiGAM1.1 and HadGAM1.1 are very similar. Both have positive RWS anomalies, centred at 170°E, with a similar shape. To the east of this,

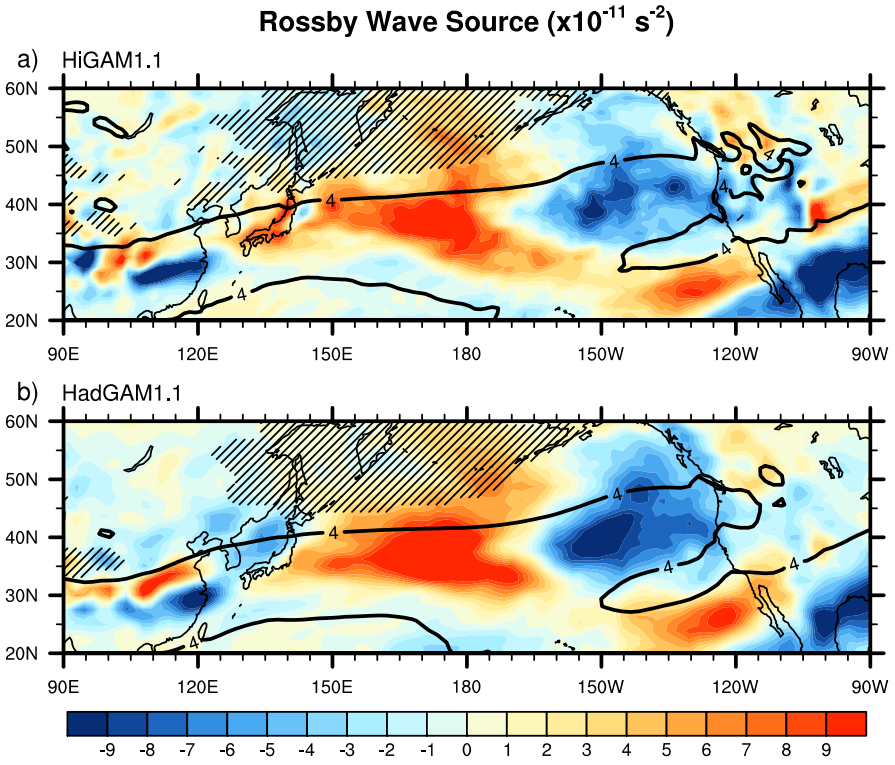

Figure 4.7: Rossby wave source anomaly patterns (colours, 10^{-11} s^{-2}) associated with a 1 °C departure of the EP index. The contour interval is 10^{-11} s^{-2}. Stationary wavenumber $K_s = 4$ is shown by a thick contour. Hatching indicates regions with reversed absolute vorticity gradient as in figure 4.6. a) HiGAM1.1, and b) HadGAM1.1.

inside the $K_s = 4$ waveguide, there is a large negative RWS anomaly centred at 140°W. The positive RWS anomaly at 125°W is a similar shape and size in both HiGAM1.1 and HadGAM1.1 and both have the stronger than observed negative RWS anomaly at 100°W. Although there are some differences, such as a sign difference over the Sea of Japan, these are on smaller scales than the similarities. The combination of similar waveguides and almost identical RWS anomalies go a long way in explaining why the upper tropospheric circulation is very similar between HiGAM1.1 and HadGAM1.1.

The strength of the RWS anomalies in both HiGAM1.1 and HadGAM1.1 are greater than those in observations (figure 3.25) over both the western and eastern Pacific. This suggests that the response to realistic El Niño SST forcing in the atmospheric components in terms of the atmospheric Rossby wave generation is stronger than observed, perhaps due to a systematic error in the atmospheric model. This is likely to be a primary factor in explaining why the upper tropospheric response to El Niño in the atmospheric components

(figure 4.5) is stronger than observed.

4.4.4 Summary

When forced with the same observed SST fields, both the high and the low resolution atmosphere models perform very well. Both models do a good job of simulating upper tropospheric circulation anomalies. The preferred Rossby wave propagation paths are shown to be very similar (in the Pacific region) between each of the models. These paths depend entirely on the mean state of the atmosphere, hence more realistic Rossby wave propagation paths in HadGAM1.1 suggest that the background state is improved over that in HadGEM1.2. It seems likely that by prescribing the SSTs, the atmosphere model is encouraged to behave more like the observed atmosphere in terms of mean state.

The same is also true for RWS. Prescribing the surface SST forcing to be the same in each model has effectively forced the RWS to be similar between HiGAM1.1 and HadGAM1.1. However, we note that the RWS anomalies in these atmosphere-only integrations are stronger than in observations. This is a likely cause of the overly strong upper tropospheric response. Other factors may have a role to play in the overly strong response in both HiGAM1.1 and HadGAM1.1. For example, if the modelled storm tracks are different from observations, this may lead to unrealistic eddy feedbacks on to the mean state, which itself could show up in the RWS diagnostic. It is also possible that baroclinic eddies could alter the extra-tropical response through direct interaction with Rossby waves (*Franzke et al.*, 2000), although this is perhaps a secondary consideration given the relative strength of the RWS anomalies.

It has been shown that the low resolution atmosphere HadGAM1.1, when run uncoupled, is capable of reproducing the observed extra-tropical response to El Niño. However, some care must be taken in interpreting this result. Integrating the atmosphere uncoupled, forced with observed SSTs, not only eliminates the ocean model but also the feedback between the atmosphere and ocean. This implies that only first order atmospheric teleconnection process from the tropics to the extra-tropics will be present in the atmosphere-only configuration, and the influence of secondary processes such as feedbacks from extra-tropical SST anomalies onto the atmosphere will be neglected. As noted in the conclusion

to chapter 3, the influence of such second order processes is likely to be small when compared to the influence of the atmospheric bridge teleconnection mechanism. Here we have established that in the context of the extra-tropical response to El Niño, atmospheric resolution is unlikely to be a performance altering factor.

4.5 Cross-resolution configurations: LoHi and HiLo

It has been established that there is no technical limitation that prevents the low resolution atmosphere HadGAM1.1 from reproducing the observed extra-tropical response to El Niño. This result suggests that in order to accurately reproduce the extra-tropical response to El Niño in a coupled model, the higher resolution atmospheric component is not necessary. Of course there could be some missing process in HadGAM1.1 that stops it from producing the extra-tropical SST anomalies. The cross-resolution integrations should help with understanding this problem, as the atmosphere and ocean resolutions are varied independently.

4.5.1 Simulation of El Niño SST anomalies

EOF 1 of NDJFM Pacific SST anomaly for LoHi and HiLo configurations are shown in figure 4.8. The EOFs are calculated and presented using the same methods as for those in chapter 3. The tropical component of each shows warming centred on the equator. However, in both cases (although it is more noticeable in HiLo) the warming south of the Equator in the eastern tropical Pacific is weaker than in any of the previously discussed coupled integrations. In fact the tropical warming is more tightly constrained to the equator than has been seen in other integrations. Both the LoHi and HiLo configurations show a significant warming in the central North Pacific, contrary to observations.

It is not immediately clear which of the cross-resolution configurations is performing better in terms of the extra-tropical SST response to El Niño. Both configurations appear to have problems. However, the HiLo configuration has an area of significant cold SST anomaly in the eastern Pacific that is the opposite sign to observations. Such a strong and unrealistic anomaly suggests that the HiLo configuration is not simulating the teleconnection mechanism as well as the LoHi configuration. Examining the atmospheric teleconnection in detail should give some more insight into the processes causing these

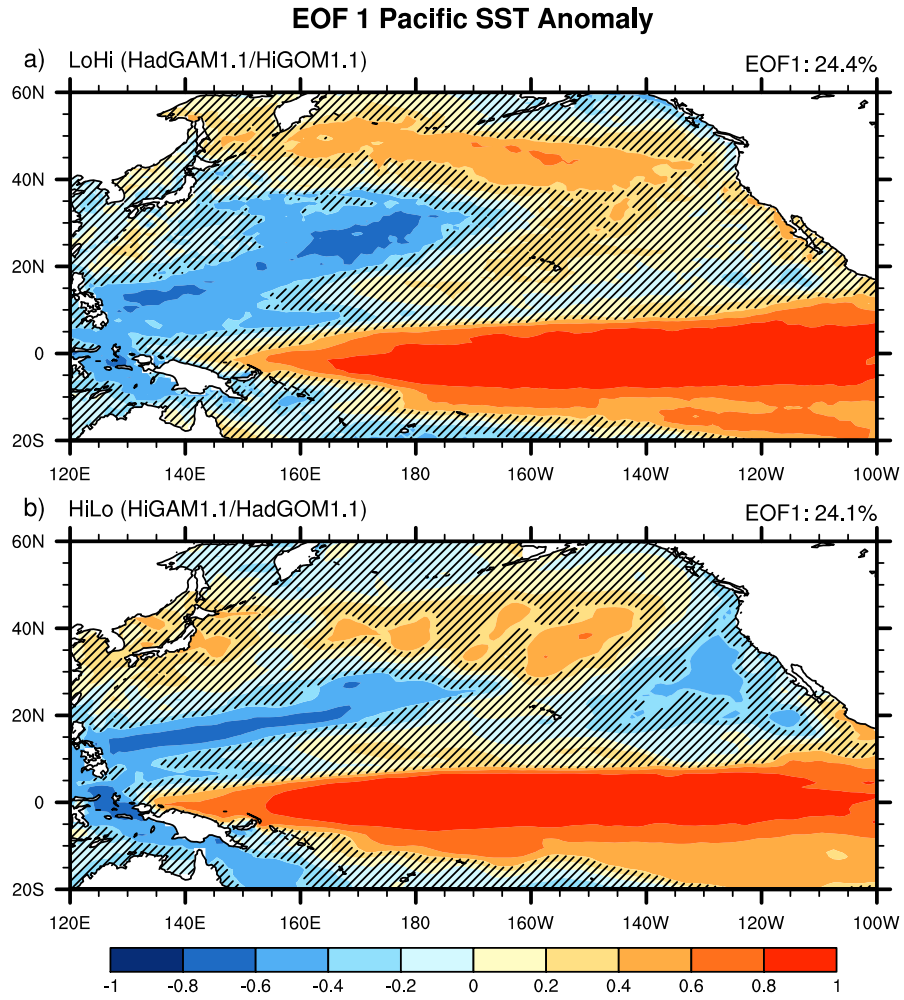

Figure 4.8: EOF 1 of northern winter (NDJFM) Pacific SST anomaly normalised by correlation. Correlations not significant at the 5% level are hatched. The contour interval is 0.2. a) LoHi, and b) HiLo.

extra-tropical SST responses.

4.5.2 Upper tropospheric circulation

Figure 4.9 shows regression maps of NDJFM 200 hPa stream function anomalies for the LoHi and HiLo configurations. The LoHi configuration (figure 4.9a) has some features similar to those in observations. Although the cyclonic stream function anomaly in the central North Pacific is too far west, it is in a location similar to the circulation anomaly over the central North Pacific in HiGEM1.1 (figure 4.2a). The same is also true of the cyclonic anomaly over North America. The anomaly patterns in the HiLo configuration (figure 4.9b) are very different to observations (figure 3.7a), particularly in the North

Pacific region. There is a cyclonic stream function anomaly positioned at 55°N, east of the Kamchatka Peninsula, an anticyclonic stream function anomaly over the north east Pacific. The presence of an anticyclonic stream function anomaly in the region is also seen in HadGEM1.2.

The LoHi configuration produces a wave train that is quite similar to that in HiGEM1.1. The performance of the HiLo configuration is much worse in this respect, with erroneous upper tropospheric circulation anomalies much like those in HadGEM1.1/1.2. Because the tropospheric circulation response in the HiLo configuration is less realistic than in the LoHi configuration, we might expect the Rossby waveguides in LoHi to be like those in HiGEM1.1 and the observations, and the HiLo waveguides to be more like those seen in HadGEM1.1/1.2.

4.5.3 Atmospheric background state

The stationary wavenumber patterns in the LoHi configuration (figure 4.10a) are similar to those in HiGEM1.1/1.2 and observations (figures 4.1, 3.18b, and 3.18a respectively). The waveguides associated with the Asian and North American jets are a similar strength to those in the observations and HiGEM1.1/1.2 and merge over the central North Pacific, allowing Rossby waves to cross between them. This merging is the most dynamically significant feature of the observed basic state and is replicated well in the LoHi configuration.

The waveguides in the HiLo configuration (figure 4.10b) look more like those in HadGEM1.1/1.2 (figure 3.18c/4.3b). There is no area of reversed vorticity gradient separating the Asian and North American jet waveguides in the east Pacific region, but it is still a region of low wavenumber. This means that Rossby waves are likely to be refracted away from this region and that the dynamics in this region in the HiLo configuration are similar to those in HadGEM1.1/1.2.

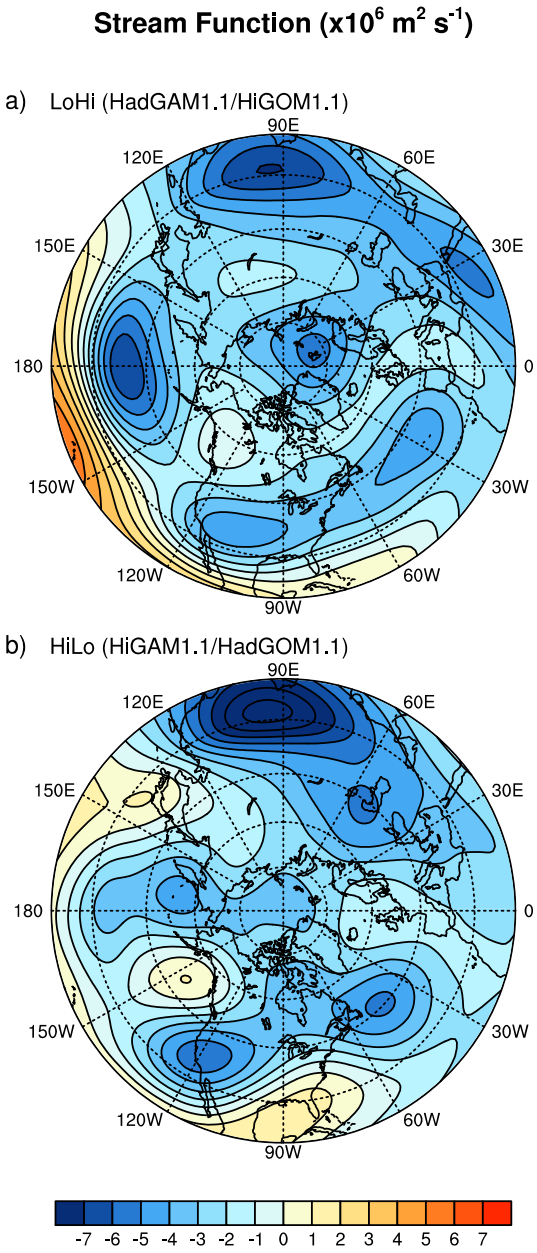

Figure 4.9: Northern winter (NDJFM) 200 hPa stream function (10^6 m^2 s^{-1}) anomaly patterns associated with a 1 °C departure of the EP index. The contour interval is 10^6 m^2 s^{-1}. a) LoHi, and b) HiLo.

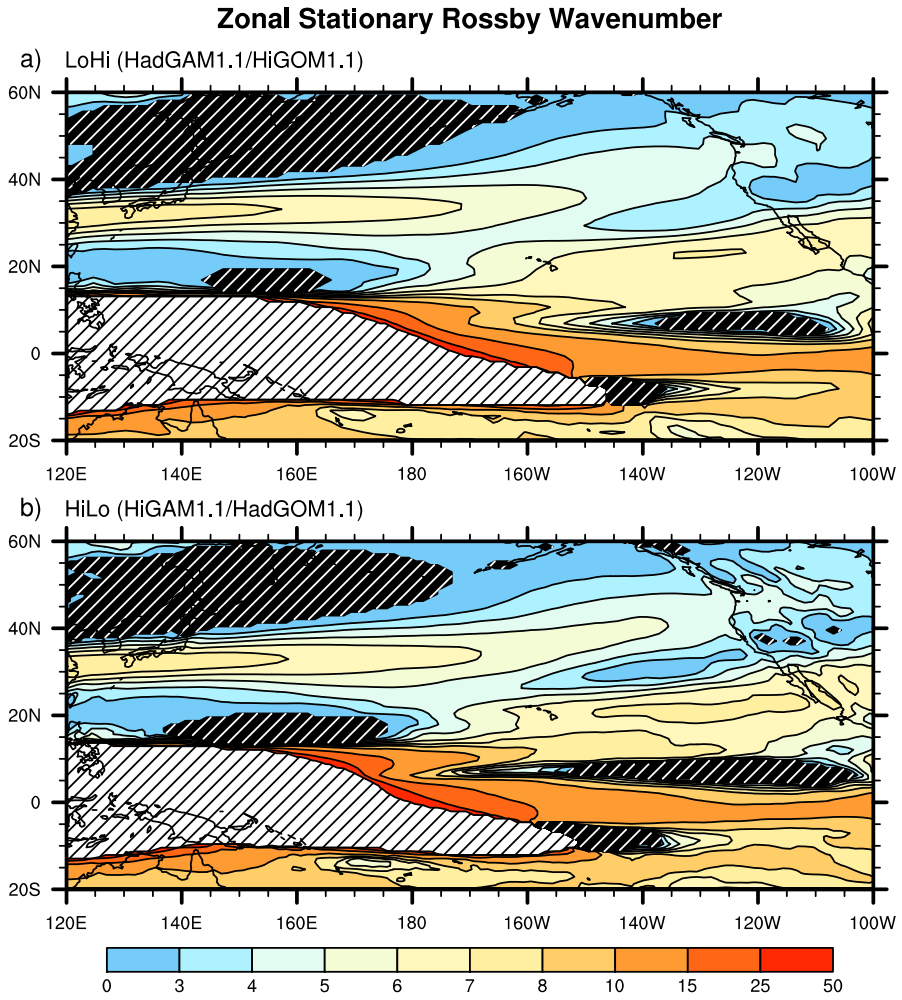

Figure 4.10: Zonal stationary wavenumber for northern winter (NDJFM) time-mean zonal wind at 200 hPa. Light (dark) Hatching indicates areas where $\bar{u}$ (β_M) is negative. a) LoHi, and b) HiLo.

4.5.4 Rossby wave source

Rossby wave source anomaly patterns in the LoHi configuration are much like those in HiGEM1.1 over the North-West Pacific (figure 4.11). Like HiGEM1.1, the LoHi configuration shows positive RWS anomaly further west over Japan than observations or HiGEM1.2. This seems likely to influence the westward shift observed in stream function anomalies (figure 4.9a). The positive anomaly in the East Pacific in the LoHi configuration is situated north-east of its position in HiGEM1.1, meaning it is outside of the $K_s = 4$ waveguide in the LoHi configuration. This is also likely to have some effect of the stream function response and perhaps the cool SST anomaly seen along the North American coast (figure 4.8a). Like HiGEM1.2, there is a negative RWS anomaly situated between these

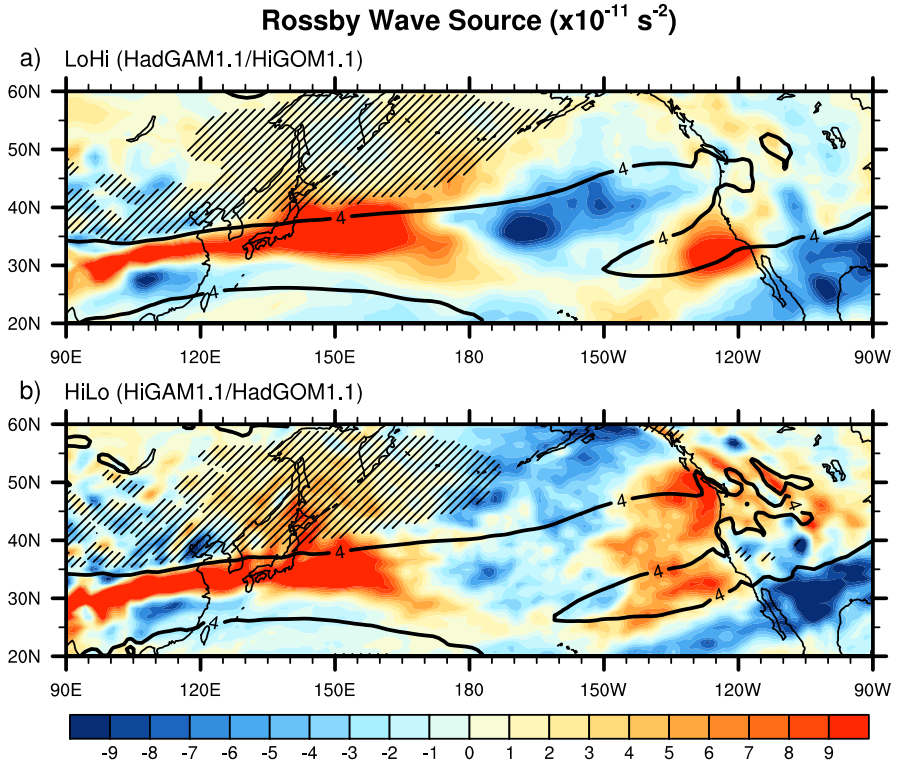

Figure 4.11: Rossby wave source anomaly patterns (colors, 10^{-11} s^{-2}) associated with a 1 °C departure of the EP index. The contour interval is 10^{-11} s^{-2}. Stationary wavenumber $K_s = 4$ is shown by a thick contour. Hatching indicates regions with reversed absolute vorticity gradient as in figure 4.10. a) LoHi, and b) HiLo.

positive anomalies at 165°W, although this anomaly is stronger in the LoHi configuration than in HiGEM1.2.

The HiLo configuration has RWS anomaly patterns more in common with HadGEM1.1 over the Pacific region. Over the eastern north Pacific the HiLo configuration shows a large positive Rossby wave source anomaly. Both the LoHi and HiLo configurations have a stronger than observed negative RWS anomaly at 100°W. It is worth noting at this point that this anomaly is stronger than observed for all the coupled model experiments considered in both chapters 3 and 4. Since this is also noted in the atmosphere-only experiments, it seems likely that this is the result of a systematic error in the atmosphere model.

4.5.5 Summary

The extra-tropical SST anomaly pattern in the HiLo configuration resembles that of HadGEM1.2 quite closely in the east extra-tropical North Pacific. The LoHi configuration

could be considered to be re-producing the extra-tropical response better than the HiLo configuration because of the more robust cold SST anomaly in the western extra-tropical North Pacific and the lack of the erroneous cold SST anomaly in the eastern Pacific. The LoHi does a better simulation of the tropics than HiLo. The tropical warm anomaly, although narrow compared to observations, is less constrained to the equator in the LoHi experiment. The tropical component is important since it provides the forcing for the atmospheric bridge teleconnection to the extra-tropical north Pacific.

Figure 4.9 shows that the upper tropospheric response is quite poor in the HiLo configuration. Although the response of the LoHi configuration is different to observations, it is much like the response in HiGEM1.1, and is much closer to the observed response than the HiLo configuration. The upper tropospheric response of the LoHi configuration is fairly similar to the response in HiGEM1.1 in terms of the positioning of anomalies. This is particularly evident in the North Pacific region.

Rossby waveguides, and hence atmospheric background state, are somewhat improved in the HiLo configuration relative to HadGEM1.1/1.2. However, the waveguides over the Pacific remain more distinct than those in the observations, being separated by areas of low stationary wavenumber. This shows that the atmospheric basic state of the HiLo configurations is more akin to that in HadGEM1.1/1.2 than the observed atmosphere. Waveguides in the LoHi configuration are more like those in HiGEM1.1/1.2 and the observed atmosphere. This shows that the dynamics of Rossby wave propagation in the LoHi configuration are more realistic than the HiLo configuration, even though this may not be immediately obvious from the extra-tropical SST response.

Rossby wave source anomalies in the LoHi configuration are similar to those in HiGEM1.1, lending support to the idea that the LoHi configuration is behaving much like HiGEM1.1. RWS anomalies in the HiLo configurations are quite like those in HadGEM1.1 in the western North Pacific. In the eastern North Pacific there is a large anomaly, much larger than in any other integration or the observations. This large deviation from what is observed is likely to be a source of error in the extra-tropical SST response in the HiLo configuration.

4.6 Discussion

The effect of horizontal resolution on the extra-tropical response to El Niño is examined by diagnosing the atmospheric bridge mechanism in atmosphere-only and cross-resolution configurations of models in the 1.1 series of HiGEM/HadGEM. Preliminary analysis of HiGEM1.1 and HadGEM1.1 showed that there are some differences between the 1.1 and 1.2 version models, such as weaker coupling from the tropics to the extra-tropics, that must be considered when interpreting the results of atmosphere-only and cross-resolution integrations. However, the main results from chapter 3 are found to be the same with HiGEM1.1 and HadGEM1.1. The extra-tropical response to El Niño in HiGEM1.1 is like that in HiGEM1.2, while the atmospheric basic state in HadGEM1.1 is erroneous, as it is in HadGEM1.2, causing a poor representation of the mechanism.

The atmospheric components of the models, when run independently (uncoupled) from the ocean model, produce extra-tropical responses to El Niño that are similar to one another. There is no indication that there is any technical limitation that prevents the low resolution atmospheric component from producing an accurate simulation of the extra-tropical response to El Niño.

When the atmospheric resolution is increased independently of the ocean, the extra-tropical SST response is quite poor. The dynamics of Rossby wave generation and propagation, part of the the atmospheric bridge teleconnection mechanism, are unrealistic. Upper tropospheric anomalies are generated differently than in observations, and the basic state upon which these anomalies propagate is quite different to that of the observed atmosphere. The dynamics of the extra-tropical response to El Niño in the HiLo configuration have a lot in common with HadGEM1.1 and HadGEM1.2. This suggests that an improvement to just the atmospheric resolution is not enough produce a realistic extra-tropical SST response in the North Pacific.

When the ocean resolution is increased independently of the atmosphere, the extra-tropical SST response in the North Pacific does not match particularly well with observations. This seemingly poor response may actually be deceptive. The dynamical structures of the atmospheric bridge mechanism in the LoHi configuration are actually very similar to those in HiGEM1.1. The westward shift in the position of upper tropospheric anomalies in HiGEM1.1 relative to observations is also present in the LoHi configuration. It is

interesting to note that this westward shift is not present in HiGEM1.2, and perhaps this would also be the case with a cross resolution integration of HiGEM1.2. If this were the case then the extra-tropical SST response in the North Pacific could be reproduced well.

Understanding why the atmospheric basic state is erroneous in the HadGEM1.1 and the HiLo configuration is aided by examining the biases in the mean SST. Figure 4.12 shows the northern winter (November–March) SST bias in each of the coupled models discussed in this chapter. The HiLo configuration (figure 4.12d) has a similar SST bias to HadGEM1.1 (figure 4.12b), as we might expect knowing that they use the same oceanic model component. The HiLo configuration does show some improvement over HadGEM1.1, particularly in the extra-tropical North Pacific. This could be due to improved representation of extra-tropical atmosphere–ocean interactions in the high resolution atmosphere. The SST bias in the LoHi configuration (figure 4.12c) is similar in both location and magnitude to HiGEM1.1 (figure 4.12a). This is most likely the reason why the LoHi configuration has a realistic atmospheric basic state which is similar to that in HiGEM1.1.

When using the higher resolution ocean model coupled to the low resolution atmosphere it is possible to produce a fairly realistic simulation of the extra-tropical response to El Niño. When using the higher resolution atmosphere coupled to the lower resolution ocean this is no longer possible. The best performance in terms of the extra-tropical SST response to El Niño is gained from using both high resolution model components. However, the performance gain when moving from low to high atmospheric resolution with a high resolution ocean is much smaller than the performance gain when moving from low to high oceanic resolution with a high resolution atmosphere. The resolution of the ocean model component appears to be more important than the atmospheric resolution in determining the ability of a coupled model system to realistically simulated the extra-tropical response to El Niño. A better representation of the upper ocean, particularly SST, in the higher resolution ocean model allows for more realistic forcing of the atmosphere and hence a more realistic atmospheric basic state.

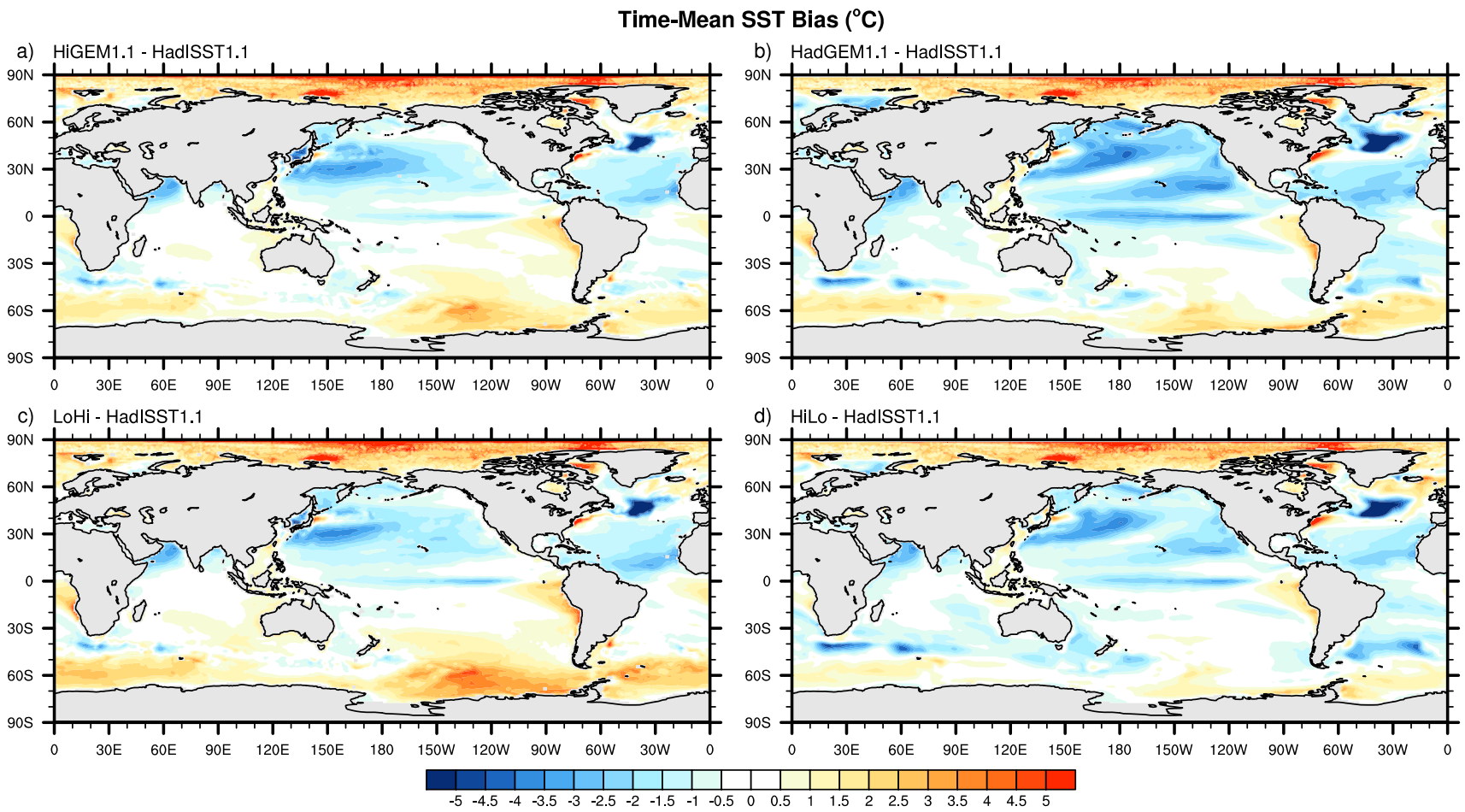

Figure 4.12: Time mean northern winter (NDJFM) SST minus the observed for a) HiGEM1.1, b) HadGEM1.1, c) LoHi, and d) HiLo.

It is possible that increasing oceanic and atmospheric resolution together provides a stable way to improve the climatological mean state and variability, since the spatial scales on which coupling can occur also decrease. However, it has been shown that whilst improving just atmospheric resolution provides few benefits, an improvement to oceanic resolution alone can make a significant difference to the ability of a coupled model system to realistically simulate mean climate and variability. This is likely to be due to the better representation of small scale features in the ocean such as tropical instability waves that flux heat back onto the equator, and the overall reduction in cold tongue bias that results. It still remains to understand why higher horizontal resolution in the ocean model leads to a better representation of the atmospheric basic state, and ultimately the extra-tropical response to El Niño.

Chapter 5

Sensitivity of the atmospheric basic state to systematic SST biases

In this chapter, the sensitivity of the atmospheric basic state to sea surface temperature (SST) perturbations is analysed. The aim is to understand if the systematic SST biases from the low resolution HadGEM1.2 can alter an atmospheric basic state in such a way that the inaccurate extra-tropical response to El Niño seen in HadGEM1.2 can be reproduced in an atmosphere-only simulation.

5.1 Introduction

Chapter 3 showed that the high resolution coupled model HiGEM1.2 is capable of accurately representing the extra-tropical response to El Niño, and that the equivalent lower resolution model HadGEM1.2 is not. The errors in the low resolution model were traced to an unrealistic representation of the atmospheric teleconnection mechanism that controls the extra-tropical SSTs during El Niño. This is due to an unrealistic atmospheric mean state, which changes the propagation characteristics of Rossby waves. Previous studies (e.g. *Guilyardi et al.*, 2004; *Navarra et al.*, 2008) have placed emphasis on the importance of atmospheric resolution in coupled model systems, with regard to simulating El Niño. However, in chapter 4 it was demonstrated that the high resolution atmosphere-only model HiGAM1.1 and the lower resolution equivalent HadGAM1.1 produce similar extra-tropical responses to El Niño when forced with the same observed SSTs. It was

also shown that the cross-resolution configuration with a high resolution oceanic component and a low resolution atmospheric component performed significantly better than the configuration with low resolution oceanic component and high resolution atmospheric component. It therefore seems more likely that ocean resolution is the dominant factor when simulating the extra-tropical response to El Niño in a coupled model.

It is reasonable to assume that the mean state of the atmosphere is heavily dependent on the mean state of the ocean. Therefore, a sensible place to start looking to understand differences in the atmospheric mean state between HiGEM1.2 and HadGEM1.2 is the oceanic mean state. Figure 5.1 shows 50 year time-mean northern winter (November-March) SST for HiGEM1.2 and HadGEM1.2 minus the equivalent observed SST field, and also the HadGEM1.2 minus HiGEM1.2 difference.

Figures 5.1a and 5.1b show areas where the modelled mean SST differs from observed mean SST, the wintertime SST bias. Both HiGEM1.2 and HadGEM1.2 have a cold SST bias in winter in the north-west Pacific. A cold SST bias in this region is noted in the climatological annual mean of many coupled models (*Randall et al.*, 2007). Both HiGEM1.2 and HadGEM1.2 have a cold SST bias in the North Atlantic. The bias is stronger and larger in HadGEM1.2 than in HiGEM1.2. This cold bias is an effect of the models having insufficient resolution to locate the Gulf Stream and North Atlantic Current, and the large SST gradients there. HiGEM1.2 has a smaller cold bias in the North Atlantic since its higher oceanic resolution allows a better representation of the orientation of the Gulf Stream than in HadGEM1.2. This particular type of model error is found in many coupled models, as discussed in *Randall et al.* (2007). HadGEM1.2 has a cold SST bias in the eastern sub-tropical Pacific centred at 20°N, 140°W. This winter time SST bias is not evident in HiGEM1.2, and hence could be one of the factors causing the representation of the atmospheric basic state in HadGEM1.2 to be inaccurate.

Figure 5.1c shows the difference between winter time mean SST in HadGEM1.2 and HiGEM1.2. This is the difference between the SST biases in the models. In the central Pacific region HadGEM1.2 is much cooler than HiGEM1.2 (figures 5.1a and 5.1b). Given that HiGEM1.2 produces a realistic atmospheric basic state even though it has considerable biases in winter time SST, and HadGEM1.2 does not, it could be that the difference between the two winter time biases is the extra factor in explaining why HadGEM1.2

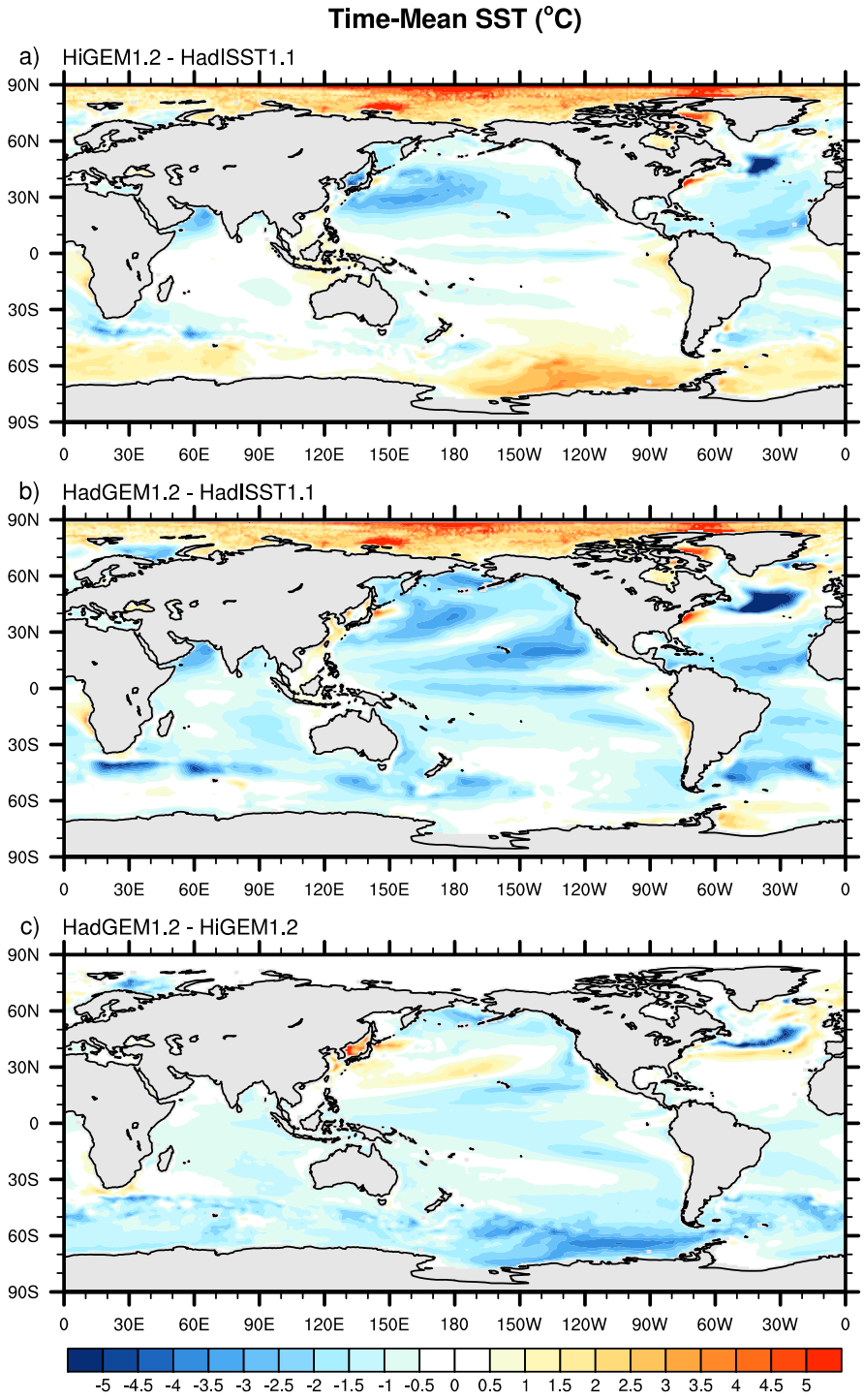

Figure 5.1: Differences in northern winter (NDJFM) 50 year time-mean SST for a) HiGEM1.2 minus HadISST1.1, b) HadGEM1.2 minus HadISST1.1, and c) HadGEM1.2 minus HiGEM1.2. The contour interval is 0.5 °C.

simulates the extra-tropical response to El Niño poorly.

5.2 Methods

Determining the effect of SST biases on the atmospheric basic state, and hence on the extra-tropical response to El Niño, during northern winter requires experimentation under controlled conditions. This can be achieved by integrating the atmospheric component of the coupled model, forced by observed SSTs with some form of climatological perturbation added. If by adding some component of the climatological SST bias from HadGEM1.2 to observed SSTs it is possible to produce an unrealistic atmospheric basic state of the type identified in HadGEM1.2 (figure 3.18c), then it would show that the atmospheric basic state in HadGEM1.2 is unrealistic because of problems in the oceanic component of the model, which are likely to be due to resolution.

It was demonstrated in chapter 4 that both the high and low resolution atmosphere-only integrations HiGAM1.1 and HadGAM1.1 produced similar realistic extra-tropical responses to El Niño. This suggests that atmospheric resolution is not a factor. This allows us to use the high resolution atmosphere model HiGAM1.2 for this work. Causing the high resolution atmospheric model to develop an unrealistic basic state just by making changes to the SST forcing would confirm that oceanic resolution is dominant over atmospheric resolution as a controlling factor in the ability for a coupled model to accurately simulate the extra-tropical response to El Niño.

The experiments in this chapter will also be run for 20 years. This provides a compromise between the ideal length of the data time series and the real and computational time available. This integration length is considerably shorter than the 50 year samples used to analyse HiGEM1.2 and HadGEM1.2 in chapter 3. However, it was demonstrated in chapter 4 that 20 year long integrations of the atmospheric models HiGAM1.1 and HadGAM1.1 were sufficient to produce realistic representations of the atmospheric basic state.

5.3 Model configuration

The experiments in this chapter use the high resolution atmosphere-only model HiGAM1.2. The aim is to understand the effect of systematic SST biases on the atmospheric basic state by integrating the HiGAM1.2 with and without imposed SST biases. However, HiGAM1.2 is quite computationally expensive, and for this reason it is not feasible to complete a full 20 year integration for each experiment. Instead, winter seasons must be integrated individually. This is a valid approach since the atmospheric states in individual winter seasons are independent of one another. Integrating each winter separately saves a considerable amount of computing time, and real time since multiple winter seasons can be integrated simultaneously. The practical cost of this approach is that we do not have information about the appropriate state of the atmosphere that should be used to initialise each winter season.

5.3.1 Model initialisation

Each winter season of the model integration uses the appropriate boundary conditions (SST etc.) for the particular year it represents. However, as discussed previously, it is not possible to initialise the model with the correct atmospheric state for the given boundary conditions. Instead, all seasons are initialised with the same atmospheric state. This initial condition will be from the same month that the season is begun from so as to prevent the atmosphere model from having to make impractically large adjustments. This approach requires that some extra integration time be allowed for the atmosphere to adjust to the boundary conditions. Atmospheric adjustment time is much shorter than oceanic adjustment time. The precise amount of time required for the atmosphere to adjust to boundary conditions from an initial condition is not known with any certainty. However, it is generally thought that one month should be sufficient. To interpret the results of these experiments with any confidence, it is necessary to confirm that starting integrations at the beginning of October will give the atmosphere model time to adjust to its boundary conditions before the start of the November-March season that will be analysed.

Three control integrations were performed to confirm the validity of the one month adjustment time allowance. These integrations are summarised in table 5.1. Each integration is started at the beginning of October and run until the end of March. The first

Integration	Initial condition (dd-mm-yyyy)	Boundary condition (dd-mm-yyyy)
S1	01-10-1982	01-10-1982
S2	01-10-1983	01-10-1983
S3	01-10-1983	01-10-1982

Table 5.1: Description of control season integrations used for determining HiGAM1.2 atmospheric adjustment time. The initial condition is the atmospheric state used to initialise the model. The boundary condition is the external forcing (e.g. SST).

integration (S1) uses boundary conditions and atmospheric state appropriate for the 1982–1983 winter season. The initial atmospheric state was generated by a previous integration started from April 1982. The second integration (S2) uses boundary conditions and atmospheric state appropriate for the 1983–1984 winter season. The initial atmospheric state was generated in the same way as for S1. Both S1 and S2 require no adjustment time as their initial condition is pre-adjusted to the boundary condition. The third control season (S3) uses boundary conditions appropriate for the 1982–1983 winter season, but is initialised with the atmospheric state from S2 (October 1983). Hence, S3 requires time for the atmosphere to adjust to the boundary conditions.

The solid line in figure 5.2 is a time series of the root mean squared (RMS) difference between zonal wind at 200 hPa in S1 and S2 for the first 60 days of the integrations. Since S1 and S2 have different boundary conditions and different initial atmospheric states, the RMS difference remains relatively constant throughout this period. The size of this RMS difference represents a base level of RMS difference that can be expected between two different atmospheric states that are adjusted to their boundary conditions.

The dashed line in figure 5.2 is a time series of the RMS difference between zonal wind at 200 hPa in S2 and S3. Initially the RMS difference is zero since S2 and S3 are initialised with the same atmospheric state. As the atmosphere in S3 adjusts to the prescribed boundary conditions, the RMS difference between S2 and S3 increases rapidly (days 1-18). After day 18 the RMS difference is no longer steadily increasing, it flattens out to a stable state. At this point S3 has adjusted to the boundary conditions. This level of relatively constant RMS difference is about the same as the base level of RMS difference between S1 and S2. This confirms that the transition from steadily increasing RMS difference to steady RMS difference around day 18 represents the end of the atmospheric

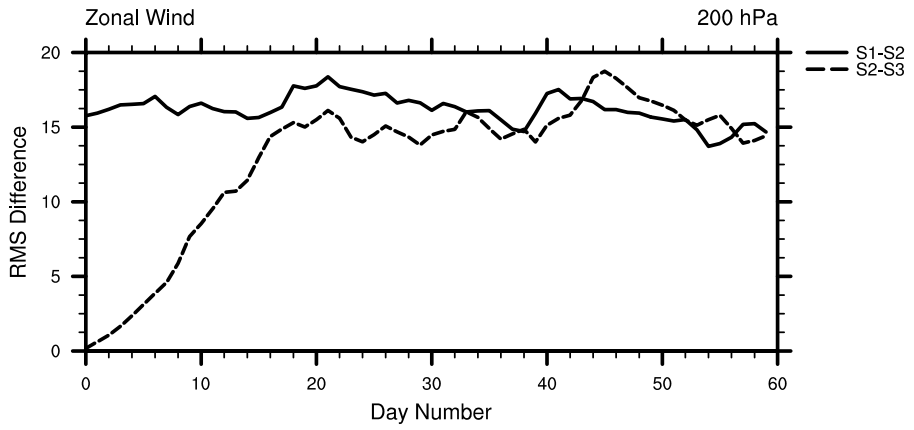

Figure 5.2: Daily RMS difference between zonal wind fields at 200 hPa in the first 60 days of a winter season integration. The solid line is the RMS difference between two atmospheres initially in equilibrium with different initial atmospheric states (S1 and S2). The dashed line is the RMS difference between an atmosphere initially in equilibrium (S2) and an atmosphere not initially in equilibrium (S3) both with the same initial atmospheric state.

adjustment time in S3. The adjustment time is less than one month, meaning that starting seasonal integrations in October, when November-March results are required, is a valid approach.

An understanding of the atmospheric adjustment time is crucial when it comes to perturbing the oceanic boundary conditions. There is no 'true' atmospheric state to initialise the model with, hence it is not be possible to produce an equilibrated initial condition for perturbed boundary conditions unless the atmosphere model is integrated continuously for the whole 20 year period. Perturbation experiments would require some spin-up time and here it has been demonstrated that 30 days of adjustment time is enough to ensure the atmosphere's behaviour is independent of the initial condition.

5.4 Control experiment

The atmosphere model HiGAM1.2 is used for the experiments in this chapter. Although a control integration of HiGAM1.1 has been discussed in chapter 4, it cannot be guaranteed that HiGAM1.2 will perform in the same manner. Therefore, it is necessary to produce a control integration for HiGAM1.2 in order to have a point of reference with which to compare perturbed experiments. The configuration of the control experiment is

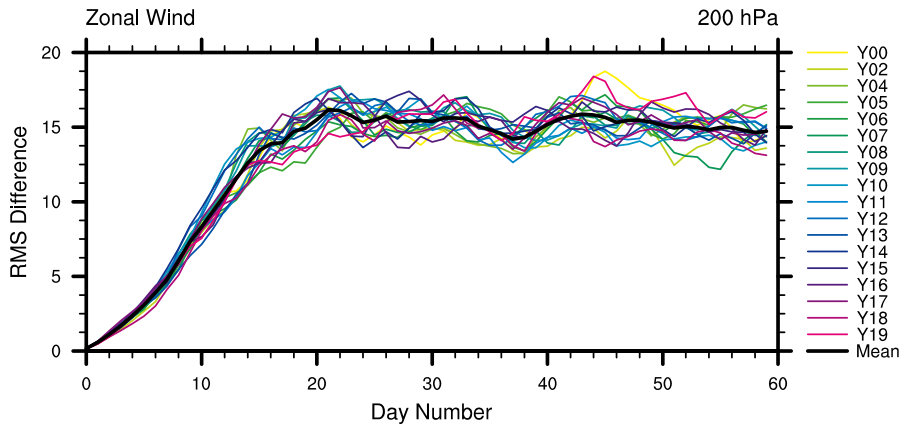

Figure 5.3: Daily RMS difference between zonal wind fields at 200 hPa in the first 60 days of selected winter seasons from the control experiment. The coloured lines are the RMS difference between the winter season from 1983–1984 (Y01) and each other winter season. The thicker black line is the mean of all the RMS difference curves.

described here. Discussion of the performance of the control experiment is integrated into sections 5.5 and 5.6.

The control experiment, referred to as the CT experiment, consists of the 20 winter (October-March) seasons for 1982/83–2001/02. Each seasonal integration was initialized with the atmospheric state from October 1983 and the ocean boundary conditions are those appropriate for the particular season of the integration. The exception to this is the winter season of 1985/86 which became numerically unstable during the first month of integration when initialised with October 1983 atmospheric state. This instability was likely caused by an unfortunate combination of initial condition and boundary conditions. The instability was prevented by changing the initial condition from the October 1983 atmospheric state to the October 1982 atmospheric state.

Based on the results of the seasonal control integrations in section 5.3.1, one month of adjustment time has been allowed before the start of the November–March winter season. To be completely confident in the results, the RMS difference method used in section 5.3.1 has been applied to zonal wind at 200 hPa for the first 60 days every winter of the CT experiment (excepting the 1985/86 winter, since it was initialized with the 1982 atmospheric initial condition). The resultant RMS differences in zonal wind between the 1983/84 winter season and each other season are plotted together in figure 5.3.

Figure 5.3 clearly shows that the atmosphere has adjusted to the prescribed boundary

conditions within 30 days for all winter seasons. This allows us to interpret the results from an analysis of November-March with a good level of confidence that the initial condition for the atmosphere is not directing the solution.

5.5 Pantropical SST bias experiment

In section 5.1 it was established that there are significant biases in the mean northern winter (NDJFM) SST in both HiGEM1.2 and HadGEM1.2 (figure 5.1a,b). As shown in chapter 3, the atmospheric basic state in HiGEM1.2 is fairly realistic with respect to allowing a realistic simulation of the extra-tropical response to El Niño, allowing it to propagate Rossby waves in a realistic manner. In HadGEM1.2 the atmospheric basic state is unrealistic, which prevents HadGEM1.2 from realistically simulating the extra-tropical response to El Niño. Since both coupled models have significant SST biases, but only HiGEM1.2 produces a realistic atmospheric basic state, then perhaps it is the difference between the SST biases (i.e., the bias that exists in HadGEM1.2 that does not exist in HiGEM1.2, figure 5.1c) that could be responsible for the unrealistic atmospheric basic state in HadGEM1.2.

To determine if the additional SST bias that is present in HadGEM1.2 but not in HiGEM1.2 could be responsible for the unrealistic HadGEM1.2 atmospheric basic state, the high resolution atmospheric model component is forced with observed SSTs plus the HadGEM1.2 minus HiGEM1.2 mean northern winter (NDJFM) SST. This experiment is referred to as the pantropical bias (PT) experiment. The aim of this is to attempt to reproduce the incorrect atmospheric basic state seen in HadGEM1.2 in the high resolution atmospheric component HiGAM1.2. Success would imply that it is not atmospheric resolution that is preventing HadGEM1.2 from producing a realistic extra-tropical response to El Niño, but rather it is errors in the simulation of the climatological mean state of the ocean that cause the unrealistic response.

5.5.1 Experiment configuration

The SST forcing for HiGAM1.2 is constructed by applying the appropriate SST bias to the monthly observed SST fields that were used to force the control experiments. The SST bias is computed separately for each month so as to allow for variations in the SST

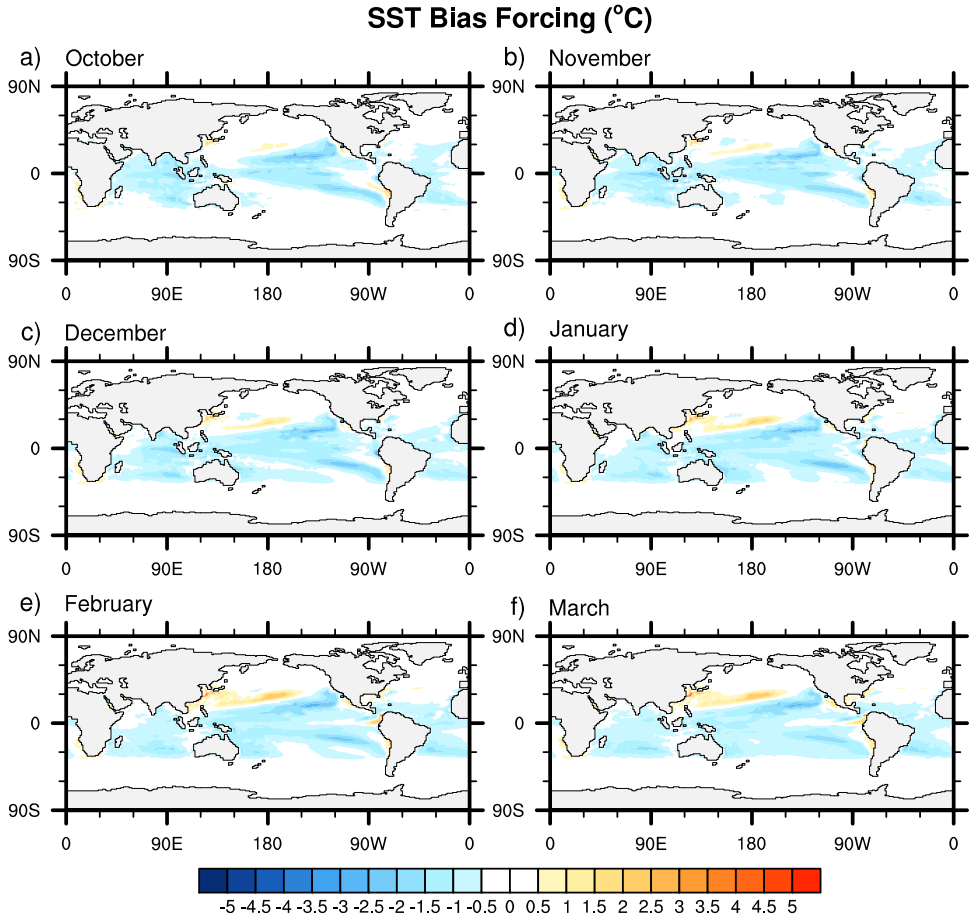

Figure 5.4: The monthly SST bias (on the atmospheric grid) included in the PT experiment (°C). The bias is composed of differences between 20 year monthly climatologies for HadGEM1.2 and HiGEM1.2 for each month of the winter season.

bias on a monthly scale. The monthly biases are computed by first computing a 20 year climatology for each of the winter months (October-March) for each of HiGEM1.2 and HadGEM1.2. The difference between the monthly climatologies for HadGEM1.2 and HiGEM1.2 is then taken to produce the monthly varying SST bias.

As it stands this bias is not suitable for adding to the observed SST forcing in its current state. There are many large magnitude SST differences at high latitudes that, if included, would interfere with the sea ice forcing. To ensure reliable results, this experiment should be as close as possible to the control experiment. Therefore, changing sea ice forcing to match SST forcing is not a viable option. Instead it is better to limit the latitudinal extent of the SST bias that is introduced. This is a reasonable strategy since most of the oceanic forcing of the atmosphere will take place in the tropics and sub-tropics

(*Graham et al.*, 1994; *Lau and Nath*, 1994). The latitudinal extent of the full SST bias is limited to the range 30°N–30°S, and is reduced linearly to zero at 40°N and 40°S. The limited latitudinal range SST bias is shown in figure 5.4. Since there are no anomalies north of 40°N or south of 40°S, there is no interference with sea ice forcing.

5.5.2 Atmospheric basic state

The diagnostic framework introduced in chapter 3 is now used to assess the impact of the imposed SST bias in the PT experiment on the atmospheric basic state. Figure 5.5 shows the time-mean northern winter (November–March) zonal wind at 200 hPa over a time period of 20 years for observations, the CT experiment, and the PT experiment. The 20 year sample for the observations is drawn from the winters of 1982/83–2001/02 so as to match the underlying SSTs driving the observed and modelled atmospheres.

The time-mean zonal wind fields in the Pacific region are quite similar in the observations and the CT experiment. The region of mean easterlies is more elongated in the CT experiment. This is also the case in HiGEM1.2 (figure 3.15b) which suggests that this is a systematic error in the atmosphere model. The strength and position of the Asian and North American jets in the CT experiment is similar to the observations and the structure of the region where the Asian and North American jets meet is qualitatively similar in the CT experiment and the observations.

The time-mean zonal wind in the PT experiment has some interesting differences when compared to the CT experiment. The clearest difference is in the structure of the region where the Asian and North American jets meet. There is a much more distinct separation of the two jets compared to the CT experiment and the entrance to the North American jet appears better defined. This difference in zonal wind structure is very like the difference between HadGEM1.2 and HiGEM1.2. The strength of the westerlies in the PT experiment are reduced compared to observations and the CT experiment. This is particularly clear in the vertical profile of zonal mean zonal wind (figure 5.6), where it is evident that the midlatitude westerlies in the Northern Hemisphere are weaker. This is consistent with the imposed pantropical SST bias causing a reduction in the equator–pole temperature gradient, and hence a reduction in the speed of the midlatitude winds.

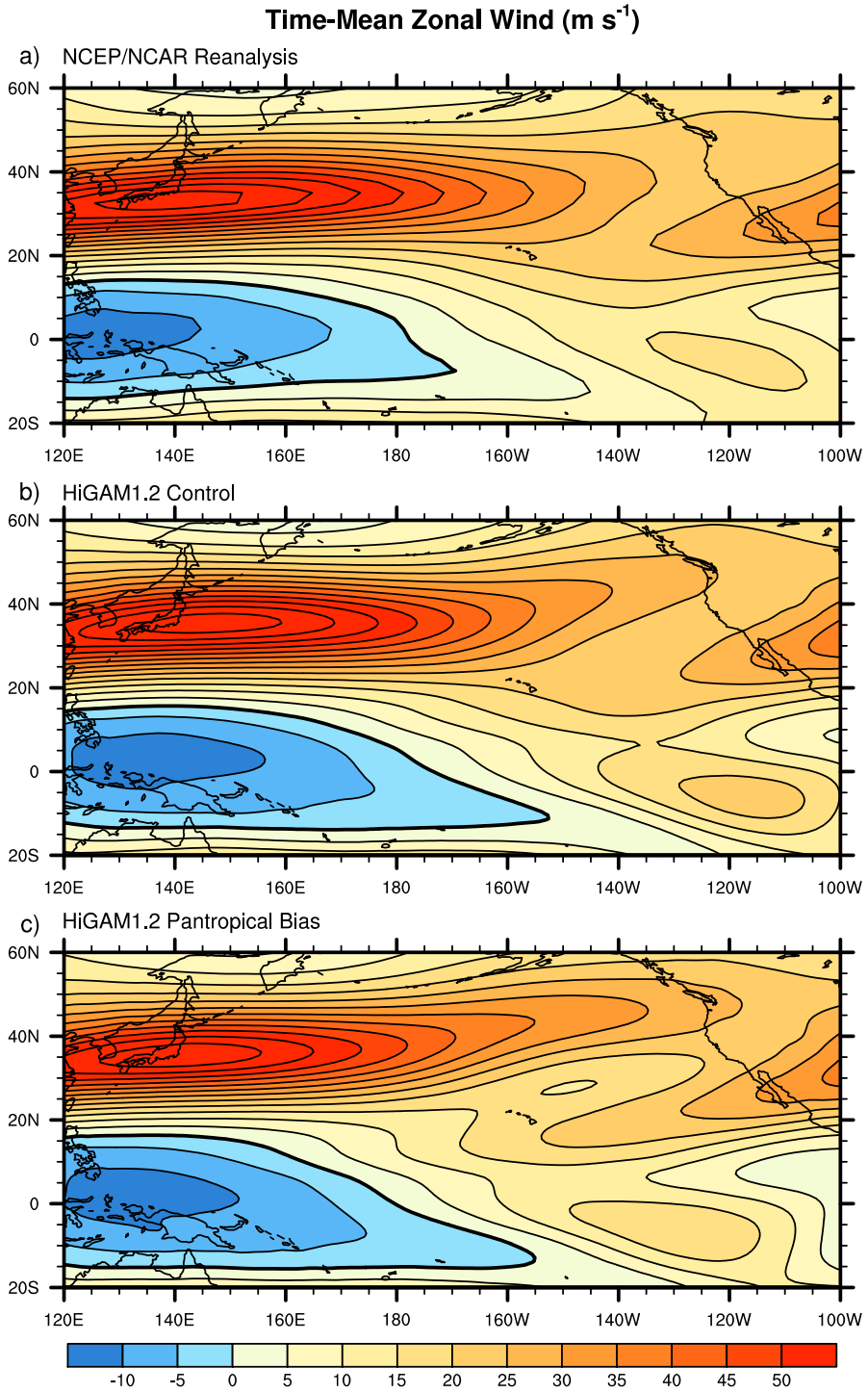

Figure 5.5: 20 year time-mean northern winter (NDJFM) zonal wind (m s^{-1}) at 200 hPa. The contour interval is 5 m s^{-1}, the zero contour is thickened. a) NCEP/NCAR Reanalysis, b) HiGAM1.2 control (CT) experiment, and c) HiGAM1.2 pantropical bias (PT) experiment.

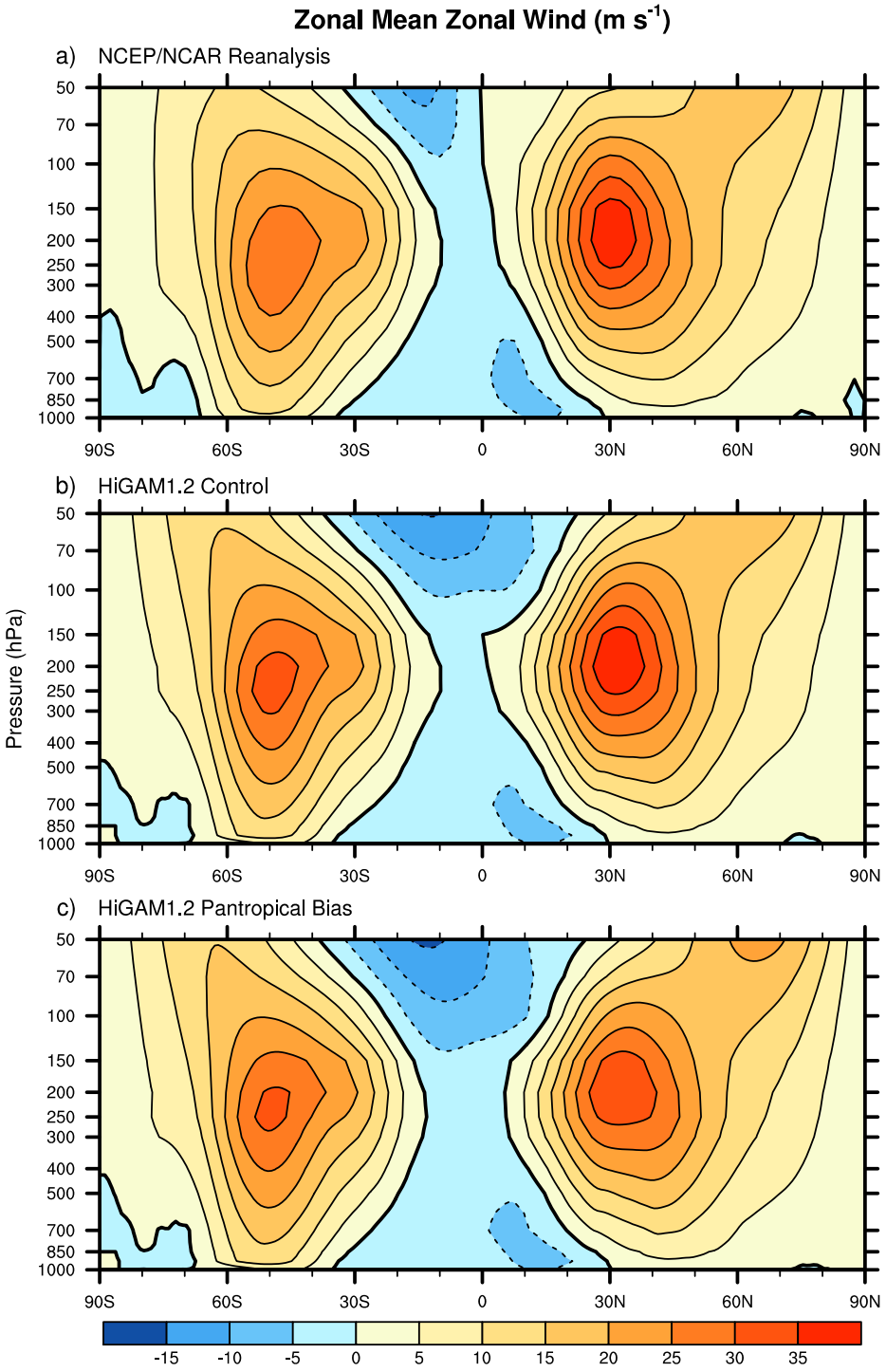

Figure 5.6: 20 year time-mean mean northern winter (NDJFM) zonal mean zonal wind (m s^{-1}). The contour interval is 5 m s^{-1}. a) NCEP/NCAR Reanalysis, b) HiGAM1.2 control (CT) experiment, and c) HiGAM1.2 pantropical bias (PT) experiment.

The atmospheric basic state in the PT experiment is further diagnosed using the stationary wave propagation framework used in previous chapters. Figure 5.7 shows the zonal stationary Rossby wavenumber in the Pacific domain for observations, the CT experiment, and the PT experiment. The CT experiment has a stationary wavenumber pattern that is both visually and dynamically similar to the observed stationary wavenumber pattern. The Asian jet waveguide and the North American jet waveguide merge over the central Pacific, potentially allowing Rossby waves to cross from one into the other. This result is expected since the basic state of the CT experiment atmosphere should be controlled by observed SSTs.

The waveguide structure in the PT experiment (figure 5.7c) is significantly different from the CT experiment and observations. The Asian jet waveguide and North American jet waveguides are distinctly separate structures. They are separated by regions of reversed absolute vorticity gradient (dark hatching) over the eastern and western Pacific. This waveguide structure is very much like that seen in HadGEM1.2 (figure 3.18c).

5.5.3 The extra-tropical response to El Niño

The implications of an unrealistic atmospheric basic state are unrealistic Rossby wave propagation which leads to erroneous surface wind anomalies. In turn, these surface wind anomalies are responsible for unrealistic surface heat flux anomalies that control extra-tropical SSTs. An unrealistic atmospheric basic state has been produced in the PT experiment, implying that the remaining portion of the atmospheric bridge mechanism will be unrealistic. However, the exact nature of the extra-tropical response to El Niño produced by this unrealistic atmospheric basic state must be determined.

Figure 5.8 shows regression maps of stream function anomalies at 200 hPa against the EP index for observations, the CT experiment, and the PT experiment. In general the pattern of anomalies over the Pacific/North American (PNA) region is similar in all three panels, although the cyclonic anomalies over North America and the central North Pacific are shifted west in the PT experiment compared with the CT experiment and observations. The stream function anomalies in the CT experiment over the PNA region are similar to observations in location, but have larger gradients (contour lines are closer) implying the anomalous circulation response in the CT experiment is stronger than observed. The

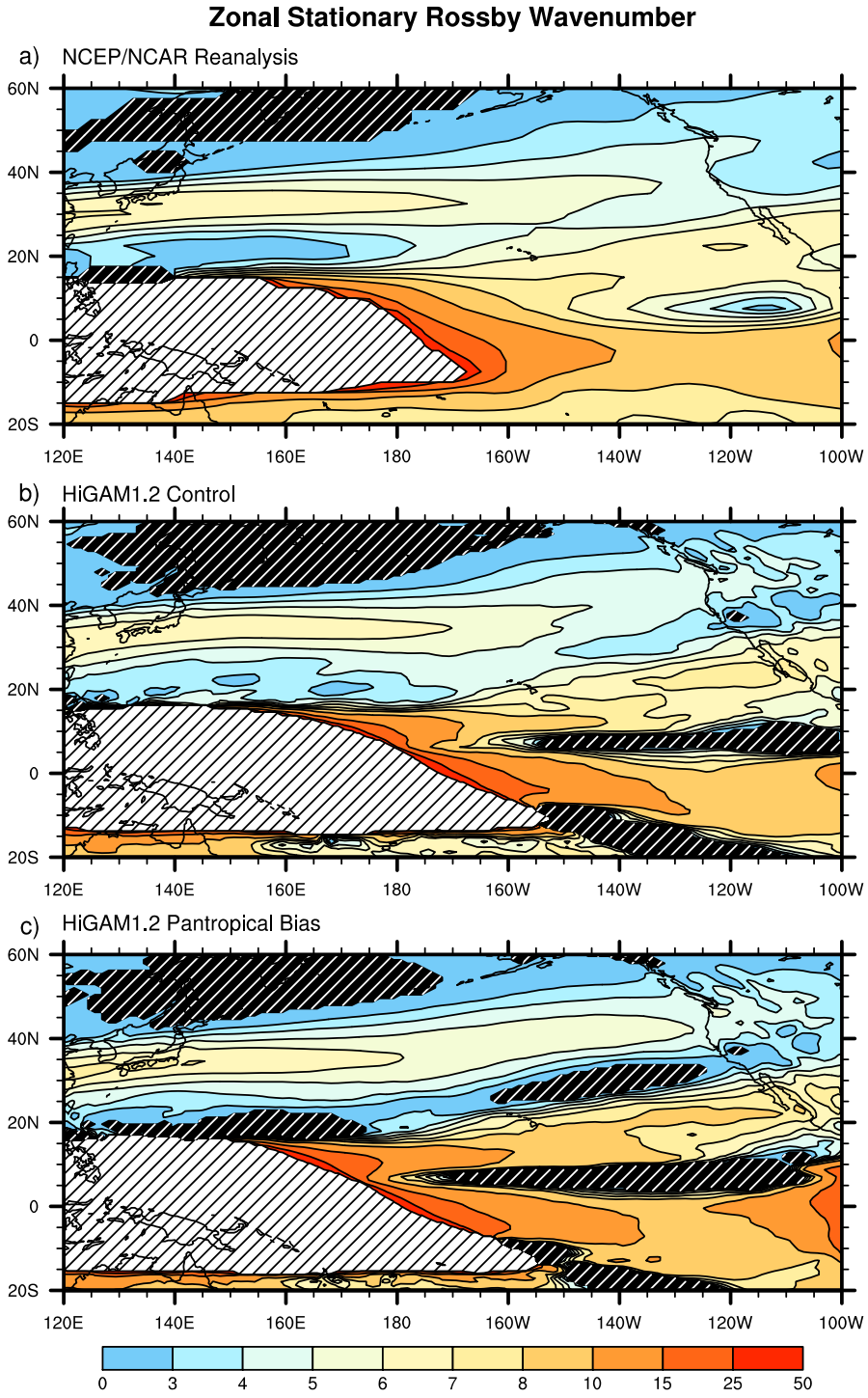

Figure 5.7: Zonal stationary wavenumber computed from northern winter (NDJFM) 20 year time-mean zonal wind at 200 hPa. Light (dark) hatching indicates areas where $\bar{u}$ (β_M) is negative. a) NCEP/NCAR Reanalysis, b) HiGAM1.2 control (CT) experiment, and c) HiGAM1.2 pantropical bias (PT) experiment.

PNA region anomalies in the PT experiment have much smaller gradients than in the CT experiment, suggesting the response is weaker in the PT experiment.

The PT experiment produces a weaker upper tropospheric response to El Niño than the CT experiment, combined with a shift in the pattern of anomalies in the PNA region. The implications of these differences might be better examined using vorticity as a diagnostic, since vorticity can be interpreted directly instead of having to consider gradients. Regression maps of anomalous 200 hPa vorticity are shown in figure 5.9.

The CT experiment is very similar to observations in most regions, particularly over the PNA region, but the negative anomaly over Japan is much weaker than observed. The PT experiment has vorticity anomaly patterns quite unlike those in the CT experiment and observations. The positive anomalies over North America and the central North Pacific are considerably weaker than those in the CT experiment, as expected from analysis of stream function. The westward shift of these anomalies is very clear in the vorticity regression map, including a weak negative anomaly over the Alaskan coast and Pacific ocean.

There are differences in the strength, location, and shape of the the upper tropospheric anomalies in the PT experiment when compared to the CT experiment. Both the westward shift of the positive vorticity (cyclonic stream function) anomalies and the introduction of negative vorticity (anticyclonic stream function) anomalies over the north east Pacific are also noted in HadGEM1.2, and were ultimately responsible for the erroneous surface circulation and heat flux anomalies that cause extra-tropical SST anomalies as a response to El Niño.

Regression maps of surface wind anomalies are shown in figure 5.10. The CT experiment and observations show similar patterns of surface wind anomaly, as would be expected from their similar upper tropospheric anomalies inducing surface circulation through the equivalent barotropic vertical structure. The CT experiment has stronger surface wind anomalies than observations in the North Pacific region. Again, this is as expected from the stronger than observed upper tropospheric anomalies in the CT experiment. The surface wind anomalies in the PT experiment are considerably weaker than those in the CT experiment, with almost no significant anomalies along the North American coast, and particularly in the south eastern portion of the domain. The westward shift of the main centre of circulation is again evident in the surface wind regression map. The

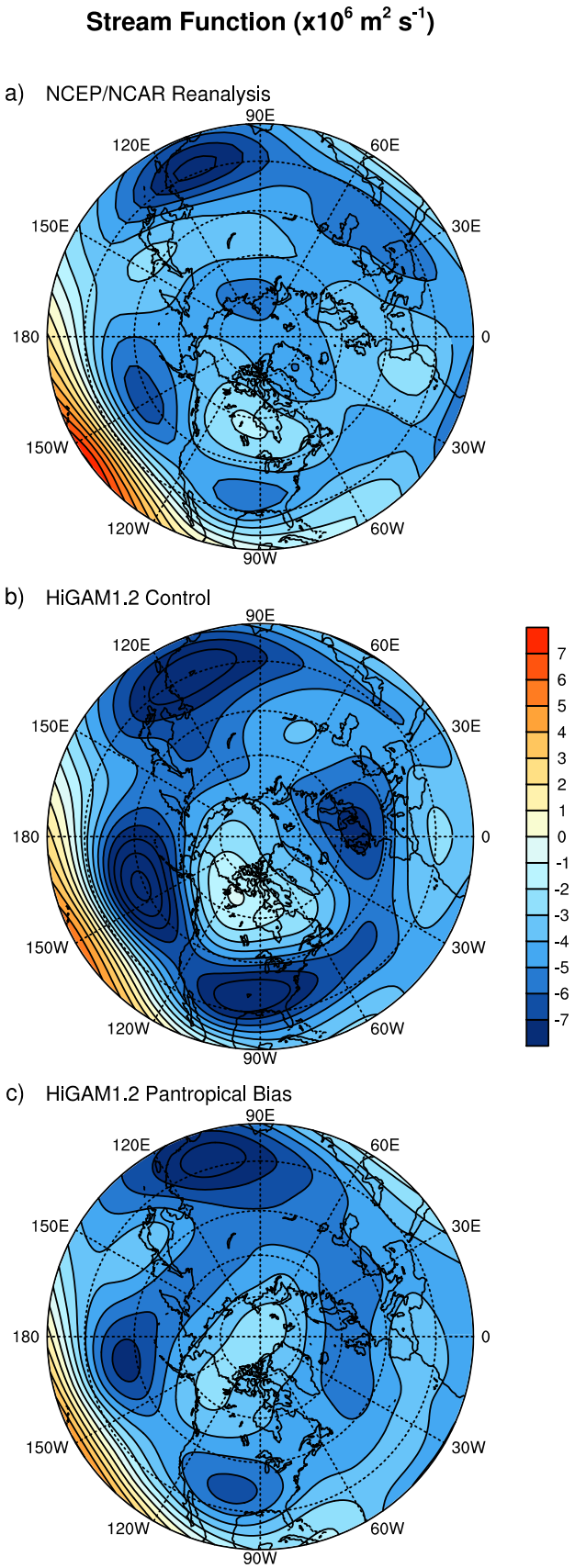

Figure 5.8: Northern winter (NDJFM) 200 hPa stream function (m^2 s^{-1}) anomaly patterns associated with a 1 °C departure of the EP index. The contour interval is 10^6 m^2 s^{-1}. a) NCEP/NCAR Reanalysis, b) HiGAM1.2 control (CT) experiment, and c) HiGAM1.2 pantropical bias (PT) experiment.

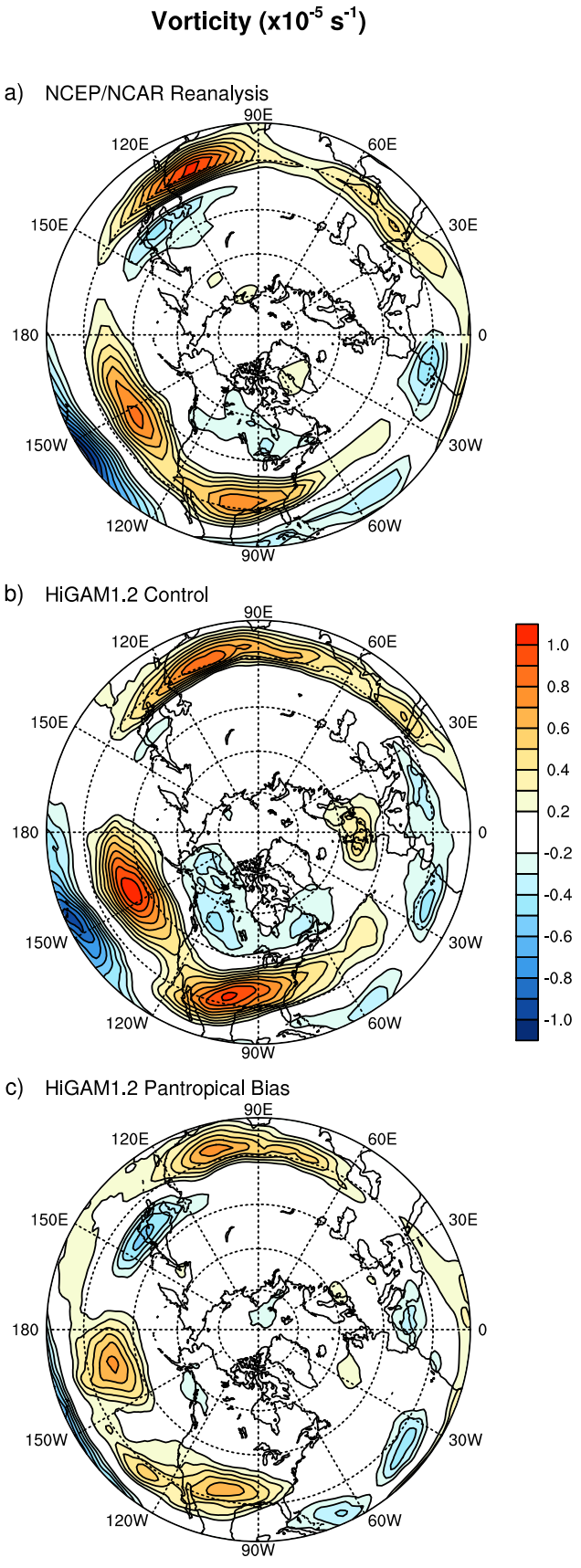

Figure 5.9: Northern winter (NDJFM) 200 hPa vorticity (s^{-1}) anomaly patterns associated with a 1 °C departure of the EP index. The contour interval is 10^{-6} s^{-1}. Contours between -2 and 2×10^{-6} s^{-1} are omitted. a) NCEP/NCAR Reanalysis, b) HiGAM1.2 control (CT) experiment, and c) HiGAM1.2 pantropical bias (PT) experiment.

consequences of these erroneous surface wind anomalies in the PT experiment would be an unrealistic representation of the surface heat flux anomalies that drive the extra-tropical SST response to El Niño.

5.5.4 Summary

Analysis of the PT experiment has confirmed that it is possible to produce an unrealistic basic state, such as is present in the low resolution coupled model HadGEM1.2, in the high resolution atmosphere model HiGAM1.2 solely by introducing a climatological SST bias. The details of the erroneous atmospheric basic state and the Rossby waves that propagate on it and form the extra-tropical response to El Niño are not exactly the same as those in HadGEM1.2. However, expecting the two to be the same would be unreasonable. Using only the SST bias that is present in HadGEM1.2 and not in HiGEM1.2 assumes a certain amount of linearity in the response of the atmosphere to SST biases, in effect assuming that the part of the SST bias in HadGEM1.2 that is also present in HiGEM1.2 makes no contribution to the erroneous atmospheric basic state at all.

As the PT experiment imposed a climatological SST bias with a longitudinally global extent, it is not clear exactly how the unrealistic atmospheric basic state develops. However, the similarities between the PT experiment and HadGEM1.2 provide evidence that the 'extra' SST bias in HadGEM1.2 is responsible for the poor representation of the atmospheric basic state.

5.6 Regional SST bias experiment

It has been established in section 5.5 that the extra SST bias present in HadGEM1.2 that is not present in HiGEM1.2 could be responsible for the unrealistic atmospheric basic state in HadGEM1.2. This SST bias created distinct separation of the waveguides over the Pacific in the PT experiment (figure 5.7c) which can then explain the unrealistic extra-tropical response. However, since the PT experiment used a longitudinally global SST bias to force the HiGAM1.2, the spatial scale of the SST bias required to produce this waveguide separation is still unknown.

A further experiment was designed to try to understand the effect of a localised SST bias on the atmospheric basic state, and to see if the separation of the Pacific waveguides

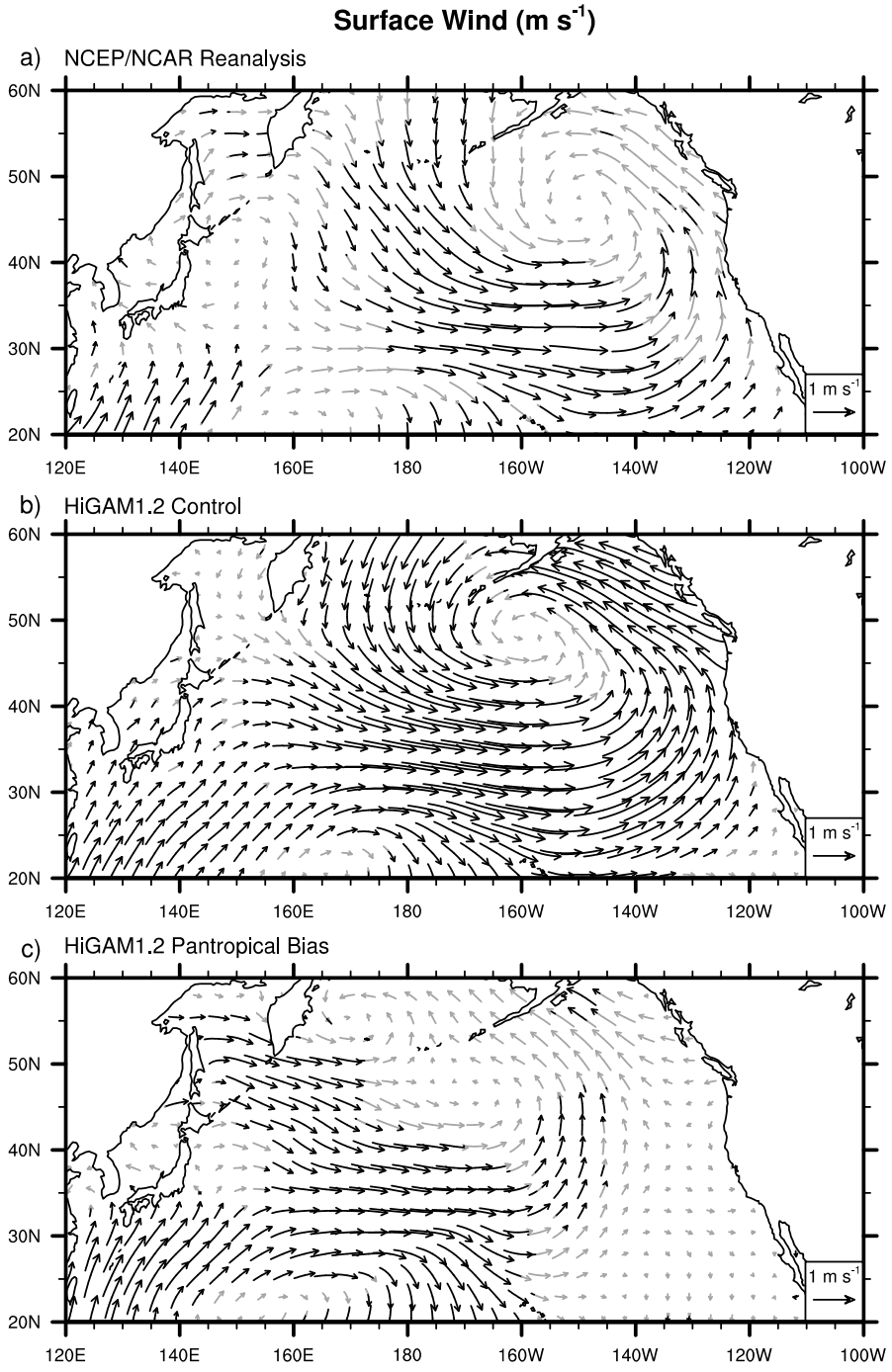

Figure 5.10: Northern winter (NDJFM) surface wind (m s^{-1}) anomaly patterns associated with a 1 °C departure of the EP index. a) NCEP/NCAR Reanalysis, b) HiGAM1.2 control (CT) experiment, and c) HiGAM1.2 pantropical bias (PT) experiment.

can be induced by such a bias in the Pacific basin. For this the HiGAM1.2 atmosphere model is forced with observed SSTs plus the HadGEM1.2 SST bias centred at 20°N, 135°W (see figure 5.1). This particular anomaly is chosen because it is particularly strong, and is not present in HiGEM1.2. Also its position and size correspond approximately to the reversed vorticity gradient separating the downstream portion of the Asian and Pacific waveguides in HadGEM1.2 (figure 3.18c). The bias added to the observed SST forcing is the full bias found in HadGEM1.2 and not the HadGEM1.2 minus HiGEM1.2 bias used in the PT experiment. This is because we wish to understand the effect of a specific part of the SST bias from HadGEM1.2, and whether it could be responsible for the split waveguide structure. This experiment is referred to as the regional bias (RB) experiment.

5.6.1 Experiment configuration

The SST forcing for the RB experiment is constructed in a similar way to the forcing for the PT experiment. As in the PT experiment, the SST bias is computed separately for each month so as to allow for variations in the SST bias on a monthly time scale. The monthly biases are computed by first computing 20 year climatologies of SST for each of the winter months (October-March) for each of HadGEM1.2 and HadISST1.1, the observed data set. The difference between these monthly climatologies is then taken to produce the monthly varying SST bias.

The SST bias is isolated by allowing the bias to have full magnitude in the region 13.3°N–26.83°N, 160°W–116.75°W. These anomalies are then reduced linearly to zero within a 9 grid point radius. This ensures that imposing the bias does not introduce sharp grid point-scale gradients. The isolated monthly varying SST bias is shown in figure 5.11. This regional SST bias is then added to the observed forcing to produce the SST forcing for the experiment.

5.6.2 Atmospheric basic state

Performance of the RB experiment with respect to the atmospheric basic state is assessed using the same approach as the PT experiment. Figure 5.12 shows time-mean northern winter (November–March) zonal wind at 200 hPa, over a time period of 20 years, for observations, the CT experiment, and the RB experiment. The top two panels are as in

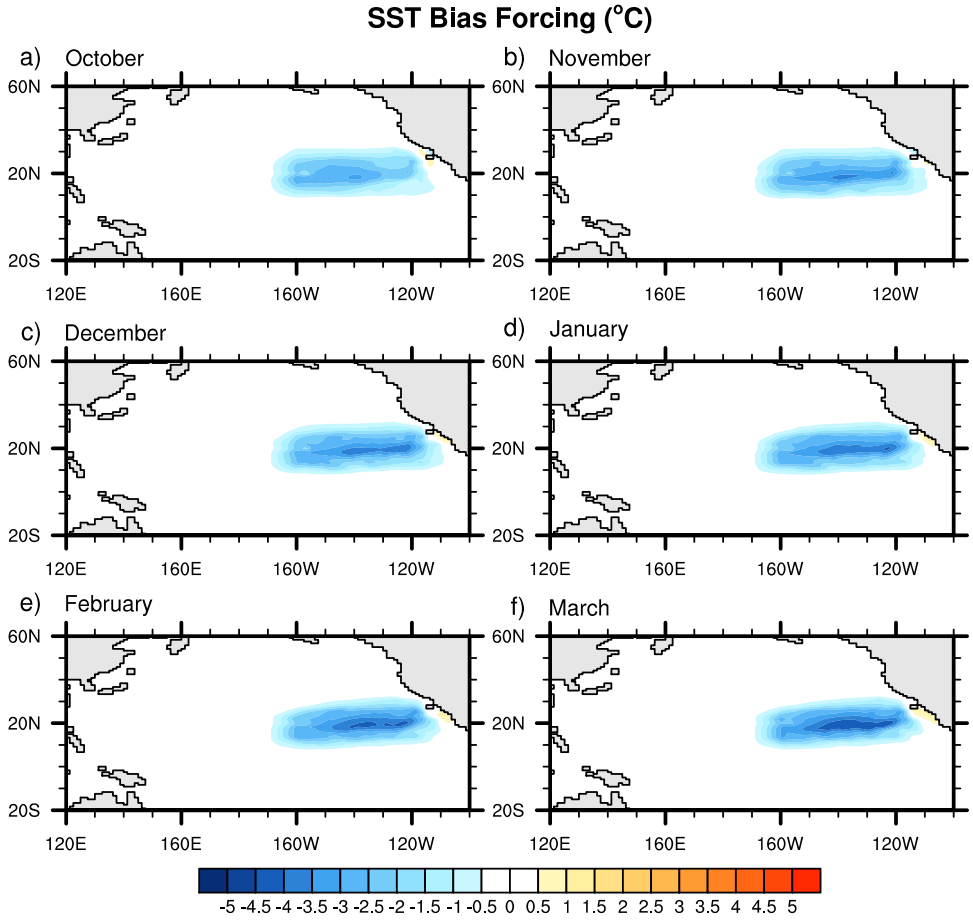

Figure 5.11: The monthly SST bias (on the atmospheric grid) included in the RB experiment (°C). The bias is composed of differences between 20 year monthly climatologies for HadGEM1.2 and HadISST1.1 for each month of the winter season.

figure 5.5. When the regional SST bias is imposed in the eastern subtropical Pacific, there is an elongation and strengthening of the entrance to the North American jet. There is also a weakening of the zonal flow north of this. This regional scale change to the time-mean flow is also present in HadGEM1.2 and the PT experiment (figure 5.5c). However, the zonal wind structure over the western Pacific is largely unchanged between the RB and CT experiments. This suggests that the imposed SST bias produces alterations only to the local and immediately downstream regions of the atmosphere.

Figure 5.13 shows the zonal stationary Rossby wavenumber in the Pacific domain for observations, the CT experiment, and the RB experiment. The top two panels are as in figure 5.7. Over the eastern Pacific there is an area of reversed meridional vorticity gradient (dark hatching) separating the waveguides associated with the Asian and North

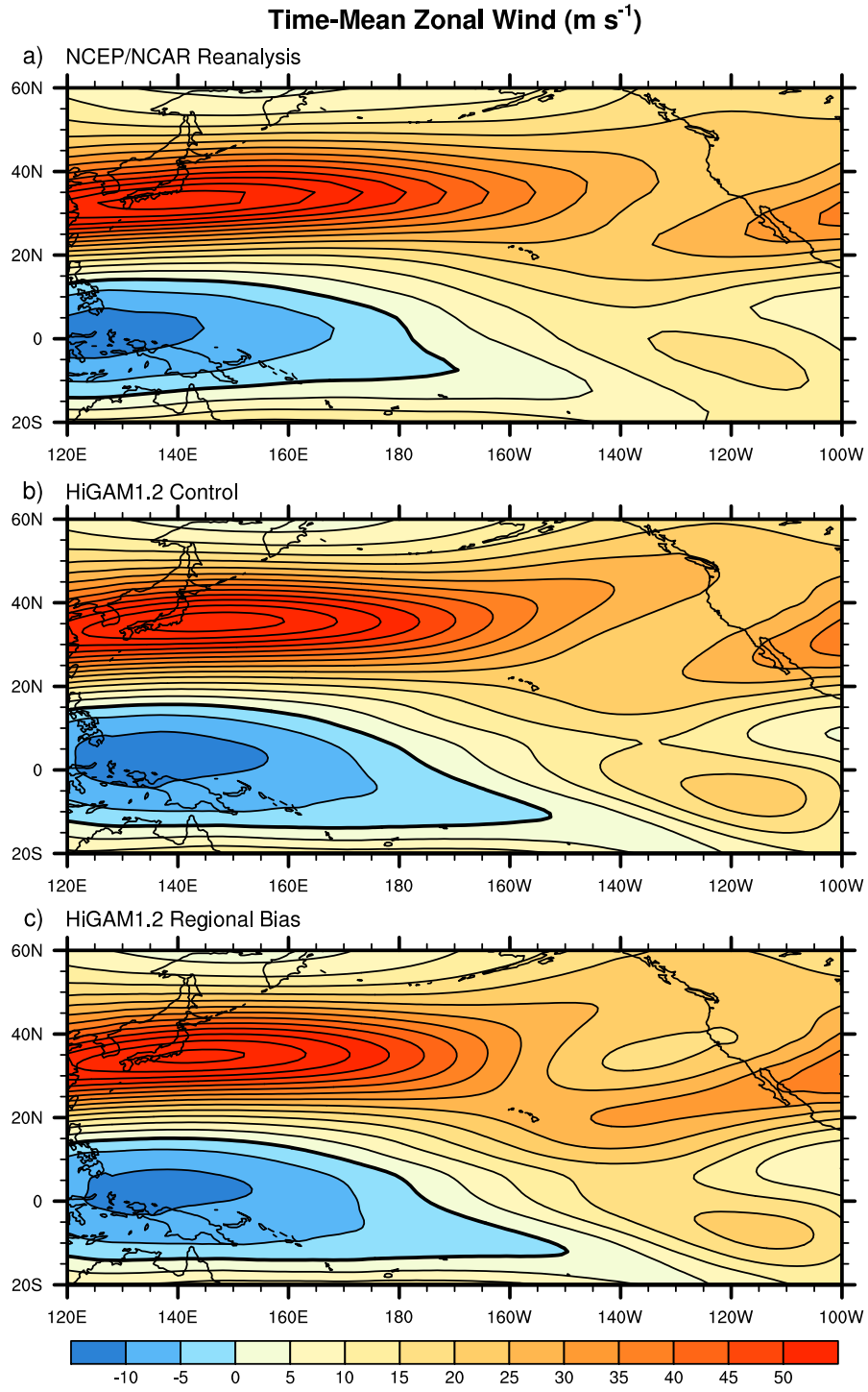

Figure 5.12: 20 year time-mean northern winter (NDJFM) zonal wind (m s^{-1}) at 200 hPa. The contour interval is 5 m s^{-1}, the zero contour is thickened. a) NCEP/NCAR Reanalysis, b) HiGAM1.2 control (CT) experiment, and c) HiGAM1.2 regional bias (RB) experiment.

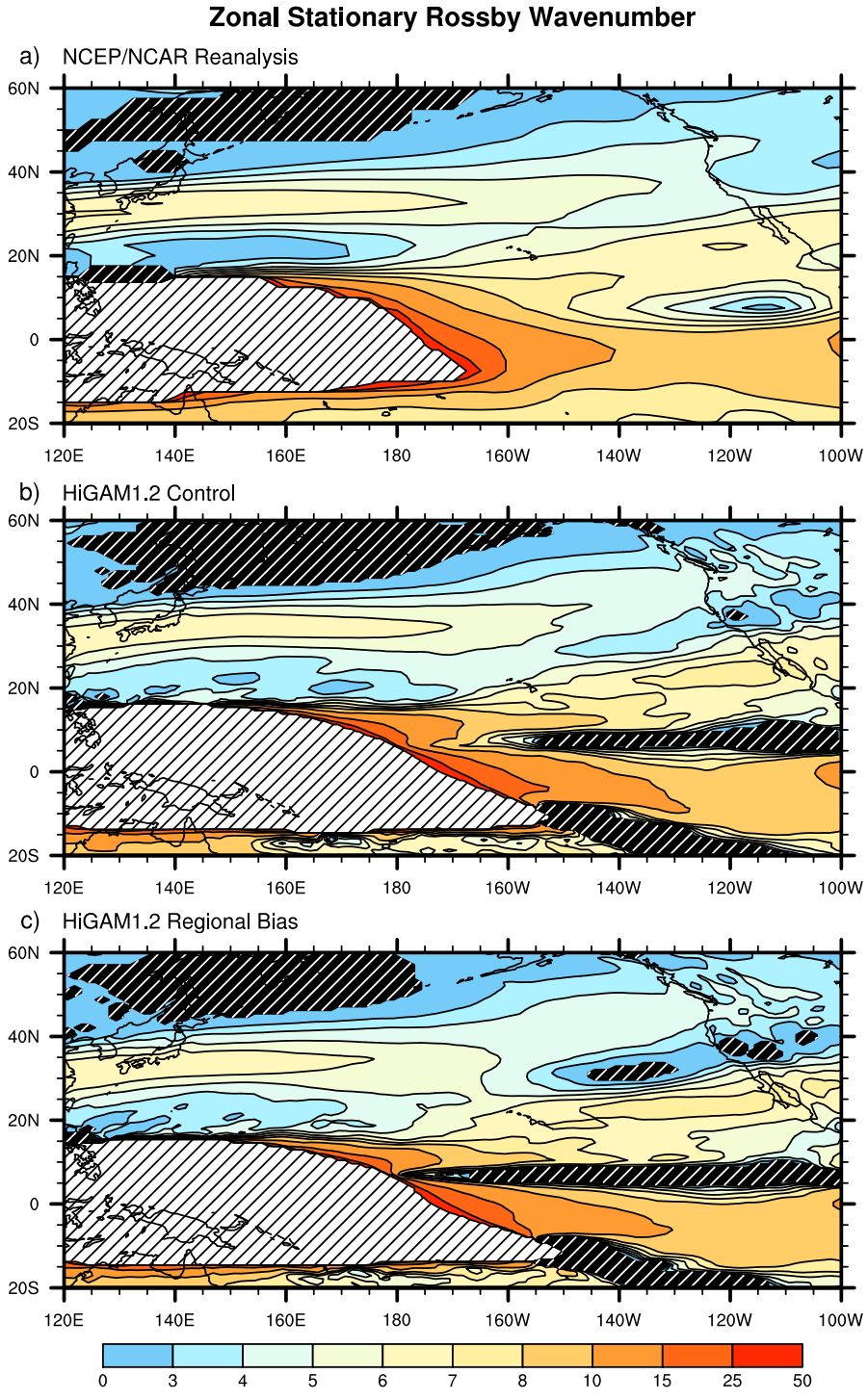

Figure 5.13: Zonal stationary wavenumber computed from northern winter (NDJFM) 20 year time-mean zonal wind at 200 hPa. Light (dark) hatching indicates areas where $\bar{u}$ (β_M) is negative. a) NCEP/NCAR Reanalysis, b) HiGAM1.2 control (CT) experiment, and c) HiGAM1.2 regional bias (RB) experiment.

American jets. This separation is characteristic of the HadGEM1.2 atmospheric basic state. However, over the western Pacific the basic state appears to be similar in the RB and CT experiments. The major dynamical difference between the HiGEM1.2 and HadGEM1.2 basic states is that waves are easily able to cross between waveguides in HiGEM1.2 and not in HadGEM1.2. Whilst Rossby waves will be partially blocked from crossing between waveguides by the area of reversed vorticity gradient, this region is much smaller than in the PT experiment and Rossby waves are likely to be able to cross between the two waveguides to the west of this region. The imposed SST bias has an isolated effect on the basic state structure, only altering a portion between waveguides downstream of the wave selection region. This suggests that the the dynamics of the RB experiment, and hence the atmospheric bridge mechanism that controls the extra-tropical response to El Niño, are likely to be much like the CT experiment, although there may be different responses downstream of the SST perturbation.

5.6.3 The extra-tropical response to El Niño

It appears that aside from differences over the eastern Pacific, the atmospheric basic state in the RB experiment is much like that in the control experiment. It seems clear from figures 5.12 and 5.13 that the SST bias has no influence over the western Pacific. Although the effect of the SST bias seems isolated, there may be some downstream effects evident in the atmospheric response.

Figure 5.14 shows regression maps of anomalous 200 hPa stream function against the EP index for observations, the CT experiment, and the RB experiment. The top two panels are as in figure 5.8. Over the North Pacific and North America the stream function anomalies in the RB experiment are much like those in the CT experiment in terms of size, shape, and location. The dipole pattern of stream function anomaly over western Europe and North Africa is shifted to the North in the RB experiment compared to the CT experiment. Generally the global atmospheric response in the RB experiment appears similar to the CT experiment.

As in section 5.5, vorticity regression maps are used as a companion diagnostic to stream function. This is particularly helpful when considering differences due to a small perturbation in the natural SST forcing. Regression maps of anomalous vorticity at 200 hPa

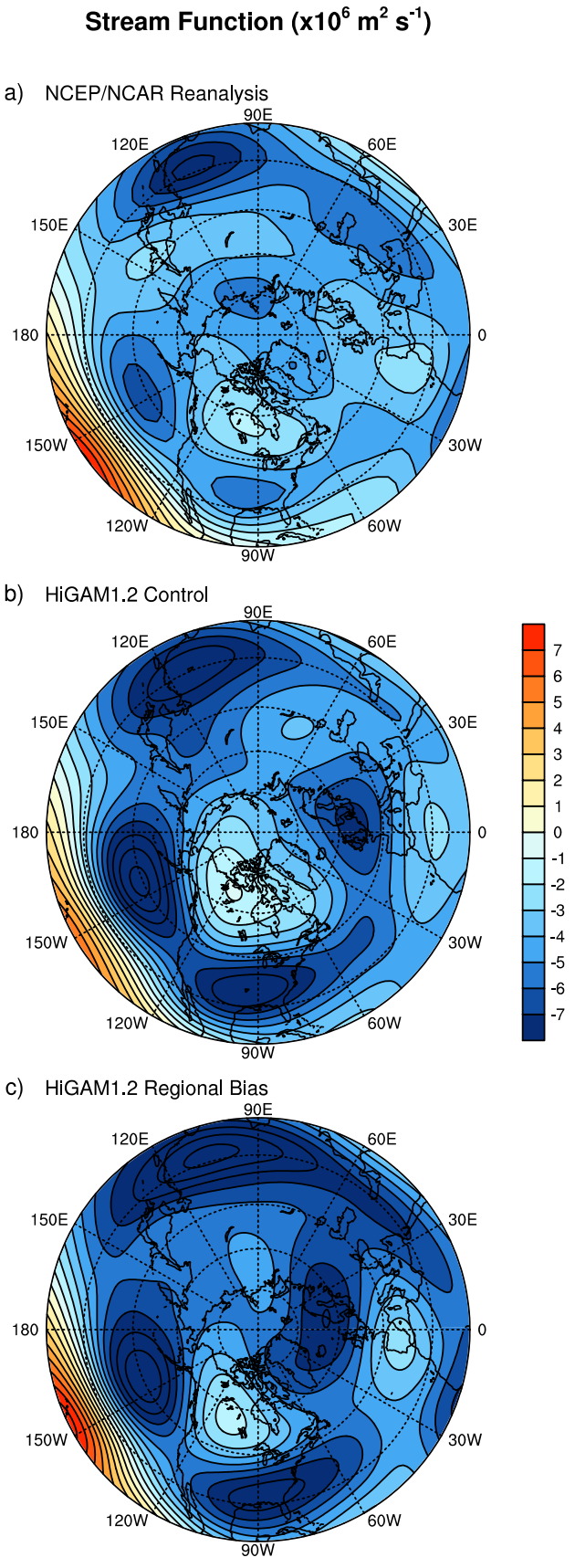

Figure 5.14: Northern winter (NDJFM) 200 hPa stream function ($m^2\ s^{-1}$) anomaly patterns associated with a 1 °C departure of the EP index. The contour interval is $10^6\ m^2\ s^{-1}$. a) NCEP/NCAR Reanalysis, b) HiGAM1.2 control (CT) experiment, and c) HiGAM1.2 regional bias (PT) experiment.

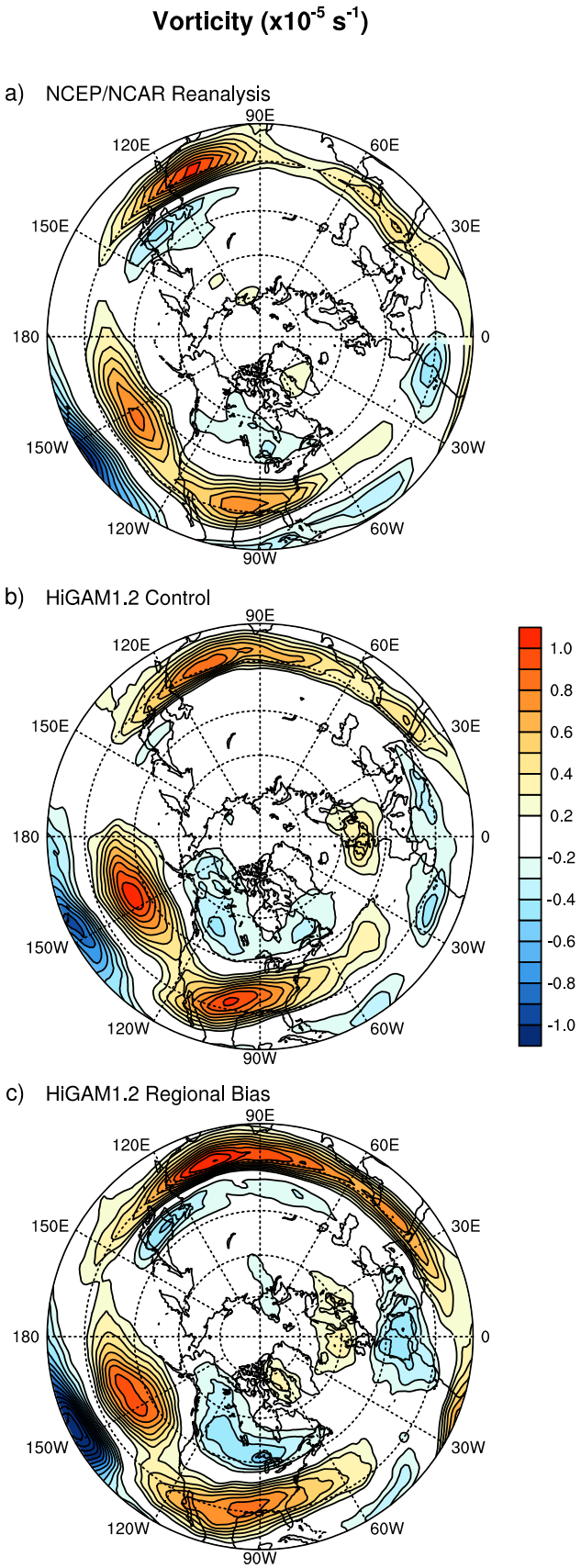

Figure 5.15: Northern winter (NDJFM) 200 hPa vorticity (s^{-1}) anomaly patterns associated with a 1 °C departure of the EP index. The contour interval is 10^{-6} s^{-1}. Contours between -2 and 2×10^{-6} s^{-1} are omitted. a) NCEP/NCAR Reanalysis, b) HiGAM1.2 control (CT) experiment, and c) HiGAM1.2 regional bias (RB) experiment.

for observations, the CT experiment, and the RB experiment are shown in figure 5.15. The top two panels are as in figure 5.9. Over the PNA region there is little difference between the RB and CT experiments. There is a small difference in the way the two positive vorticity anomalies over the North Pacific and North America join, as we might expect from the isolated differences in basic state in that region. However, it is clear that aside from this local effect and a northward displacement of the vorticity dipole over western Europe and North Africa, there is little difference between the RB and CT experiments downstream of the imposed SST bias.

Given the similarity of the upper tropospheric responses in the RB and CT experiments, it is expected that the surface wind anomalies are also similar. Regression maps of surface wind anomaly for observations, the CT experiment, and the RB experiment are shown in figure 5.16. The top two panels are as in figure 5.10. As expected there is very little difference between the anomaly patterns from the RB and CT experiments. There is a slight change in the shape of the anomalous surface circulation in the RB experiment, having no discernible tilt, compared with the slight westward tilt of this circulation anomaly in the CT experiment. The surface wind anomalies are deemed to be statistically significant in the same locations and have similar strengths across the Pacific domain. There is nothing in the RB experiment anomaly pattern that suggests that any of the physics of the atmospheric bridge mechanism, including the locations of extra-tropical SST anomalies due to El Niño, would be changed due to the presence of the regionally imposed SST bias.

5.6.4 Summary

The RB experiment has shown us that the presence of a relatively small area of SST bias can affect the atmospheric basic state, and that the separation of the North American and Asian jet waveguides in this region in HadGEM1.2 is likely to be caused partly by the presence of this particular SST bias. The separation of the waveguides in the region local to the imposed SST bias is much like that in HadGEM1.2. However, this separation occurs downstream from the wave selection region where the waveguides have already merged. Thus the effect of this change in the atmospheric basic state is very local and does not have any global influence. It seems likely that the erroneous atmospheric basic state in HadGEM1.2 is not the direct result of one or two regions of SST bias, but rather it is the

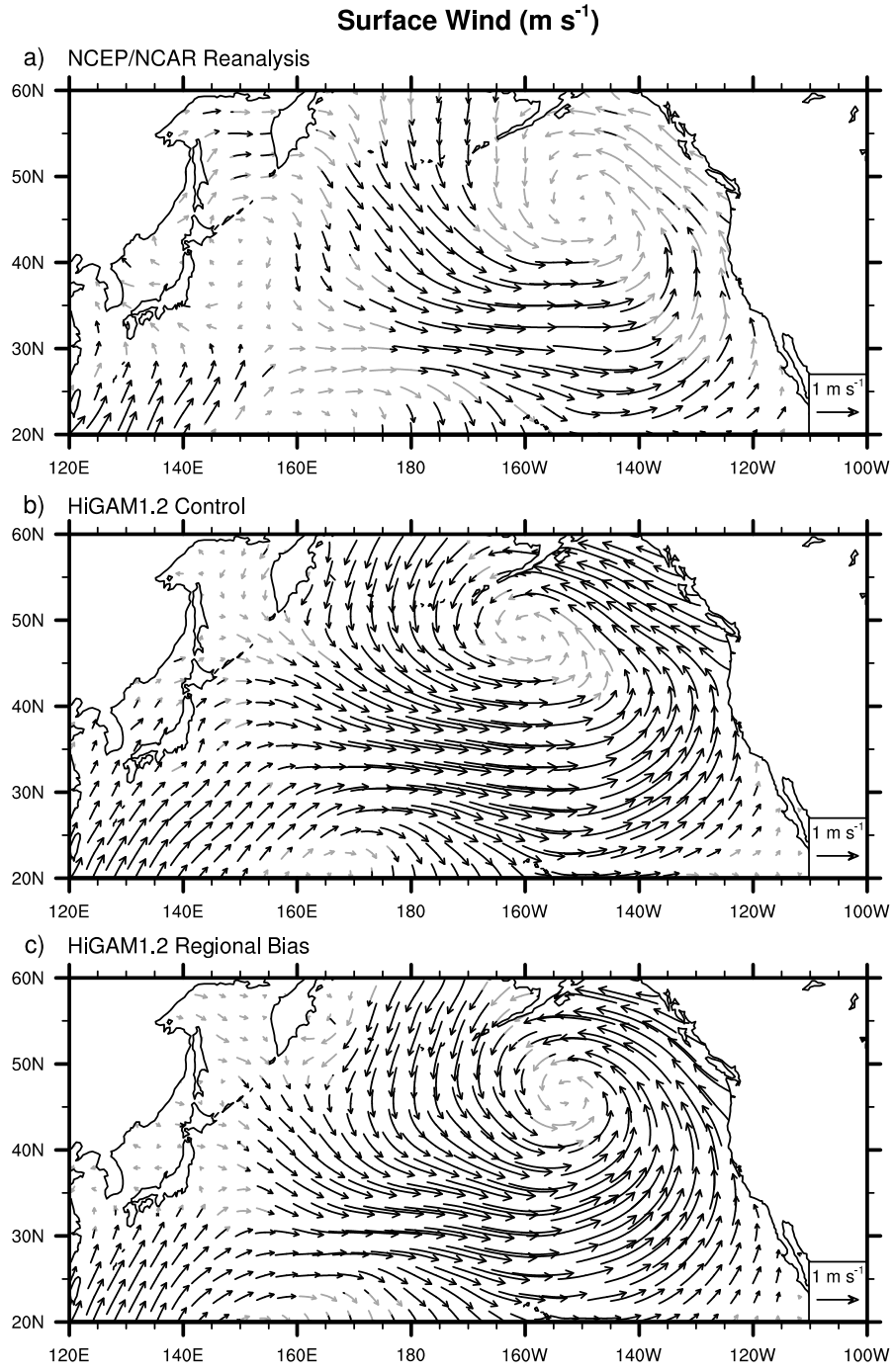

Figure 5.16: Northern winter (NDJFM) surface wind (m s^{-1}) anomaly patterns associated with a 1 °C departure of the EP index. a) NCEP/NCAR Reanalysis, b) HiGAM1.2 control (CT) experiment, and c) HiGAM1.2 regional bias (RB) experiment.

mean state over the whole Pacific basin that is at fault.

5.7 Discussion

The performance of the high resolution atmosphere model HiGAM1.2 with respect to the atmospheric bridge mechanism introduced in chapter 3, both in a control configuration and with perturbed SST boundary conditions has been analysed. The aim is to show that with suitable perturbations to the climatological SST boundary conditions, the high resolution atmosphere can be made to reproduce the incorrect atmospheric response to El Niño observed in HadGEM1.2.

The control configuration simulates atmospheric basic state, and the extra-tropical response that propagates on it, in a realistic manner. This, and the analysis of the HiGAM1.1 control simulation in chapter 4, confirms that there are no serious systematic errors in the atmospheric model component that would impede the realistic simulation of the extra-tropical response to El Niño in a coupled configuration.

When the SST boundary conditions are perturbed so as to impose the global climatological SST difference between HadGEM1.2 and HiGEM1.2 onto the observed SST forcing, HiGAM1.2 produces an unrealistic atmospheric basic state much like that in HadGEM1.2. The atmospheric response to El Niño that propagates on this basic state is considerably different to the response under natural SST forcing. This demonstrates that errors in the SST forcing for HadGAM1.2 can be responsible for the incorrect atmospheric basic state. This provides more evidence that it is not atmospheric resolution that is preventing HadGEM1.2 from realistically simulating the extra-tropical response to El Niño. A more likely cause is lack of resolution in the ocean, which allows biases in the climatological state of the ocean to be produced, that is in turn responsible for the incorrect atmospheric basic state and poor simulation of extra-tropical response to El Niño in HadGEM1.2.

When a more localised SST bias from HadGEM1.2, one that is not evident in HiGEM1.2, is included in the SST forcing HiGAM1.2 produces a split waveguide structure over the eastern Pacific. However, the main waveguides merge over the central Pacific, meaning the local splitting effect does not have a significant effect on the overall dynamics of the extra-tropical response to El Niño. Although imposing this specific bias induced a

feature in the atmospheric basic state that is similar in some respects to the corresponding feature in HadGEM1.2, it does not appear that an isolated SST bias could cause the majority of the error in the HadGEM1.2 basic state. It is more likely that the combination of multiple SST biases are responsible.

It may not be possible to determine which SST biases are most influential on the atmospheric basic state. Certainly it is difficult to test this using the same methodology used here. Imposing a global or localised SST bias is relatively straightforward, the former imposes conditions like those in HadGEM1.2 and the latter tries to understand a small component of the unrealistic atmospheric basic state. However, imposing multiple or larger scale regional biases would mean there is a good chance of significantly altering the Pacific circulation in such a way that does not happen in HadGEM1.2. Doing so would mean you are no longer just studying a small component of the bias to understand its effect (as in the regional bias experiment here) but are potentially introducing undesirable side effects and physics that are unlike the physics in either HadGEM1.2 or the observed atmosphere. For example, imposing an SST bias only in the western Pacific would alter the Walker circulation, introducing significant errors that are not components of the error in HadGEM1.2, but rather are errors due to new physical constraints put upon the system.

This work has shown that the unrealistic atmospheric basic state in HadGEM1.2, which has horizontal resolution typical of the models used in the AR4 climate change assessment, is caused by errors in the oceanic component of the model. When the resolution of the oceanic component is improved as in HiGEM1.2, there is a better representation of the upper ocean and SST in particular. This improvement to the climatological SST allows the atmospheric basic state to develop realistically and hence allows the extra-tropical response to El Niño to occur in a realistic way. This emphasizes a key point in climate modelling, showing that it is critical to simulate the long term climatological behaviour of the ocean and atmosphere in order to be able to realistically represent climate variability.

Chapter 6

The effect of climate change on the extra-tropical response to El Niño

In this chapter the effect of climate change, due to increased concentration of atmospheric carbon dioxide (CO_2), on the extra-tropical response to El Niño is studied.

6.1 HiGEM climate change experiment

In this chapter we will examine a climate change experimental configuration of HiGEM1.1. This experiment is similar to the control experiment discussed in chapter 4 (*Roberts et al.*, 2009), but with altered atmospheric carbon dioxide (CO_2) forcing. The experiment begins with atmospheric CO_2 concentrations based on observed modern day concentrations (345 ppm), as in the HiGEM1.1 control experiment. Starting from model year 30, the concentration of atmospheric CO_2 begins to be increased by 2% per year, until a maximum concentration of 4 times the initial value (1380 ppm) is reached in model year 100. After model year 100 the atmospheric CO_2 concentration is stable at 4 times the initial concentration for the rest of the integration, which is 130 years in total.

This experiment performs a large increase in atmospheric CO_2 concentration over a relatively short amount of time. Potentially this provides an unrealistically rapid representation of climate change. However, a large perturbation such as this provides the opportunity to understand whether or not processes such as the extra-tropical response to El Niño could be affected by climate change, and to understand the mechanisms behind any differences with a good degree of certainty.

In this chapter the core diagnostics produced in chapter 3 (EOF 1 of Pacific SST anomaly, upper tropospheric stream function, zonal stationary wavenumber) will be reproduced for the HiGEM1.1 climate change experiment. The dynamics of the atmospheric bridge teleconnection that controls the extra-tropical response to El Niño are now well understood in terms of these diagnostics, so any changes to the extra-tropical response to El Niño should be clear in them.

6.2 Understanding climate change in HiGEM

Before attempting to determine if climate change due to increased atmospheric CO_2 affects the extra-tropical response to El Niño, it is worthwhile taking time to understand the impact of increased CO_2 concentration on the mean climate. Figure 6.1 shows 50 year time-mean November–March sea surface temperature (SST) for 50 years of the HiGEM1.1 control experiment and for the last 50 years of the HiGEM1.1 climate change experiment. The difference between the climate change and control experiments is also shown.

In general there is a warming of SSTs in the climate change experiment. This result is unsurprising given the *greenhouse* effect of increased atmospheric CO_2 concentration. An important point to note is that the spatial distribution of the warming is non-uniform. The typical temperature increase is of the order of 2–3 °C, although in some areas the difference is greater than 5 °C. The strongest SST warmings are in the Arctic Ocean north of Scandinavia and Russia, the North West Atlantic Ocean in the Gulf Stream/North Atlantic current region, the North Pacific Ocean, and in the South Atlantic and South Indian Oceans. The areas of strong warming in the HiGEM1.1 climate change experiment are broadly consistent with those in a winter time multi-model mean (*Meehl et al.*, 2007). In contrast to these strong warmings, there are several areas of SST that are cooler in the climate change run than in the control. These are in the North Atlantic Ocean and the Southern Ocean. Cooling in the Southern Ocean is not consistent with the overall picture from the IPCC AR4, although some models used in the AR4 did produce this.

In the Pacific region the warming pattern can be described as El Niño-like, with more warming in the tropical eastern Pacific than the west and sub-tropical western North Pacific. This El Niño-like climate change is noted in climate change scenarios of most

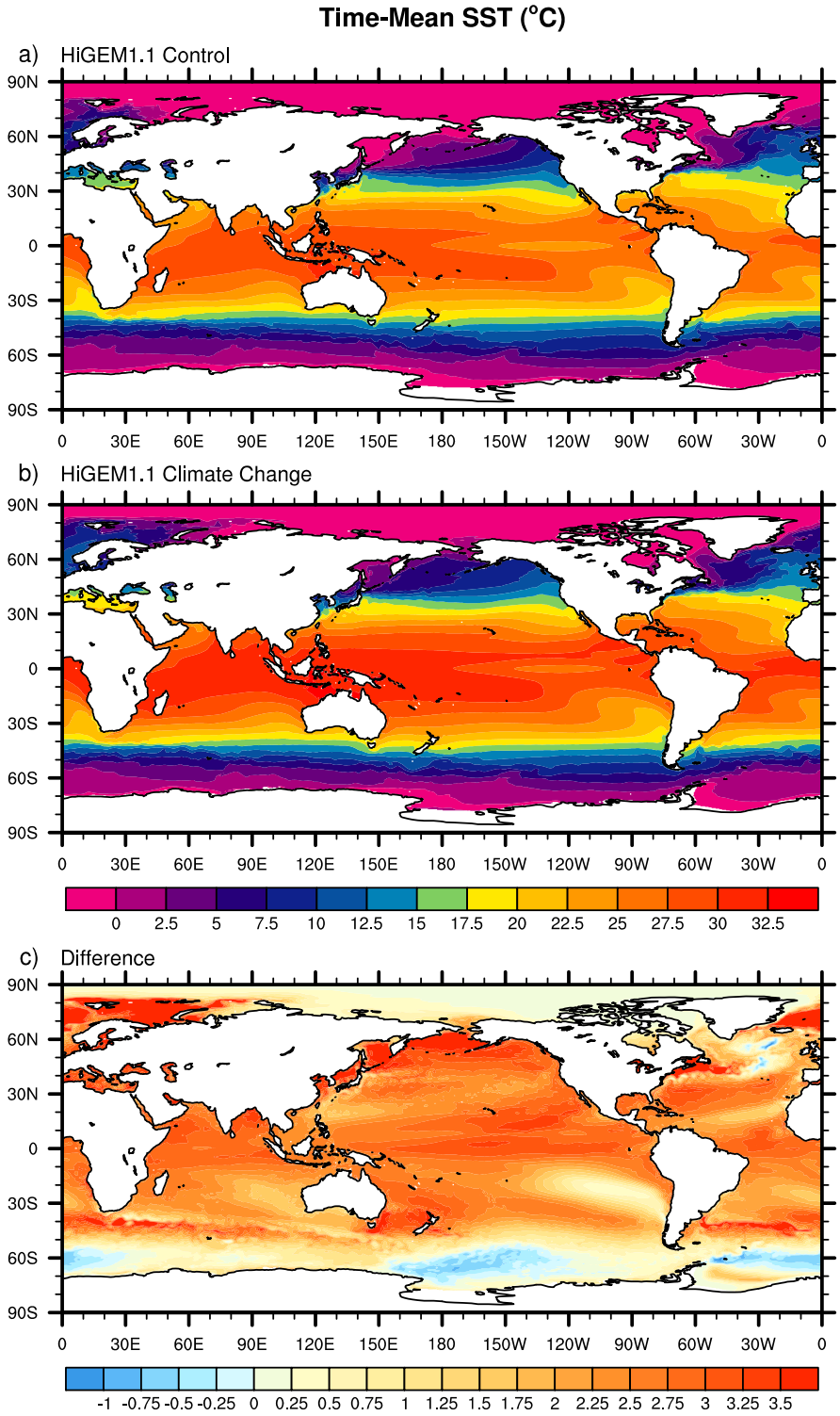

Figure 6.1: 50 year northern winter (November-March) time-mean sea surface temperature. a) years 21–70 of the HiGEM1.1 control integration, b) years 81–130 of the HiGEM1.1 climate change integration, c) the difference between the HiGEM1.1 climate change and control integrations. The contour intervals are 2.5 °C for mean SST and 0.25 °C for the difference.

IPCC AR4 models (*Meehl et al.*, 2007; *Vecchi and Soden*, 2007,). This change could be attributable to the weakening of tropical circulation, and in particular, a weakening of the Walker cell due to the increased atmospheric CO_2 concentration (*Vecchi et al.*, 2006; *Vecchi and Soden*, 2007,).

6.3 The extra-tropical response to El Niño in a climate change scenario

The diagnostic framework developed in chapter 3 is now utilised for comparing the extra-tropical response to El Niño in the HiGEM1.1 climate change experiment to that in the HiGEM1.1 control experiment. For consistency with the analysis of the HiGEM1.1 control experiment in chapter 4, a 50 year sampling period will be used. This sample comes from the last 50 years of the HiGEM1.1 climate change experiment. During the first 20 years of this sample period the atmospheric CO_2 concentration is increasing, and during the last 30 years the atmospheric CO_2 concentration is stabilised at 4 times the concentration in the control experiment.

6.3.1 The global warming trend

Due to the nature of the climate change integration it is not possible to use the analysis procedure described above directly on northern winter (November–March) anomalies. For example, performing EOF analysis on November–March SST anomalies from the climate change experiment produces a leading EOF that shows warm SST anomalies over the whole Pacific domain. This is because the leading EOF is being dominated by the climate change signal, and not the variability associated with El Niño that we are interested in. An analogous problem would occur when using the regression technique on any anomaly field. Therefore, in order to understand the SST variability associated with El Niño under climate change, the actual climate change signal must be removed from anomaly data prior to analysis.

The solid blue line in figure 6.2a shows the leading principal component time series (PC) associated with the leading EOF of November–March SST anomaly. There is a general positive trend in PC 1, which is the global warming signal due to the increasing

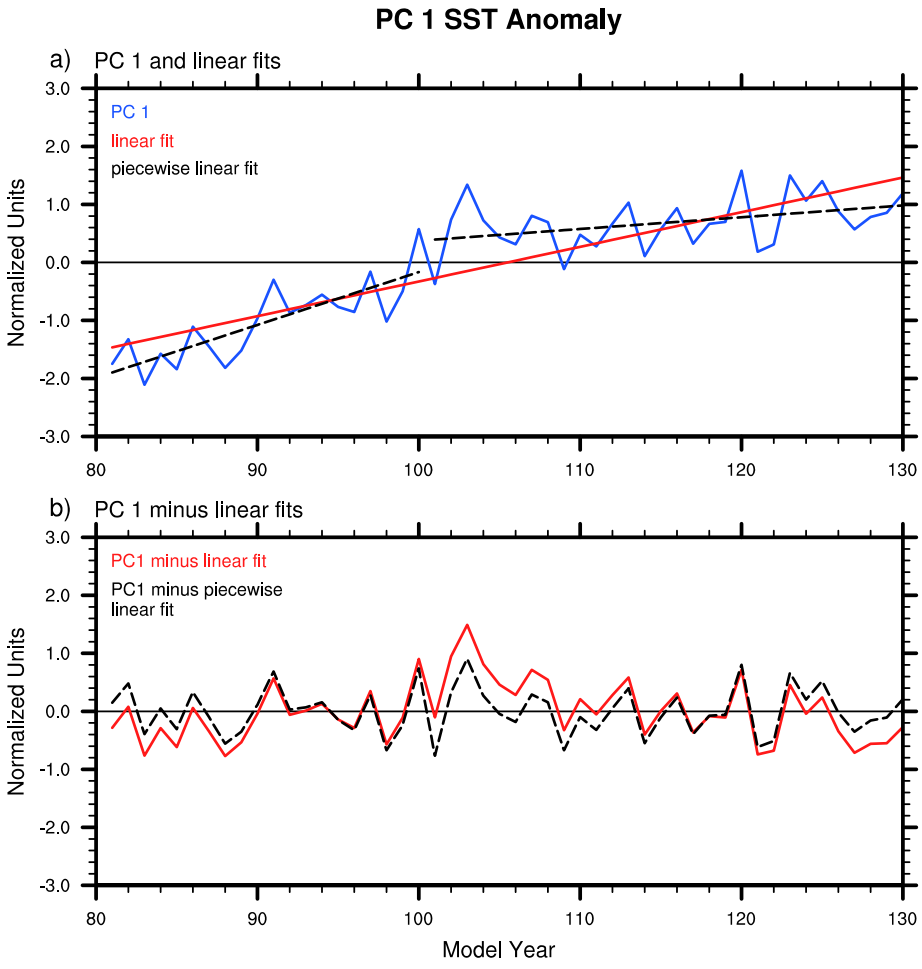

Figure 6.2: The leading principal component time series associated with EOF 1 for EOF analysis of northern winter (November-March) sea surface temperature anomaly a) solid blue line, and the linear fits for the full time series (solid red line) and the partitioned time series (dashed black lines). b) minus the full linear fit (solid red curve) and minus the partitioned fits (dashed black curve).

atmospheric CO_2 concentration. The warming appears to be stronger during model years 81–100, where the atmospheric CO_2 concentration is being actively increased, and weaker in subsequent years when the Earth system is still responding to increased atmospheric CO_2 concentrations even, though they are stabilised.

The solid red line shows the linear best fit to the leading PC. This linear fit could be considered a reasonable first order approximation of the global warming trend, and shows a warming of about 0.06°C per year. This linear trend only approximates the warming trend, and does not reflect the physical change that occurs between model years 100 and 101. The solid red curve in figure 6.2b shows PC 1 of November–March SST anomaly with this linear trend removed. The curve shows a cold bias at the start and end of the

time series and a warm bias in the middle. These biases are artefacts of the trend removal, which suggests that removing the linear trend of the full time series is not the best way of removing the global warming trend.

A better approximation of the warming trend can be obtained by partitioning the time series into its two physically meaningful sections: years 81–100, where the atmospheric CO_2 concentration is being increased, and years 101–130, where the atmospheric CO_2 concentration has stabilised. The linear trends for the two partitions are shown by the dashed black lines in Figure 6.2a. The idea is that the partitioned trends will better represent the warming trends in the two physically different parts of the time series. The dashed black curve in Figure 6.2b shows PC 1 with the partitioned linear trends removed. This curve does not show any noticeable bias, suggesting that this method is a more suitable way of removing the global warming signal.

Removing the piecewise linear trend from the time series at each grid point in the winter SST anomalies that are input to the EOF analysis should remove this approximately linear climate change signal, leaving other modes of variability intact. Throughout this chapter the anomalies for the HiGEM1.1 climate change experiments have had the global warming trend removed using this method, and from here on references to anomalies in the HiGEM1.1 climate change experiment refer to these de-trended anomalies.

6.3.2 Pacific SST anomalies associated with El Niño

The leading EOF of northern winter (November–March) SST anomaly for the HiGEM1.1 control experiment, and the leading EOF for de-trended SST anomaly for the HiGEM1.1 climate change experiment are shown in figure 6.3. The two EOF 1 patterns are similar. Both have a significant warm anomaly along the equator extending across the Pacific basin from the east, a significant cold anomaly in the western Pacific, and a warm anomaly around south-east Asia and Japan.

The equatorial warming in both experiments is consistent with tropical SST anomalies during El Niño. The shape of this warm anomaly is changed somewhat in the climate change experiment, becoming more equatorially constrained than in the control. This is particularly evident in the eastern Pacific. The cold anomaly in the western Pacific is stronger over a larger area in the climate change experiment, although the total area of this

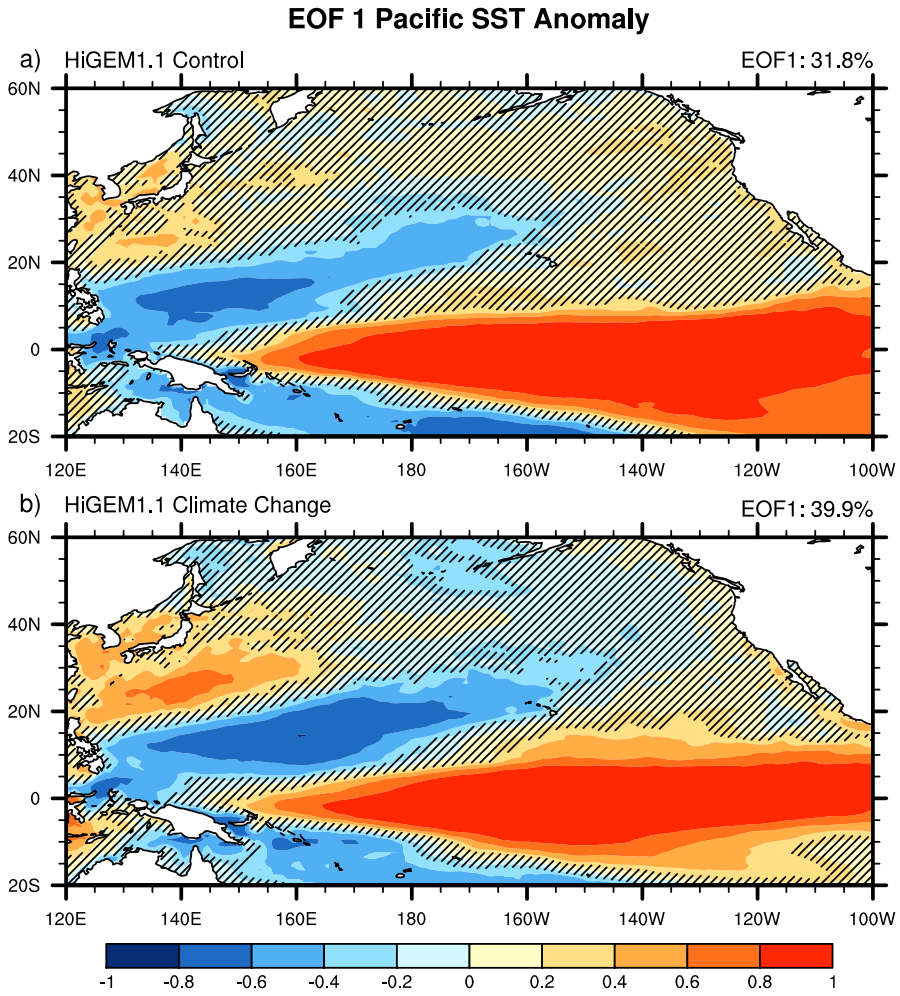

Figure 6.3: EOF 1 of northern winter (NDJFM) Pacific SST anomaly normalised by correlation. Correlations not significant at the 5% level are hatched. The contour interval is 0.2. a) HiGEM1.1 control integration (the same as figure 4.1a), and b) HiGEM1.1 climate change integration.

anomaly is comparable between the experiments. The warm anomaly around south-east Asia and Japan is stronger in the climate change experiment than in the control experiment. Since this anomaly is stronger, more of the spatial area that it occupies is deemed to be statistically significant at the 5% level. Note that the anomaly is the same sign over the same area in the control experiment but due to its strength is not deemed to be statistically significant at the 5% level.

The pattern of the leading mode of SST variability is similar in the control and climate change experiments. All of the significant extra-tropical anomalies that exist in the control experiment are present in the climate change experiment, although the extra-tropical anomalies in the climate change experiment are generally stronger than those in

the control experiment. Also, there are no additional significant anomalies in the climate change experiment that are not present in the control experiment. At this stage there are no particularly clear differences between the control and climate change experiments. This suggests that the teleconnection mechanism that controls the extra-tropical response to El Niño may behave similarly in the control and climate change experiments.

6.3.3 Atmospheric response to El Niño

The response of the atmosphere to El Niño in the control and climate change integrations is now examined. Regression maps of 200 hPa stream function anomaly for the HiGEM1.1 control experiment, and 200 hPa de-trended stream function anomaly for the HiGEM1.1 climate change experiment are shown in figure 6.4. On first inspection the two regression maps appear to be dissimilar. This is particularly evident over the Pacific region, where there is no distinct centre of circulation associated with the Aleutian low over the North Pacific in the climate change integration. However, there are similarities in other locations. For example both the control and climate change integrations have visible centres of circulation over the USA, the North Atlantic, North Africa, and eastern Asia. The stream function gradients in the climate change integration are smaller (stream function contours are further apart) which corresponds to lower wind speeds, however it does not necessarily imply that similar anomalous circulation structures are not present. In this case it is rather difficult to understand the upper tropospheric circulation anomalies associated with El Niño in terms of the stream function. Vorticity is used in place of stream function as a diagnostic to understand circulation anomalies.

Vorticity represents the same part of the flow (the rotating component) as stream function. However, vorticity can be interpreted more directly since the magnitude of vorticity can be understood to represent magnitude of rotation. This is not the case with stream function where we must consider the gradients of the stream function field in order to understand circulation strength. Regression maps of vorticity anomaly at 200 hPa for the HiGEM1.1 control experiment, and de-trended vorticity anomaly at 200 hPa for the HiGEM1.1 climate change experiment are shown in figure 6.5.

Both the control and climate change experiments have positive vorticity anomalies over North America and the north-eastern Pacific. These anomalies are weaker in the

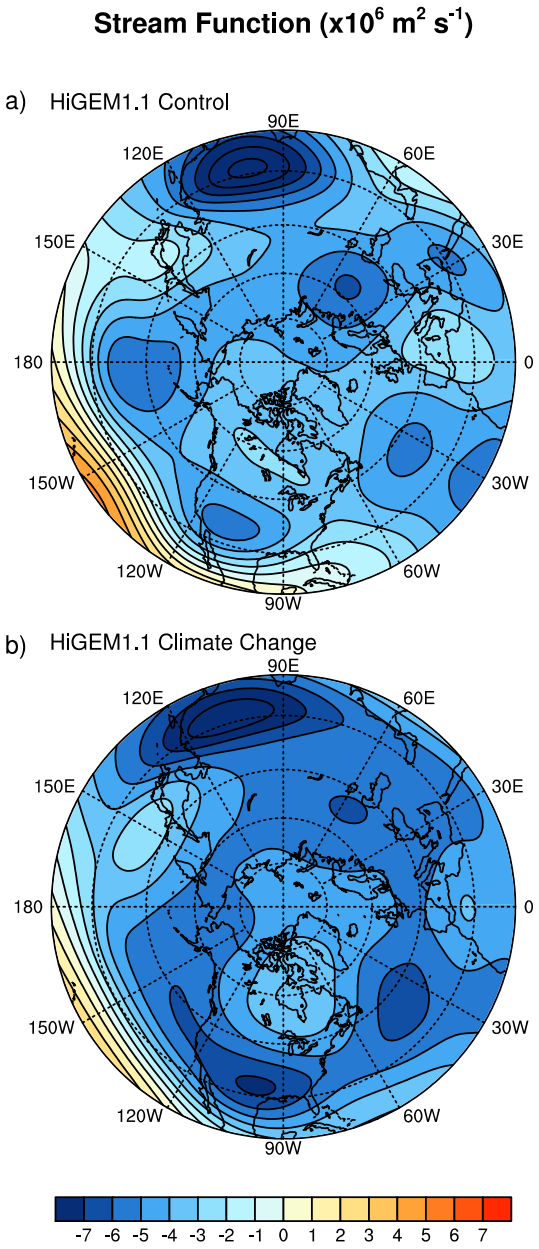

Figure 6.4: Northern Winter (NDJFM) 200 hPa stream function ($\times 10^6$ m^2 s^{-1}) anomaly patterns associated with a 1 °C departure of the EP index. The contour interval is 1×10^6 m^2 s^{-1}. a) HiGEM1.1 control integration, and b) HiGEM1.1 climate change integration.

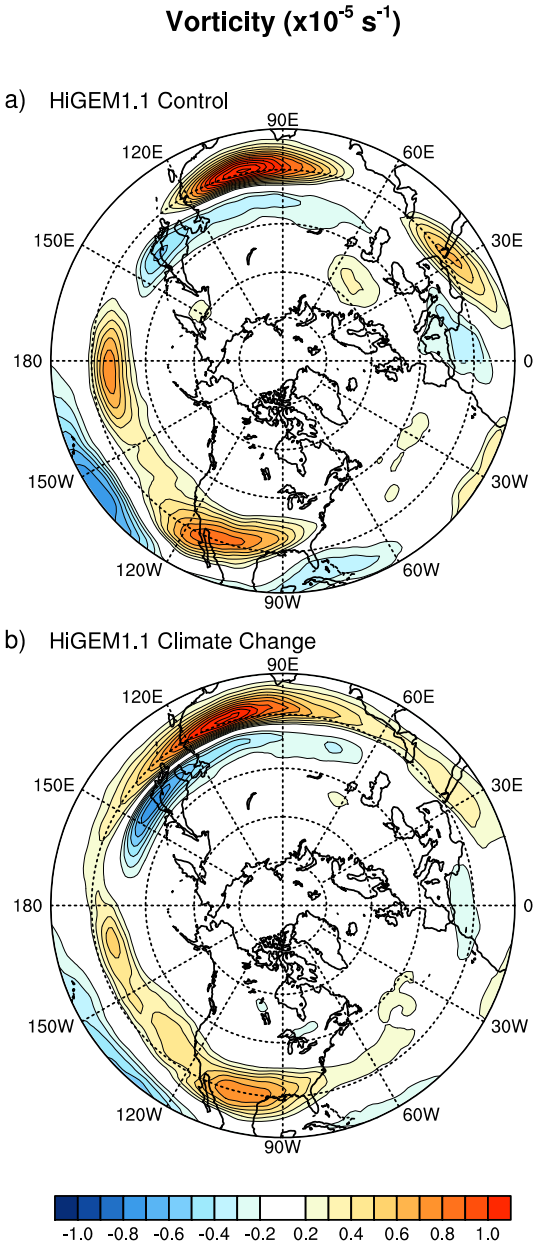

Figure 6.5: Northern Winter (NDJFM) 200 hPa vorticity ($\times 10^{-5}$ s^{-1}) anomaly patterns associated with a 1 °C departure of the EP index. The contour interval is 1×10^{-6} s^{-1} and contours from -2 to 2×10^{-6} s^{-1} have been omitted. a) HiGEM1.1 control integration, and b) HiGEM1.1 climate change integration.

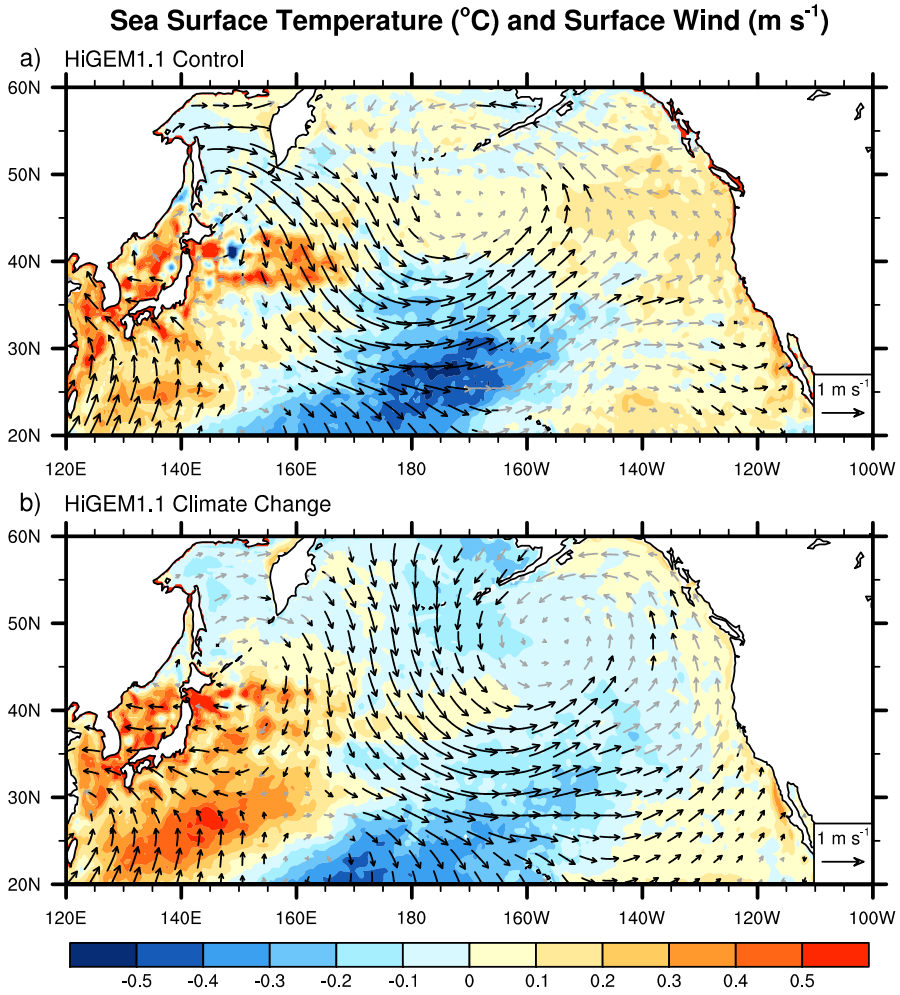

Figure 6.6: Northern winter (NDJFM) SST (colours, °C) and surface wind (arrows, m s^{-1}) anomaly patterns associated with a 1 °C departure of the EP index. The contour interval is 0.5 °C. a) HiGEM1.1 control integration, and b) HiGEM1.1 climate change integration.

climate change experiment, and shifted to the east by approximately 8° of longitude. This is consistent with the work of *Meehl et al.* (2006) who noted a weakening and eastward shift of the Aleutian low in future warmer climates. These weakened vorticity anomalies in the climate change experiment imply that the associated surface circulation anomalies will also be weaker. Elsewhere, the vorticity anomalies in the climate change experiment are generally weaker than in the control experiment, with the exception of the negative vorticity anomaly centred over Japan. This anomaly is stronger and, like the positive vorticity anomaly immediately to the south of it, more zonally constrained in the climate change experiment than in the control experiment.

Figure 6.6 shows surface wind anomalies overlaid on SST anomalies. The surface

wind anomalies allow us to understand the effect that the anomalies induced in the upper troposphere (figures 6.4 and 6.5) have at the surface. The most noticeable feature is the eastward shift of the circulation centre in the North Pacific in the climate change experiment. This is directly related to the shift in longitude of the positive vorticity anomaly in the troposphere directly above relative to the same anomaly in the control experiment.

The surface wind anomalies are significant in similar locations in the control and climate change experiments. Even though there is a large longitudinal shift in the longitude of the main circulation anomaly, the surface circulation anomaly patterns are strikingly similar. This adds weight to the interpretation of upper tropospheric vorticity anomalies being similar.

The similarity of both the upper tropospheric anomaly patterns and surface circulation anomaly patterns associated with El Niño between the HiGEM1.1 control and climate change simulations implies that the atmospheric basic state that controls the upper tropospheric anomalies will be dynamically similar in the control and climate change experiments. This is examined in the next section.

6.3.4 Atmospheric basic state

Given the similarities in the upper tropospheric and surface circulation between the control and climate change experiments in section 6.3.3, and the importance of the atmospheric basic state established in chapter 3, it seems likely that the atmospheric basic state in the climate change integration will be similar to that in the control integration. However, in chapter 5 it was shown that the oceanic mean state is a controlling factor for the atmospheric basic state, and the oceanic mean state in the climate change integration is considerably different to that in the control integration (figure 6.1).

The northern winter (November–March) 50 year time-mean zonal wind at 200 hPa is shown in figure 6.7 for the HiGEM1.1 control and climate change experiments. The extent of the mean tropical easterlies in the climate change experiment in smaller than in the control experiment. The westerly duct is also weaker over the tropical eastern Pacific. The westerly winds in the region where the Asian and North American jets meet over the North East Pacific are stronger in the climate change experiment than in the control

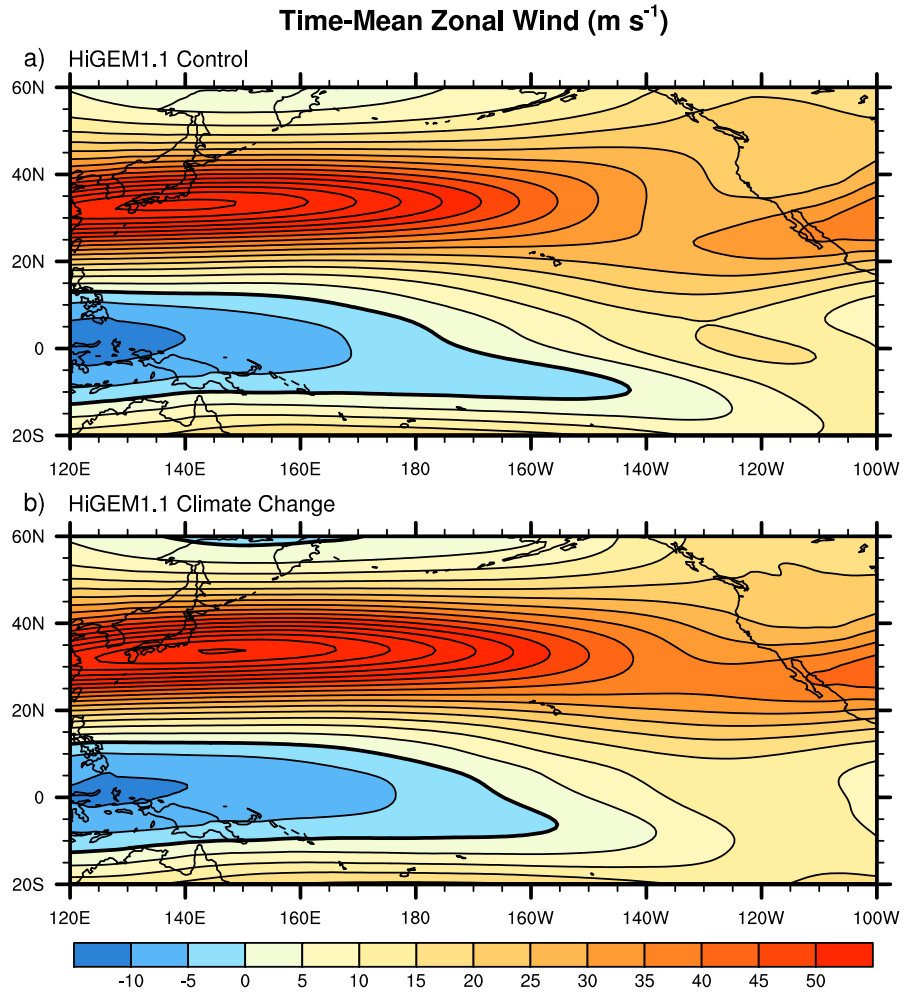

Figure 6.7: Northern winter time-mean eastward wind at 200hPa. The contour interval is 5 m s^{-1}. a) HiGEM1.1 control experiment, and b) HiGEM1.1 climate change experiment.

experiment. In the zonal mean (figure 6.8) we note that the Northern Hemisphere mid-latitude westerlies are somewhat increased in strength in the climate change experiment. This difference is relatively minor and the general structure of the midlatitude westerlies in both hemispheres appears to be similar in the climate change and control experiments.

Figure 6.9 shows the zonal stationary wavenumber computed from a 50 year time-mean of zonal wind at 200 hPa for the HiGEM1.1 control and climate change experiments. The stationary wavenumber patterns are very similar between the control and climate change experiments. The structures of the Asian jet waveguides are similar, both being of comparable strength, location, and orientation. The waveguides in both the control and climate change experiments merge together over the central North Pacific, allowing for waves to cross between the waveguides. This indicates the same dynamics as the real

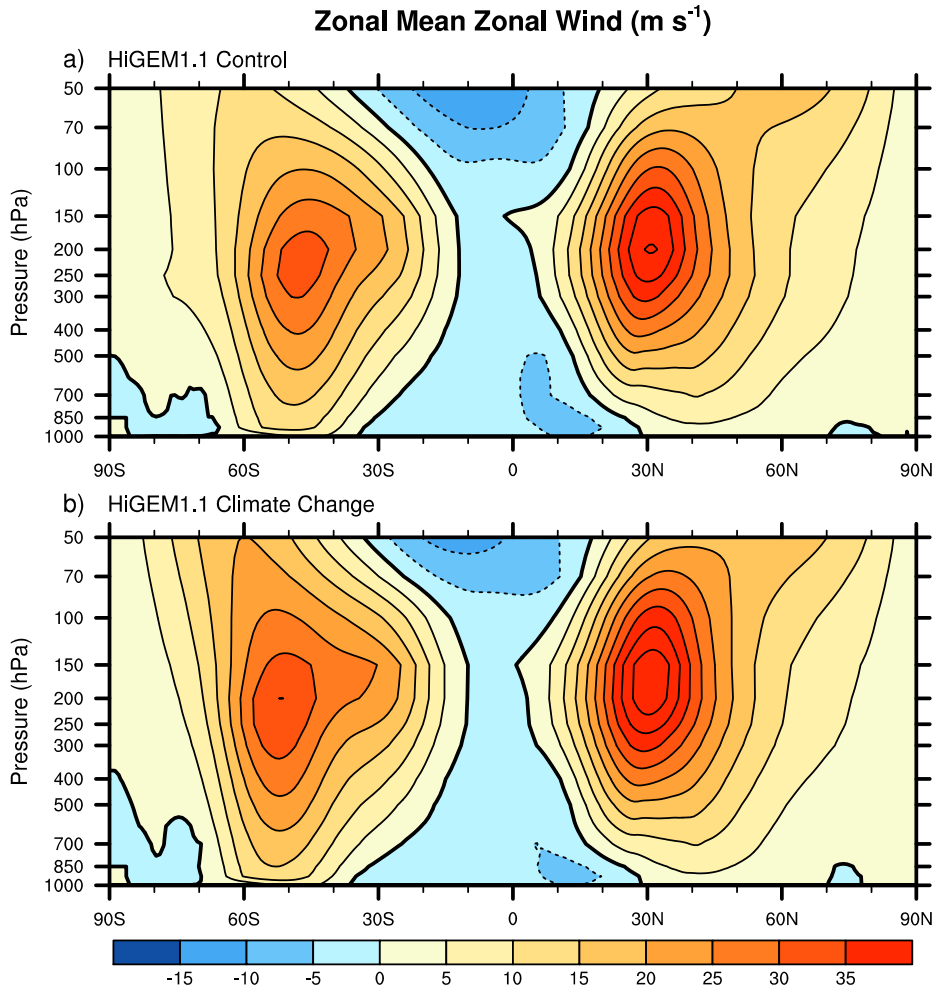

Figure 6.8: Northern winter time-mean zonal mean eastward wind. The contour interval is 5 m s^{-1}. a) HiGEM1.1 control experiment, and b) HiGEM1.1 climate change experiment.

atmosphere as discussed in chapter 3.

There are fewer areas of reversed vorticity gradient in the tropics in the climate change experiment compared to the control integration. Notably the area of reversed vorticity gradient in the tropical eastern Pacific has disappeared in the climate change integration. This could be due to the El Niño-like SST warming (figure 6.1) reducing the impact of any eastern tropical Pacific cold bias in HiGEM1.1. It could be argued that the stationary wavenumber pattern in the HiGEM1.1 climate change integration is most like the observed pattern (3.18a). This is mostly due to the disappearance of the reversed meridional vorticity gradient in the eastern tropical Pacific. However, the observed stationary wavenumber field does have an area of lower zonal wavenumber ($0 \leq K_s \leq 4$) in this region.

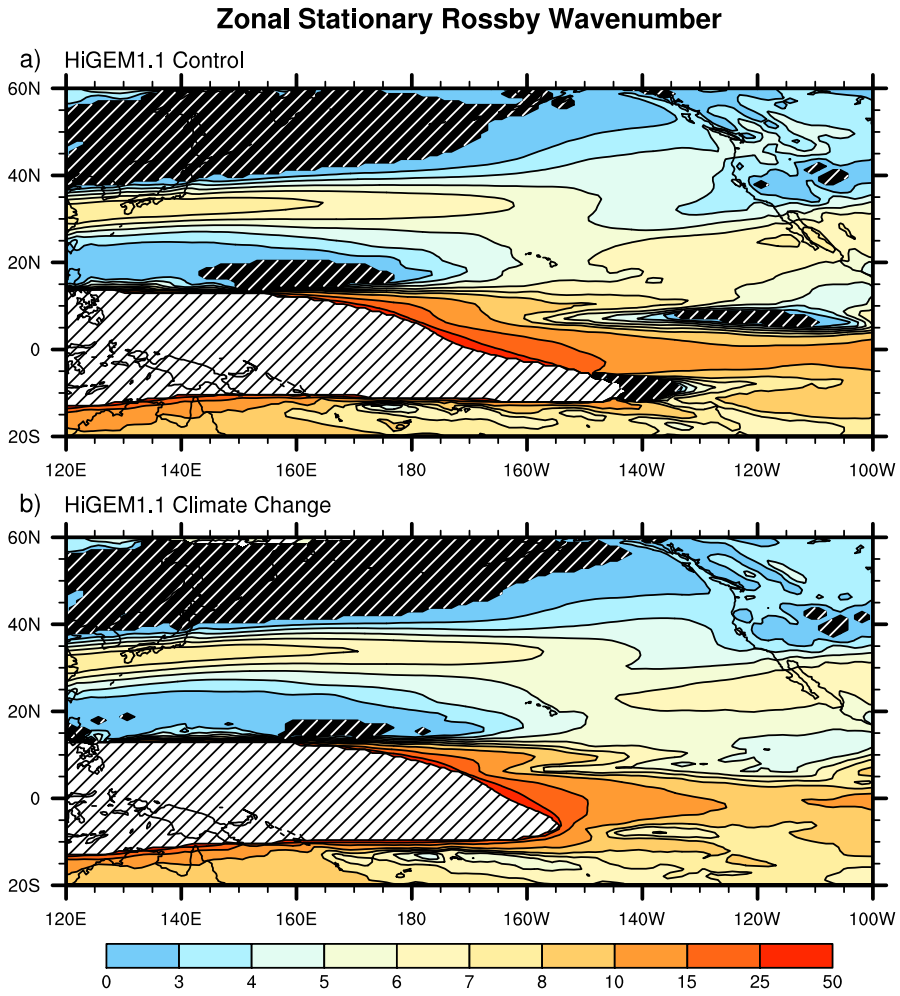

Figure 6.9: Zonal stationary wavenumber for northern winter (NDJFM) time-mean zonal wind at 200 hPa. Light (dark) hatching indicates areas where $\bar{u}$ (β_M) is negative. a) HiGEM1.1 control integration, and b) HiGEM1.1 climate change integration.

The HiGEM1.1 climate change integration has a zonal wavenumber of $K_s \geq 4$ in this region and thus is not necessarily more realistic than the control experiment or HiGEM1.2.

6.4 Rossby wave generation

The large change in mean state in the climate change experiment could have far reaching impacts on atmospheric circulation in general. Figure 6.10 shows the zonal mean meridional mass stream function, a diagnostic that shows atmospheric overturning. Either side of the equator there is a strong overturning cell, the Hadley Cell. The Hadley circulation appears to have weakened as a result of climate change forcing. This response to a global

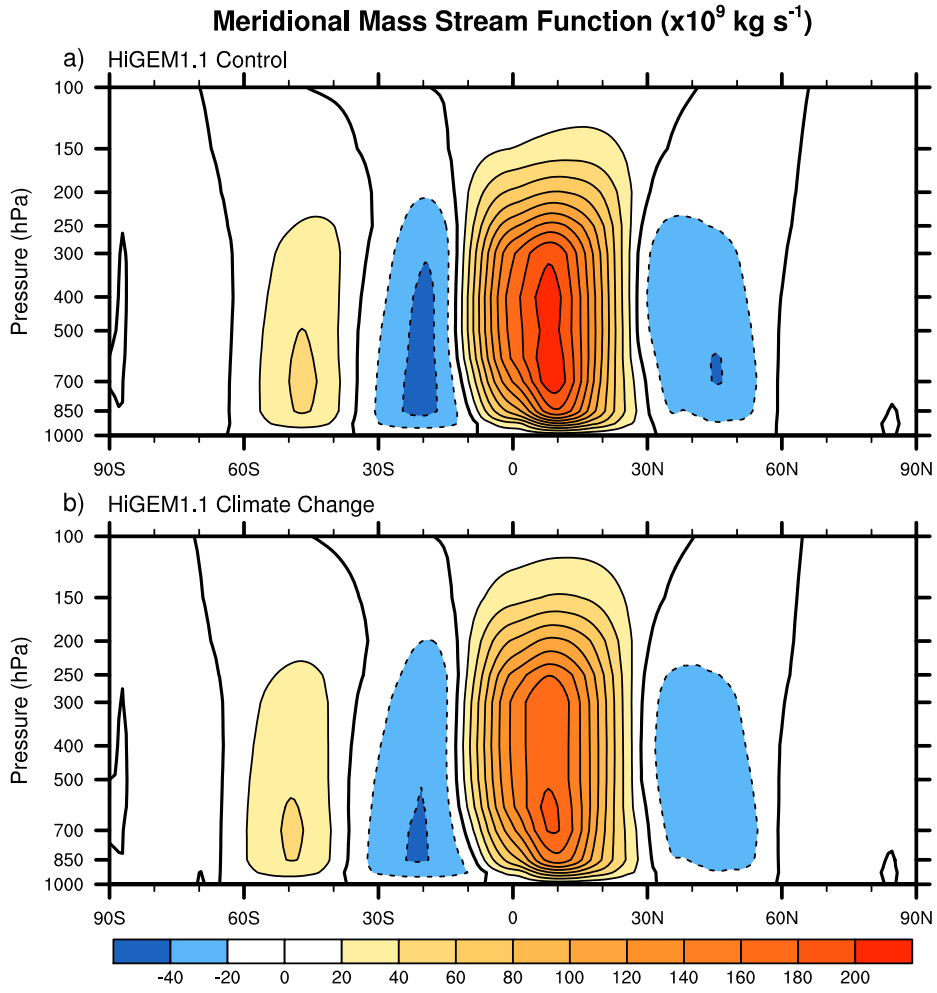

Figure 6.10: Zonal mean meridional mass stream function (10^9 kg s^{-1}) computed from the time-mean northern winter (NDJFM) meridional flow. a) HiGEM1.1 control integration, b) HiGEM1.1 climate change integration.

warming scenario is noted in many coupled models (*Tanaka et al.*, 2005) but is not consistent accross all models, and there is significant ambiguity in the observed changes and causes of changes in the Hadley circulation (e.g., *Chen et al.*, 2002; *Quan et al.*, 2004; *Mitas and Clement*, 2005). In the HiGEM1.1 climate change experiment we observe no widening of the tropical Hadley cell, a phenomenon that has been widely researched (e.g., *Hu and Fu*, 2007; *Seidel and Randel*, 2007; *Lu et al.*, 2007; *Seager et al.*, 2007; *Seidel et al.*, 2008). It seems that the large change in SST in the climate change experiment (figure 6.1) does not significantly alter the structure of the tropical circualtion, but does have some impact on the strength. Changes in strength of the Hadley circulation may have

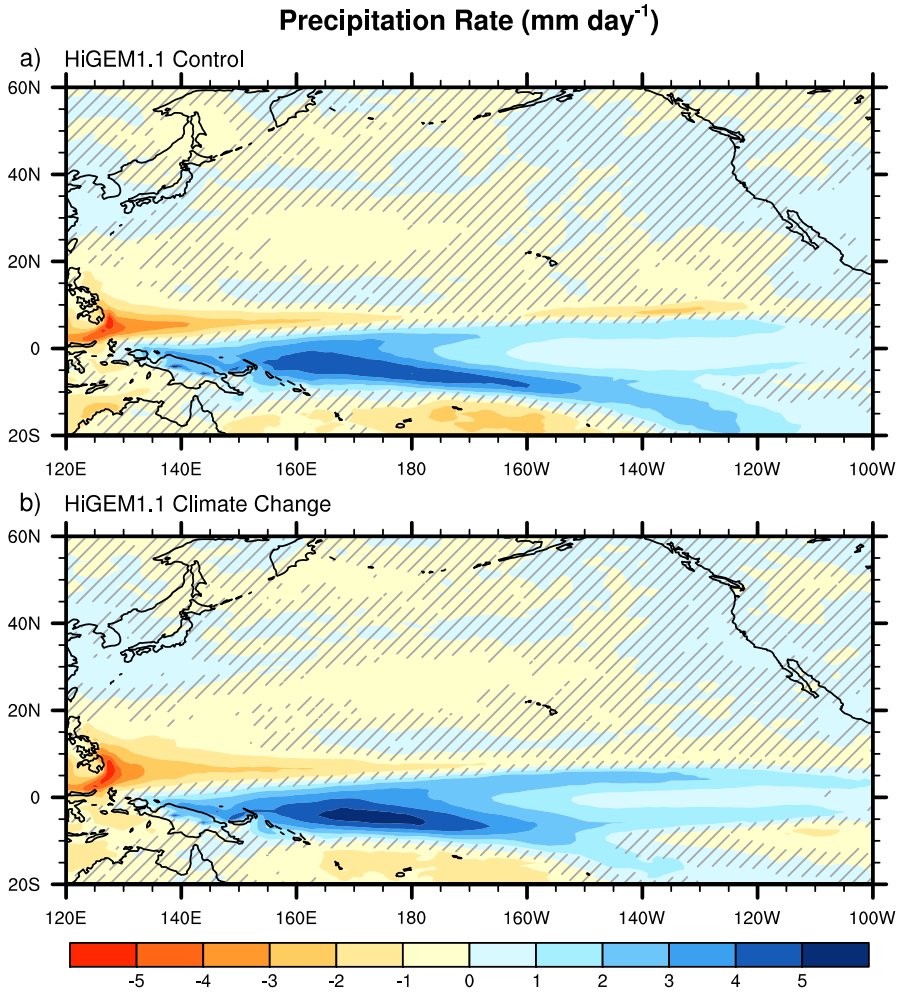

Figure 6.11: Northern winter (NDJFM) precipitation rate (mm day^{-1}) anoamly patterns associated with a 1 °C departure of the EP index. The contour interval is 1 mm day^{-1}. a) HiGEM1.1 control integration, and b) HiGEM1.1 climate change integration.

some impact on the anomalous convection that causes Rossby waves to be generated, and ultimately the extra-tropical response to El Niño.

The relatively minor differences in the basic states noted in section 6.3.4 do not allow us to explain why the upper tropospheric response (figure 6.5) in the HiGEM1.1 climate change experiment is weaker than in the control. In order to try and understand this difference we turn to the forcing diagnostics used in earlier chapters, namely precipitation rate and the Rossby wave source (RWS). Regression maps of precipitation rate (figure 6.11) show tropical anomalies that are similar between the control and climate change experiments: positive anomalies in the central tropical Pacific, and negative anomalies in the vicinity of the Pacific warm pool. These are indicitive of the eastward movement of the

Pacific warm pool during El Niño. In the eastern tropical Pacific in the HiGEM1.1 climate change experiment the positive precipitation anomalies are more equatorially confined, consistent with the distribution of warm SST anomalies (figure 6.3) in that region. The tropical anomalies in the climate change experiment have greater magnitude than in the control experiment. Away from the tropics there is a negative anomaly between 20–30°N, which would typically be associated with anomalous upper level convergence. In the climate change experiment this anomaly extends further to the east than in the control, which may have implications for the generation of Rossby waves over the North Pacific.

Figure 6.12 shows regression maps of RWS anomaly over the North Pacific. The most obvious difference between the control and climate change experiments is the greater eastward extent of the positive anomaly over the North Pacific in the climate change experiment. It seems likely that this eastward shift could explain the eastward shift of the upper tropospheric anomalies (figure 6.5) in the climate change experiment. Aside from this difference there are other potentially important differences. The positive RWS anomaly seen over the eastern Pacific at around 25°N in the control experiment is considerably weaker in the climate change experiment. This anomaly is also less connected to the previously mentioned positive anomaly in the North Pacific in the climate change experiment. These changes are highly likely to have an impact on the magnitude of the Rossby wave anomalies they induce, and could go some way to explaining the weaker upper tropospheric response of the climate change experiment.

6.5 Conclusions

The extra-tropical response to El Niño in a high resolution model under a climate change scenario is compared to that in an equivalent control experiment. The spatial distribution of extra-tropical SST anomaly during El Niño appears almost unchanged in the climate change experiment, with only minor discrepancies involving the magnitude of the SST anomaly. Upper tropospheric circulation anomalies are compared using stream function and vorticity as diagnostics. In the North Pacific region these circulation anomalies are weaker in the climate change experiment and shifted to the east somewhat. However, the general pattern of upper tropospheric anomalies is similar in both the control and climate

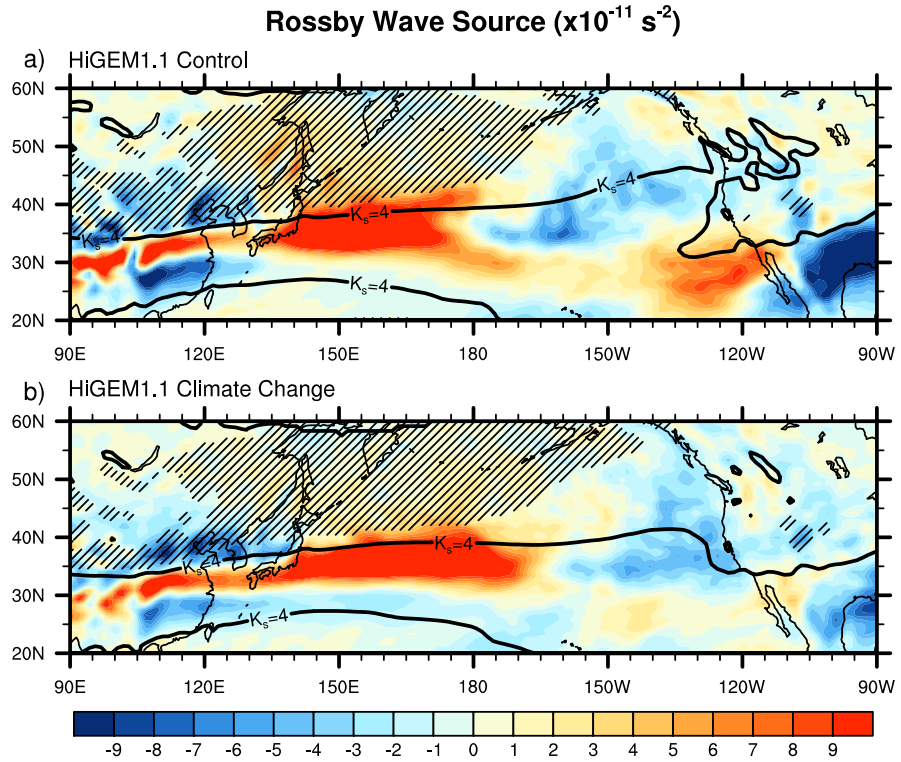

Figure 6.12: Rossby wave source anomaly patterns (colors, 10^{-11} s^{-2}) associated with a 1 °C departure of the EP index. The contour interval is 10^{-11} s^{-2}. Stationary wavenumber $K_s = 4$ is shown by a thick contour. Hatching indicates regions with reversed absolute vorticity gradient as in figure 6.9. a) HiGEM1.1 control integration, and b) HiGEM1.1 climate change integration.

change experiments. Regression maps of surface wind anomaly (figure 6.6) showed significant anomalies in similar locations in both the control and climate change experiments. This showed that the eastward shift of the circulation anomaly over the North Pacific has very little effect of the extra-tropical response to El Niño.

The atmospheric basic state is dynamically very similar in the control and climate change experiments. The main waveguides in the North Pacific have similar locations and orientations, although the North American waveguide is weaker in the climate change experiment. Rossby waves are still able to pass between the two waveguides, leading to similar dynamics and ultimately a similar extra-tropical response to El Niño. The mean zonal winds under the climate change scenario are somewhat stronger than in a control climate. However this seems to have a negligible effect of the waveguide structure that determines the propagation characteristics of Rossby waves. The stationary wavenumber diagnostic does not enable further understanding of the eastward shift in upper tropospheric

anomalies, or their decreased magnitude in the climate change experiment. Analysis of precipitation and the Rossby wave source diagnostic, both indicators of the forcing felt in the upper troposphere due to anomalous SSTs, suggested that in the case of climate change forcing, changes to the way Rossby waves are generated are likely to be more important that direct changes to the atmospheric basic state on which they propagate. It is possible that the eastward shift of the positive vorticity anomaly over the North Pacific in the climate change experiment could be counteracting the noted westward shift in the same anomaly from HiGEM1.2 to HiGEM1.1 (chapters 3 and 4, figures 3.7 and 4.2). It is therefore important to question whether such a change in response would exist in a climate change integration of HiGEM1.2? The different response in the HiGEM1.1 climate change experiment appears to be well explained by a change in the forcing for Rossby wave generation. Potential causes for this difference have been identified, for example changes to the Hadley circulation. The degree to which this change in response can be explained strongly suggests that it may be a robust change. However it is of course not possible to know for sure without producing an equivalent climate change experiment for HiGEM1.2.

This study has shown that under a climate change scenario there is a change in the magnitude and spatial pattern of the extra-tropical response to El Niño. The scale of the difference is small compared to the difference between the high horizontal coupled model HiGEM1.2 and its lower horizontal resolution configuration HadGEM1.2 (chapter 3). *Zelle et al.* (2005) noted that in order to predict the behaviour of the tropical component of El Niño in a future warming scenario, it is necessary that the model used for predictions be able to simulate El Niño realistically to begin with. The same argument follows for the extra-tropical response to El Niño. The HiGEM1.1 control experiment simulates this mechanism fairly realistically, and a change in the mechanism in a future warming scenario is observed. Since the observed change is small compared to the change due to lower horizontal resolution, it would not be possible to use the lower resolution configuration HadGEM1.1 to predict the behaviour of the extra-tropical response to El Niño in a future warming scenario. Any changes in the teleconnection mechanism that may be due to increased atmospheric CO_2 concentration would likely be overshadowed by the general poor quality of the simulation of the teleconnection mechanism.

There is a lot of uncertainty surrounding the behaviour of El Niño in a future warming climate (*Meehl et al.*, 2007; *Collins et al.*, 2010). *Yeh and Kirtman* (2006) found that changes in El Niño amplitude in $4 \times CO_2$ projections is highly model dependent. Similar results were produced by the multi-model studies of *van Oldenborgh et al.* (2005) and *Merryfield* (2006). Individual models were found to have statistically significant changes in El Niño amplitude, but in the forms of both increasing and decreasing amplitudes. Here we have shown that there is little change in the extra-tropical response to El Niño in a warming scenario. However, we must bear in mind the uncertainty about the behaviour of El Niño itself in a warming scenario, and how this might relate to the extra-tropical response.

Chapter 7

Preliminary investigations into decadal variability in the Pacific

In this chapter, a preliminary examination of decadal scale variability in the North Pacific ocean is conducted. Decadal scale variability in both high and low resolution models is considered, in an attempt to understand whether or not the models can simulate decadal scale variations in a realistic manner. The question of whether horizontal resolution affects the ability to simulate these processes, or the fidelity of any simulation, is addressed. An attempt is made to understand the physical mechanisms that are involved in decadal scale variability in the high resolution coupled model.

7.1 Introduction

Many authors have noted decadal scale sea surface temperature (SST) variability in the North Pacific Ocean. There has been particular interest in the so called 'climate shift' of 1976/77, where SSTs in the North Pacific shifted from generally warmer than average to generally cooler than average. *Trenberth and Hurrell* (1994) determined that this climate shift was of tropical origin. *Deser et al.* (1996) concluded that the atmosphere played a dominant role in forcing the interdecadal change in SST at this time, but did not rule out the possibility of positive feedback from the ocean to the atmosphere.

As well as studies of this particular event, there have been studies concerning the more general phenomenon of decadal scale variability in the Pacific. *Deser and Blackmon* (1995) described EOF 2 in an analysis of observed Pacific (20°S–60°N) SSTs as a North

Pacific mode (EOF 1 being the canonical El Niño mode). They observed long period variability in the temporal signature of this EOF. *Mantua et al.* (1997) conducted an EOF analysis of Pacific SSTs pole-ward of 20°N. They noted long period variability in the leading principal component (PC 1). The term Pacific Decadal Oscillation (PDO) was coined for the phenomenon and PC 1 became known as the PDO index. The spatial pattern of their EOF 1 is similar to El Niño, but with a broader warming in the tropics. The cool signal in the North Pacific is stronger than the broadened tropical warming and extends to the Pacific western boundary. *Mantua et al.* concluded that El Niño and the PDO must be related, describing the PDO as El Niño-like interdecadal climate variability, and that their results are showing one of two things: Either interdecadal climatic shifts as a response to individual (tropical) El Niño events, or a state of interdecadal PDO constrains the envelope of interannual El Niño variability. The former describes a situation where the combination of individual El Niño or La Niña events produce extended warm or cool periods in the North Pacific. The latter describes a physical modulation of El Niño variability by some other process.

Zhang et al. (1997) performed EOF analysis of both high-pass and low-pass filtered SST, over a variety of spatial areas for the period 1950–1993. The leading principal component time series for the low-pass filtered SST is defined as a decadal index, and the high-pass PC 1 the El Niño index. However, *Zhang et al.* refrain from referring to regression maps of leading PCs for each filter type as physical modes of variation. *Zhang et al.* also used a longer 1900-1993 time series. For this time series they removed the spatial mean of the anomaly fields at each time before EOF analysis. This was in an effort to remove the global warming signal that can dominate the analysis at longer time scales. *Zhang et al.* recovered similar patterns of spatial variability to *Mantua et al.* (1997). It was the opinion of *Zhang et al.* that mode separation is not an ideal method for defining decadal scale variability, since the PDO and El Niño seem so closely linked.

Folland et al. (1999) performed an EOF analysis of low-pass filtered un-interpolated SST. They found that EOF 3 of the global domain (or EOF 2 of just the Pacific domain) had a spatial pattern similar to those produced by *Mantua et al.* (1997) and *Zhang et al.* (1997). However, *Folland et al.* (1999) acknowledged many caveats with this approach, the primary problem being degeneracy of the EOFs when changes to the sampling period

were made. They also acknowledged that many areas with large amplitude spatial patterns in EOF 2, and to some extent EOF 3, were data sparse regions in the uninterpolated input. These problems in data analysis mean that drawing firm conclusions from the analysis is extremely difficult.

Newman et al. (2003) found that the PDO is dependent on El Niño for all time scales. They propose a first order approximation of the PDO as the reddened response to El Niño and atmospheric noise, and not a dynamical mode. Such a reddening process allows for variability on longer scales than is present in either of the physical processes. *Schneider and Cornuelle* (2005) propose that the PDO is forced by at least three physical mechanisms, these being atmospheric variability over the North Pacific, El Niño SST variability, and oceanic variability in the Kuroshio–Oyashio extension. They suggest that the relative importance of each of these mechanisms is dependent on the time scale, with El Niño and the variability of the Aleutian low being the most important at longer time scales. The study of *Schneider and Cornuelle* (2005) as well as many other studies (e.g., *Trenberth and Hurrell*, 1994; *Graham*, 1994) suggest that both tropical and extra-tropical processes are important to the PDO, with tropical forcing producing teleconnections to the extra-tropical North Pacific, and feedbacks in the extra-tropics allowing for the generation of persistent anomalies.

Despite extensive studies, there is still much uncertainty regarding the nature of decadal scale variability in the Pacific Ocean. One aspect that is universally agreed on is that decadal variability in the Pacific and El Niño appear to be related. It seems unlikely that decadal variability in the Pacific is explained by a completely separate physical process from El Niño, but how decadal variability is generated, either as a dynamic or stochastic mode, is not well understood.

The term Pacific Decadal Oscillation, or PDO, is not a generic term but has a rather specific definition. The PDO is defined as PC 1 computed from the method of *Mantua et al.* (1997). There are other similar sounding definitions such as the Inter-decadal Pacific Oscillation (IPO) which generally refers to the inclusion of variability in both the northern and southern parts of the Pacific basin. Due to the variety of terms in use to describe decadal scale variability in the Pacific, and the slightly different meanings or definitions for these terms, the scientific meaning of the terms can be confusing. Therefore, to avoid

confusion, in this study any reference to the PDO specifically refers to the PDO as defined by *Mantua et al.* (1997), and other decadal scale variability will be referred to in generic terms.

Decadal variability in the North Pacific has impacts both locally and remotely. Temperature changes in the North Pacific can have a significant effect on the local ecosystem (e.g., *Mantua et al.*, 1997; *Beamish et al.*, 1999; *Hare et al.*, 1999). Remote effects of the PDO include changes to the surface climate (e.g., temperature and precipitation) in Australia, South and North America, the Russian Far East, much of eastern Asia, and the maritime continent (*Mantua and Hare*, 2002). Improved understanding of decadal variability in the North Pacific could lead to a better understanding of climate variability in these remote regions.

7.2 Method development

In order to determine if decadal variability is present in either of HiGEM1.2 and HadGEM1.2, it is necessary to develop a suitable methodology that can be used consistently between models and observational data sets, and whose results can be interpreted with confidence. A variety of methods have been used to examine long period SST variability in the Pacific ocean. As stated in *Mantua and Hare* (2002), the outcome of this type of analysis appears to be extremely sensitive to the choice of method. Hence, it is critical to afford a great deal of consideration on method development, and produce explicitly defined requirements that any potential methodology must meet.

Many authors closely associate decadal scale variability in the North Pacific with El Niño (e.g., *Mantua et al.*, 1997; *Zhang et al.*, 1997; *Newman et al.*, 2003; *Schneider and Cornuelle*, 2005; *Imada and Kimoto*, 2009) . Hence, it is important that the results of this study be directly comparable to the results of the work on El Niño and its extra-tropical teleconnections as discussed in chapters 3 and 4. This will allow decadal scale signals that are extracted to be compared with the equivalent El Niño signal to ensure they are not simply a different representation of the El Niño signal. For these reasons it is sensible to work with the same region as used for the El Niño analysis, and use the same sampling technique, working with northern winter (November–March) anomaly fields. *Newman et al.* (2003) found that the PDO had little multi-year persistence during summer, and so

suggested that decadal variability of North Pacific SSTs is largely a winter and spring phenomenon. This finding suggests the choice of a winter only sampling procedure for this analysis is reasonable.

It is important that the method used to extract decadal scale variability should be as robust as possible. The same method will need to be applied to observations and model simulations with a good level of consistency. If EOF analysis is used, the results for the observed data set should not be sensitive to the temporal domain, as this would not yield a general method for extracting decadal scale variability. It would be desirable to extract the leading EOF of SST as decadal variability as in *Mantua et al.* (1997) or *Zhang et al.* (1997) rather than as a second or third mode as in *Folland et al.* (1999). Using higher modes increases the likelihood that the EOF is an artefact of the orthogonality constraint (see appendix B.3) and not representative of a physical mode of variability.

The use of low-pass filters on input data prior to EOF analysis is not desired. Using a low-pass filter is an acceptable method provided that it is known that a low frequency signal exists in the time series. The use of a low-pass filter is certain to extract a low frequency signal. However, if we do not know whether or not such a signal exists in the input, as is the case for HiGEM and HadGEM, then the output of the filter may simply be an artefact of the filtering process and not be representative of a physical process.

Bearing these requirements in mind, the methodology chosen for use in this study is similar to the methodology of *Mantua et al.* (1997). This involves an EOF analysis of northern winter (NDJFM) SST anomalies in the North Pacific between 20°N and 60°N. This domain is chosen so as not to include the core tropical variability of El Niño. EOF analysis of the same SST anomalies in the tropical Pacific between 20°S and 20°N will also be computed. The combination of these two domains will yield a "pure North Pacific" domain and a "pure El Niño" domain. The principal component time series from the tropical domain is to be the reference time series and should contain the core variability associated with El Niño, and be similar to the EP index defined in chapter 3. The PC time series from the North Pacific domain can then be compared to this to establish whether or not the variability contained in it appears to be different from El Niño type temporal variability.

The following sections are a more detailed discussion of specific aspects of this methodology, dealing with the issues of how to sample the input SST data and how to deal with the global warming trend that may cause problems when dealing with longer time series.

7.2.1 Sample length considerations

When examining long period variability it is beneficial to have as long a time series as possible. Clearly the maximum number of winters available for study is limited by the length of the model integrations. However, there are also serious limits imposed on the length of the observational data record that can be used. Many gridded data products, including HadISST1.1 used in this study, have missing data in-filled using a technique based on EOF analysis. The specific technique used for filling missing points in HadISST1.1 is reduced space optimum interpolation (RSOI) (*Rayner et al.*, 2003; *Kaplan et al.*, 1997). This technique involves extracting modes of variability from the modern portion of the data where there is a comprehensive global spread of observations, and projecting them back to fill the missing values in times when observed data coverage was sparse. This is an effective method for filling missing values in a physically meaningful way (as opposed to simple interpolation). However, when employing EOF analysis to study long term variability in such a data set it is possible to simply recover the spatial patterns that were used to perform the interpolation. Clearly this is an undesirable situation that must be avoided. Therefore we only use the temporal portions of the product where a minimal amount of interpolation has been performed.

To understand which parts of the HadISST1.1 record are suitable for this study, it is useful to examine the uninterpolated SST data set HadSST2 (*Rayner et al.*, 2006). HadSST2 will provide an idea of the type of observational data set that was used to produce the interpolated HadISST1.1 data set. HadSST2 is a high quality observational data set, having undergone rigorous quality control procedures. To show the temporal variation in observation density, December–January–February (DJF) seasonal means for 1899–1900, 1928–1929, 1957-1958, and 1989–1990 are constructed such that a grid point in the seasonal mean field is only counted as missing if that point is missing in all three months making up the season. Figure 7.1 shows maps of these DJF seasons. Blue colouring indicates that an observation was available for at least one of the DJF months. No colouring

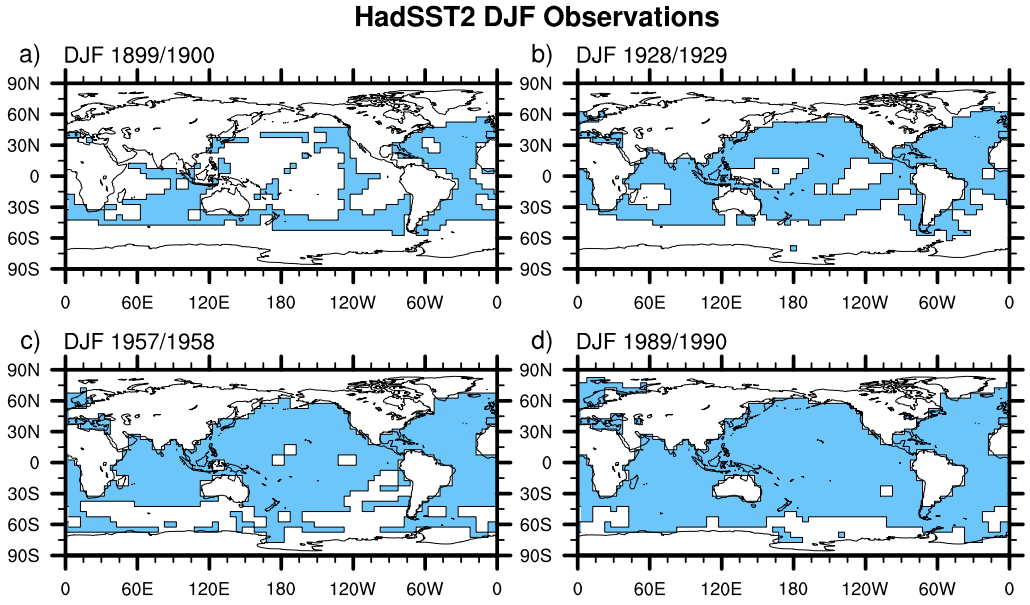

Figure 7.1: HadSST2 DJF observations. Blue colouring indicates points where at least one observation exists in the DJF season. No colouring (white) indicates points with no observations in the DJF season.

(white) indicates that no observation was available for any of the DJF months.

Figure 7.1 allows the visualisation of how many in situ observations make up the HadISST1.1 data set, and how much is in-filled using the RSOI technique in each of four temporal periods. It should be clear that at the beginning of the twentieth century (figure 7.1a) the observational coverage in the Pacific basin is poor. Around the late 1920s (figure 7.1b) the number of observations in the North Pacific is sufficient for a useful EOF analysis, rather than simply recovering the modes used for in-filling the missing values. The number of observations in the tropical Pacific remains small until the late 1950s (figure 7.1c). For this reason it would be unwise to conduct an EOF analysis of tropical SSTs including data from any earlier, as the primary modes recovered are likely to be those used for interpolation, and therefore would not reveal anything new about the dynamics previous to the late 1950s. Since the satellite era (figure 7.1d) there is near global coverage of observed SST. Locations that are not well covered by satellite observations are the extreme north and south, which are not relevant in this study.

The shortage of SST observations restricts the use of the HadISST1.1 time series to the most recent 50 years when studying the tropical Pacific, and the last 80 years when studying the extra-tropical north Pacific. Of course these limitations do not affect model

output, only the ability to compare model results to an equivalent observational analysis.

7.2.2 The global warming trend

Other studies have noted the dominance of the global warming trend in global and regional EOF analyses with long (of the order of a century) time series (e.g., *Zhang et al.*, 1997; *Folland et al.*, 1999). Hence, it is important that the global warming trend in the SST data be accounted for before proceeding with EOF analysis.

Folland et al. (1999) achieved this implicitly by extracting the global warming signal as the leading mode of variability (EOF 1) and recovering a mode with decadal scale variation later (EOF 3). Global EOF analysis is not desirable, and in an EOF analysis over a smaller spatial domain the variance associated with global warming and that associated with decadal scale variation could be too closely related to be separated (*North et al.*, 1982). Hence, removal of the global warming signal via mode separation is unlikely to be successful given the temporal and spatial constraints prescribed for this analysis. Interestingly, *Folland et al.* noted that their EOFs were extremely dependent on the exact temporal sample period used. This further suggests that mode separation is a bad choice for this study, since robustness of the method is a key requirement (as outlined in section 7.2).

Zhang et al. (1997) removed the spatial mean of the SST anomaly fields from each grid point at each time before EOF analysis. This method has the benefit of not assuming the global warming trend to be linear. However, this is at the expense of assuming that the global warming signal is uniform in space. Recall from chapter 6 that the climate change signal in SST in HiGEM1.1 was not spatially uniform, suggesting that this assumption is flawed. Also EOF 1 of *Folland et al.* (1999) shows that the global warming effect on SSTs has a good deal of spatial variation.

Another option is to remove the linear trend from each grid point in the SST input before EOF analysis. This has the benefit of allowing spatial variability in the magnitude of the global warming signal. However, it does of course make the assumption that the global warming trend is linear. While this is likely to be a good approximation, it may not be strictly valid for every grid point in the input SST. However, it is an acceptable compromise. Therefore, the input SST data will have the least-squares fitted linear trend removed from each grid point before EOF analysis is used.

7.2.3 Method Summary

The methodology used to extract decadal scale variability is as follows. EOF analysis will be used over two domains: 20°S–20°N for the tropical domain, and 20°N–60°N for the extra-tropical North Pacific domain. Both domains have the same longitudinal extent that was used in chapters 3 and 4 (120°E–100°W). The sample length for analysis of observed SST will be no more than 50 years in the tropical domain and no more than 80 years in the extra-tropical North Pacific domain. The SST data that is input into the EOF analysis will be sampled as in chapters 3 and 4, that being November-March winter anomalies. Additionally the SST data will have the least-square fitted linear trend removed from each grid point to remove the global warming trend.

7.3 Extraction of decadal scale variability

The methodology described in the previous section is now applied to the observational dataset HadISST1.1 and the models HiGEM1.2 and HadGEM1.2. The aim is to validate the methodology as a method of extracting decadal scale variability signals from both observed data and model output, and to create a starting point for further study of decadal variability in HiGEM1.2 and HadGEM1.2.

7.3.1 EOF validation

An initial step of checking the leading EOFs for degeneracy must be taken prior to any other interpretation. Figure 7.2 shows the first 10 eigenvalues and the associated typical sampling errors, scaled as percentage of total variance, for EOF analysis of the tropical domain. The eigenvalues and typical errors for EOF analysis of the extra-tropical North Pacific domain are shown in figure 7.3. The typical errors are calculated by the method of *North et al.* (1982) as in chapter 3.

It is clear that the leading EOF for the tropical Pacific domain is well separated in observations and both models. This is expected as this mode represents an El Niño mode which is known to exist in the observations and both models (see chapter 3). However, the leading EOF for the extra-tropical North Pacific domain is well separated only in

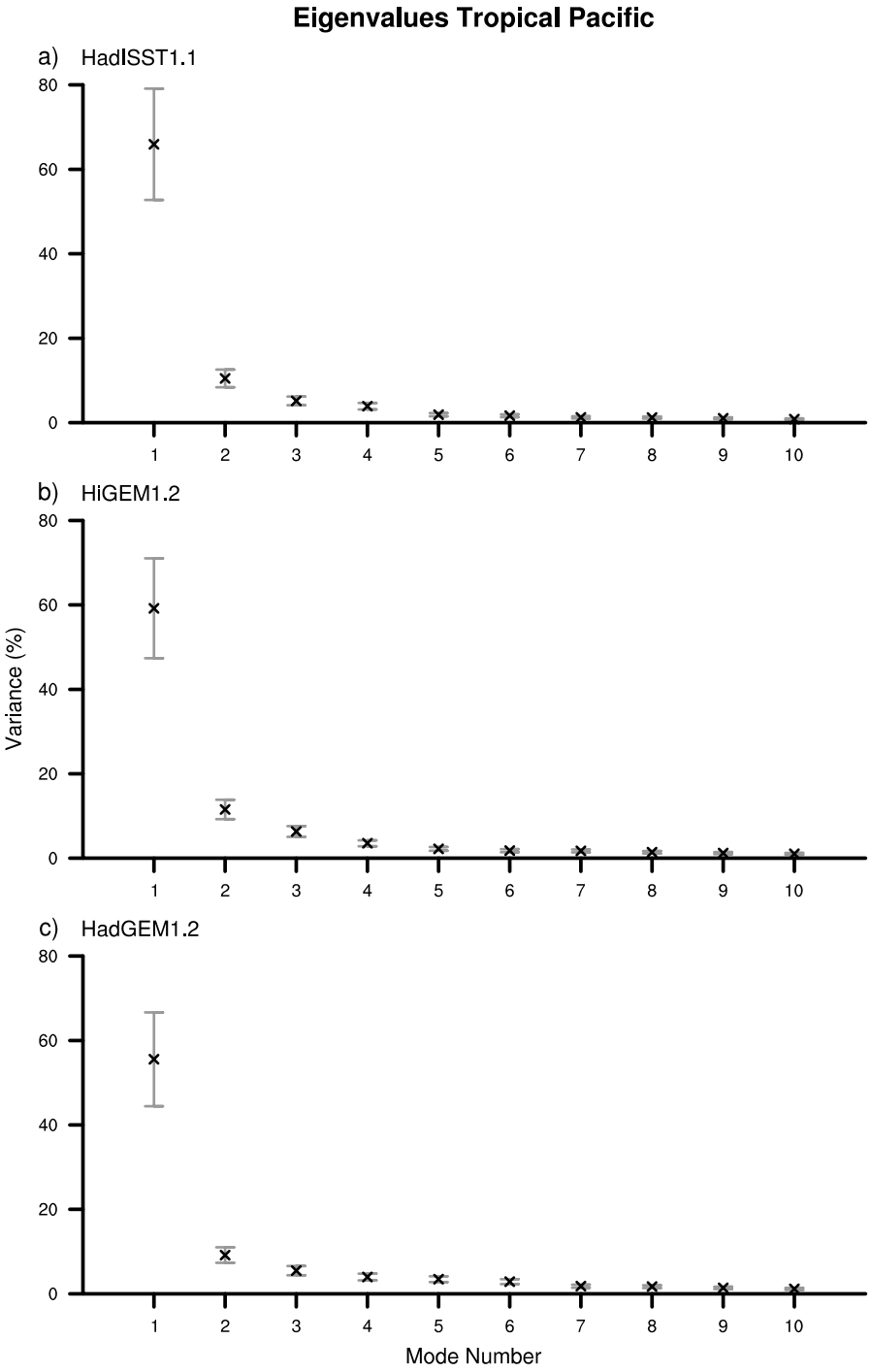

Figure 7.2: Eigenvalues and typical errors, expressed as percentage of variance explained, for EOF analysis of SST anomaly in the tropical Pacific domain (20°S–20°N). a) HadISST1.1, b) HiGEM1.2, and c) HadGEM1.2.

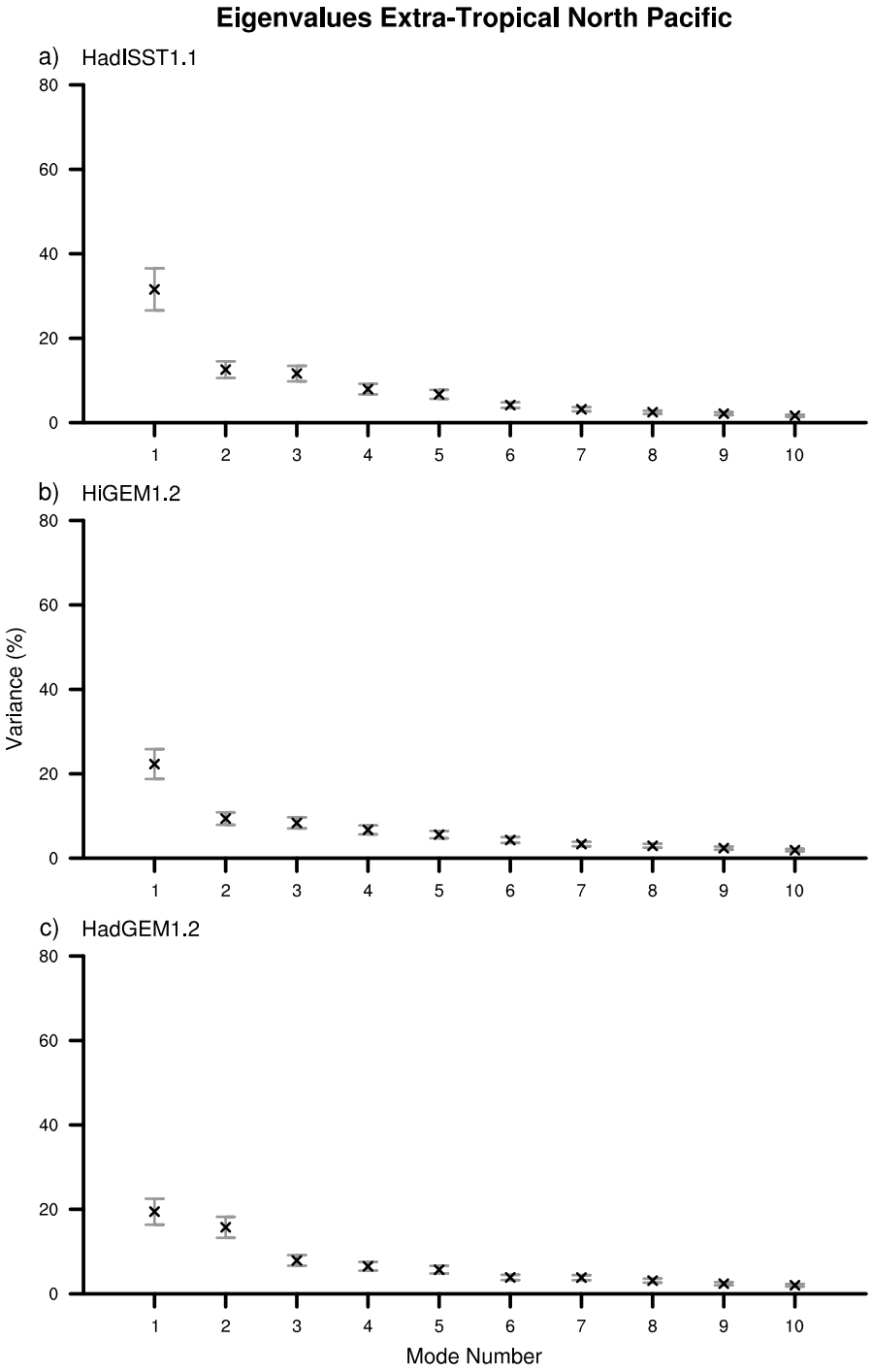

Figure 7.3: Eigenvalues and typical errors, expressed as percentage of variance explained, for EOF analysis of SST anomaly in the extra-tropical North Pacific domain (20°N–60°N). a) HadISST1.1, b) HiGEM1.2, and c) HadGEM1.2.

observations and HiGEM1.2, not in HadGEM1.2. The first two eigenvalues for the extra-tropical North Pacific domain EOF analysis in HadGEM1.2 are not well separated and could be considered a degenerate pair.

An attempt to separate these modes was made using rotation. Rotation is a technique that may reduce the noise in the EOF calculation and make the results easier to interpret. When standard EOFs are rotated using the *varimax* criterion (see *Preisendorfer*, 1988) the result is EOFs that are orthogonal. However, the principal components derived by projecting the rotated spatial patterns onto the data are not orthogonal. This implies that the principal components will no longer be un-correlated. The degenerate pair of extra-tropical North Pacific EOFs from HadGEM1.2 were rotated using this technique to try and separate the leading two EOFs. However, the rotated EOFs remained un-separated. The consequence of this is that the leading EOF for HadGEM1.2 cannot be interpreted as a distinct mode of the HadGEM1.2 system as some of its variance may be swapped with EOF 2. The degenerate leading EOF from HadGEM1.2 may still be useful for this analysis. However, the degeneracy must be considered when drawing conclusions from analysis of this mode.

7.3.2 Spatial variability

The spatial patterns for the leading EOF of SST anomaly for observations, HiGEM1.2, and HadGEM1.2 in both the tropical and extra-tropical domains are shown in figures 7.4 and 7.5 respectively. These spatial patterns are presented as the correlation between the PC time series associated with EOF 1 and the SST anomaly time series at each grid point (as in chapter 3). Although the maps are extended outside of the EOF calculation domain so that each map covers both the tropical and extra-tropical domains, the EOFs were only calculated for the sub-domain they represent. The boundary between the two sub-domains is marked with a dashed line at 20°N.

The EOFs for the tropical domain (figure 7.4) are all very similar to their counterparts presented in chapter 3. This leading EOF represents the pattern of variability associated with El Niño in the tropics very well in all cases. The projection of this EOF outside the tropical Pacific sub-domain are also consistent with the extra-tropical components of the EOFs in figure 3.2.

The leading EOF for observations in the extra-tropical North Pacific domain (figure 7.5a) bears some similarity to its tropical counterpart (figure 7.4a). The correlations over the whole Pacific domain do resemble the the pattern in figure 7.4a, but with a broader, weaker warm anomaly in the tropics and a stronger correlations in the extra-tropics. We might expect the correlations in the extra-tropics to be stronger and those in the tropics to be weaker simply because only data from the extra-tropical North Pacific contributed to the EOF computation. However, it is not only the relative strengths of the spatial pattern that are different. The shape of the North Pacific cold anomaly is quite different, it has a greater westward extent, extending to the Pacific west coast. The warm anomaly in the tropics in the extra-tropical North Pacific domain has a greater latitudinal extent than in the tropical domain. The spatial pattern recovered for observations is similar to that of *Mantua et al.* (1997, figure 2).

The leading EOF in the HiGEM1.2 extra-tropical domain (figure 7.5b) has similar large scale features to the observations. There is a cold anomaly in the central North Pacific extending westward to Japan and south-east Asia. This is surrounded by warm anomalies. A large part of the warm anomaly in the tropics is not deemed to be statistically significant at the 5% level. This warm anomaly appears to be composed of separate parts, with a weakening in the centre where there is a cold (although not statistically significant) anomaly at about 10°N. This might suggest that the type of variability being experienced in HiGEM1.2 is not quite the same as that in the observations.

The leading EOF in the HadGEM1.2 extra-tropical domain (figure 7.5c) is similar to that in HiGEM1.2. There is a cold anomaly in the central North Pacific that extends westward to the Asian coastline. This anomaly covers a smaller area than in HiGEM1.2 or observations. However, it has a similar shape and position to the equivalent anomaly in HiGEM1.2. The spatial patterns in the two models are more similar to one another than either of them are to the observed spatial pattern.

The similarities between the spatial patterns in the extra-tropical domain in HadGEM1.2 and HiGEM1.2 implies that the EOF analysis is extracting the same mode of variability from both models. However, the leading mode in HadGEM1.2 has not stood out as well against noise as that in HiGEM1.2. This is likely to be a consequence of the degeneracy of EOF 1 in HadGEM1.2.

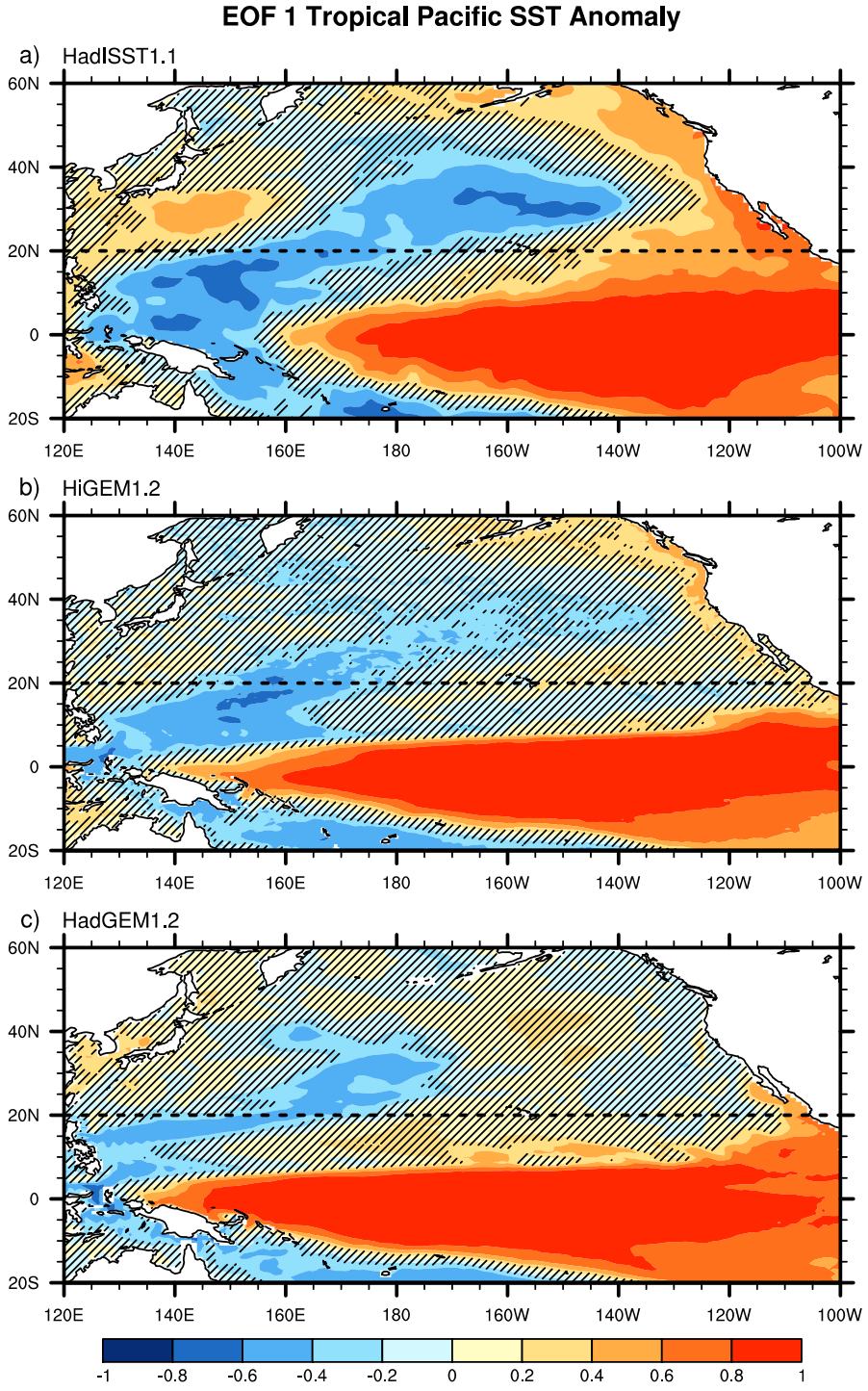

Figure 7.4: Correlation maps of EOF 1 of observed SST with anomalous observed SST in the tropical Pacific domain (20°S–20°N). The contour interval is 0.2. Hatching indicates correlations not significant at the 5% level. The horizontal line at 20°N marks the boundary between the tropical Pacific and extra-tropical North Pacific domains. a) HadISST1.1, b) HiGEM1.2, and c) HadGEM1.2.

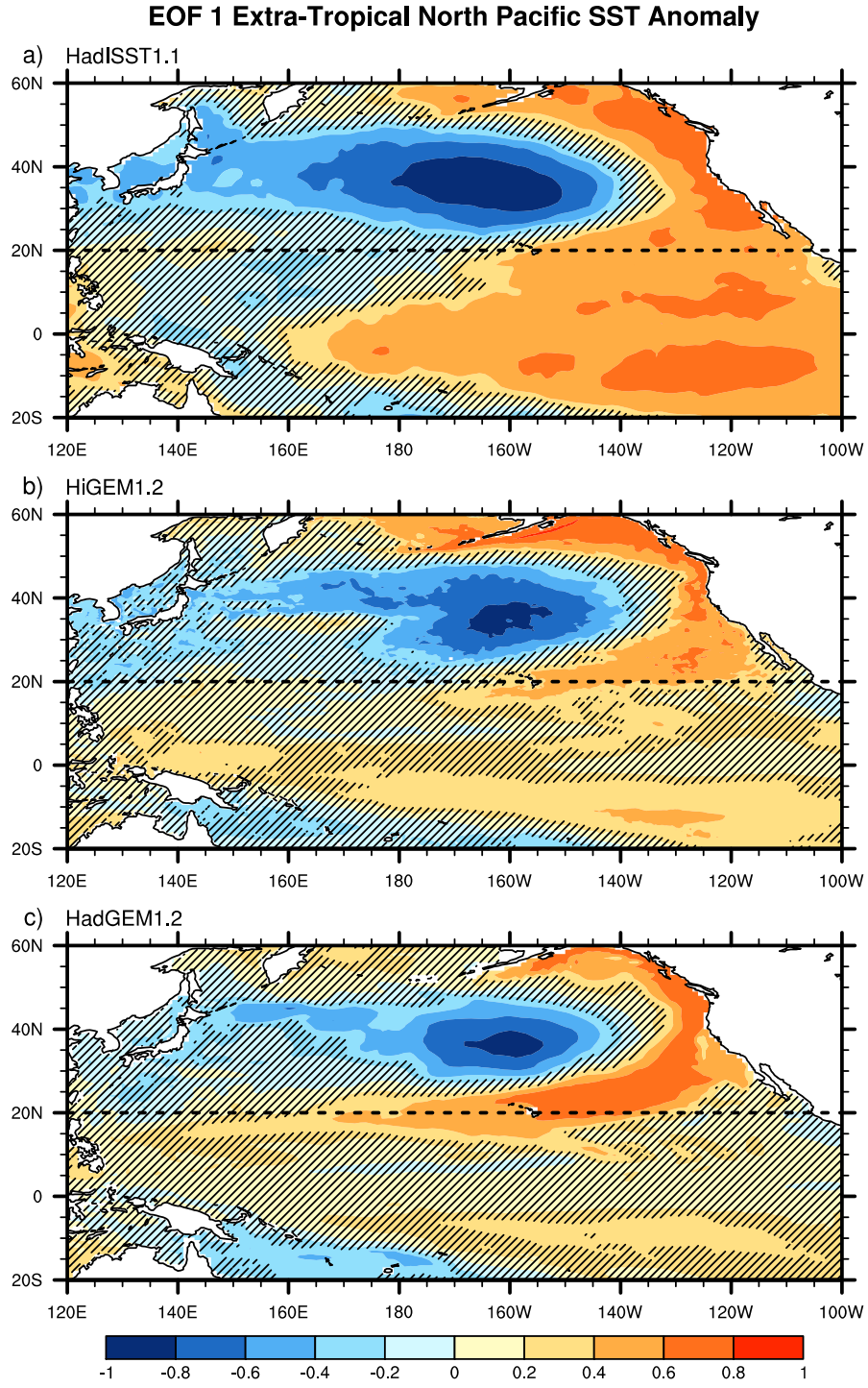

Figure 7.5: Correlation maps of EOF 1 of observed SST with anomalous observed SST in the extra-tropical North Pacific domain (20°N–60°N). The contour interval is 0.2. Hatching indicates correlations not significant at the 5% level. The horizontal line at 20°N marks the boundary between the tropical Pacific and extra-tropical North Pacific domains. a) HadISST1.1, b) HiGEM1.2, and c) HadGEM1.2.

7.3.3 Temporal variability

The principal component time series associated with EOF 1 for observations, HiGEM1.2, and HadGEM1.2 for both the tropical and extra-tropical domains are shown in figures 7.6 and 7.7 respectively. The PCs for both the high and low resolution models in the tropical domain use only the first 50 years of data that is used in the extra-tropical domain. A shorter length is used to be consistent with observations, and the first 50 years is chosen as this makes the results of the EOF analysis directly comparable to the work in chapter 3.

The PCs for the tropical domain (figure 7.6) show relatively short-scale variability. This type of variability is exactly the type that is typically associated with El Niño SST variability. The dashed black curve in figure 7.6a shows the NINO3 index[1], a time series representative of the core SST variability in the eastern equatorial Pacific cold tongue during El Niño. It is clear from figure 7.6a that PC 1 for observations and the NINO3 index represent the same type of variability. This confirms that the EOF analysis of the tropical domain is isolating El Niño as the leading mode of variation in the domain.

The leading PC for the observed data in the extra-tropical domain (figure 7.7a) is quite different to that in the tropical domain. The temporal scale of the variability is visually longer in the extra-tropical domain. There are oscillations between warm and cold SST anomalies on the scale of approximately 20 years. From visual interpretation it seems unlikely that the extra-tropical PC1 is simply a low-frequency representation of the PC from the tropical domain. This suggests that the choice of methodology has yielded a temporal variability signal that is not simply a low-pass filtered version of the tropical variability but potentially could be an independent signal.

The dashed black line in figure 7.7a shows the Pacific Decadal Oscillation (PDO) index[2] computed using the method of *Mantua et al.* (1997), a method that is commonly used as a standard. The monthly values of the PDO index were averaged into NDJFM means for plotting. The leading PC for observations calculated for this study is very similar to the *Mantua et al.* PDO index. There are some differences, most likely due to the different methods of removing the global warming trend. The overall similarity confirms that the method used here is capable of extracting decadal scale variability.

[1] NINO3 index available from the Climate Prediction Center http://www.cpc.ncep.noaa.gov/data/indices/

[2] PDO index data obtained from the Joint Institute for the Study of the Atmosphere and Oceans at the University of Washington (http://jisao.washington.edu/pdo/PDO.latest)

The leading PC for HiGEM1.2 in the extra-tropical domain (figure 7.7b) also shows longer scale variability than the PC for the tropical domain. The longer scale variations are particularly evident in the first half of the PC time series, after which the frequency of the variability appears to increase somewhat. This apparent switch between low and high frequencies of oscillation is also noticeable during the end quarter of the observed PC time series. This suggests that there could be a mechanism of decadal variability in HiGEM1.2 that is behaving similarly to observations.

HadGEM1.2 shows a rather different type of variability in its leading PC (figure 7.7c). Of course, it must be borne in mind that EOF/PC 1 in HadGEM1.2 is degenerate. However, given the similarities between the spatial patterns in HiGEM1.2 and HadGEM1.2 we might assume that the two EOFs/PCs are representative of the same kind of variability. There is a considerable amount of high-frequency variability in the first two-thirds of the HadGEM1.2 extra-tropical PC 1. However, the last third of the PC time series does show some indication of decadal scale variability.

7.3.4 Summary of results

The method described in section 7.2 has been applied to SSTs from observations and both high and low resolution coupled models. The results from the observed SSTs are similar to the results of *Mantua et al.* (1997) and *Zhang et al.* (1997) in terms of the spatial patterns of variability and the temporal characteristics of their PDO index. Performing analysis in two mutually exclusive domains has allowed the extraction of a spatial mode of North Pacific SST variability that can confidently be described as distinct from the mode associated with El Niño in the tropics. The core variability in this mode has the form of a cold SST anomaly in the central Pacific that extends westward all the way to the Pacific western boundary. This characteristic is different from the tropical mode where a cold anomaly is present in the North Pacific but an anomaly of the opposite sign is present on the Pacific western boundary at the same latitude. This pattern of spatial variability in the North Pacific is reproduced by both high and low resolution models.

It is evident from figures 7.6 and 7.7 that there is longer scale variability occurring in the North Pacific mode than in the tropical mode. However there is also a good deal of high frequency variability in the PCs for the North Pacific domain. All of the PCs show

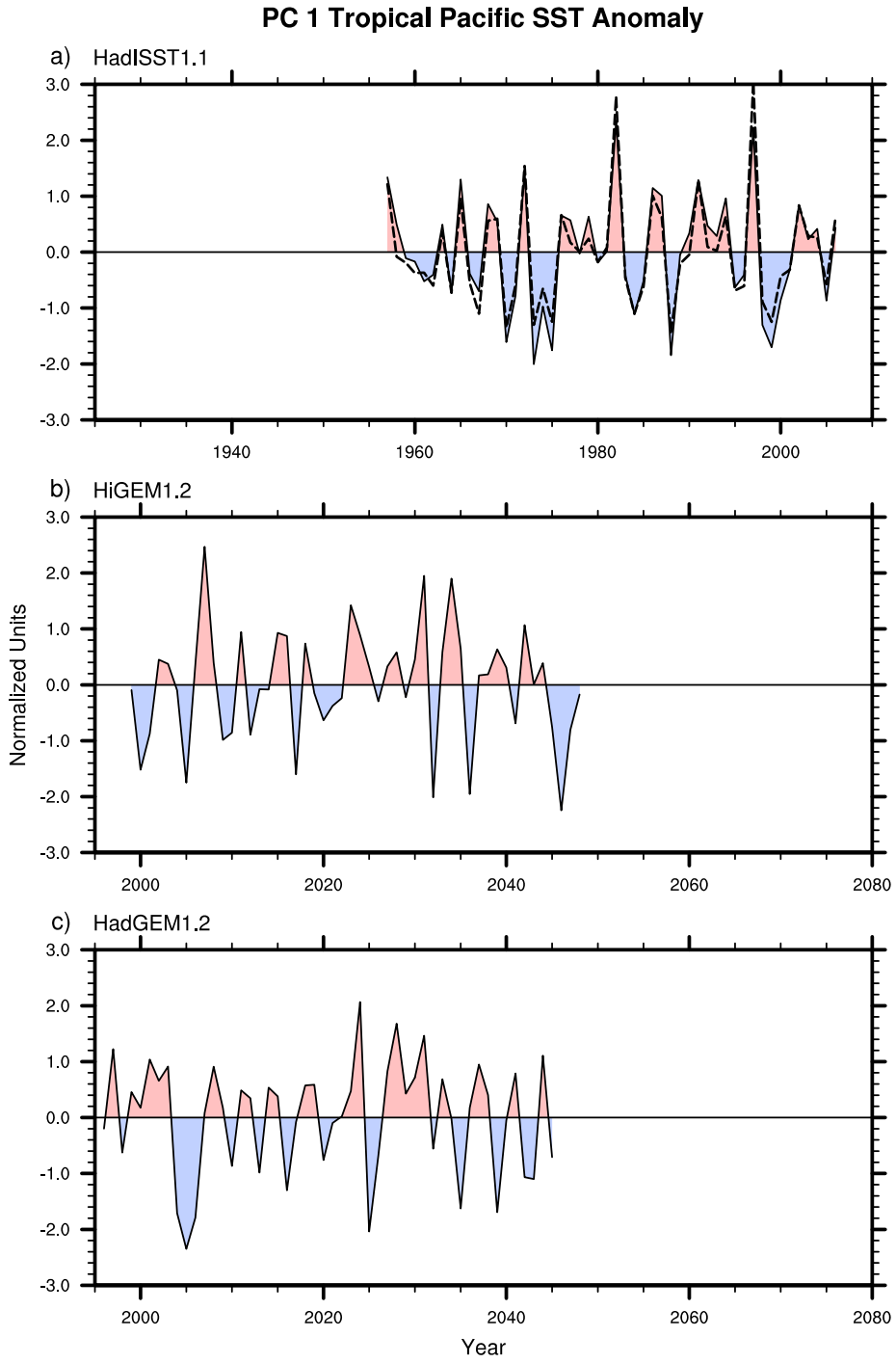

Figure 7.6: Leading principal component time series (PC 1) of SST anomaly in the tropical Pacific domain (20°S–20°N). a) HadISST1.1 with the NINO3 index shown as the dashed line, b) HiGEM1.2, and c) HadGEM1.2.

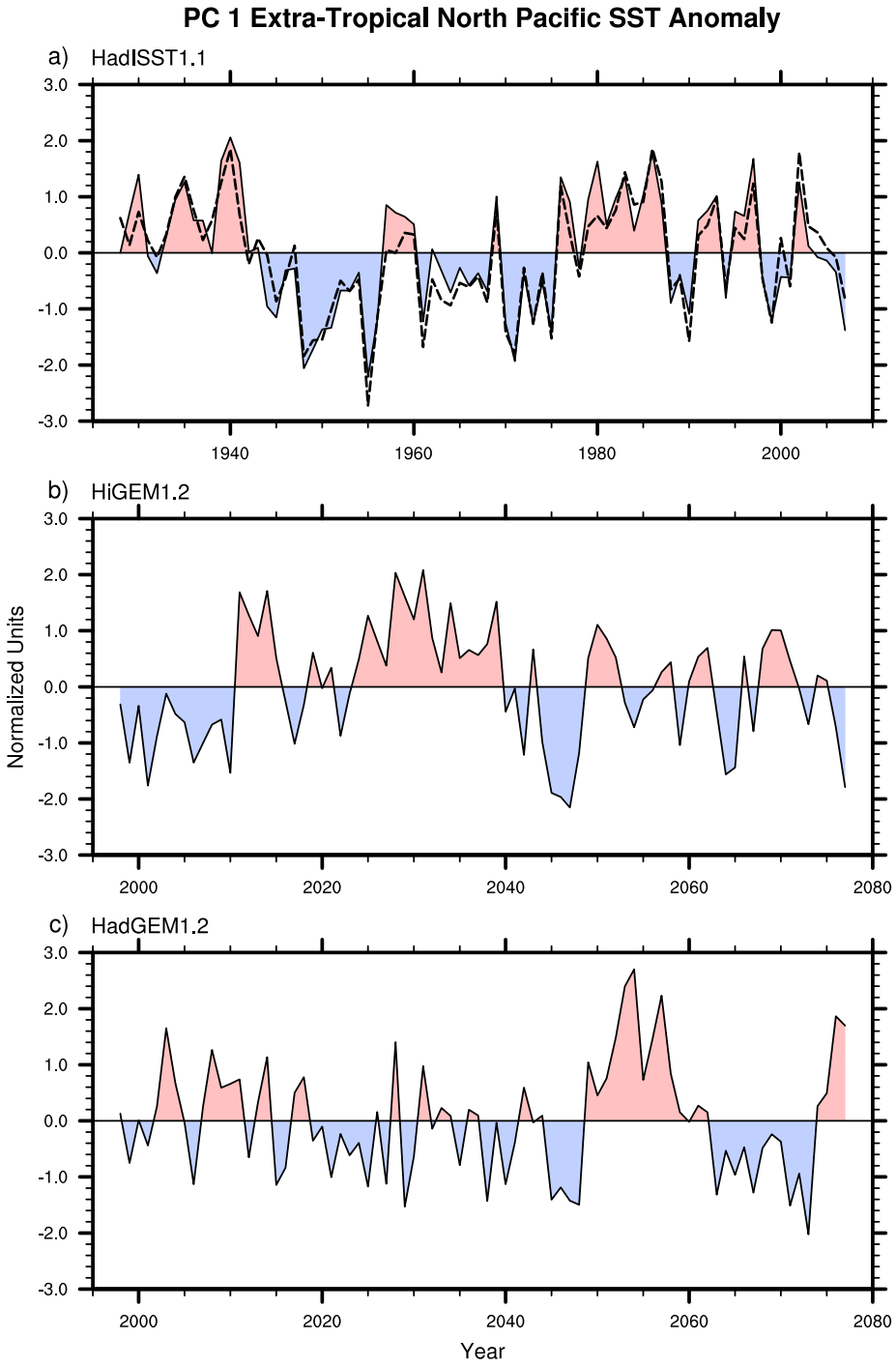

Figure 7.7: Leading principal component time series (PC 1) of SST anomaly in the extra-tropical North Pacific domain (20°N–60°N). a) HadISST1.1 with the NDJFM mean of the PDO index as constructed by *Mantua et al.* (1997) shown as the dashed line, b) HiGEM1.2, and c) HadGEM1.2.

some portions that appear to be exhibiting decadal variability and some portions that have decidedly shorter scale variations. This is particularly evident in HadGEM1.2, but this is likely to be due in part to the HadGEM1.2 time series being more contaminated with noise due to the degeneracy of the leading mode. The short sample period used effectively rules out performing any spectral analysis on the time series, since any results would be difficult to interpret in terms of statistical significance. Thus the frequency composition of the PCs for the North Pacific domain cannot be confidently determined and therefore the dominant time scales of variability cannot be formally assessed. We now look for a physical mechanism behind the variability we have diagnosed in the extra-tropical North Pacific.

7.4 Mechanisms generating decadal variability in HiGEM1.2

We now want to understand how the preferred pattern of SST seen in figure 7.5b develops and varies in the HiGEM1.2 model. A solid starting point is to understand whether it is the atmosphere or the ocean, or both that is forcing the SST anomaly pattern in the North Pacific evident in figure 7.5b. This is assessed by examining the heat budget of the ocean in this region.

7.4.1 Ocean heat budget

Heat can be put into a region of the ocean either by transfer of heat between the atmosphere and the ocean or by heat transport internally within the ocean. To determine a closed heat budget it is necessary to consider a closed volume of the ocean. Since the area of interest is the centre of action of EOF 1 (cold anomaly in figure 7.5b), the heat budget for the closed volume of the Pacific Ocean bounded by the sections along 30°N and 42°N, the coasts at the eastern and western boundaries, the sea floor and the sea surface will be considered.

Heat fluxes are the amount of energy transported across a given unit of area in a given unit of time. The heat flux budget of a closed volume of the ocean is directly related to the heat content of that volume, and not necessarily directly to SST. Therefore comparing heat fluxes to ocean heat content instead of SST is preferred. Of course SSTs and heat content are closely linked. It is well known that persistent oceanic heat content anomalies

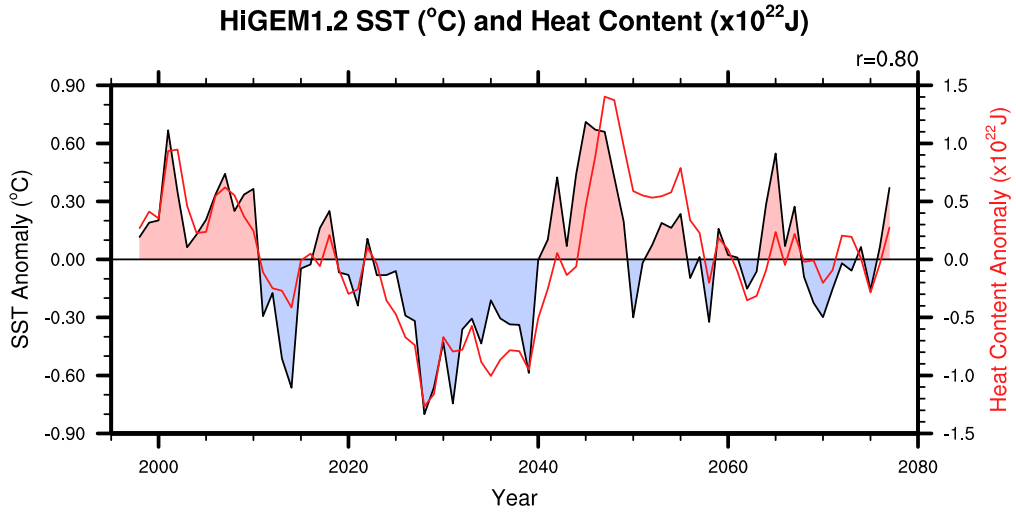

Figure 7.8: Northern winter (NDJFM) SST anomaly averaged over the region bounded by 30°N, 42°N, and the Pacific eastern and western coasts (black, shaded above and below the time axis) and ocean heat content anomaly for the volume bounded by 30°N and 42°N, the Pacific coasts at the eastern and western boundaries, the sea surface and the level surface at a depth of 500 m (red).

can be exposed to the surface, during winter, due to fluctuations of mixed layer depth (e.g., *Alexander et al.*, 1999; *Watanabe and Kimoto*, 2000; *Timlin et al.*, 2002). The heat content H of a given volume V of the ocean is given by

$$H = \iiint_V \rho_0 c_p T \, dV, \tag{7.1}$$

where T is temperature, ρ_0 is a reference density, and c_p is the specific heat capacity of ocean water. In the case of this study, the volume V is defined as the volume bounded by the sections along 30°N and 42°N, the coasts at the eastern and western boundaries, the sea surface and the level surface at a depth of 500 m. A depth of 500 m was chosen as this is the depth above which most of the temperature variability occurs.

The curve shaded above and below the time axis in figure 7.8 shows the 80 year time series of SST anomaly averaged over the region bounded by 30°N, 42°N, and the Pacific eastern and western coasts. This time series of SST is very similar to PC 1 (figure 7.7b), but with the opposite sign (correlation coefficient $r = -0.90$). The red curve shows an 80 year time series of November–March ocean heat content anomalies in the volume bounded by the sections along 30°N and 42°N, the coasts at the eastern and western boundaries, the sea surface and a depth of 500 m. There is a strong relationship between the northern

winter SST and ocean heat content anomalies. The two are highly correlated ($r = 0.80$) and clearly match well in terms of the low frequency variability. This close relationship suggests that the dominant cause of the northern winter SST anomalies is the exposure of ocean heat content anomalies during winter.

At this point it is worth taking time to consider the exact relationship between heat fluxes and heat content. Heat fluxes are expressed in units of Watts per square metre (W $m^{-2} \equiv$ J s^{-1} m^{-2}) and heat content is expressed in Joules (J). These two quantities can be made more comparable by integrating the heat flux over the area it passes through, for example the surface area of the Pacific Ocean between 30°N and 42°N in the case of the surface heat flux, and over time. This results in a cumulative time series of anomalous energy input into the ocean measured in Joules.

In order to compute the time integral of the heat flux anomalies, the time series must be continuous. This precludes the possibility of integrating a time series of November–March anomalies since they contain no information about the summer heat fluxes. Instead time series of annual (July–June) anomalies are used, with July–June being used so that whole winter seasons are kept together. Oceanic heat content anomalies are likely to build up over periods of time longer than a winter season, with only the winter time anomalies becoming exposed to the surface as SST anomalies. This suggests that we should be interested in anomalies of heat input into the ocean on annual time scales, and that using annual anomalies is particularly useful as well as being a practical necessity.

The curve shaded above and below the time axis in all panels of figure 7.9 shows the same time series of winter (November–March) ocean heat content anomalies as shown in figure 7.8. The curves overlaid on figures 7.9a (black), 7.9b (blue), 7.9c (red), are the integrated anomalies of total heat flux, surface heat flux, and internal ocean heat transport convergence respectively. The ocean heat transport convergence anomaly is simply the difference between the heat transported into the volume across 30°N and the heat transported out across 42°N. The sign of the flux anomalies are positive for heat into the study volume. It is clear from figure 7.9a that the anomalies in the total heat flux computed from annual means match closely to the November–March heat content anomalies. The curves do not match exactly due to the different sampling periods. This shows that anomalies in the heat that is input into the ocean over the whole year account for the winter time

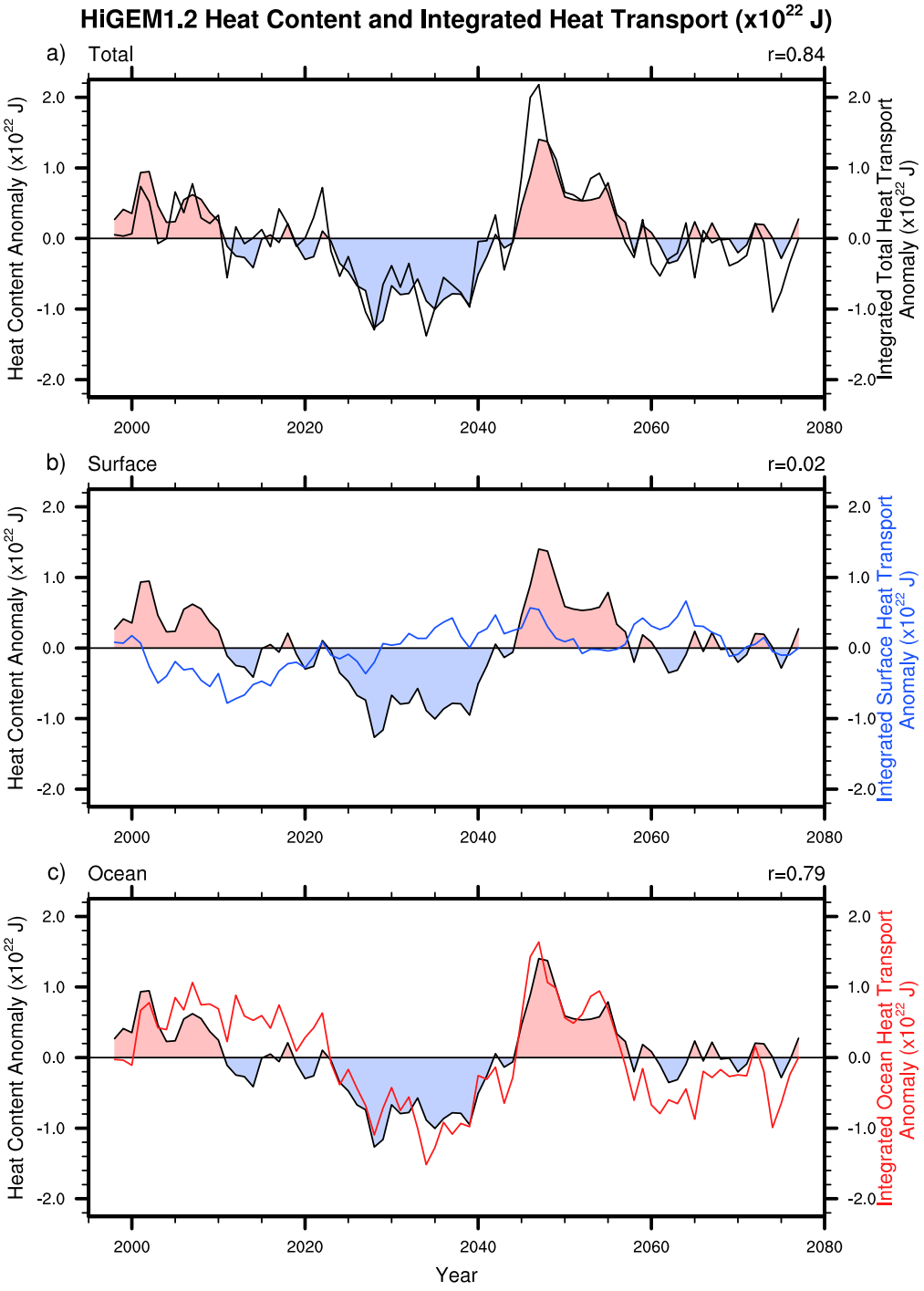

Figure 7.9: Ocean heat content anomaly for the volume bounded by 30°N and 42°N, the Pacific coasts at the eastern and western boundaries, the sea surface and the level surface at a depth of 500 m (black, shaded above and below the time axis) and a) total (surface+ocean) heat flux anomaly, b) surface heat flux anomaly, and c) anomalous internal ocean heat transport convergence. All heat flux anomalies have been integrated with respect to time and over the area they pass through into the study volume. These integrated heat fluxes are anomalies relative to the July–June annual mean.

changes in heat content. Comparing figures 7.9b, and 7.9c, it is clear that anomalies in the internal ocean heat transport account for the majority of the winter heat content anomalies both in terms of the magnitude and the low frequency variability. This finding appears to show that it is year-round anomalous transport of heat in the ocean that causes the winter time heat content anomalies, and ultimately the northern winter SST anomalies.

7.4.2 Ocean heat transport

The ocean heat transport diagnostic will now be examined in more detail using a perturbation analysis technique. We first consider the total ocean heat transport into the volume of ocean bounded by 30°N and 42°N, the Pacific coasts at the eastern and western boundaries, the sea surface and the sea floor

$$Q_{vT} = \rho_0 c_p \int_{X_W}^{X_E} \int_{-H}^{0} vT \, dz \, dx \Big|_{30^\circ\mathrm{N}} - \rho_0 c_p \int_{X_W}^{X_E} \int_{-H}^{0} vT \, dz \, dx \Big|_{42^\circ\mathrm{N}}, \tag{7.2}$$

where ρ_0 is a reference density, c_p is the specific heat capacity of ocean water, v is the meridional component of ocean velocity, T is temperature, x is distance eastward, z is the depth co-ordinate, and integrals over x and z represent the zonal integral across the width of the basin from the west coast at X_W to the east coast at X_E, and the vertical integral over the depth of the water column from the sea floor at $z = -H$ to the sea surface at $z = 0$ respectively. Splitting v and T into a time-mean component ($\overline{v}$ and $\overline{T}$) and a perturbation component (v' and T') allows us to understand vT as four separate components

$$vT = \left(\overline{v} + v'\right)\left(\overline{T} + T'\right) = \left(\overline{v}\,\overline{T} + \overline{v}T' + v'\overline{T} + v'T'\right), \tag{7.3}$$

and thus the total heat transport can be represented as four components:

$$Q_{vT} = Q_{\overline{v}\,\overline{T}} + Q_{\overline{v}T'} + Q_{v'\overline{T}} + Q_{v'T'}. \tag{7.4}$$

The first term $Q_{\overline{v}\,\overline{T}}$ represents the effect of the mean temperature being transported by the mean meridional velocity. This term does not vary with time and so makes no contribution to the variability. The next two terms, $Q_{\overline{v}T'}$ and $Q_{v'\overline{T}}$, represent the transport of anomalous temperature by the mean meridional velocity, and the transport of the mean temperature

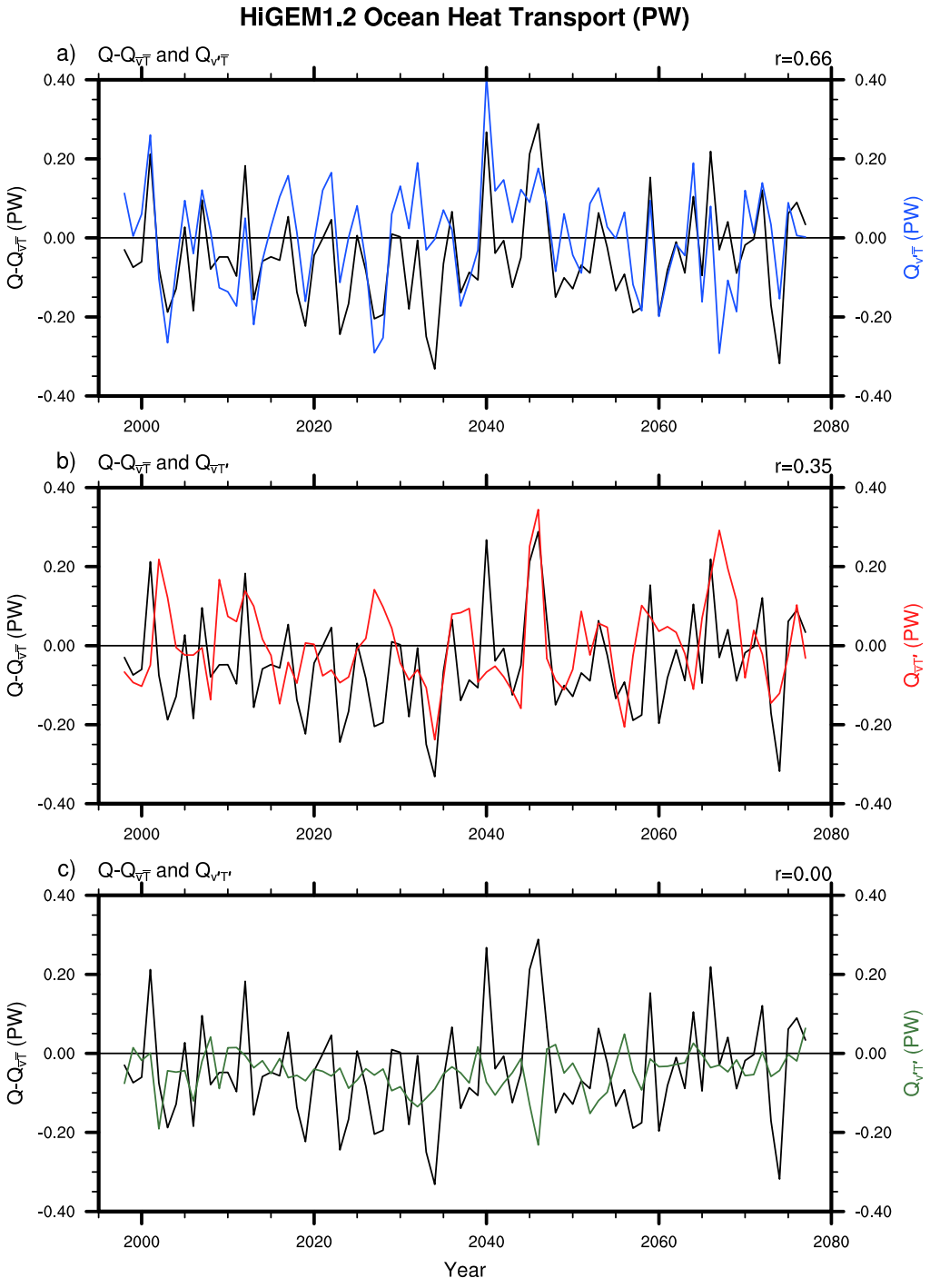

Figure 7.10: Ocean heat transport into the volume bounded by 30°N and 42°N, the Pacific coasts at the eastern and western boundaries, the sea surface and the sea floor (black, all panels) and anomalous ocean heat transport into the same volume due to a) transport of the mean temperature by anomalous meridional velocity ($Q_{v'\overline{T}}$), b) transport of anomalous temperature by the mean meridional velocity ($Q_{\overline{v}T'}$), and c) transport of anomalous temperature by anomalous meridional velocity ($Q_{v'T'}$).

by anomalous meridional velocity respectively. The last term, $Q_{v'T'}$, is the non-linear effect of transport of anomalous temperature by anomalous meridional velocity.

To understand the variability of the year-round ocean heat transport anomalies the total heat transport is computed in components from July-June annual means. The non-linear $Q_{v'T'}$ term is not computed directly but is computed as a residual. The components of anomalous ocean heat transport convergence into the reference volume are shown in figure 7.10. It is clear that the $Q_{v'\overline{T}}$ term (figure 7.10a; blue line) accounts for more variability in the total ocean heat transport ($r = 0.66$). However, some specific events such as the positive heat transport anomly present in 2045–2046, can be accounted for by the $Q_{\overline{v}T'}$ term (figure 7.10b; red line). This suggests that while the $Q_{v'\overline{T}}$ term dominates, the $Q_{\overline{v}T'}$ term is not entirely negligible. The non-linear $Q_{v'T'}$ term (figure 7.10c; green line) is uncorrelated with the total heat transport anomaly time series and typically has a smaller magnitude than the other terms, suggesting it can be regarded as noise.

7.4.3 Wind driven ocean heat transport

It has been demonstrated that the majority of the variability in ocean heat transport is due to transport of the mean temperature by anomalous meridional velocity. This suggests that we might be able to explain the heat content anomalies, and hence the SST anomalies, by considering only changes to the meridional velocity.

Sverdrup (1947) showed that the circulation in the upper layer of the ocean is driven by the wind. A key result of this work, known as the Sverdrup relation, relates the vertically integrated mass transport to the curl of the surface wind stress. The relation is commonly expressed in the following form (e.g., *Gill*, 1982)

$$V = \frac{1}{\rho_0 \beta} \hat{\mathbf{k}} \cdot \nabla \times \boldsymbol{\tau}, \tag{7.5}$$

where V is the vertically integrated meridional mass transport, $\hat{\mathbf{k}}$ is the unit vector in the vertical (z) direction, $\boldsymbol{\tau}$ is the surface wind stress, and β is the meridional gradient of planetary vorticity. The Sverdrup relation allows us to understand the circulation in the ocean that is driven by the wind.

An approximation to $Q_{v'\overline{T}}$ can be made using the Sverdrup relation. The meridional mass transport computed from equation 7.5 is used in place of meridional velocity and the

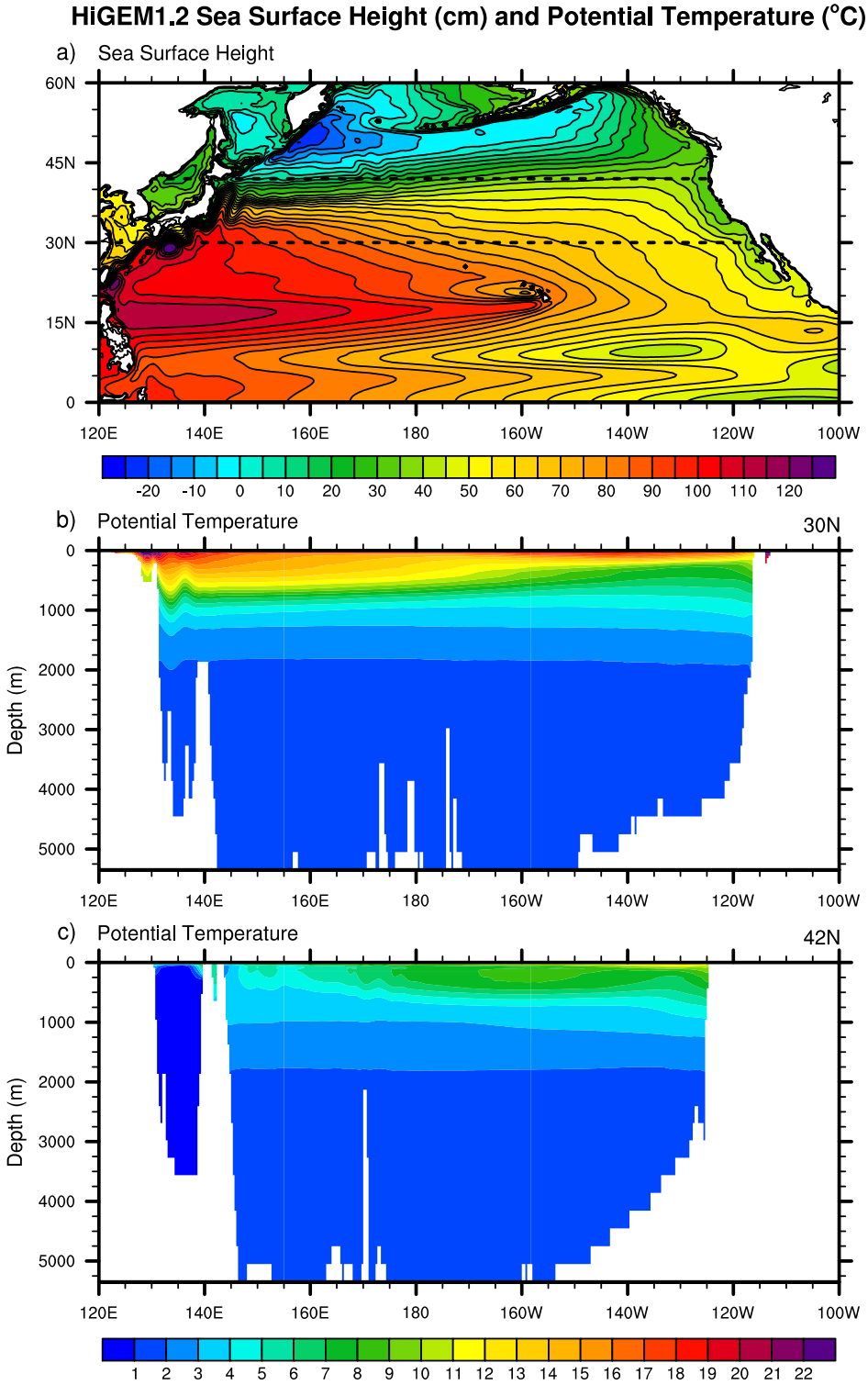

Figure 7.11: HiGEM1.2 long term means of a) sea surface height (SSH), and potential temperature along b) 30°N, and c) 42°N. The contour interval is 5 cm for SSH and 1 °C for potential temperature.

depth integral of mean temperature is used in place of temperature when computing the approximated ocean heat transport. Doing so assumes that the anomalous heat transport is due to the horizontal wind driven circulation, and that Sverdrup balance holds in the North Pacific. The latter has been confirmed by the observational study of *Hautala et al.* (1994). The Sverdrup equation only provides a mass transport valid in the interior of the ocean. Therefore, special treatment is needed for the western boundary region. Defining X_B to be the location of the eastern edge of the western boundary current, the following approximation to $Q_{v'\overline{T}}$ is made

$$A_{v'\overline{T}} = \left[\rho_0 c_p \int_{X_B}^{X_E}\left(V' \int_{-H_{\mathrm{NM}}}^{0} \overline{T}dz\right)dx - \rho_0 c_p \int_{X_B}^{X_E} V'dx \frac{1}{X_B - X_W}\int_{X_W}^{X_B}\left(\int_{-H_{\mathrm{NM}}}^{0} \overline{T}dz\right)dx\right]\Bigg|_{30^\circ\mathrm{N}}$$
$$-\left[\rho_0 c_p \int_{X_B}^{X_E}\left(V' \int_{-H_{\mathrm{NM}}}^{0} \overline{T}dz\right)dx - \rho_0 c_p \int_{X_B}^{X_E} V'dx \frac{1}{X_B - X_W}\int_{X_W}^{X_B}\left(\int_{-H_{\mathrm{NM}}}^{0} \overline{T}dz\right)dx\right]\Bigg|_{42^\circ\mathrm{N}}, \tag{7.6}$$

where V' is the anomalous meridional mass transport computed from equation 7.5. The integral of $\overline{T}$ over depth is from a level of no motion at $-H_{\mathrm{NM}}$ to the sea surface. Choosing a level of no motion rather than integrating over the full depth is consistent with the theory of the Sverdrup relation. The first term in within the first brace of equation 7.6 is simply the transport of temperature by meridional Sverdrup mass transport, which is valid in the ocean interior. The second term is an adjustment for the western boundary region, where it is assumed a mass transport equal and opposite to that in the interior transports the mean temperature of the western boundary current region.

The values of X_W and X_E are taken as the locations of the eastern and western Pacific coasts. The value of X_B must be chosen so as to separate the interior from the western boundary current. Figure 7.11 shows the long term mean of sea surface height (SSH) and temperature profiles along 30°N and 42°N. Contours of SSH are interpreted as streamlines for near surface geostrophic flow, with the western boundary current clearly visible as the area with very small streamline spacing parallel to the western boundary. Figures 7.11b and 7.11c show the profiles of ocean temperature along 30°N and 42°N. Using these figures as a reference for the structure and position of the western boundary current the locations 134°E and 145°E, for 30°N and 42°N respectively, were chosen to separate the

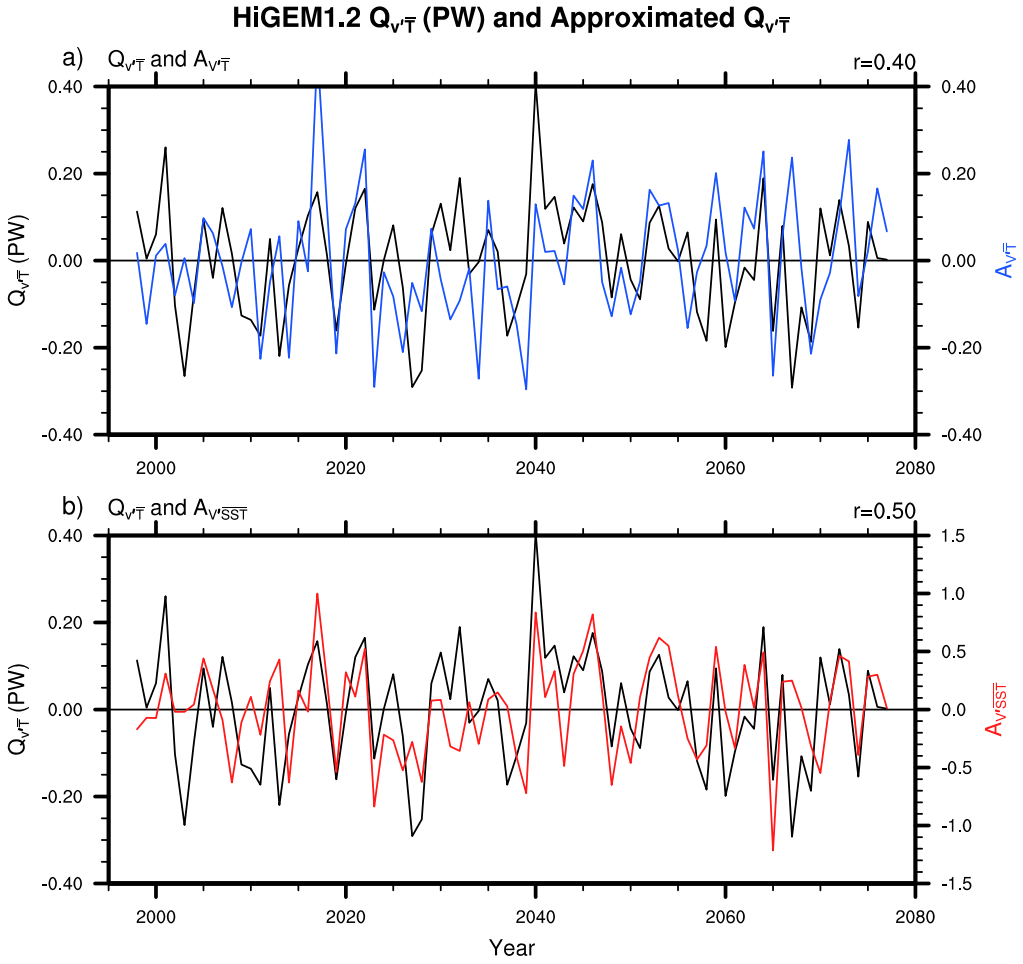

Figure 7.12: Ocean heat transport into the volume bounded by 30°N and 42°N, the Pacific coasts at the eastern and western boundaries, the sea surface and a level of no motion due to transport of the mean temperature by anomalous meridional velocity ($Q_{v'\overline{T}}$, black) and the approximations using a) depth integrated $\overline{T}$ (equation 7.6, blue), and b) northern winter mean SST (equation 7.7, red).

western boundary current from the Sverdrup interior. A depth of 1500 m was chosen as the level of no motion.

The approximation $A_{v'\overline{T}}$ is shown in figure 7.12a. The correlation between $Q_{v'\overline{T}}$ and $A_{v'\overline{T}}$ is 0.4, which is significant at the 5% level. The strength of this relationship suggests that much of the variability in $Q_{v'\overline{T}}$ can be explained by variability in the wind stress. Given the close relationship between $Q_{v'\overline{T}}$ and the total ocean heat transport shown earlier (figure 7.10a), this suggests that much of the variability in total ocean heat transport may also be explained by variations in wind stress curl.

A further approximation to the meridional heat transport is made using only surface

fields. If only surface fields are used in the computation then the same approximation could be computed using observed data. With this in mind the following approximation using SST in place of depth integrated temperature is made

$$A_{V'\overline{\mathrm{SST}}} = \left[\rho_0 c_p \int_{X_B}^{X_E} V'\overline{T}_{\mathrm{SST}}\, dz\, dx - \rho_0 c_p \int_{X_B}^{X_E} V'\, dx \frac{1}{X_B - X_W} \int_{X_W}^{X_B} \overline{T}_{\mathrm{SST}}\, dx\right]\Bigg|_{30^\circ\mathrm{N}}$$
$$- \left[\rho_0 c_p \int_{X_B}^{X_E} V'\overline{T}_{\mathrm{SST}}\, dz\, dx - \rho_0 c_p \int_{X_B}^{X_E} V'\, dx \frac{1}{X_B - X_W} \int_{X_W}^{X_B} \overline{T}_{\mathrm{SST}}\, dx\right]\Bigg|_{42^\circ\mathrm{N}}, \qquad (7.7)$$

where $\overline{T}_{\mathrm{SST}}$ is the northern winter time mean SST. Winter SSTs are used because during winter stratification is eroded and water from the interior exposed to the surface, allowing the use of SST as a proxy for the internal temperature of the ocean. In the summer stratification is strong and therefore the surface temperature is not representative of internal temperature. Note that the magnitude of $A_{V'\overline{\mathrm{SST}}}$ is not directly comparable with the magnitude of $Q_{v'\overline{T}}$ since only surface temperatures are used. However the variability of $A_{V'\overline{\mathrm{SST}}}$ can be compared to the variability of $Q_{v'\overline{T}}$. The red curve in figure 7.12 shows this approximation. Like the previous approximation, it is significantly correlated with $Q_{v'\overline{T}}$ at the 5% level. The implication of this is that we are able to approximate the variability of the $Q_{v'\overline{T}}$ component of the total heat flux to a reasonable degree using only fields that can be measured at the surface.

The correlations between the approximations and the calculated time series are statistically significant at the 5% level in both cases. Although significant, the magnitude of these correlations does not exceed 0.5. This likely reflects the considerable leap that has been made from computing the $Q_{v'\overline{T}}$ component of the meridional heat transport from model fields of v and T, to computing approximations using just surface winds and SST.

The Sverdrup/SST approximation $A_{V'\overline{\mathrm{SST}}}$ (equation 7.7) has been shown to represent the variability of $Q_{v'\overline{T}}$. Since the computation of $A_{V'\overline{\mathrm{SST}}}$ requires only surface fields, it can readily be computed for observations. In figure 7.13 $A_{V'\overline{\mathrm{SST}}}$ for both HiGEM1.2 and observations is shown plotted with the time-derivative of SST anomaly averaged over the region bounded by 30°N, 42°N, and the Pacific east and west coasts. This is a comparison between rate of change of SST (which is closely related to heat content during winter) to anomalous ocean heat transport, which are physically comparable quantities.

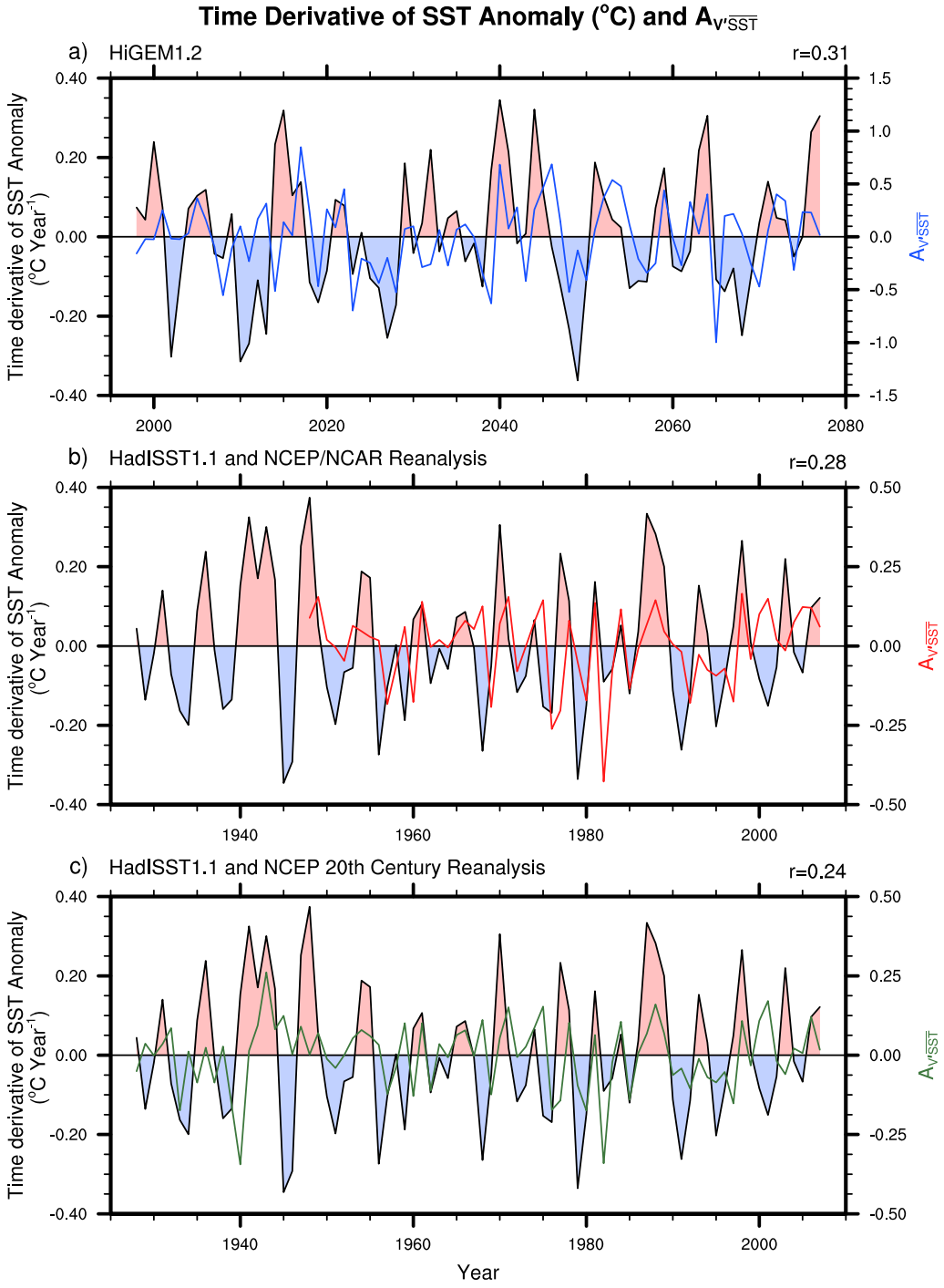

Figure 7.13: Rate of change of SST anomaly averaged over the region bounded by 30°N, 42°N, and the Pacific east and west coasts and the Sverdrup/SST approximation to $Q_{v'\overline{T}}$ ($A_{V'\overline{SST}}$, equation 7.7) for a) HiGEM1.2, b) HadISST1.1 and NCEP/NCAR Reanalysis, c) HadISST1.1 and NCEP 20th Century Reanalysis.

There are two panels for observational data. Figure 7.13b uses the same NCEP/NCAR reanalysis data that is used throughout this thesis. This data set extends back to 1948. Figure 7.13c uses the more recently developed data set from the NCEP Twentieth Century Reanalysis Project (*Compo et al.*, 2011), which extends back to 1871. In all three cases the approximated ocean heat transport is significantly correlated with the rate of change of SST at the 5% level. We also observe that the magnitude of the correlation coefficient is similar in all three cases. This implies that the physics we know are occurring in HiGEM1.2, that we have approximated with $A_{V'\overline{\mathrm{SST}}}$, may also be occurring in the real ocean.

It has been demonstrated that year-round anomalous heat transport in the North Pacific is primarily due to transport of heat by anomalous meridional velocities, with transport of anomalous temperatures making a secondary but not insignificant contribution. It has also been demonstrated that the component of anomalous heat transport due to anomalous meridional velocity can be approximated from wind stress using the Sverdrup relation and winter SST. The variability of the Sverdrup derived heat transport is related to the variability of SST in HiGEM1.2 and observations, suggesting that the same physics that are responsible for the North Pacific SST variability in HiGEM1.2 are operating in the real world.

7.4.4 Persistence of North Pacific SST anomalies

It has been suggested that persistent SST anomaly patterns that are part of long term variability may be generated by self sustaining mechanisms (e.g., *Latif and Barnett*, 1994; *Nakamura et al.*, 1997; *Peng and Whitaker*, 1999). In the previous section it was demonstrated that anomalous wind driven ocean circulation is related to the long term North Pacific SST variability in HiGEM1.2. It could be possible that the SST anomaly pattern in the North Pacific associated with decadal scale variability forces a spatial pattern of wind stress that in turn reinforces the SST anomaly. This would allow the SST anomaly to persist. The following work represents a preliminary attempt to explain how North Pacific SST anomalies develop and persist on time scales longer than interannual.

The contours in figure 7.14 show November–March wind stress curl anomaly regressed onto SST averaged over the area bounded by 30°N, 42°N, and the Pacific east and west coasts for HiGEM1.2. The arrows are the regressed wind stress anomaly vectors.

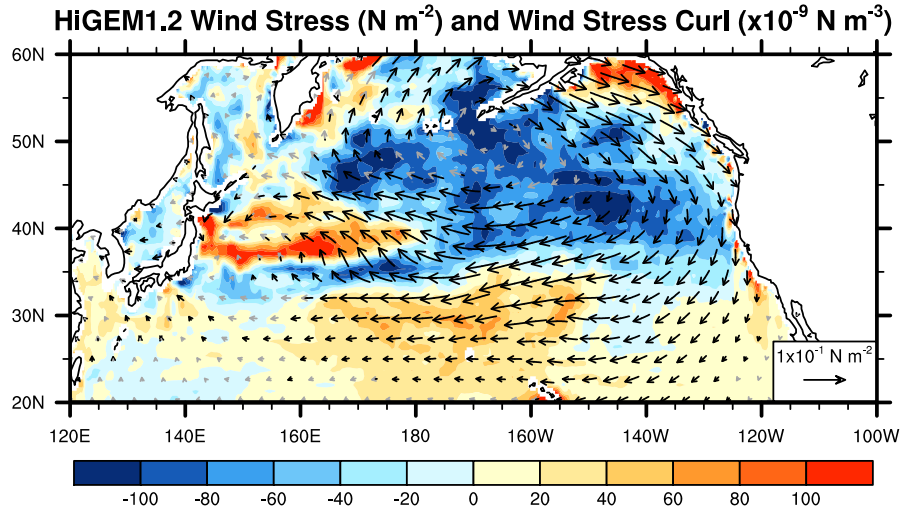

Figure 7.14: Wind stress curl (contours, $\times 10^{-8}$ N m^{-3}) and wind stress (arrows, N m^{-2}) anomalies regressed onto SST averaged over the area bounded by 30°N, 42°N, and the Pacific east and west coasts for HiGEM1.2. These are anomalies associated with a warm SST anomaly in the North Pacific. The contour interval is 20×10^{-9} N m^{-3}.

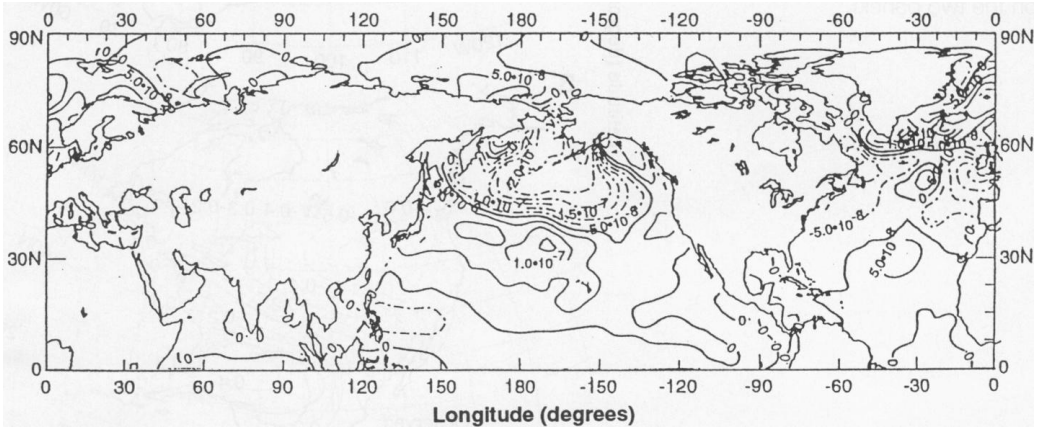

Figure 7.15: Wind stress curl (N m^{-3}) response to a warm SST anomaly in the North Pacific. Contour interval is 5×10^{-8} N m^{-3}. From *Latif and Barnett* (1994).

These are wind stress and wind stress curl anomaly patterns associated with a warm SST anomaly in the North Pacific. There is a negative wind stress curl anomaly in the north east Pacific with accompanying anticyclonic wind stress anomalies. This is indicative of wind stress forcing due to a shallower than usual Aleutian low.

It is important to make the distinction between these associated atmospheric anomalies and atmospheric anomalies that are directly caused by the anomalous SST. The type of atmospheric anomaly that is caused by North Pacific SST anomalies typical of those associated with decadal variability have been investigated by other groups working on a variety of problems. *Latif and Barnett* (1994) applied SST forcing typical of the spatial pattern of decadal scale SST variability to the atmospheric component of the ECHO model (*Latif et al.*, 1994), and present the atmospheric response as a map of wind stress curl anomaly (figure 7.15). *Peng and Whitaker* (1999) applied an SST perturbation much like that in the North Pacific EOF 1 for observations (7.5a). Although they do not present any results in terms of wind stress or wind stress curl, they do present the stream function response which is qualitatively similar to the stream function response presented by *Latif and Barnett* over the North Pacific. These two studies find consistent patterns of atmospheric response to a North Pacific SST anomaly. The wind stress and wind stress curl responses of *Latif and Barnett* are qualitatively similar to the anomaly patterns in figure 7.14. This suggests that the pattern of wind stress anomaly associated with a warm SST anomaly in the North Pacific is the same as the pattern of wind stress caused by a warm SST anomaly in the North Pacific, and that the extra-tropical SST anomalies cause the associated atmospheric response. This is a somewhat speculative result, as we only compare the associated anomaly pattern to a single anomaly response found by forcing a single coupled model with a decadal-type SST pattern. We are therefore not in a position to be able to draw a robust conclusion regarding the physical mechanism that occurs.

The wind stress curl anomaly pattern in figure 7.14 can be used as input to the Sverdrup approximation to oceanic heat transport (equation 7.6) to approximate the transport of heat into the region of the North Pacific bounded by 30°N and 42°N by this particular wind stress pattern. The magnitude of this value, which corresponds to the anomaly associated with a 1°C change in SST, should be comparable to the magnitude of the time series of $A_{V'\overline{T}}$ in figure 7.12b. The resulting value ($A_{V'\overline{T}} = 0.38$) is positive which implies

that the pattern of wind stress curl associated with a warm SST anomaly in the North Pacific acts to converge more heat into this region of the North Pacific. The magnitude of this value is comparable to the size of the peaks in figure 7.12a, and it is clear that this anomalous transport of heat is significant. It was tentatively suggested previously that the atmospheric and SST anomalies act to sustain one another, and this finding strongly supports that suggestion, and further provides a mechanism by which this is achieved.

However, the self sustaining mechanism concept cannot be used to explain the pseudo-oscillatory nature of the decadal variability in the North Pacific. We note that only the larger amplitude anomalies in PC 1 (figure 7.7b) persist for longer than a year or two. In the framework of a self sustaining mechanism this suggests that there could be a critical amplitude of SST anomaly that is sufficient to force the wind stress pattern in order to sustain itself. This idea would explain why only the larger magnitude perturbations are persistent. Even this does not explain how an anomaly can be eroded once it is established. It is likely that the wind stress forcing that sustains the SST anomaly pattern is eroded by stochastic forcing, that is by the variability due to random and chaotic atmospheric transients over the North Pacific. Eventually the wind stress forcing will be eroded to an extent that the SST anomaly is too weak to generate the required atmospheric forcing to sustain itself. This would cause the anomaly to be completely eroded and the opportunity for an another anomaly to become established.

7.5 Discussion

A method to isolate spatial and temporal patterns of decadal scale variability in the Pacific has been developed. A key requirement of the method was that these spatial and temporal signatures should be able to be compared to those associated with El Niño, in order that the decadal scale modes could be confidently described as different from those associated with El Niño. This meant the method could not make use of low-pass filtering (e.g., *Zhang et al.*, 1997) or systematic mode separation (e.g., *Folland et al.*, 1999). The method instead utilises EOF analysis in two mutually exclusive domains, a tropical Pacific domain and an extra-tropical North Pacific domain.

The spatial and temporal patterns obtained from analysis of the tropical Pacific domain for observations and both high and low resolution models describe El Niño. The spatial

and temporal patterns obtained from analysis of the extra-tropical North Pacific domain show spatial and temporal variability different from that associated with El Niño. In general the spatial patterns show a significant cold SST anomaly in the North Pacific that extends westward to the Pacific western boundary, and a warming in the tropical Pacific that is broader and weaker than that associated with El Niño. In a general sense, the temporal variability of the SST anomaly in the extra-tropical North Pacific domain appears to be on longer time scales than El Niño, although there is still a significant amount of high frequency variability, particularly in HadGEM1.2. The signal of decadal scale variability in HadGEM1.2 has not stood out against noise as well as in HiGEM1.2 or observations, as evidenced by the degeneracy of the leading EOF pair. This could be due to erroneous interannual variability due to the erroneous North Pacific SST response to El Niño (chapter 3) interfering with the mechanism that controls longer scale variability. The higher horizontal resolution of HiGEM1.2 has resulted in a clearer decadal scale variability signal, perhaps due in part to its accurate representation of the extra-tropical response to El Niño.

The physical mechanism causing the North Pacific spatial SST anomaly patterns and their associated temporal variability in HiGEM1.2 is investigated through analysis of the heat budget of a slab of the Pacific Ocean containing the centre of action of EOF 1. This analysis revealed that the cumulative effects of heat transport anomalies in the ocean is responsible for producing heat content anomalies which are exposed to the surface as SST anomalies during northern winter. It was found that the wind driven component of the ocean heat transport was the primary driver of the ocean heat transport anomalies.

A proposed mechanism for the decadal scale variability in HiGEM1.2 is as follows. Initially an SST anomaly develops, which causes an atmospheric response. The wind stress associated with this atmospheric response acts to reinforce the SST anomaly that caused it, through alterations to the transport of heat in the ocean. This self sustaining mechanism allows the SST anomaly to persist. The SST anomaly is then eroded, likely due through the action of chaotic transient atmospheric disturbances eroding the pattern of wind stress forcing. It seems there may be a critical value, below which SST anomalies are unable to develop this self sustaining feedback mechanism. Once an SST anomaly is eroded below this level it dies away. This proposed oscillatory mechanism could account

for the both the low frequency, and the high frequency variability noted in the temporal signature of extra-tropical North Pacific variability. However, in light of relying on the results of *Latif and Barnett* (1994), the evidence for this mechanism is perhaps somewhat circumstantial.

Chapter 8

Conclusions

The broad aim of this thesis was to understand the impact of higher horizontal resolution in coupled climate models on tropical–extra-tropical interactions in the Pacific. Conclusions are now drawn regarding the representation of a number of key dynamical climate processes in higher horizontal resolution.

8.1 Summary of results

The key results of this thesis can be summarised as follows:

The extra-tropical response to El Niño in coupled models: A coupled climate model HadGEM1.2, with horizontal resolution typical of the models used for the Intergovernmental Panel on Climate Change (IPCC) fourth assessment report (AR4), suffers from serious errors in the representation of the extra-tropical response to El Niño. However, a higher resolution configuration of the same model (HiGEM1.2) is able to simulate this process with a good degree of accuracy. The immediate cause of the error in the low resolution model is an erroneous atmospheric basic state upon which Rossby wave anomalies propagate.

The effect of independently varying atmospheric and oceanic resolution on the extra-tropical response to El Niño: Integrations of the high and low resolution atmospheric components with the same prescribed surface forcing show similar realistic performance with respect to the extra-tropical response to El Niño. When varying the resolution of the

atmospheric and oceanic components independently, the model with high resolution in the oceanic component and low resolution in the atmospheric component performs significantly better, with respect to the extra-tropical response to El Niño, than the model with low resolution in the oceanic component and high resolution in the atmospheric component. These findings suggest that the primary source of the error in the representation of the atmospheric basic state in the low resolution coupled model is in the oceanic component and not in the atmospheric component.

SST biases as the cause of the erroneous low resolution extra-tropical response to El Niño: The errors in the atmospheric basic state in the low resolution model can be explained by errors in the mean sea surface temperature (SST) field. Forcing the high resolution atmospheric component with erroneous sea surface temperature boundary conditions representative of the SST in the low resolution coupled model generates an erroneous atmospheric basic state of the kind observed in the low resolution model. Perturbing the high resolution atmospheric component with a localised SST bias from the low resolution model produces features in the atmospheric basic state that are consistent with the atmospheric basic state in the low resolution coupled model.

The extra-tropical response to El Niño in a changing climate: Under a strong climate change scenario there is a shifted and reduced magnitude extra-tropical response to El Niño. Changes in the forcing of Rossby waves, rather than changes in their preferred propagation paths, are most important when considering the climate change response. The change in the extra-tropical response to El Niño in a climate with atmospheric CO_2 concentrations four times more than in the control is much less than the change due to a reduction in horizontal resolution, meaning the lower resolution models are not suitable for climate change predictions relating to the extra-tropical response to El Niño.

Identification and analysis of low frequency variability in the North Pacific: Low frequency SST variability in the North Pacific ocean is evident in both high and low resolution coupled models. The low resolution model does not have as strong a low frequency signal as the high resolution model. This is perhaps because the poor representation of the

North Pacific SST response to El Niño in the low resolution model interferes with the processes controlling low frequency variability in the North Pacific. Variability in horizontal ocean circulation is the primary cause of the heat transport anomalies that cause this low frequency signal in HiGEM1.2. The anomalous heat transport can be approximated for using only surface fields. This approximation has similar variability in observations and HiGEM1.2 suggesting the same physics operate in the real ocean–atmosphere system. It is speculated that this type of variability could be be caused by a positive feedback mechanism between the ocean and the atmosphere, whereby anomalous SSTs induce atmospheric circulation anomalies which in turn induce ocean heat transport anomalies that reinforce the original SST anomaly.

8.2 Discussion

A common theme of the results from chapters 3, 4, and 5 is that an accurate simulation of climate variability requires an accurate simulation of the time-mean climatology. A model with a climatology shifted from that of observations does not simply exhibit the observed mechanisms of climate variability about a shifted mean state. Instead the physics that are responsible for the climate variability can be altered thus producing variability that is different to that observed. This is a vital point for climate model development, and cannot be overemphasised.

The results of this work have demonstrated that in order to produce a realistic simulation of the extra-tropical response to El Niño, a realistic simulation of the atmospheric basic state over the North Pacific is essential. A key influence on the atmospheric basic state is the simulation of SST, and particularly the mean state SST bias. Minimising these SST biases is therefore of critical importance. Higher horizontal resolution in the oceanic model component has been shown to reduce these mean state SST biases, suggesting that with respect to simulating the extra-tropical response to El Niño, increased oceanic horizontal resolution is more valuable than increased horizontal resolution in the atmospheric model component.

The higher resolution of the HiGEM models and reduced mean state biases has allowed them to perform better than the lower resolution HadGEM configurations. This performance gain with respect to the atmospheric bridge mechanism and the extra-tropical

response is now well understood, and allowed the high resolution model to be used with confidence for the climate change projection study. It was shown that the atmospheric basic state in terms of Rossby wave propagation paths is not the dominating factor in the climate change response, but rather it is changes to the way Rossby waves are generated that are important. This implies that models must show high fidelity not just in the spatial structure of the atmospheric jets, but also in the simulation of atmospheric circulation features such as the Hadley cell.

8.2.1 Evaluation of methodology

It would have been preferable to use version 1.2 of the HiGEM and HadGEM model components for the cross coupled experiments in chapter 4 and for the climate change experiments in chapter 6 because the 1.2 version of HiGEM has the most realistic simulation of the extra-tropical response to El Niño of all the models considered. However, integrations of the 1.2 version in these configurations have not been performed and would have taken an unfeasibly large amount of extra time to perform for this work. The result of this is a somewhat increased uncertainty when evaluating the performance of cross resolution configurations and climate change projections on the extra-tropical response to El Niño. It would have been beneficial to perform the same type of analysis on integrations of other newly developed high resolution models such as those to be submitted to the imminent Coupled Model Intercomparison Project (CMIP5) and the the IPCC's fifth assessment report (AR5). This would allow the testing of sensitivity to a changing climate in a multi-model ensemble. Unfortunately these integrations will arrive too late to be included in this work.

A lot of time was spent testing methods for the extraction of decadal scale variability signals. Many of the methodologies used by other authors (e.g., *Zhang et al.*, 1997; *Folland et al.*, 1999) were attempted on data from HadISST1.1, HiGEM, and HadGEM, but no interpretable results were yielded. Although this process did not yield any useful results, it was an excellent exercise in rigorous data analysis. Initial analysis of the nature of decadal scale variability in HiGEM1.2 and HadGEM1.2 could have been more straightforward had longer integrations for both models been available. This would have

allowed for the use of time series analysis techniques such as spectral analysis to determine the frequency characteristics of the variability in the North Pacific. Such a technique was successfully applied by *Deser and Kwon* (2007) on a 650 year control integration of the NCAR Community Climate System Model (*Kiehl and Gent*, 2004), although this is a comparatively low resolution coupled model. A longer time series of observed SST is almost certainly required in order to make robust conclusions about the nature of long term variability in the North Pacific, highlighting the importance of computer models in this area of science.

It was shown that long term variability in the North Pacific was due to variability of heat transport internally in the HiGEM1.2 ocean. Several layers of approximation were then required to demonstrate that the same mechanism is likely to operate in the real ocean. Confirmation of this result can only really be achieved when a sufficiently long time series of sub-surface ocean observations are available. In the future, the data collected from observational campaigns such as the Argo Project's profiling floats (e.g., *Gould*, 2005) could be used with great effect for this type of study. In the mean time we must rely on our improving computer models for this task.

8.2.2 Further work

Many answers have been provided regarding the behaviour of the extra-tropical response to El Niño in high and low resolution coupled models. However, there is still much work that could usefully be done in this area using the HiGEM/HadGEM models. This work showed that SST biases could explain the poor extra-tropical response to El Niño in low resolution, but the question of why the low resolution model has such SST biases was not formally addressed. Better understanding of the processes that lead to climatological biases in coupled models would form an important contribution to the science of climate modelling. One avenue of research that could achieve this is the development of even higher resolution coupled models. These would allow the detailed quantitative study of small scale processes that control the heat transports in the ocean. Understanding the role of these processes in setting up a realistic oceanic mean state, and how they interact with the atmosphere, could lead to better physical paramterisations being developed and applied to lower resolution coupled models.

A key question arising from the study of the extra-tropical response to El Niño in a warming climate presented here is as follows: if HiGEM had a smaller (or no) SST bias, would the extra-tropical response to El Niño remain unchanged in a future warming scenario? This is a difficult question to address using only the HiGEM models. However, investigating the same processes in all the AR5 models that are able to realistically simulate the extra-tropical response to El Niño could provide more insight. In particular it would be valuable to know whether the conclusion found here, that changes to Rossby wave generation are dominant over changes in the atmospheric basic state in determining the climate change response, is robust in an ensemble of different high resolution coupled models.

The proposed mechanism for decadal variability in the North Pacific introduced the idea of a self-sustaining atmosphere–ocean interaction. This idea is speculative at present, as it is partly based on a comparing a response to an SST anomaly pattern in HiGEM1.2 with the response to forcing a single model (different to HiGEM) with a pattern of SST that is like, but not the same as the decadal SST pattern found in HiGEM1.2. This preliminary theory could be tested by performing the forcing experiment with the HiGAM1.2 atmospheric component to obtain a result that is at least self-consistent. Further to this, the idea of critical SST amplitudes is also testable. A series of model experiments with imposed SST anomalies of varying strengths could allow us to learn if this idea is valid. This further study has the potential to shed more light on the physics behind decadal scale variations in the North Pacific.

Appendix A

List of acronyms

Acronym	Expansion
AR4	IPCC Fourth Assessment Report
AR5	IPCC Fifth Assessment Report
CDAT	Climate Data Analysis Tools
CMAP	CPC Merged Analysis of Precipitation
CMIP	Coupled Model Intercomparison Project
COADS	Comprehensive Ocean-Atmosphere Data Set
CPC	(NOAA) Climate Prediction Center
CT	Control (experiment)
DJF	December–January–February
ECMWF	European Centre for Medium range Weather Forecasting
ENSO	El Niño-Southern Oscillation
EOF	Empirical Orthogonal Function
EP	Equatorial Pacific
ERA	ECMWF Re-Analysis
GCM	General Circulation Model
HadGAM	Hadley Centre Global Atmosphere Model
HadGEM	Hadley Centre Global Environment Model
HadGOM	Hadley Centre Global Ocean Model
HiGAM	High resolution Global Atmosphere Model

Acronym	Expansion
HiGEM	High resolution Global Environment Model
HiGOM	High resolution Global Ocean Model
IPCC	Intergovernmental Panel on Climate Change
IPO	Inter-decadal Pacific Oscillation
ITCZ	Inter-Tropical Convergence Zone
LAPACK	Linear Algebra PACKage
MJO	Madden-Julian Oscillation
NAO	North Atlantic Oscillation
NCAR	National Center for Atmospheric Research
NCEP	National Center for Environmental Prediction
NCL	NCAR Command Language
NDJFM	Novermber–December–January–February–March
NOAA	National Oceanic and Atmospheric Administration
PC	Principal Component
PCA	Principal Component Analysis
PDO	Pacific (inter-)Decadal Oscillation
PNA	Pacific North American
PT	Pantropical (experiment)
RB	Regional Bias (experiment)
RMS	Root-Mean-Squared
RSOI	Reduced Space Optimum Interpolation
RWS	Rossby Wave Source
SSH	Sea Surface Height
SST	Sea Surface Temperature
SVD	Singular Value Decomposition
TAR	IPCC Third Assessment Report
UKMO	United Kingdom Meteorological Office
UM	(UKMO) Unified Model

Appendix B

EOF analysis

B.1 Mathematical description

The data set to be analysed consists of observations of a variable at M positions in space, $x_1, x_2, \ldots, x_M$, at N times, $t_1, t_2, \ldots, t_N$. We arrange these observations into the matrix $\mathbf{F}$, dimensioned $N \times M$, such that a row is a map of observations at a given time, and a column is a time series of observations at a single location in space. The structure of this matrix is:

$$\mathbf{F} = \begin{pmatrix} x_{1,1} & x_{1,2} & \cdots & x_{1,M} \\ x_{2,1} & x_{2,2} & \cdots & x_{2,M} \\ \vdots & \vdots & \ddots & \vdots \\ x_{N,1} & x_{N,2} & \cdots & x_{N,M} \end{pmatrix}. \tag{B.1}$$

The time mean is removed from each of the M time series to form the anomaly matrix $\mathbf{A}$ whose columns have zero mean, and the covariance matrix $\mathbf{R}$ is computed from

$$\mathbf{R} = \mathbf{A}^{\mathsf{T}}\mathbf{A}. \tag{B.2}$$

This matrix, dimensioned $M \times M$, contains the sample variances of the M variables along its leading diagonal, and their covariances in the off-diagonal elements. This can be interpreted as the covariance matrix because all the columns of $\mathbf{A}$ have a zero mean.

The matrices of eigenvectors, $\mathbf{C}$, and eigenvalues, Λ, of $\mathbf{R}$ are then computed by solving the eigenvalue problem

$$\mathbf{RC} = \mathbf{C}\Lambda. \tag{B.3}$$

The eigenvectors (columns of **C**) are ordered according to the size of their corresponding eigenvalue, from largest to smallest. The first eigenvector, associated with the largest eigenvalue, represents the most dominant spatial pattern of variability in **A**. The subsequent eigenvectors describe spatial structures of variability, each orthogonal to all those before it, in order of decreasing contribution to the total variance in **A**. It is the ordered eigenvectors of **A** that are referred to as EOFs. Due to the orthogonality constraint, the eigenvectors are uncorrelated in space.

The fraction of the total variance in **A** that is accounted for by a particular EOF is represented by its eigenvalue. Precisely, it is the corresponding eigenvalue divided by the sum of all the eigenvalues. The covariance matrix **R** is positive definite, meaning its eigenvalues are all non-negative. Since **R** is also symmetric, it follows from the spectral representation theorem that the eigenvalues, λ_i, and column eigenvectors, $\mathbf{c}_i$, decompose R in the following manner:

$$\mathbf{R} = \lambda_1 \mathbf{c}_1 \mathbf{c}_1^{\mathsf{T}} + \lambda_2 \mathbf{c}_2 \mathbf{c}_2^{\mathsf{T}} + \cdots + \lambda_M \mathbf{c}_M \mathbf{c}_M^{\mathsf{T}}. \tag{B.4}$$

Each orthogonal projection, $\mathbf{c}_i \mathbf{c}_i^{\mathsf{T}}$, is multiplied by its eigenvalue in the summation in equation B.4. Since all the eigenvalues, λ_i, are positive we can interpret the sum of the eigenvalues as the total variance, and each individual eigenvalue as the variance contribution of a particular mode towards the total.

The EOFs describe spatial patterns of variability. The time evolution of the EOFs is computed from the projections of the maps in **A** onto the EOFs:

$$\mathbf{P} = \mathbf{AC}. \tag{B.5}$$

The columns of **P** are the time series referred to as principal components (PCs). The PCs are uncorrelated in time, which can be shown by examining the covariance structure of **P**:

$$\mathbf{P}^{\mathsf{T}}\mathbf{P} = (\mathbf{AC})^{\mathsf{T}} (\mathbf{AC}) = \mathbf{C}^{\mathsf{T}}\mathbf{A}^{\mathsf{T}}\mathbf{AC} = \mathbf{C}^{\mathsf{T}}\mathbf{RC}. \tag{B.6}$$

Since the column eigenvectors in **C** are mutually orthogonal (this follows from the symmetry of **R**), the following is true:

$$\mathbf{C}^{\mathsf{T}}\mathbf{C} = \mathbf{I}, \tag{B.7}$$

where $\mathbf{I}$ is the identity matrix. The eigenvalue problem for $\mathbf{R}$ (equation B.3) can now be re-written as

$$\mathbf{R} = \mathbf{C}\Lambda\mathbf{C}^{\mathsf{T}}. \tag{B.8}$$

Substituting this into equation B.6 and simplifying using equation B.7 gives

$$\mathbf{P}^{\mathsf{T}}\mathbf{P} = \Lambda. \tag{B.9}$$

This is an important result which demonstrates that the variance of a PC is equal to its associated eigenvalue, and that the PCs are uncorrelated since the off-diagonal elements of Λ are zero.

B.2 Computational issues

There are difficulties associated with EOF analysis of large data sets. The large number of grid points in climate models with high horizontal resolution means that the number of variables, M, is large. Conventional EOF analysis requires computation of the $M \times M$ covariance matrix, and solution of its eigenvalue problem. This is difficult, even on modern computers, when M is large. Hence, it is desirable to avoid computing the covariance matrix at all when working with large data sets.

This aim can be achieved by first considering the scaling of the PCs. Since the eigenvalues of $\mathbf{R}$ are non-negative, it is possible to define a useful normalisation for the PCs. A normalised PC, ϕ_j, can be defined as

$$\phi_j = \frac{\mathbf{p}_j}{\sqrt{\lambda_j}}, \tag{B.10}$$

where $\mathbf{p}_j$ is a column of $\mathbf{P}$. When the ϕ_j are ordered as the column vectors of the matrix Φ we get the result

$$\Phi^{\mathsf{T}}\Phi = \mathbf{I}. \tag{B.11}$$

Hence, this normalisation results in each PC having unit variance. By rearranging equation B.5, and defining a diagonal matrix $\mathbf{D}$ with $\sqrt{\lambda_j}$ on the diagonal, it is possible to write an expression for the anomaly matrix $\mathbf{A}$ in terms of normalised principal component

time series and eigenvectors:

$$\mathbf{A} = \mathbf{P}\mathbf{C}^{\mathsf{T}} = \mathbf{\Phi}\mathbf{D}\mathbf{C}^{\mathsf{T}}. \tag{B.12}$$

This expresses the anomaly matrix $\mathbf{A}$ in terms of its singular value decomposition (SVD). SVD is a general matrix decomposition that decomposes any $n \times m$ matrix $\mathbf{A}$ into the form:

$$\mathbf{A} = \mathbf{U}\Gamma\mathbf{V}^{\mathsf{T}}, \tag{B.13}$$

where $\mathbf{U}$ is an $n \times n$ orthonormal matrix, Γ is a diagonal $n \times m$ matrix, and $\mathbf{V}$ is an $m \times m$ orthonormal matrix. The elements on the diagonal of Γ, $\gamma_{i,i}$, are the singular values of $\mathbf{A}$. The columns of $\mathbf{U}$ and $\mathbf{V}$ contains the singular vectors of $\mathbf{A}$. The SVD of $\mathbf{A}$ can be computed without having to compute the covariance matrix, yet gives an equivalent result to solving the eigenvalue problem of $\mathbf{R}$. The equivalence of these methods can be verified by comparing expressions for the covariance matrix $\mathbf{R}$. Firstly equation B.8, and secondly the covariance matrix formed by first taking the SVD of the anomaly matrix

$$\mathbf{R} = \mathbf{A}^{\mathsf{T}}\mathbf{A} = \left(\mathbf{U}\Gamma\mathbf{V}^{\mathsf{T}}\right)^{\mathsf{T}}\left(\mathbf{U}\Gamma\mathbf{V}^{\mathsf{T}}\right) = \mathbf{V}\Gamma^{\mathsf{T}}\mathbf{U}^{\mathsf{T}}\mathbf{U}\Gamma\mathbf{V}^{\mathsf{T}} = \mathbf{V}\Gamma^{\mathsf{T}}\Gamma\mathbf{V}^{\mathsf{T}}. \tag{B.14}$$

It is clear that from equations B.8 and B.14 that $\mathbf{C} = \mathbf{V}$ and $\Lambda = \Gamma^{\mathsf{T}}\Gamma$. This confirms that the right singular vectors $\mathbf{V}$ are the eigenvectors of $\mathbf{R}$, and the squared singular values, γ_i^2, are the eigenvalues of $\mathbf{R}$. An extra benefit of using the SVD method to compute the EOF solution is that the normalized PCs are returned as the left singular vectors $\mathbf{U}$ (equation B.13).

If the anomaly matrix $\mathbf{A}$ is non-square with M larger than N, the rank of $\mathbf{R}$ can be at most N. This means that the number of zero singular values/eigenvalues is at least $M - N$. Since singular vectors/eigenvectors with a corresponding singular value/eigenvalue of zero make no contribution to the total variance, they can be neglected whilst still maintaining an exact solution. Some computational routines for calculating the singular value decomposition are able to compute only those singular vectors that have non-zero eigenvalues[1], which can greatly reduce the time taken to find the solution. Performing EOF

[1] The routine used for this work is the Fortran subroutine DGESDD from LAPACK (*Anderson et al.*, 1999) via Numerical Python, available online at: http://numpy.scipy.org/.

analysis using the SVD and only computing singular vectors that are potentially physically meaningful, allows what was a very large and unmanageable problem to be solved on an average personal computer in a short amount of time.

B.3 Physical interpretation

The procedure for computing EOFs is purely mathematical, there is no physics involved. Any physical interpretation is that imposed by the user. Therefore a great deal of care must be taken when attempting to apply a physical interpretation to the results of EOF analysis. There are two key situations that can arise during EOF analysis that must be considered.

Firstly, the EOF solution is restricted by the orthogonality constraint, which requires that each computed eigenvector must be orthogonal to all those preceding it. Satisfying the orthogonality constraint may introduce non-physical modes of variability that do not exist in reality. This is a major issue when attempting to interpret the lower order EOFs (i.e., EOF 2 and beyond).

Secondly, when two neighbouring EOFs explain a similar amount of variance, it is possible that the variability in the modes are 'mixed'. This leads to EOFs that could be composed of linear combinations of actual modes of variability, but are themselves non-physical. Physical interpretations of such EOFs is extremely unwise as the patterns, which may represent independent processes in the underlying dynamics, cannot be separated. There are several options for determining which eigenvectors may be interpreted and which should not. *von Storch and Zwiers* (1999) recommend against 'selection rules', and instead favour the method of *North et al.* (1982), often referred to as North's rule of thumb. *North et al.* (1982) used scaling arguments to show that the typical error between two neighbouring eigenvalues λ and between two neighbouring eigenvectors (EOFs) $\mathbf{c}$ are

$$\Delta\lambda_k \approx \sqrt{\frac{2}{N}}\lambda_k, \tag{B.15}$$

$$\Delta\mathbf{c}_k \approx \frac{\Delta\lambda_k}{\lambda_j - \lambda_k}\mathbf{c}_k, \tag{B.16}$$

where λ_j is the eigenvalue closest to λ_k and N is the number of independent temporal

samples. Pairs of eigenvalues are considered to be statistically separated if

$$| \lambda_k - \lambda_j | > \Delta\lambda_k. \tag{B.17}$$

If the condition in equation B.17 is not met and the typical error for an eigenvalue is greater than or comparable to the difference between the eigenvalue and its closest neighbouring eigenvalue then the typical error for the associated eigenvector, $\Delta\mathbf{c}$, will be comparable to the size of the closest neighbouring eigenvector. Hence the EOF will be contaminated by sampling uncertainty and be degenerate. In EOF analysis, it is typical that the first few eigenvectors are well separated. These represent the dominant physical signals. The rest of the eigenvectors will then form a degenerate set and be considered as noise.

B.4 Data preparation

EOF analysis is usually used on anomaly data. This allows for the removal of dominant known signals from the dataset such as the annual cycle. It is also important so that we can interpret the mathematical results of the EOF analysis correctly in terms of variances. The exact choice of method for generating anomalies depends upon the the study at hand, the only requirement being that the time series at each grid point has a mean of zero. The anomalies will still contain the same variances and mutual relationships as the original data, no information is lost. The input anomalies used for this work are winter anomalies relative to the winter mean.

When using EOF analysis on regions away from the equator, particularly those that span more than a few degrees of latitude, it is critically important to take into account the convergence of meridians. Weighting the input anomalies before EOF analysis prevents data at higher latitudes from carrying more importance than they should. For EOF analysis, the appropriate weighting scheme is to weight each grid cell by the square-root of the cosine of its latitude. This produces a covariance matrix that reflects the area of each matrix element.

Before EOF analysis, the input anomalies from both models are transformed onto a $1^\circ \times 1^\circ$ grid. This is so that they match the grid configuration of the observational data

they are to be compared with. This may seem like a counter-productive action, given that the main objective of this study is to determine the role of resolution. However, we must distinguish between computing physics at low resolution, and reducing the resolution of the output of a model whose physics are computed at high resolution.

Computing physics at low resolution may neglect certain interactions between small scale and large scale variability, simply because the small scale variability cannot be resolved. Computing physics at high resolution then changing the output resolution to match observations does not eliminate any physics that allowed small scale processes to interact with the large scale. It simply ensures that variability on spatial scales smaller than are resolved in the observed data set is not present in the input to EOF analysis. If this smaller scale variability were included then the resultant EOFs would likely be more noisy, and each mode would likely account for less of the total variability simply due to the noise. In the real world variability occurs on all spatial scales, but in this case we are choosing to observe the result on a $1^\circ \times 1^\circ$ grid. In essence, reducing the resolution of the model output is akin to 'observing' the models at the resolution of the observations. Standardizing the resolution of the models to the observational resolution is in fact necessary to ensure a fair comparison of the results of EOF analysis in terms of variance.

References

AchutaRao, K., and K. Sperber (2002), Simulation of the El Niño Southern Oscillation: Results from the Coupled Model Intercomparison Project, *Clim. Dynam.*, *19*(3), 191–209.

Alexander, M. A. (1990), Simulation of the response of the North Pacific Ocean to the anomalous atmospheric circulation associated with El Niño, *Clim. Dynam.*, *5*(1), 53–65.

Alexander, M. A. (1992a), Midlatitude atmosphere–ocean interaction during El Niño. Part I: The North Pacific Ocean, *J. Clim.*, *5*(9), 944–958.

Alexander, M. A. (1992b), Midlatitude atmosphere–ocean interaction during El Niño. Part II: The Northern Hemisphere atmosphere, *J. Clim.*, *5*(9), 959–972.

Alexander, M. A., C. Deser, and M. S. Timlin (1999), The reemergence of sst anomalies in the North Pacific Ocean, *J. Clim.*, *12*(8), 2419–2433.

Alexander, M. A., I. Bladé, M. Newman, J. R. Lanzante, N.-C. Lau, and J. D. Scott (2002), The atmospheric bridge: The influence of ENSO teleconnections on air-sea interaction over the global oceans, *J. Clim.*, *15*(16), 2205–2231.

Allan, R. J. (2000), ENSO and Climatic Variability in the Last 150 years, in *El Niño and the Southern Oscillation: Multiscale Variability, Global and Regional Impacts*, edited by H. F. Diaz and V. Markgraf, 1st ed., pp. 3–56, Cambridge University Press, Cambridge, UK.

Anderson, E., Z. Bai, C. Bischof, S. Blackford, J. Demmel, J. Dongarra, J. Du Croz, A. Greenbaum, S. Hammarling, A. McKenney, and D. Sorensen (1999), *LAPACK Users' Guide*, third ed., Society for Industrial and Applied Mathematics, Philadelphia, PA.

Beamish, R. J., D. J. Noakes, G. A. McFarlane, L. Klyashtorin, V. V. Ivanov, and V. Kurashov (1999), The regime concept and natural trends in the production of Pacific salmon, *Can. J. Fish. Aquat. Sci.*, *56*(3), 516–526.

Bjerknes, J. (1969), Atmospheric teleconnections from the equatorial Pacific, *Mon. Weather Rev.*, *97*(3), 163–172.

Brayshaw, D., B. Hoskins, and M. Blackburn (2008), The storm-track response to idealized SST perturbations in an aquaplanet GCM, *J. Atmos. Sci.*, *65*(9), 2842–2860.

Bryan, K. (1969), A numerical method for the study of the circulation of the world ocean, *Journal of Computational Physics*, *4*(3), 347–376.

Chen, J., B. E. Carlson, and A. D. Del Genio (2002), Evidence for strengthening of the tropical general circulation in the 1990s., *Science*, *295*(5556), 838–841.

Clarke, A. J. (2008), *Dynamics of El Niño & the Southern Oscillation*, 1st ed., 308 pp., Elsevier, Amsterdam, The Netherlands.

Collins, M., S.-I. An, W. Cai, A. Ganachaud, E. Guilyardi, F.-F. Jin, M. Jochum, M. Lengaigne, S. Power, A. Timmermann, G. Vecchi, and A. Wittenberg (2010), The impact of global warming on the tropical Pacific Ocean and El Niño, *Nat. Geosci.*, *3*(6), 391–397.

Compo, G. P., J. S. Whitaker, P. D. Sardeshmukh, N. Matsui, R. J. Allan, X. Yin, B. E. Gleason, R. S. Vose, G. Rutledge, P. Bessemoulin, S. Brönnimann, M. Brunet, R. R. Crouthamel, A. N. Grant, P. Y. Groisman, P. D. Jones, M. Kruk, A. C. Kruger, G. J. Marshall, M. Maugeri, H. Y. Mok, Ø. Nordli, T. F. Ross, R. M. Trigo, X. L. Wang, S. D. Woodruff, and S. J. Worley (2011), The Twentieth Century Reanalysis Project, *Q. J. Roy. Meteor. Soc.*, *137*(654), 1–37.

Cox, M. D. (1984), A primitive equation, three dimensional model of the ocean, *Tech. Rep. 1*, Ocean Group, GFDL, Princeton, NJ.

Davies, T., M. J. P. Cullen, A. J. Malcolm, M. H. Mawson, A. Staniforth, A. A. White, and N. Wood (2005), A new dynamical core for the Met Office's global and regional modelling of the atmosphere, *Q. J. Roy. Meteor. Soc.*, *131*(608), 1759–1782.

Dawson, A., A. J. Matthews, and D. P. Stevens (2011), Rossby wave dynamics of the extra-tropical response to El Niño: Importance of the basic state in coupled GCMs, *Clim. Dynam.*, doi:10.1007/s00382-010-0854-7, published on-line.

Deser, C., and M. L. Blackmon (1995), On the relationship between tropical and North Pacific sea surface temperature variations, *J. Clim.*, *8*(6), 1677–1680.

Deser, C., and Y.-O. Kwon (2007), North Pacific decadal variability in the Community Climate System Model version 2, *J. Clim.*, *20*(11), 2416–2433.

Deser, C., M. A. Alexander, and M. S. Timlin (1996), Upper-ocean thermal variations in the North Pacific during 1970–1991, *J. Clim.*, *9*(8), 1840–1855.

Dukowicz, J. K., and R. D. Smith (1994), Implicit free-surface method for the Brian-Cox-Semtner ocean model, *J. Geophys. Res.*, *99*(C4), 7991–8014.

Folland, C. K., D. E. Parker, A. W. Colman, and R. Washington (1999), Large scale Modes of Ocean Surface Temperature Since the Late Nineteenth Century, in *Beyond El Niño: Decadal and Interdecadal Climate Variability*, edited by A. Navarra, 1st ed., pp. 73–102, Springer-Verlag, Berlin, Germany and New York, NY, USA.

Franzke, C., K. Fraedrich, and F. Lunkeit (2000), Low-frequency variability in a simplified atmospheric global circulation model: Storm-track induced 'spatial resonance', *Q. J. Roy. Meteor. Soc.*, *126*(569), 2691–2708.

Gent, P. R., and J. C. McWilliams (1990), Isopycnal mixing in ocean circulation models, *J. Phys. Oceanogr.*, *20*(1), 150–155.

Gill, A. E. (1982), *Atmosphere–Ocean Dynamics*, 1st ed., 662 pp., Academic Press, London.

Gordon, C., C. Cooper, C. A. Senior, H. Banks, J. M. Gregory, T. C. Johns, J. F. B. Mitchell, and R. A. Wood (2000), The simulation of SST, sea ice extents and ocean heat transports in a version of the Hadley Centre coupled model without flux adjustments, *Clim. Dynam.*, *16*(2), 147–168.

Gould, W. J. (2005), From Swallow floats to Argo–the development of neutrally buoyant floats, *Deep-Sea Res. Pt. II*, *52*(3–4), 529–543.

Graham, N. E. (1994), Decadal-scale climate variability in the tropical and North Pacific during the 1970s and 1980s: Observations and model results, *Clim. Dynam.*, *10*(3), 135–162.

Graham, N. E., T. P. Barnett, R. Wilde, M. Ponater, and S. Schubert (1994), On the roles of tropical and midlatitude SSTs in forcing interannual to interdecadal variability in the winter Northern Hemisphere circulation, *J. Clim.*, *7*(9), 1416–1441.

Guilyardi, E., S. Gualdi, J. Slingo, A. Navarra, P. Delecluse, J. Cole, G. Madec, M. Roberts, M. Latif, and L. Terray (2004), Representing El Niño in coupled ocean–atmosphere GCMs: The dominant role of the atmospheric component, *J. Clim.*, *17*(24), 4623–4629.

Haltiner, G. J., and R. T. Williams (1980), *Numerical Prediction and Dynamic Meteorology*, John Wiley and Sons, New York.

Hare, S. R., N. J. Mantua, and R. C. Francis (1999), Inverse production regimes: Alaska and West Coast Pacific salmon, *Fisheries*, *24*(1), 6–14.

Hautala, S. L., D. H. Roemmich, and W. J. Schmitz, Jr. (1994), Is the North Pacific in Sverdrup balance along 24°N?, *J. Geophys. Res.*, *99*(C8), 16,041–16,052.

Holton, J. R. (2004), *An Introduction to Dynamic Meteorology*, 4th ed., 535 pp., Academic Press, London.

Hoskins, B. J., and T. Ambrizzi (1993), Rossby wave propagation on a realistic longitudinally varying flow, *J. Atmos. Sci.*, *50*(12), 1661–1671.

Hoskins, B. J., and D. J. Karoly (1981), The steady linear response of a spherical atmosphere to thermal and orographic forcing, *J. Atmos. Sci.*, *38*(6), 1179–1196.

Hoskins, B. J., M. E. McIntyre, and A. W. Robertson (1985), On the use and significance of isentropic potential vorticity maps, *Q. J. Roy. Meteor. Soc.*, *111*(470), 877–946.

Houghton, J. T., G. J. Jenkins, and J. J. Ephraums (Eds.) (1990), *Climate Change: The IPCC Scientific Assessment*, Cambridge University Press, Cambridge, United Kingdom and New York, NY, USA.

Houghton, J. T., L. G. Meira Filho, B. A. Callander, N. Harris, A. Kettenberg, and K. Maskell (Eds.) (1995), *Climate Change 1995: The Science of Climate Change. Contribution of Working Group I to the Second Assessment Report of the Intergovernmental Panel on Climate Change*, Cambridge University Press, Cambridge, United Kingdom and New York, NY, USA.

Houghton, J. T., Y. Ding, D. J. Griggs, M. Noguer, P. J. van der Linden, X. Dai, K. Makell, and C. A. Johnson (Eds.) (2001), *Climate Change 2001: The Scientific Basis. Contribution of Working Group I to the Third Assessment Report of the Intergovernmental Panel on Climate Change*, Cambridge University Press, Cambridge, United Kingdom and New York, NY, USA.

Hu, Y., and Q. Fu (2007), Observed poleward expansion of the Hadley circulation since 1979, *Atmos. Chem. Phys.*, *7*, 5229–5236.

Hurrell, J. W., J. J. Hack, A. S. Phillips, J. Caron, and J. Yin (2006), The dynamical simulation of the Community Atmosphere Model version 3 (CAM3), *J. Clim.*, *19*(11), 2162–2183.

Imada, Y., and M. Kimoto (2009), ENSO amplitude modulation related to Pacific decadal variability, *Geophys. Res. Let.*, *36*(L03706).

Inatsu, M., H. Mukougawa, and S. Xie (2002), Tropical and extratropical SST effects on the midlatitude storm track, *J. Meteorol. Soc. Jpn.*, *80*(4B), 1069–1076.

Johns, T. C., C. F. Durman, H. T. Banks, M. J. Roberts, A. J. McLaren, J. K. Ridley, C. A. Senior, K. D. Williams, A. Jones, G. J. Rickard, S. Cusack, W. J. Ingram, M. Crucifix, D. M. H. Sexton, M. M. Joshi, B.-W. Dong, H. Spencer, R. S. R. Hill, J. M. Gregory, A. B. Keen, A. K. Pardaens, J. A. Lowe, A. Bodas-Salcedo, S. Stark, and Y. Searl (2006), The new Hadley Centre climate model (HadGEM1): Evaluation of coupled simulations, *J. Clim.*, *19*(7), 1327–1353.

Kalnay, E., M. Kanamitsu, R. Kistler, W. Collins, D. Deaven, L. Gandin, M. Iredell, S. Saha, G. White, J. Woolen, Y. Zhu, A. Leetmaa, B. Reynolds, M. Chelliah, W. Ebisuazaki, W. Higgins, J. Jonowiak, K. C. Mo, C. Ropelewski, J. Wang, R. Jenne, and D. Joseph (1996), The NCEP/NCAR 40–year reanalysis project, *B. Am. Meteorol. Soc.*, *77*(3), 437–471.

Kaplan, A., Y. Kushnir, M. A. Cane, and M. B. Blumenthal (1997), Reduced space optimal analysis for historical data sets: 136 years of Atlantic sea surface temperatures, *J. Geophys. Res.*, *102*(C13), 27,835–27,860.

Karoly, D. (1983), Rossby wave propagation in a barotropic atmosphere, *Dynam. Atmos. Oceans*, *7*(2), 111–125.

Kiehl, J. T., and P. R. Gent (2004), The Community Climate System Model, version 2, *J. Clim.*, *17*(19), 3666–3682.

Kiladis, G. N., and K. M. Weickmann (1992), Circulation anomalies associated with tropical convection during northern winter, *Mon. Weather Rev.*, *120*(9), 1900–1923.

Kushnir, Y., W. A. Robinson, I. Bladé, N. M. J. Hall, S. Peng, and R. Sutton (2002), Atmospheric GCM response to extratropical SST anomalies: Synthesis and evaluation, *J. Clim.*, *15*(16), 2233–2256.

Latif, M., and T. P. Barnett (1994), Causes of decadal climate variability over the North Pacific and North America, *Science*, *266*(5185), 634–637.

Latif, M., T. Stockdale, J. Wolff, G. burgers, E. Maier-Reimer, M. M. Junge, K. Arpe, and L. Bengtsson (1994), Climatology and variability in the ECHO coupled GCM, *Tellus A*, *46*(4), 351–366.

Lau, N.-C., and M. J. Nath (1994), A modeling study of the relative roles of tropical and extratropical SST anomalies in the variability of the global atmosphere–ocean system, *J. Clim.*, *7*(8), 1184–1207.

Lu, J., G. A. Vecchi, and T. Reichler (2007), Expansion of the Hadley cell under global warming, *Geophys. Res. Let.*, *34*(L06805).

Luksch, U., and H. von Storch (1992), Modelling the low-frequency sea surface temperature variability in the North Pacific, *J. Clim.*, *5*(9), 893–906.

Madden, R. A., and P. R. Julian (1971), Detection of a 40–50 day oscillation in the zonal wind in the tropical Pacific, *J. Atmos. Sci.*, *28*(5), 702–708.

Mantua, N. J., and S. R. Hare (2002), The Pacific Decadal Oscillation, *J. Oceanogr.*, *58*(1), 35–44.

Mantua, N. J., S. R. Hare, Y. Zhang, J. M. Wallace, and R. C. Francis (1997), A Pacific interdecadal climate oscillation with impacts on salmon production, *B. Am. Meteorol. Soc.*, *78*(6), 1069–1079.

Martin, G. M., M. A. Ringer, V. D. Pope, A. Jones, C. Dearden, and T. J. Hinton (2006), The physical properties of the atmosphere in the new Hadley Centre Global Environment Model (HadGEM1). Part I: Model description and global climatology, *J. Clim.*, *19*(7), 1274–1301.

Mechoso, C. R., A. W. Robertson, N. Barth, M. K. Davey, P. Delecluse, P. R. Gent, S. Ineson, B. Kirtman, M. Latif, H. L. Treut, T. Nagai, J. D. Neelin, S. G. H. Philander, J. Polcher, P. S. Schopf, T. Stockdale, M. J. Suarez, L. Terray, O. Thual, and J. J. Tribbia (1995), The seasonal cycle over the tropical Pacific in coupled ocean–atmosphere general circulation models, *Mon. Weather Rev.*, *123*(9), 2825–2838.

Meehl, G. A., H. Teng, and G. Branstator (2006), Future changes of el Niño in two global coupled climate models, *Clim. Dynam.*, *26*(6), 549–566.

Meehl, G. A., T. F. Stocker, W. D. Collins, P. Friedlingstein, A. T. Gaye, H. M. Gregory, A. Kitoh, R. Knutti, J. M. Murphy, A. Noda, S. C. B. Raper, I. G. Watterson, A. J. Weaver, and Z.-C. Zhao (2007), Global Climate Projections, in *Climate Change 2007: The Physical Science basis. Contribution of Working Group I to the Fourth Assessment Report of the Intergovernmental Panel on Climate Change*, edited by S. Solomon, D. Qin, M. Manning, Z. Chen, M. Marquis, K. B. Averyt, M. Tignor, and H. L. Miller, Cambridge University Press, Cambridge, United Kingdom and New York, NY, USA.

Merryfield, W. J. (2006), Changes to ENSO under CO_2 doubling in a multimodel ensemble, *J. Clim.*, *19*(16), 4009–4027.

Mitas, C. M., and A. Clement (2005), Has the Hadley cell been strengthening in recent decades?, *Geophys. Res. Let.*, *32*(L03809).

Nakamura, H., G. Lin, and T. Yamagata (1997), Decadal climate variability in the North Pacific during the recent decades, *B. Am. Meteorol. Soc.*, *78*(10), 2215–2225.

Navarra, A., S. Gualdi, M. S., S. Behera, J.-J. Luo, S. Masson, E. Guilyardi, P. Delecluse, and T. Yamagata (2008), Atmospheric horizontal resolution affects tropical climate variability in coupled models, *J. Clim.*, *21*(4), 730–750.

Newman, M., G. P. Compo, and M. A. Alexander (2003), ENSO-forced variability of the Pacific Decadal Oscillation, *J. Clim.*, *16*(23), 3853–3857.

Norris, J. R. (2000), Interannual and interdecadal variability in the storm track, cloudiness, and sea surface temperature over the summertime North Pacific, *J. Clim.*, *13*(2), 422–430.

North, G. R., T. L. Bell, R. F. Cahalan, and F. J. Moeng (1982), Sampling errors in the estimation of empirical orthogonal functions, *Mon. Weather Rev.*, *110*(7), 669–706.

Pedlosky, J. (1990), *Geophysical Fluid Dynamics*, 2nd ed., 710 pp., Springer-Verlag, New York, NY, USA.

Peng, S., and W. A. Robinson (2001), Relationships between atmospheric internal variability and the responses to an extratropical SST anomaly, *J. Clim.*, *14*(13), 2943–2959.

Peng, S., and J. S. Whitaker (1999), Mechanisms determining the atmospheric response to midlatitude SST anomalies, *J. Clim.*, *12*(5), 1393–1408.

Philander, S. G. (1990), *El Niño, La Niña, and the Southern Oscillation*, 1st ed., 287 pp., Academic Press, London.

Philander, S. G. H., W. J. Hurlin, and R. C. Pacanowski (1986), Properties of long Equatorial waves in models of the seasonal cycle in the tropical Atlantic and Pacific oceans, *J. Geophys. Res.*, *91*(C12), 14,207–14,211.

Pope, V., and R. Stratton (2002), The processes governing horizontal resolution sensitivity in a climate model, *Clim. Dynam.*, *19*(3), 211–236.

Pope, V. D., M. L. Gallani, P. R. Rowntree, and S. R. A. (2000), The impact of new physical parametrizations in the Hadley Centre climate model: HadAM3, *Clim. Dynam.*, *16*(2–3), 123–146.

Preisendorfer, R. W. (1988), *Principal Component Analysis in Meteorology and Oceanography*, first ed., 425 pp., Elsevier, Amsterdam.

Quan, X.-W., H. F. Diaz, and M. P. Hoerling (2004), Changes in the tropical Hadley cell since 1950, in *The Hadley Circulation: Present, Past, and Future*, edited by H. F. Diaz and R. S. Bradley, Kluwer Academic Publishers, Dordrecht, The Netherlands.

Randall, D. A., R. A. Wood, S. Bony, R. Colman, T. Fichefet, J. Fyfe, V. Kattsov, A. Pitman, J. Shukla, J. Srinivasan, R. J. Stouffer, A. Sumi, and K. E. Taylor (2007), Climate Models and Their Evaluation, in *Climate Change 2007: The Physical Science Basis. Contribution of Working Group I to the Fourth Assessment Report of the Intergovernmental Panel on Climate Change*, edited by S. Solomon, D. Qin, M. Manning, Z. Chen, M. Marquis, K. B. Averyt, M. Tignor, and H. L. Miller, Cambridge University Press, Cambridge, United Kingdom and New York, NY, USA.

Rayner, N. A., D. E. Parker, E. B. Horton, C. K. Folland, L. V. Alexander, D. P. Rowell, E. C. Kent, and A. Kaplan (2003), Global analyses of sea surface temperature, sea ice, and night marine air temperature since the late nineteenth century, *J. Geophys. Res.*, *108*(D14), 4407.

Rayner, N. A., P. Brohan, D. E. Parker, C. K. Folland, J. J. Kennedy, V. M., T. J. Ansell, and S. F. B. Tett (2006), Improved analyses of changes and uncertainties in sea surface temperature measured in situ since the mid-nineteenth century: The HadSST2 dataset, *J. Clim.*, *19*(3), 446–469.

Ringer, M. A., G. M. Martin, C. Z. Greeves, T. J. Hinton, P. M. James, V. D. Pope, A. A. Scaife, R. A. Stratton, P. M. Inness, J. M. Slingo, and G.-Y. Yang (2006), The physical properties of the atmosphere in the new Hadley Centre Global Environment Model (HadGEM1). Part II: Aspects of variability and regional climate, *J. Clim.*, *19*(7), 1302–1326.

Roberts, M. J., and D. Marshall (1998), Do we require adiabatic dissipation schemes in eddy-resolving ocean models?, *J. Phys. Oceanogr.*, *28*(10), 2050–2063.

Roberts, M. J., H. Banks, N. Gedney, J. Gregory, R. Hill, S. Mullerworth, A. Pardaens, G. Rickard, R. Thorpe, and R. Wood (2004), Impact of an eddy-permitting ocean resolution on control and climate change simulations with a global coupled GCM, *J. Clim.*, *17*(1), 3–20.

Roberts, M. J., A. Clayton, M.-E. Demory, J. Donners, P. L. Vidale, W. Norton, L. Shaffrey, D. P. Stevens, I. Stevens, R. A. Wood, and J. Slingo (2009), Impact of resolution on the tropical Pacific circulation in a matrix of coupled models, *J. Clim.*, *22*(10), 2541–2556.

Sardeshmukh, P. D., and B. J. Hoskins (1988), The generation of global rotational flow by steady idealized tropical divergence, *J. Atmos. Sci.*, *45*(7), 1228–1251.

Schneider, N., and B. D. Cornuelle (2005), The forcing of the Pacific Decadal Oscillation, *J. Clim.*, *18*(21), 4355–4373.

Seager, R., M. Ting, I. Held, Y. Kushnir, J. Lu, G. Vecchi, H.-P. Huang, N. Harnik, A. Leetmaa, N.-C. Lau, C. Li, J. Velez, and N. Naik (2007), Model projections of an imminent transition to a more arid climate in southwestern North America, *Science*, *316*(5828), 1181–1184.

Seidel, D. J., and W. J. Randel (2007), Recent widening of the tropical belt: Evidence from tropopause observations., *J. Geophys. Res.*, *112*(D20113).

Seidel, D. J., Q. Fu, W. J. Randel, and T. J. Reichler (2008), Widening of the tropical belt in a changing climate, *Nat. Geosci.*, *1*(1), 21–24.

Shaffrey, L. C., I. Stevens, W. A. Norton, M. J. Roberts, P. L. Vidale, J. D. Harle, A. Jrrar, D. P. Stevens, M. J. Woodage, M.-E. Demory, J. Donners, C. D. B., A. Clayton, J. W. Cole, S. S. Wilson, W. M. Connolley, T. M. Davies, A. M. Iwi, T. C. Johns, J. C. King, A. L. New, J. M. Slingo, A. Slingo, L. Steenman-Clark, and G. M. Martin (2009), UK-HiGEM: The new UK High Resolution Global Environment Model. Model description and basic evaluation, *J. Clim.*, *22*(8), 1861–1896.

Solomon, S., D. Quin, M. Manning, Z. Chen, M. Marquis, K. B. Averyt, M. Tignor, and H. L. Miller (Eds.) (2007), *Climate Change 2007: The physical science basis. Contribution of working group I to the fourth assessment report of the Intergovernmental Panel on Climate Change*, Cambridge University Press, Cambridge, United Kingdom and New York, NY, USA.

Sverdrup, H. U. (1947), Wind-driven currents in a baroclinic ocean; with application to the equatorial currents of the Eastern Pacific, *P. Natl. Acad. Sci. USA*, *33*(11), 318–326.

Tanaka, H. L., N. Ishizaki, and D. Nohara (2005), Intercomparison of the intensities and trends of Hadley, Walker and monsoon circulations in the global warming projections, *Scientific Online Letters on the Atmosphere*, *1*, 77–80, doi:10.2151/sola.2005-021.

Tanimoto, Y., N. Iwasaka, K. Hanawa, and Y. Yoba (1993), Charcteristic variations of sea surface temperature with multiple time scales in the North Pacific, *J. Clim.*, *6*(6), 1153–1160.

Taylor, K. E., D. Williamson, and F. Zwiers (2000), The sea surface temperature and sea-ice boundary conditions for AMIP II simulations, *Tech. Rep. 60*, Program for Climate Model Disagnostics and Intercomparison, Lawrence Livermore National Laboratory, Livermore, California, http://www-pcmdi.llnl.gov/publications/pdf/60.pdf.

Timlin, M. S., M. A. Alexander, and C. Deser (2002), On the reemergence of North Atlantic SST anomalies, *J. Clim.*, *15*(18), 2707–2712.

Trenberth, K. E. (1997), The definition of El Niño, *B. Am. Meteorol. Soc.*, *78*(12), 2771–2777.

Trenberth, K. E., and J. W. Hurrell (1994), Decadal atmosphere–ocean variations in the Pacific, *Clim. Dynam.*, *9*(6), 303–319.

Trenberth, K. E., P. D. Jones, P. Ambenje, R. Bojariu, D. Easterling, A. Klein Tank, D. Parker, F. Rahimzadeh, J. A. Renwick, M. Rusticucci, B. Soden, and P. Zhai (2007), Observations: Surface and atmospheric climate change, in *Climate Change 2007: The Physical Science Basis. Contribution of Working Group I to the Fourth Assessment Report of the Intergovernmental Panel on Climate Change*, edited by S. Solomon, D. Qin, M. Manning, Z. Chen, M. Marquis, K. B. Averyt, M. Tignor, and H. L. Miller, Cambridge University Press, Cambridge, United Kingdom and New York, NY, USA.

Uppala, S. M., P. W. Kållberg, A. J. Simmons, U. Andrae, V. Da Costa Bechtold, M. Fiorino, J. K. Gibson, J. Haseler, A. Hernandez, G. A. Kelly, X. Li, K. Onogi, S. Saarinen, N. Sokka, R. P. Allan, E. Andersson, K. Arpe, M. A. Balmaseda, A. C. M. Beljaars, L. Van De Berg, J. Bidlot, N. Bormann, S. Caires, F. Chevallier, A. Dethof, M. Dragosavac, M. Fisher, S. Fuentes, M. Hagemann, E. Hólm, B. J. Hoskins, L. Isaken, P. A. E. M. Janssen, R. Jenne, A. P. McNally, J.-F. Mahfouf, J.-J. Morcrette, N. A. Rayner, R. W. Saunders, P. Simon, A. Sterl, K. E. Trenberth, A. Untch, D. Vasiljevic, P. Viterbo, and J. Woollen (2006), The ERA-40 Reanalysis, *Q. J. Roy. Meteor. Soc.*, *131*(612), 2961–3012.

van Oldenborgh, G. J., S. Y. Phillip, and M. Collins (2005), El Niño in a changing climate: A multi-model study, *Ocean Sci.*, *1*(2), 81–95.

Vecchi, G. A., and B. J. Soden (2007,), Global warming and the weakening of the tropical circulation, *J. Clim.*, *20*(17), 4316–4340.

Vecchi, G. A., B. J. Soden, A. T. Wittenberg, I. M. Held, A. Leetmaa, and M. J. Harrison (2006), Weakening of tropical Pacific atmospheric circulation due to anthropogenic forcing, *Nature*, *441*(4), 73–76.

von Storch, H., and F. W. Zwiers (1999), *Statistical Analysis in Climate Research*, 1st ed., 484 pp., Cambridge University Press, Cambridge.

Watanabe, M., and M. Kimoto (2000), On the persistence of decadal SST anomalies in the North Atlantic, *J. Clim.*, *13*(16), 3017–3028.

Wilks, D. S. (2006), *Statistical Analysis in the Atmospheric Sciences*, 2nd ed., 627 pp., Academic Press, London.

Willett, C. S., R. R. Leben, and M. F. Lavín (2006), Eddies and tropical instability waves in the eastern tropical Pacific: A review., *Prog. Oceanogr.*, *69*(2–4), 218–238.

Woodruff, S. D., R. J. Slutz, R. L. Jenne, and P. M. Steurer (1987), A Comprehensive Ocean–Atmosphere Data Set, *B. Am. Meteorol. Soc.*, *68*(10), 1239–1250.

Woodruff, S. D., S. J. Lubker, K. Wolter, S. J. Worley, and J. D. Elms (1993), Comprehensive Ocean–Atmosphere Data Set (COADS) release 1a: 1980–1992, *Earth Syst. Monit.*, *4*(1), 4–8.

Yeh, S.-W., and B. P. Kirtman (2006), ENSO amplitude changes due to climate change projections in different coupled models, *J. Clim.*, *20*(2), 203–217.

Zelle, H., G. J. van Oldenborgh, G. Burgers, and H. Dijkstra (2005), El Niño and greenhouse warming: Results from ensemble simulations with the NCAR CCSM, *J. Clim.*, *18*(22), 4669–4683.

Zhang, Y., J. M. Wallace, and D. S. Battisti (1997), ENSO-like interdecadal variability: 1900-93, *J. Clim.*, *10*(5), 1004–1020.